

Molecular Dynamics Study of the Interactions between Cations/Carbon Dioxide and  
Selected Mineral Surfaces

by

Zeinab Naderi Khorshidi

A thesis submitted in partial fulfillment of the requirements for the degree of

Doctor of Philosophy

in

Chemical Engineering

Department of Chemical and Materials Engineering

University of Alberta

© Zeinab Naderi Khorshidi, 2018

## **Abstract**

Undoubtedly, we need to become increasingly aware of the changes and problems introduced to our environment. Oil sands industrial waste disposal and greenhouse gas emission are the two major by-products of the industrial processes that cause environmental concerns, such as huge tailing ponds and global warming. Reducing the impact of these harmful by-products on our environment is inevitable and based on many studies clay minerals can be useful in this regard. However, due to the complex structure of the minerals, experimental procedures cannot always provide a decent insight into the interaction and reaction of minerals with the environment. Nowadays, with advancements in computing facilities, computer molecular simulation is a powerful tool which enables us to describe the behavior of the materials in different conditions in more details in higher resolution in molecular levels.

For treatment of oil sands tailings, alkali-activation of these tailings is considered as an appropriate solution which turns tailing ponds to the geopolymer through geopolymerization. The geopolymerization involves the dissolution of aluminosilicates in an alkali solution followed by the polymerization of the dissolved aluminate and silicate oligomers to form an amorphous geopolymer. It is generally accepted that the dissolution determines the properties of the resultant geopolymer. Accordingly, in the first part of the study (chapter four, five and six), a series of molecular dynamics (MD) simulations were carried out in the isothermal-isobaric (NPT) ensemble at 298 K and 1 atm to study the initial stage of dissolution process that takes place at the two basal surfaces (tetrahedral and

partially deprotonated octahedral) of kaolinite in alkali media. Two different alkali media containing  $\text{Na}^+$  and  $\text{K}^+$  cations were modeled at 1 M, 3 M, and 5 M concentrations. The influence of structural vacancies on the interaction of the basal surfaces of kaolinite exposed to alkali media was studied in chapter five and the chapter six is particularly aimed at elucidating the dissolution mechanism of kaolinite in alkali media with the presence of aqueous medium contaminants. The MD results showed that cations migrated to the vicinity of the deprotonated sites, triggering the dissociation of the nearby surface hydroxyl and aluminate groups into the solution. However,  $\text{Na}^+$  and  $\text{K}^+$  exhibited different dissolution mechanisms. In particular,  $\text{Na}^+$  induced more dissociation of the surface hydroxyl groups, whereas  $\text{K}^+$  resulted in more dissociation of aluminate groups.

Regarding the defect sites, Al vacancies on the octahedral surface promoted the dissolution of aluminate groups into the solution compared to the surface without Al vacancies. However, there existed a vacancy concentration (2 Al vacancies per 576 Al atoms) at which the dissolution amount was the maximum and above which the dissolution decreased with increasing Al vacancy concentration. In presence of inorganic salts contaminants (i.e.,  $\text{CaCl}_2$  and  $\text{MgCl}_2$ ) atomic density profiles show that all cations including those from the contaminants adsorbed on the two basal surfaces intensifying the dissociation of the aluminate groups from the deprotonated octahedral surface. The number of the aluminate groups dissociated decreased with increasing contaminants concentration. Structural analyses of the deprotonated octahedral surface indicated that the crystallinity of the surface decreased with increasing simulation time and alkali solution concentration. No dissolution of the tetrahedral surface was observed for all systems studied.

In chapter seven, MD simulation was used to study the role of water in the intercalation of carbon dioxide in a model Mg-Al-Cl-hydrotalcite mineral at ambient pressure and temperature. It was observed that high CO<sub>2</sub> storage capacity could be achieved at low water concentrations or even without the presence of water. However, high water concentrations could also yield similar CO<sub>2</sub> storage capacity but in this case, the presence of water led to a significant interlayer spacing expansion. The expansion was due to the change in the orientation distribution of the CO<sub>2</sub> molecules. Analyzing the orientation of CO<sub>2</sub> molecules revealed that they preferred to orientate parallel to the mineral surface at low water concentrations. However, as water concentration increased, CO<sub>2</sub> molecules exhibited a wider range of orientations with a significant fraction of them oriented perpendicular to the mineral surface, especially at high CO<sub>2</sub> concentrations. Also, it was observed that water molecules formed extensive hydrogen bonds network.

## Preface

The materials presented in the current thesis are parts of the research project under the supervision of Dr. Phillip Choi, which has been financially supported by Natural Sciences and Engineering Research Council (NSERC) of Canada, the Institute for Oil Sands Innovation (IOSI), Canada's Oil Sands Innovation Alliance (COSIA) and the Canadian Centre for Clean Coal/Carbon and Mineral Processing Technologies (C<sup>5</sup>MPT).

Chapter 4 of this thesis is published as **Z. Naderi Khorshidi, X. Tan, Q. Liu, P. Choi, 2017, "Molecular Dynamics Study of the Dissolution Mechanism of Kaolinite Basal Surfaces in Alkali Media"**, Journal of Applied Clay Science.

Chapter 5 of this thesis is published as **Z. Naderi Khorshidi, X. Tan, Q. Liu, P. Choi, 2017, "Influence of Structural Al and Si Vacancies on the Interaction of Kaolinite Basal Surfaces with Alkali Cations: A Molecular Dynamics Study"**, Journal of Computational Materials Science. Some parts of Chapter 5 are presented as **Z. Naderi Khorshidi, Q. Liu, P. Choi, "Molecular Dynamics Study of Influence of Vacancies on the Dissociation of Kaolinite in Alkali Media"** in 54<sup>th</sup> annual meeting of Clay Mineral Society (CMS2017), June 2017, Edmonton, AB.

Chapter 6 of this thesis is submitted to the **Journal of Physical Chemistry C** as **Z. Naderi Khorshidi, X. Tan, Q. Liu, P. Choi, 2017, "Effect of Inorganic Salt Contaminants on the Dissolution of Kaolinite Basal Surfaces in Alkali Media: A Molecular Dynamics Study"**.

Some parts of Chapter 6 are presented as **Z. Naderi Khorshidi, Q. Liu, P. Choi, "Molecular Dynamics Study of Dissolution of Kaolinite Basal Surfaces in Alkali Media: Effect of**

**Aqueous Medium Impurities**” in 67<sup>th</sup> Canadian Society of Chemical Engineering Conference (CSCHE2017), October 2017, Edmonton, AB.

Chapter 7 of this thesis is submitted to the **Journal of Physical Chemistry C** as **Z. Naderi Khorshidi, M. Khalkhali, H. Zhang, P. Choi, 2017, “Molecular Dynamics Study of the Role of Water in the Carbon Dioxide Intercalation in Chloride Ions Bearing Hydrotalcite**”. In all the research papers, I was responsible for the data collection and analysis as well as the manuscript composition. Building of simulations cells and molecular dynamics simulations as well as data analysis were carried out using, Materials Studio 8.0, LAMMPS, VMD and OVITO, respectively. In all the aforementioned publications, all other co-authors contributed to the manuscript composition and edits.

It should be mentioned that the format of this thesis is paper-based and there may be some repetition.

To My Parents

تقدیم به پدرم و مادرم ...

## Acknowledgments

I would like to thank my supervisor, Dr. Phillip Choi, for his guidance, support and patience throughout my whole PhD experience which helped me to develop my knowledge and personality.

I would especially like to acknowledge and thank Dr. Qi Liu, Dr. Hao Zhang and Dr. Xiaoli Tan for their kind guidance and helpful suggestions. A special gratitude to all my friends and colleagues for all of their continuous support and encouragement throughout my doctoral program. A special gratitude to my friends Saeed El-Kheir Nusri, Dr. Mohammad Khalkhali, Dr. Abolfazl Noorjahan, Monir Hosseini-Anvari and Sahar Saadat for being there for me when I needed good advice.

I would like to acknowledge the *Institute for Oil Sands Innovation (IOSI)* and *Canada's Oil Sands Innovation Alliance (COSIA)* and the *Canadian Centre for Clean Coal/Carbon and Mineral Processing Technologies (C<sup>5</sup>MPT)* for financial support.

I would like to gratefully express my gratitude to my dear parents and my siblings, without whom I could have never reached this stage in my life. My last, but not least, appreciation goes to my husband, Mohsen, whose love, patience and support was always with me.

# Contents

<b>Abstract</b> .....	ii
Preface.....	v
Acknowledgments .....	viii
Contents.....	ix
List of Figures .....	xiii
List of Tables.....	xix
<b>Chapter 1</b> .....	1
1. Introduction .....	1
1.1. Motivation .....	1
1.2. Objectives of the Research Project .....	7
<b>Chapter 2</b> .....	8
2. Background.....	8
2.1. Tailings .....	8
2.1.1. Tailings Treatment Technologies .....	10
2.1.1.1. Geopolymer and Geopolymerization.....	11
2.1.2. Clay Minerals .....	13
2.1.2.1. Tetrahedral Sheets .....	14
2.1.2.2. Octahedral Sheets .....	16
2.1.2.3. Layers .....	16
2.1.2.4. Interlayer Material.....	16
2.1.2.5. Adsorption and Desorption.....	18
2.2. CO <sub>2</sub> Emission .....	21

2.2.1.	Carbon capture and storage (CCS) .....	23
2.2.2.	Technologies for CO <sub>2</sub> Capture .....	23
2.2.3.	Hydrotalcite-like Compounds (HTlcs).....	25
2.3.	Summary of the Literature.....	26
<b>Chapter 3</b>	.....	<b>27</b>
3.	Molecular Dynamics Simulation.....	27
3.1.	Introduction.....	27
3.1.1.	The quasi-ergodic hypothesis.....	29
3.1.2.	Simulation ensembles .....	30
3.1.3.	Nosé-Hoover Thermostat .....	30
3.1.4.	Nosé-Hoover Barostat.....	32
3.1.5.	Periodic boundary conditions.....	33
3.2.	Force Field.....	34
3.2.1.	Non-bonded Interaction.....	35
3.2.1.1.	Electrostatic Interaction.....	35
3.2.1.2.	Van der Waals Interaction .....	38
3.2.2.	Bonded Interaction .....	39
3.2.2.1.	Bond stretching.....	39
3.2.2.2.	Angle bending.....	39
<b>Chapter 4</b>	.....	<b>41</b>
4.	Molecular Dynamics Study of the Dissolution Mechanism of Kaolinite Basal Surfaces in Alkali Media.....	41
4.1.	Introduction.....	41
4.2.	Simulation Method.....	44
4.3.	Results and Discussion.....	48
4.4.	Conclusions.....	67
<b>Chapter 5</b>	.....	<b>69</b>

5. Influence of Structural Al and Si Vacancies on the Interaction of Kaolinite Basal Surfaces with Alkali Cations: A Molecular Dynamics Study .....	69
5.1. Introduction.....	69
5.2. MD Simulation Method.....	71
5.3. Results and Discussion.....	77
5.4. Conclusions.....	89
<b>Chapter 6</b> .....	<b>91</b>
6. Effect of Aqueous Medium Impurities (MgCl <sub>2</sub> and CaCl <sub>2</sub> ) on the Dissolution of Kaolinite Basal Surfaces in Alkali Media: A Molecular Dynamics Study .....	91
6.1. Introduction.....	91
6.2. MD Simulations Methodology.....	93
6.3. Results and Discussion.....	96
6.4. Conclusion.....	112
<b>Chapter 7</b> .....	<b>113</b>
7. Molecular Dynamics Study of the Role of Water in the Carbon Dioxide Storage Capacity of Chloride Ions Bearing Hydrotalcite .....	113
7.1. Introduction.....	113
7.2. Molecular Models and Simulation Details.....	113
7.3. Results and Discussion.....	118
7.4. Conclusions.....	134
<b>Chapter 8</b> .....	<b>136</b>
8. Conclusion and Future Work.....	136
8.1. Summary and conclusion .....	136
8.2. Recommendation for the future work.....	139
<b>References</b> .....	<b>141</b>
<b>Appendix A</b> .....	<b>161</b>

Radial Distribution Function Graphs.....	161
The RDF graphs of 5 M Na <sup>+</sup> and 3 M K <sup>+</sup> systems containing different concentrations of CaCl <sub>2</sub> and MgCl <sub>2</sub> impurities are shown in Fig. A-1. ....	161
Atomic Density Profile .....	162
<b>Appendix B</b> .....	163
Atomic Density Profile .....	163
Radial Distribution Function Graphs.....	175

# List of Figures

Figure 1-1 Tailing and waste products of oil sands industry have severe effect on the environment (extracted from: [www.thestar.com/covering\\_the\\_oilsands.html](http://www.thestar.com/covering_the_oilsands.html))..... 2

Figure 1-2 Emission of CO<sub>2</sub> from different industries lead to the increase in carbon concentration in the atmosphere <sup>1</sup> (extracted from: <http://www.oica.net/category/climate-change-and-co2/>). ..... 3

Figure 1-3 analyzing a problem steps from scientific viewpoint. .... 5

Figure 1-4 Different levels of modeling and simulation <sup>3</sup>..... 6

Figure 2-1 Anatomy of oil sands tailing..... 9

Figure 2-2 Oil sands tailings pond (Extracted from CAPP website). ..... 10

Figure 2-3 The process sequences of formation of zeolite and geopolymer <sup>33</sup>..... 13

Figure 2-4 (a) Tetrahedron structure of Si and (b) octahedron structure of Al atoms in clay minerals structure. .... 14

Figure 2-5 Top view of (a) tetrahedral and (b) octahedral surface. .... 15

Figure 2-6 Front view of octahedral and tetrahedral sheets connected together via bringing oxygens. .... 15

Figure 2-7 (a) Scanning electron microscopy image of kaolinite <sup>36</sup> and (b) Its atomic structure. .... 18

Figure 2-8 (a) Scanning electron microscopy of hydrotalcite <sup>59</sup> with Mg/Al = 3 and (b) its schematic structure..... 26

Figure 3-1 Periodic boundary conditions used in MD simulations. .... 34

Figure 4-1 The two basal surfaces of kaolinite in contact with a 1 M Na<sup>+</sup> solution: (a) initial configuration, (b) a snapshot of the system described after 10 ps of NPT MD simulation, (c) a snapshot of the system after 1 ns of NPT MD simulation, and (d) a snapshot of the system in a 5 M Na<sup>+</sup> solution after 1 ns of NPT MD simulation. All NPT MD simulations were carried out at 298 K and 1 atm. The color scheme is: violet for aluminum, navy for silicon, white for oxygen, yellow for hydrogen, red for Na<sup>+</sup> (a – c) and K<sup>+</sup> (d) and blue dots are water..... 51

Figure 4-2 Schematic illustrations of the sequences of the dissociation (a) the OH group and (b) the aluminate group in the solutions containing Na<sup>+</sup> and K<sup>+</sup>, respectively, as a result of interaction between a deprotonated site on the octahedral surface and the cations..... 54

Figure 4-3 Part of the octahedral surface (top view) upon 1 ns NPT MD simulation at 298 K and 1 atm (a) initial structure, (b) 1 M Na<sup>+</sup>, (c) 5 M Na<sup>+</sup>, (d) 1 M K<sup>+</sup>, (e) 5 M K<sup>+</sup>, (f) 1 M 50/50 Na<sup>+</sup>/K<sup>+</sup>, (g) 5 M 50/50 Na<sup>+</sup>/K<sup>+</sup>. The color scheme here is violet, white, yellow, orange and dark green for Al, O, H, Na<sup>+</sup> and K<sup>+</sup>, respectively..... 57

Figure 4-4 Radial distribution functions of Al–O of the octahedral surface: (a) 1 M solutions and (b) 5 M solutions..... 59

Figure 4-5 Atomic density profiles of aluminum atoms (black), cations (red), oxygen atoms (green) and hydrogen atoms (blue) after 1 ns of NPT MD simulations: (a) 1 M Na<sup>+</sup> solution, (b) 1 M K<sup>+</sup> solution and (c) 1 M Na<sup>+</sup>/K<sup>+</sup> solution..... 62

Figure 4-6 Relative atomic fractions of hydroxyl groups released into the alkali solution and aluminum atoms (in the form of aluminates) drifted away from their initial positions for the systems containing different cations at different concentrations: (a) 1 M and (b) 5 M..... 63

Figure 4-7 Number of (a) hydroxyl groups and (b) aluminum atoms dissociated from the octahedral surface and entered into the alkali solution versus simulation time for 5 M solutions containing different cations (i.e., Na<sup>+</sup>, K<sup>+</sup>, Na<sup>+</sup>/K<sup>+</sup>)..... 65

Figure 4-8 Coordination numbers of the aluminum atoms on the octahedral surface of kaolinite, (a) 1 M solutions, (b) 5 M solutions..... 67

Figure 5-1 Top view of the kaolinite’s octahedral surface before the removal of Al atoms for the cases (a) 2, (b) 4 and (c) 6 Al vacancies. Here, Al atoms shown in blue were removed. Figures 1(d), 1(e) and 1(f) show the structures after the removal of the Al atom (atoms colored in blue in Figures 1(a), 1(b) and 1(c)) but before the molecular dynamics simulation. The color scheme here is purple, red and white for Al, O and H, respectively. For easy viewing, only surface Al, O and H atoms are shown..... 72

Figure 5-2 Top view of vacancies on the kaolinite tetrahedral surface before running simulation for (a) two, (b) four and (c) six Si vacancies. The color scheme here is yellow, red and white for Si, O and H, respectively. For clarification, solely surface Si, O and H atoms are shown. .... 74

Figure 5-3 Top view of the kaolinite’s octahedral surface with (a) 2, (b) 4 and (c) 6 Al vacancies in contact with a solution containing 5 M Na<sup>+</sup> after 1 ns of NPT MD simulation. The color scheme here is purple, red, white and navy for Al, O, H and Na<sup>+</sup>, respectively. For ease viewing, only surface Al, O and H atoms along with Na<sup>+</sup> are shown..... 78

Figure 5-4 Mean numbers of Al atoms in the kaolinite’s octahedral surface containing different amounts of Al vacancies completely dissociated into the Na<sup>+</sup> solutions as a function of simulation time (a) 3 M and (b) 5 M..... 80

Figure 5-5 Dissociation mechanisms of (a, b) an OH group and (c, d) an aluminate group from the NPT MD simulations..... 81

Figure 5-6 Configuration of the Al atoms on the octahedral surface (a) in the reference system and (b) in the system containing Al vacancies during a NPT MD simulation. .... 83

Figure 5-7 Radial distribution functions derived from the NPT MD simulations for Al atoms and structural O atoms on the kaolinite’s octahedral surface in contact with a 5 M Na<sup>+</sup> solution without and with different amounts of Al vacancies..... 84

Figure 5-8 The average number of Al atoms in kaolinite structure completely released to the solution area as a function of time in the existence of Al vacancies for K<sup>+</sup> solution at concentrations of (a) 3 M, (b) 5 M..... 86

Figure 5-9 Plot of the average number of cations (Na<sup>+</sup> and K<sup>+</sup>) diffused into the octahedral surface against the number of Al vacancies for the 3 M and 5 M solutions. .... 87

Figure 5-10 Top view of vacancies on the kaolinite’s tetrahedral surface after 1 ns NPT MD simulation run for 5 M Na<sup>+</sup> solution for the systems containing (a) two, (b) four and (c) six Si vacancies. The color scheme here is yellow, red, white and navy for Si, O, H and Na<sup>+</sup>, respectively. For easy viewing, only surface Si, O and H atoms along with Na cations are shown. .... 88

Figure 5-11 Radial distribution functions derived from MD simulations for Si atoms and structural O atoms on the tetrahedral surface of kaolinite in contact with a 5 M Na<sup>+</sup> solution without vacancies and kaolinite with different numbers of Si vacancies..... 89

Figure 6-1 Initial configurations of the 3 M Na<sup>+</sup> systems (all species initially placed in the middle of the solutions) containing (a) 0.1 M CaCl<sub>2</sub>, (c) 0.3 M CaCl<sub>2</sub> and (e) 0.5 M CaCl<sub>2</sub>, and the corresponding final configurations of the systems of (b) 3 M Na<sup>+</sup>-0.1 M CaCl<sub>2</sub>, (d) 3 M Na<sup>+</sup>-

0.3 M CaCl<sub>2</sub>, (f) 3 M Na<sup>+</sup>-0.5 M CaCl<sub>2</sub>, after 1 ns NPT simulation. The color scheme is: orange for aluminum, navy for silicon, white for oxygen, yellow for hydrogen, pink for Na<sup>+</sup>, blue for Cl<sup>-</sup>, red for Ca<sup>2+</sup> and tiny blue dots are water. .... 98

Figure 6-2 Atomic density profile of the 3 M Na<sup>+</sup> system containing (a) and (b) 8 CaCl<sub>2</sub> molecules, (c) 8 MgCl<sub>2</sub> molecules and (d) 4 CaCl<sub>2</sub> and 4 MgCl<sub>2</sub> molecules, (e) 26 CaCl<sub>2</sub> molecules, (f) 26 MgCl<sub>2</sub> molecules, (g) 13 CaCl<sub>2</sub> and 13 MgCl<sub>2</sub> molecules, (h) 42 CaCl<sub>2</sub> molecules, (i) 42 MgCl<sub>2</sub> molecules and (i) 21 CaCl<sub>2</sub> and 21 MgCl<sub>2</sub> molecules. ....103

Figure 6-3 The number of aluminate groups dissociated from the octahedral surface as a function of simulation time in the presence of (a) 3 M Na<sup>+</sup> and different concentrations of CaCl<sub>2</sub>, (b) 3 M Na<sup>+</sup> and different concentrations of MgCl<sub>2</sub> molecules, (c) 3 M Na<sup>+</sup> and different concentrations of 50/50 CaCl<sub>2</sub> and MgCl<sub>2</sub> mixture, (d) 5 M Na<sup>+</sup> and different concentrations of CaCl<sub>2</sub>, (e) 5 M Na<sup>+</sup> and different concentrations of MgCl<sub>2</sub> and (f) 5 M Na<sup>+</sup> and different concentrations of 50/50 CaCl<sub>2</sub> and MgCl<sub>2</sub> mixture. ....106

Figure 6-4 The number of aluminate groups dissociated from the octahedral surface as a function of simulation time in the presence of (a) 3 M K<sup>+</sup> and different concentrations of CaCl<sub>2</sub>, (b) 3 M K<sup>+</sup> and different concentrations of MgCl<sub>2</sub>, (c) 3 M K<sup>+</sup> and different concentrations of a 50/50 mol/mol mixture of CaCl<sub>2</sub> and MgCl<sub>2</sub>, (d) 5 M K<sup>+</sup> and different concentrations of CaCl<sub>2</sub>, (e) 5 M K<sup>+</sup> and different concentrations of MgCl<sub>2</sub> and (f) 5 M K<sup>+</sup> and different concentrations of a 50/50 mol/mol mixture of CaCl<sub>2</sub> and MgCl<sub>2</sub>. ....109

Figure 6-5 Radial distribution functions of Al – O of the octahedral surface for 3 M Na<sup>+</sup> alkali solutions containing (a) CaCl<sub>2</sub> at different concentrations and (b) MgCl<sub>2</sub> at different concentrations. ....111

Figure 7-1 Schematic representation of the front view of the Cl-hydrotalcite/H<sub>2</sub>O/CO<sub>2</sub> system used in the present work. Color scheme: H<sub>2</sub>O molecules are shown in light blue, CO<sub>2</sub> molecules are shown in black (C) and red (O), green balls are chlorine ions, Mg, Al, O, and H atoms that make up of hydrotalcite are shown in navy, light red, white, and light yellow, respectively.....119

Figure 7-2 Change in the z dimension of the simulation cell as a function of the H<sub>2</sub>O/ Cl<sup>-</sup> ratio. ....120

Figure 7-3 Atomic density profiles of interlayer H<sub>2</sub>O and CO<sub>2</sub> in the simulation cell along the z dimension (perpendicular to the mineral surface) for the system containing 120 CO<sub>2</sub> and 864 H<sub>2</sub>O.....121

Figure 7-4 The z dimension of simulation cell as a function of number of water molecules per number of hydrotalcite unit cell at fixed numbers of CO<sub>2</sub> molecules. ....122

Figure 7-5 Histograms of angular distribution for CO<sub>2</sub> orientation relative to the axis normal to mineral surface at different water concentrations: (a) 36 H<sub>2</sub>O, (b) 72 H<sub>2</sub>O, (c) 144 H<sub>2</sub>O, (d) 432 H<sub>2</sub>O, and (e) 864 H<sub>2</sub>O. ....125

Figure 7-6 O (CO<sub>2</sub>) – H (H<sub>2</sub>O) radial distribution function at different water concentrations: (a) 36 H<sub>2</sub>O, (b) 72 H<sub>2</sub>O, (c) 144 H<sub>2</sub>O, (d) 432 H<sub>2</sub>O, and (e) 864 H<sub>2</sub>O.....128

Figure 7-7 CO<sub>2</sub> diffusion coefficient as a function of CO<sub>2</sub> concentration in Cl<sup>-</sup> ions bearing hydrotalcite with different H<sub>2</sub>O concentrations. ....129

Figure 7-8 . O (CO<sub>2</sub>) – H (OH) radial distribution function at different water concentrations: (a) 36 H<sub>2</sub>O, (b) 72 H<sub>2</sub>O, (c) 144 H<sub>2</sub>O, (d) 432 H<sub>2</sub>O, and (e) 864 H<sub>2</sub>O.....134

## List of Tables

Table 4-1 Nonbonded parameters used in the CLAYFF force field <sup>23</sup> .....	45
Table 4-2 Bonded parameters used in the CLAYFF force field <sup>23</sup> .....	45
Table 7-1 Numbers of H <sub>2</sub> O and CO <sub>2</sub> molecules used in the interlayer spacing of the model hydrotalcite.....	118
Table 7-2 The number of H <sub>2</sub> O and CO <sub>2</sub> close contacts due to dipole-quadrupole interaction for the systems listed in Table 7-1. ....	130
Table 7-3 Number of hydrogen bonds of the systems at different H <sub>2</sub> O and CO <sub>2</sub> concentrations listed in Table 7-1. ....	131

# Chapter 1

## 1. Introduction

### 1.1. Motivation

Over the past century, nature has been unintentionally damaged by using the resources found in nature by some industries. In spite of valuable products produced through the industrial processes, such as oil and gas extraction, these processes have generated waste materials leading to the appearance of a series of harmful and severe environmental problems, such as global warming and long-term waste disposal. For example, the oil sands industry is one of the key industries in Canada which provides the needs of oil and its by-products to North America. Although this industry provides long term energy resources, its operation is not so environmentally friendly. In order to reduce the impact of oil sands tailings on the environment, massive amount of waste disposal in the form of tailings should be removed after bitumen extraction. Process water, clay minerals, residual bitumen and some other organic and inorganic components exist in the oil sands tailings which sits in ponds for decades or even centuries. Beside the environmental problems, many toxic components existent in these tailings threaten the animal species life in Alberta (Fig. 1-1). Mineral hydration and changing the form of such these tailings (solidification) are of the serious concerns of oil sands industry.



Figure 1-1 Tailing and waste products of oil sands industry have severe effect on the environment (extracted from: [www.thestar.com/covering\\_the\\_oilsands.html](http://www.thestar.com/covering_the_oilsands.html)).

For solidification of tailings, its components should be analyzed and characterized. In recent years, many studies have been devoted on extraction of valuable materials and components such as  $\text{TiO}_2$  from tailings, but there is no success to make it solid in economical way. Another serious environmental problem of the extraction and usage of fossil fuels is greenhouse gas emission which is considered as a main cause of global warming. The most environmentally problematic part of greenhouse gas emission is considered to be  $\text{CO}_2$  emission. As indicated in Fig. 1-2, many industries which are using fossil fuels as their energy sources increase the  $\text{CO}_2$  concentration in the atmosphere which cannot be balanced by nature.

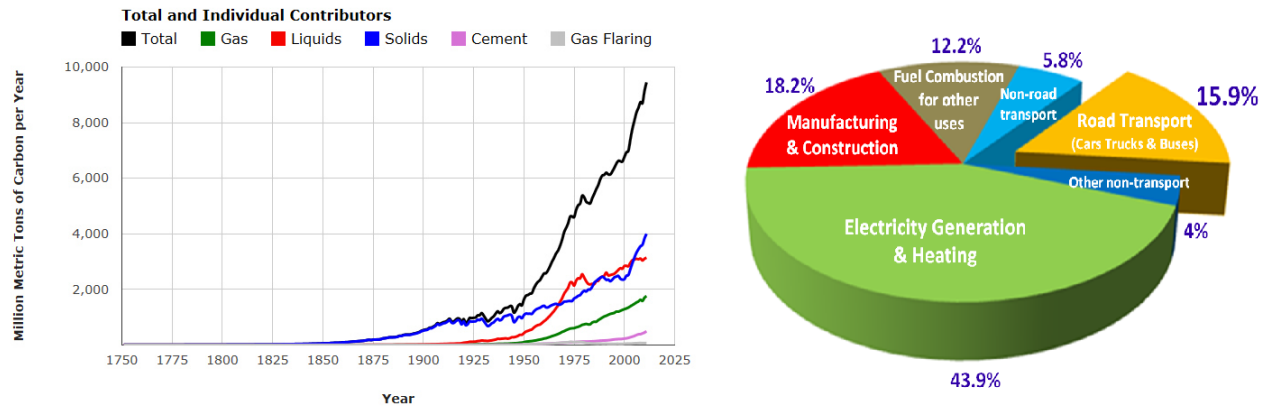


Figure 1-2 Emission of CO<sub>2</sub> from different industries lead to the increase in carbon concentration in the atmosphere <sup>1</sup> (extracted from: <http://www.oica.net/category/climate-change-and-co2/>).

To solve the environmental problems of these industries, it is not possible to shut down these industries due to the global needs for their products. Therefore, many researches have been conducted towards reducing the negative effects of these harmful waste materials. To reduce the oil sands tailings impact, one may consider changing them to the environmentally friendly products by removing the toxic components, recovering the water and solidifying the rest. With reference to CO<sub>2</sub>, it is essential to capture CO<sub>2</sub> from the atmosphere and change it to the other products. Many studies have been done in order to reduce the CO<sub>2</sub> concentration in the atmosphere by capturing CO<sub>2</sub> before and/or after combustion process; however, the reliable storage is necessary to prevent CO<sub>2</sub> from escaping. Cap rocks and layered minerals are one of the most practical materials for CO<sub>2</sub> capture and storage; however, their permeability would change due to the interaction of CO<sub>2</sub> with the clays.

To minimize the impact of these environmental problems, many experimental studies have been done and some of them showed successful outputs. For example, some studies have suggested that changing the pH of the tailings by addition of NaOH leads to the more

interaction of clay minerals in tailings. However, the details of the effect of NaOH on clays, such as kaolinite which is abundantly found in tailing, is not clear yet. Regarding the CO<sub>2</sub> emission, the effect of water entrapment on CO<sub>2</sub> capturing process as well as the effect of CO<sub>2</sub> on the properties of its storage materials are sometimes difficult to be understood experimentally. In addition, understanding the complex structure of the clay minerals and the mechanism of their intercalation with water medium cannot be obtained by experimental works, especially, since many of the layered materials are restricted to micro- and nano-sized morphologies and are less suitable for experimental analysis. In fact, to fully understand the changes of the mineral crystal surface and the processes within the mineral-water interface, it is necessary to study the interface changes via advance powerful computing techniques <sup>2</sup>. In this situation, theoretical approaches and molecular modeling techniques, such as molecular dynamics simulation, allow us, to some extent, understand the process at the molecular level.

Nowadays, computers provide a powerful tool which can help scientists to study the behavior of materials at the atomic and molecular levels. Molecular simulation is a powerful method that can reveal some details of the system behavior under different conditions and can provide higher resolution insight into the atomic interaction of the system. However, the computer simulation is in its early stage and prediction of the properties of materials just by molecular simulation and without any help from experimental data is not possible. Therefore, by considering some previous experimental data, we have tried to understand the reason of some behavior of the system in a hope of finding some valuable points to save environments. For understanding behavior of some materials, the experimental analysis provides the general information about the final product of the process; however, for

understanding the fundamental details more investigation is needed. The necessary steps of understanding a problem from scientific point of view is shown in Fig. 1-3.

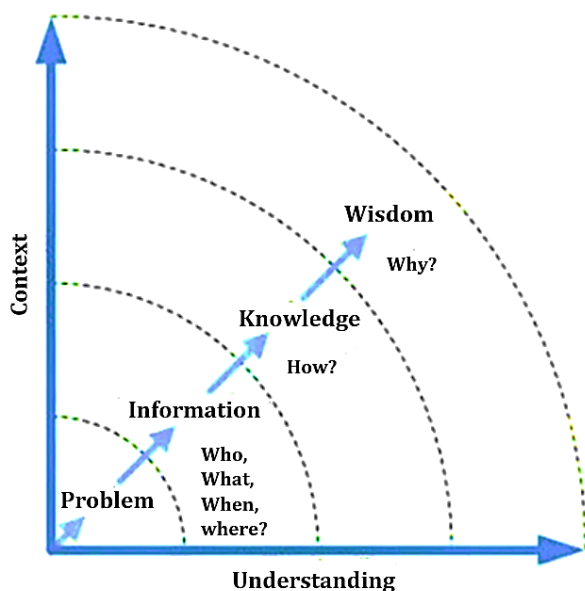


Figure 1-3 analyzing a problem steps from scientific viewpoint.

Depending on our knowledge about the process and how clear it is, different methods of modeling and simulation from atomic level to macro levels can be considered (Fig. 1-4). As mentioned earlier, in spite of substantial advancements in computing power, this is not possible to model every details of the systems and as such it is needed to simplify systems prior to molecular modeling. However, from these simplified models valuable details could be obtained which can facilitate the explanation of the system behavior in many aspects.

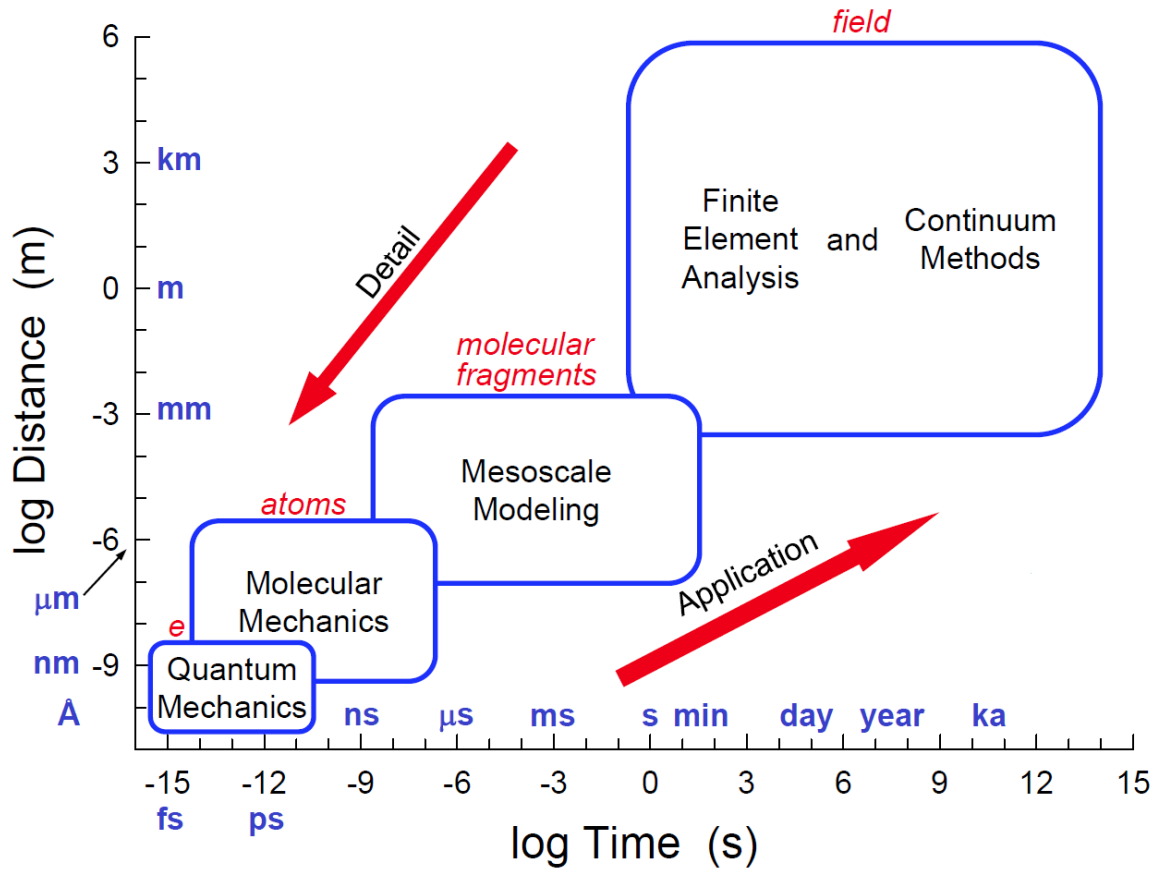


Figure 1-4 Different levels of modeling and simulation <sup>3</sup>.

Therefore, the objectives of this thesis is to evaluate and understand the mechanism of interaction of minerals with selected environments. To study the treatment of clay minerals, present in oil sands tailings, kaolinite, the most abundant component in the tailings, was chosen to study the interaction of alkali solutions with kaolinite at molecular level. Several previous studies have shown that geopolymerization process is a cost effective technique to alter the tailings to the cross-linked inorganic polymer which is fairly solid and environmental friendly. Geopolymerization is the activation of aluminosilicate source material, e.g., kaolinite, in alkali solution. A series of molecular dynamics simulations were carried out to investigate and understand the mechanism of interaction of kaolinite in alkali

solution in the early stage of the geopolymerization process. In the second part of this thesis, hydrotalcite, an abundantly found mineral in nature and also easy to synthesize, was chosen in an effort to evaluate its capacity to capture and store CO<sub>2</sub> at ambient condition using molecular dynamics simulation.

## 1.2. Objectives of the Research Project

- Studying the mechanism of the interaction of kaolinite basal surfaces with aqueous medium containing different alkali cations (e.g., Na<sup>+</sup>, K<sup>+</sup> and Na<sup>+</sup>/K<sup>+</sup>)
- Influence of structural vacancies on the interaction of basal surfaces of kaolinite and alkali solution
- Evaluation of the effect of process water impurities, such as MgCl<sub>2</sub> and CaCl<sub>2</sub>, on the interaction of kaolinite with alkali solution
- Studying the capacity of Cl<sup>-</sup>-hydrotalcite to capture and storage CO<sub>2</sub> at ambient condition
- Effect of Cl<sup>-</sup>-hydrotalcite water concentration on the CO<sub>2</sub> adsorption capacity
- Influence of KCl impurity on the Cl<sup>-</sup>-hydrotalcite CO<sub>2</sub> capture and storage capacity

# Chapter 2

## 2. Background

### 2.1. Tailings

Although oil sands industry provides the sources of oil and its by-products to North America, the waste materials generated in the form of tailings cause severe environmental problems. Tailings, which contain process water, clays, minerals and metals along with inorganic and organic chemicals <sup>4</sup>, are generally discharged into a large above ground structures - tailings ponds - where they await reclamation <sup>5</sup>. Large sand/mineral particles in tailings can be separated as they settle quickly to form stable deposits. However, as shown in Fig. 2-1, finer clay particles known as mature fine tailings (MFT) remain suspended in the form of sludge and take years or centuries to settle and to solidify <sup>6</sup>. This has led to the accumulation of millions of cubic meters of MFT in the Fort McMurray region of Alberta alone as a consequence of bitumen mining operations <sup>7</sup> or in central Florida due to the phosphate deposits minerals recovery <sup>8</sup>.

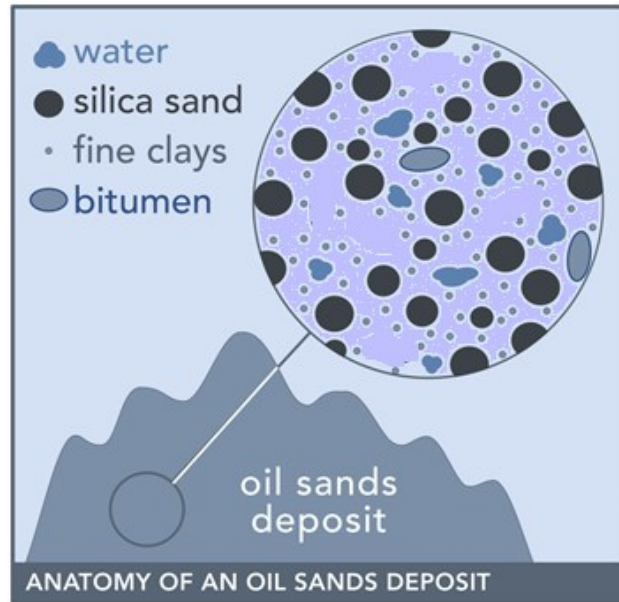


Figure 2-1 Anatomy of oil sands tailing (Extracted from: <http://www.oilsandsmagazine.com/technical/mining/tailings/directive-074>).

Despite efforts on increasing the settling rate of the tailings for efficient water recycling and to compact the tailings sediment, increasing the settling rate of tailings is still one of the main challenges in tailings management <sup>9</sup>. Large storage volume and long time-scale tailings treatment need result in the large environmental footprints for individual site after tailings production (Fig. 2-2) <sup>10</sup>. These environmental challenges include tailings management and mitigation of impact from inorganic and organic contaminants present and emission of biogenic greenhouse gases (CH<sub>4</sub> and CO<sub>2</sub>) <sup>11</sup>. The severe and sometimes irreversible economic and environmental consequences of poor tailings management, emphasize the necessity of considered and careful tailings management of the environmental and economic challenges <sup>12</sup>. Tailings water chemistry (e.g., ionic strength and pH) is critical for the settlement of fine clays. Existence of residual organic substance on the clay particle surfaces during mineral processing led to the hydrophobicity of clay particles <sup>13</sup>. To control the pH during mineral processing some chemical aids such as sodium hydroxide (NaOH) are often

added which also adjusts the wettability of clays <sup>14</sup>. Due to the role of clays existent in tailings on tailings settlement, they have drawn extensive attention in the recent years. However, understanding the interactions among clay particles is one of the most critical issues for the study of tailings and their disposal.

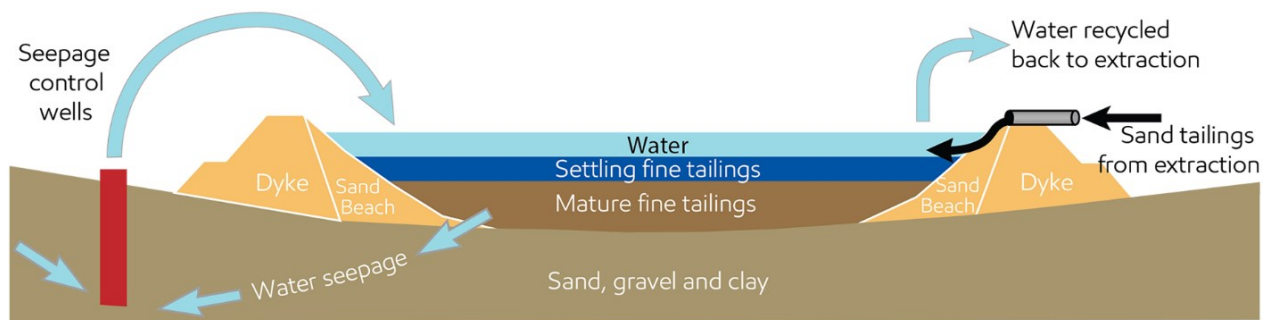


Figure 2-2 Oil sands tailings pond (Extracted from CAPP website).

### 2.1.1. Tailings Treatment Technologies

Tailings treatment technologies are controlled by; (i) the operation and maintenance expenses that the tailings ponds impose due to the amount of tailings produced every day and (ii) the need to reduce influences on the surrounding natural environments. Tailings treatment includes land reclamation and water recovery which can be reused within mining processes. The treatment technologies available for dewatering tailings can be categorized as <sup>9</sup>:

- Physical/Mechanical processes which include the use of different technologies to separate tailings water without using any chemicals (e.g., filtration, centrifuging, heating, and electrical treatments).

- Chemical/biological processes include changing the properties of the tailings to make the water/solid separation easier (e.g., thickening, using flocculants, and bio-drying).

Geopolymerization is a method for tailing solidifications in which chemicals, such as hydroxide or silicate-hydroxide, are added to the tailings to form a geopolymer-like material. Work done by Nusri *et al.* <sup>15</sup> showed that the surface geopolymerization of MFT led to the condensation and solidification of tailings.

#### 2.1.1.1. Geopolymer and Geopolymerization

The French scientist and engineer, Prof. Joseph Davidovits, invented the term 'geopolymer' which referred to alkali-activated aluminosilicate cements <sup>16</sup>. Geopolymer is also called as mineral polymers, inorganic polymers, inorganic polymer glasses, alkali-bonded ceramics, alkali ash material, soil cements, hydroceramics, and a variety of other names <sup>16-18</sup>. In general, since the late 1970s, the term 'geopolymer' has been applied to a wide range of alkali hydroxide- or silicate-activated aluminosilicate binders of composition  $M_2O \cdot mAl_2O_3 \cdot nSiO_2$ , usually with  $m \approx 1$  and  $2 \leq n \leq 6$ . M represents one or more alkali metals <sup>19</sup>.

Geopolymers has become increasingly widespread over the past several decades as the need for high-performance and/or environmentally sustainable alternatives for Portland cement intensifiers <sup>19</sup>. However, the underlying mechanisms controlling geopolymer formation and aluminosilicate source material dissolution are currently not well understood <sup>20,21</sup>. Geopolymers can be produced by alkaline activation of aluminosilicates obtained from industrial wastes <sup>22-25</sup>, calcined clays <sup>26-28</sup>, natural minerals <sup>29</sup>, or mixtures of two or more of these materials <sup>30</sup>. To dissolve the silica and alumina from precursor material as well as to catalyze the condensation reaction, alkali metal salts and/or hydroxide are necessary.

Although there is not a proper agreement on geopolymer structure, it is possible to state that geopolymers consist of alumina and silica tetrahedrally interlinked alternately by sharing all the oxygen atoms. A polymeric structure of Al-O-Si constitutes the main building blocks of geopolymeric structure. Since aluminum in the structure is in 4-fold position, some cations such as Na, K, Ca and other metallic cations must be presented to keep the structure neutral <sup>31</sup>. It is still not clear whether these ions play a charge-balancing role or are actively bonded into the matrix. The mechanism of immobilization is expected to be the combination of chemical and physical interactions. Basically, geopolymer is formed in a similar manner as the zeolite do <sup>32</sup>. However, zeolites usually form in closed hydrothermal systems but geopolymers do not. Furthermore, geopolymers are amorphous to semi-crystalline, whereas zeolites are usually crystalline in nature (Fig. 2-3).

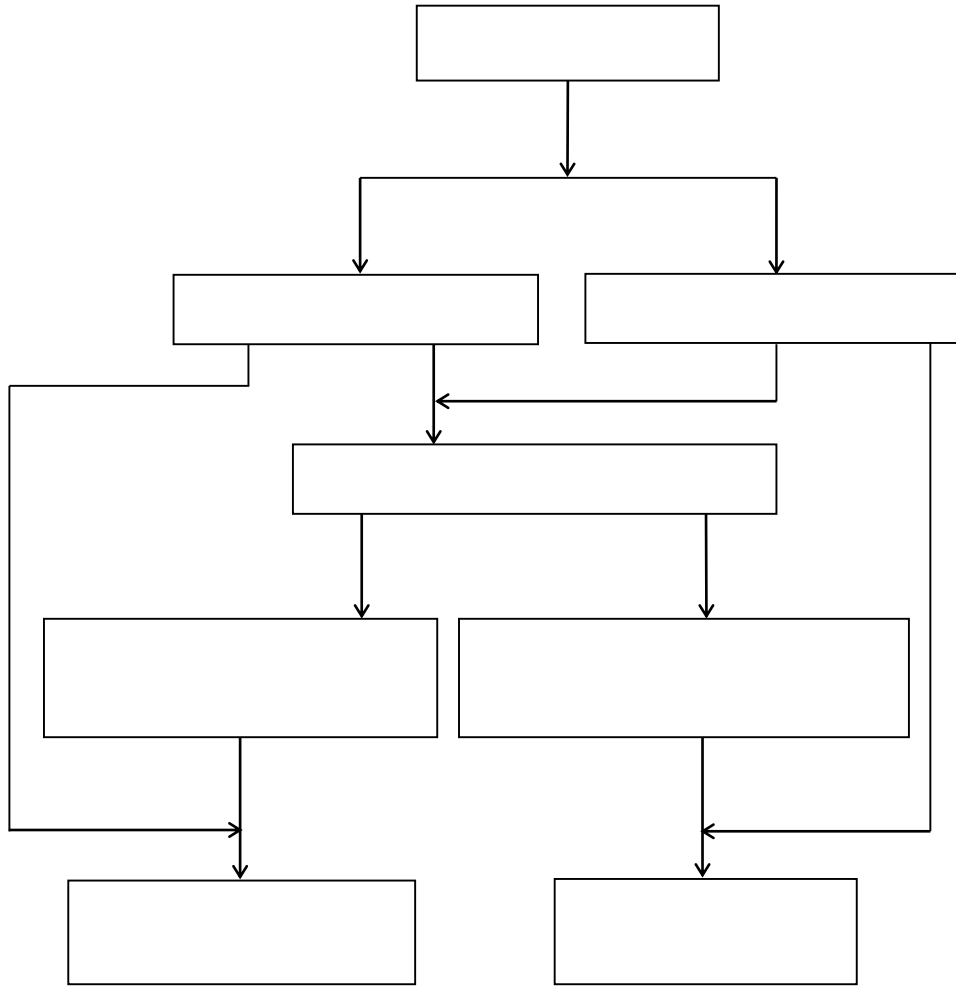


Figure 2-3 The process sequences of formation of zeolite and geopolymer <sup>33</sup>.

Due to the complexity of understanding the geopolymerization process, molecular simulation can reveal the effect of alkali hydroxide on the aluminosilicate materials which is one of the subject of this thesis.

### 2.1.2. Clay Minerals

Clay minerals are abundantly found in soils and sedimentary rocks. The properties of clay minerals such as acidity, high surface area and cation exchange capacity (CEC) make them play important roles such as catalysts, supports and adsorbents for toxic substances <sup>34</sup>. Clay

minerals are commonly phyllosilicates or layer silicates. There are two basic components to the structure: a sheet of atoms in tetrahedral situation (corner-connected atom) and a sheet of edge-sharing octahedra. Figure 2-4 illustrates the atoms to form both tetrahedra and octahedra, whereas Figure 2-5 illustrates the linkages of each to form the two varieties of sheets.

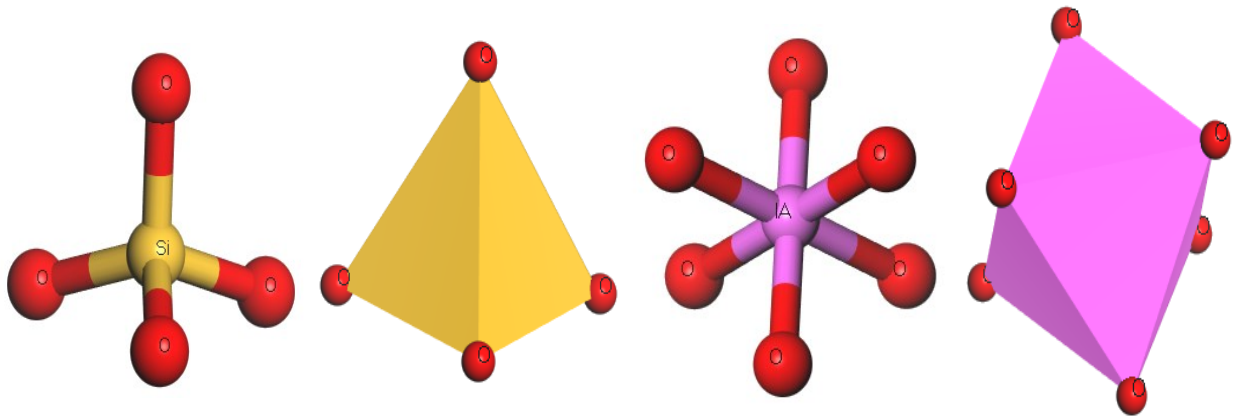


Figure 2-4 (a) Tetrahedron structure of Si and (b) octahedron structure of Al atoms in clay minerals structure.

#### 2.1.2.1. Tetrahedral Sheets

The dominant atom in the tetrahedron is the  $\text{Si}^{4+}$  cation, however, sometimes the  $\text{Al}^{3+}$  cation can occur also at this site and caused stacking defaults in the structure. This is important because the substitution of  $\text{Al}^{3+}$  for  $\text{Si}^{4+}$  produces a charge that must be balanced somewhere in the structure. Clay particles obtain electric charge by substitution of cations in the layers. A negative charge occurs when a tetravalent silicon ion is replaced by a trivalent aluminum ion because of the similar morphology of the ions. This charging mechanism is known as isomorphous substitution of ions. The charges on basal planes are considered permanent charges, independent of pH while primary alumina and silica bonds broken along particle

edges lead to pH dependent charges <sup>35</sup>. In order to form a tetrahedral sheet, three corners of each tetrahedron connected together (Fig. 2-4). For each corner that is shared between two tetrahedra, only one oxygen is involved in the connection which means fewer oxygens needs to complete a sheet of tetrahedra compared to the same number of individual and unlinked tetrahedra.

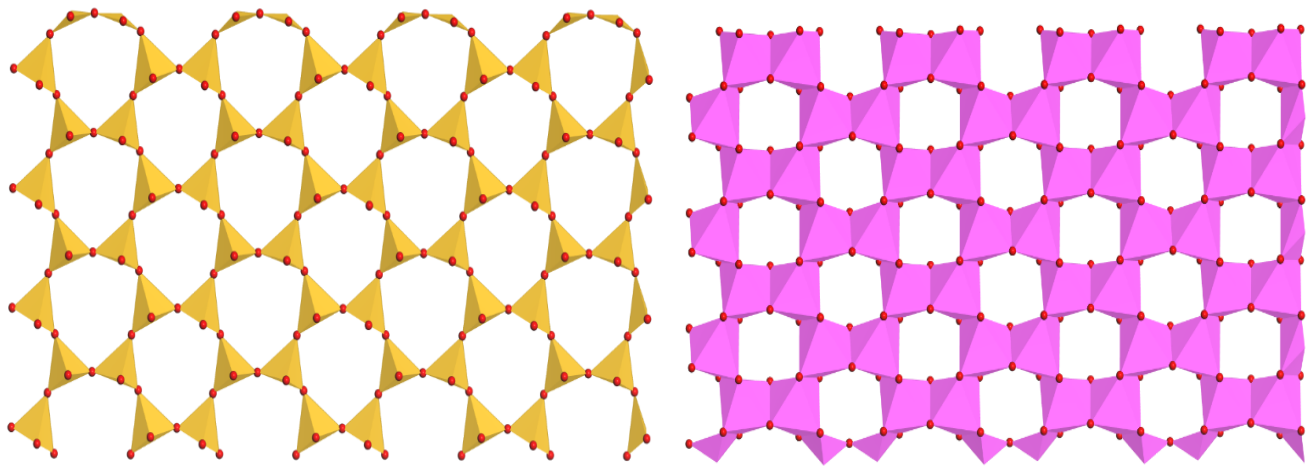


Figure 2-5 Top view of (a) tetrahedral and (b) octahedral surface.

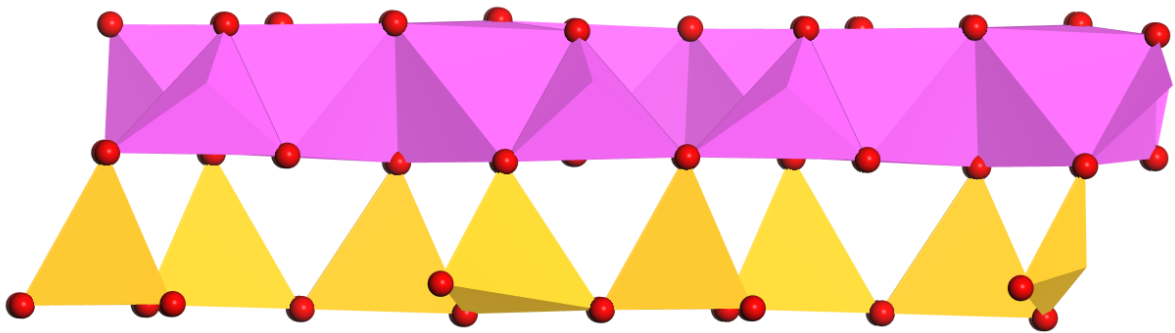


Figure 2-6 Front view of octahedral and tetrahedral sheets connected together via bridging oxygens.

#### 2.1.2.2. Octahedral Sheets

The octahedral sheet is formed by edge-sharing octahedra and in different clay, different cations can be found in the octahedral position. However, mostly trivalent cations such as  $\text{Al}^{3+}$  is in the octahedral and in order to balance the charge of the structure it is required that for every two octahedra that contain  $\text{Al}^{3+}$ , there is an empty octahedron. The position of  $\text{Al}^{3+}$  and vacant sites is illustrated in Fig. 2-5 b which is the reason for calling this structure "dioctahedral". In Contrast, in a "trioctahedral" sheet all three sites are occupied, which occurs for octahedra occupied by divalent cations (e.g.,  $\text{Mg}^{2+}$ ). Structural impurities usually occur in clay structures as in many phyllosilicates a small number of divalent cations can be found in a dioctahedral sheet or a small number of trivalent cations is in a trioctahedral sheet. This phenomenon caused a small deficiency in charge of the structure that must be compensated elsewhere in the structure.

#### 2.1.2.3. Layers

In order to form a layer in phyllosilicates the two octahedral and tetrahedral sheets must join together. The lateral dimensions of the two sheets are close to each other therefore it is possible to join them together. By sharing the oxygen atoms from the two surfaces, some oxygens are common junction between the two sheets. Thus, some of the oxygens that belong to the tetrahedral sheets also belong to the octahedral sheet. Only the hydroxyl ions do not link directly to the tetrahedra.

#### 2.1.2.4. Interlayer Material

Some cations such as  $\text{Na}^+$ ,  $\text{K}^+$ ,  $\text{Ca}^{2+}$ , or  $\text{Mg}^{2+}$  or even organic molecules can be placed in the interlayer regions of phyllosilicates. Regularly, depending on the nature of the cation, polar

H<sub>2</sub>O molecules enter the interlayer. For example, high amounts of H<sub>2</sub>O go into the interlayer with Na<sup>+</sup>, whereas many fewer H<sub>2</sub>O molecules enter the interlayer with Ca. In addition, it is fairly easy to replace interlayer cations with other material, as long as there is a large amount of that material in the immediate environment. For example, an aqueous solution containing many Na<sup>+</sup> cations around a montmorillonite grain will readily allow for Na<sup>+</sup> to exchange for K<sup>+</sup>, if K<sup>+</sup> is in the interlayer. Therefore, these cations are often called "exchangeable cations". To understand how cation exchange works, it is necessary to define "internal" vs "external" surfaces of a clay particle and to determine how they attract cations and anions. The internal surfaces are the two planes of atoms on either side of the interlayer space at the base of the tetrahedral and octahedral sheets. External surfaces are the broken edges of the layer. Because there are no broken bonds on the internal surfaces the internal surfaces attract both cations and anions. In contrast, however, the external surfaces generally attract negatively charged anions because the cations on the broken surface require the negative charge to compensate.

Scanning electron microscopy image of layered structure of kaolinite and tetrahedral and octahedral sheets of kaolinite are shown in Fig. 2-7. These layers are held together partly by van der Waals forces and partly by hydrogen bonds from the hydroxyl groups of the octahedral sheet. Three-layered clay particles, such as illite or montmorillonite, comprise an octahedral aluminum-oxide sheet in between two tetrahedral silicon-oxygen sheets.

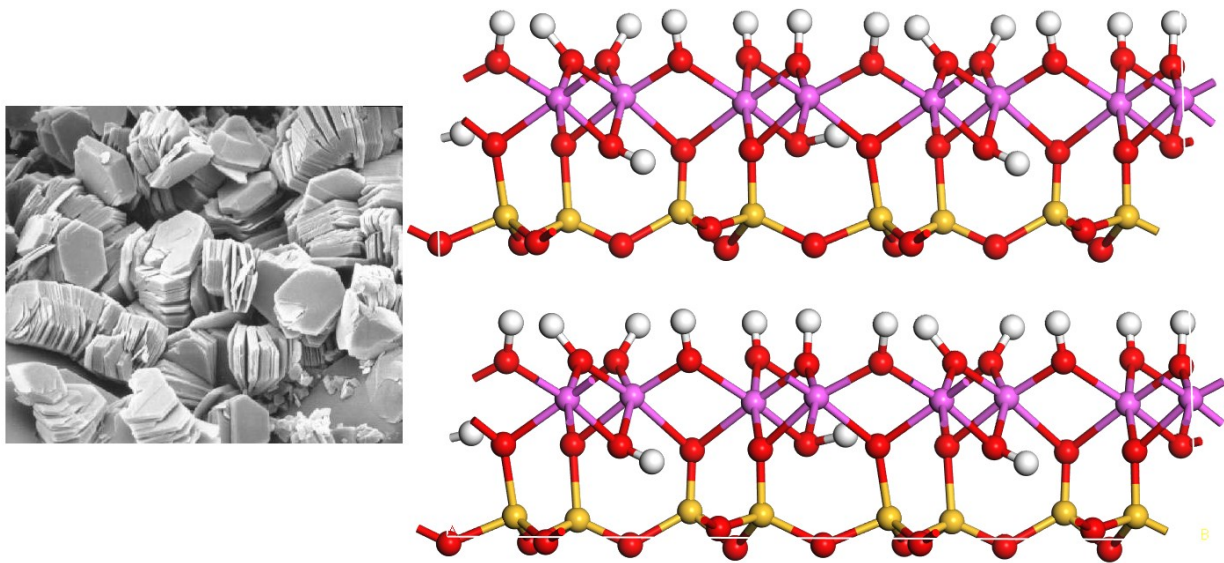


Figure 2-7 (a) Scanning electron microscopy image of kaolinite <sup>36</sup> and (b) Its atomic structure. The color scheme is: purple for aluminum, yellow for silicon, red for oxygen, white for hydrogen.

Kaolinite is a good candidate for geopolymerization process and was studied in this study as this clay is abundantly found in MFT and also has its simple 1:1 structure to model by molecular simulation.

#### 2.1.2.5. Adsorption and Desorption

Adsorption is defined as the accumulation of a matter at an interface of two phases, without the formation of crystal structure. However, in contrast, desorption is the loss of matter from the interface. The substance that accumulates at the interface is called adsorbate and the surface where accumulation takes place on is adsorbent. The term adsorptive refers to any chemical species in the bulk solution that may potentially be adsorbed. In contrast, the term sorbate, sorbent and sorptive apply in situations where the precise mechanism of solid-liquid transfer is not known and may include surface precipitation or solid state diffusion. In a sorption or desorption reaction, a solute becomes associated with or dissociate from the

solid phase, respectively. Sorption-desorption processes generally comprise multiple reactions or steps involving solid and aqueous phase components<sup>37</sup>. In addition to chemical reactions, i.e., formation or rupture of chemical bonds, these steps include transport processes, i.e., displacement of adsorptives in the liquid phase and adsorbates at the interface.

Essentially, the fundamental physical and chemical properties of crystalline materials is dependent on their long-range crystal structure which is expressed internally as the periodic lattice. However, water is known as the most common solvent for most of materials. It is the dominant medium in which rocks and minerals interact through chemical precipitation and dissolution reactions. It is understood that the mobility of ions to and from sites in the solid bulk crystal is extremely limited through diffusion at room temperature. However, dissolution and precipitation reactions usually, to some extent, occur at the mineral-water interface. This interface is basically where the interaction between the surface atoms of the solid and the aqueous medium takes place.

In addition to water molecules, the dissolved components in water, such as salts, hydrogen and hydroxyl ions, organic molecules and gases (e.g., CO<sub>2</sub> and O<sub>2</sub>), interact with the mineral surface, resulting in a complex distribution of species and functional groups (moieties). This interaction at the liquid-solid interface alters both the surface layers of the crystal matter (i.e., mineral surface) and the boundary layer of the liquid. Although the bulk liquid may be in turbulent motion, e.g., a stirred reactor, the intermolecular attractive forces through the mineral surface and the liquid bring the velocity of fluid closely to zero, which is known as no-slip condition. In classical theory, this constraint reduces advection and turbulent at the surface.

The surface of a crystal matter is fundamentally different from its bulk. These differences comprise dangling bonds, surface molecular relaxation and chemical composition. However, the crystal structure of the surface is related (but not identical) to the crystal structure of the bulk. Those differences create a strong driving force to reorganize and equilibrate the surface with the liquid. This overall process is accomplished by reactions such as hydration, adsorption of dissolved components, protonation/deprotonation and detachment of adatoms.

The interactions of the Mineral and water primarily happen at the external mineral surfaces <sup>38</sup>, which are typically surface-controlled at the temperatures and pressures near the ambient condition. In the case of crystal dissolution, the term surface-controlled refers to the fact that the reaction rate is limited by the basic molecular processes that finally lead to the detachment of a molecule from the bulk crystal structure into the solution <sup>39</sup>. In contrast, however, the surface-water interaction/reaction is called transport-controlled if the transport of molecules to and from the mineral surface in the bulk solution is rate limiting <sup>39</sup>. The latter case is observed if the transport of molecules into the solution is slower than all the processes that lead to the formation of an adatom. An example for such a situation is “no significant flow of the fluid across the mineral surface, i.e., stagnant fluid conditions often observed on internal surfaces”. In all other cases, the interaction/reaction becomes surface-controlled. It is worth to recall that adsorption, surface nucleation, dissolution, and crystal growth are all microscopic processes that occur at the mineral surface.

In fact, to fully understand the alterations of the mineral crystal surface and the processes within the mineral-water interface, it is needed to study the interface changes via advance powerful analytical techniques <sup>40</sup>, which undoubtedly increases the complexity of the

mineral-water interface investigations. Moreover, if we approach the atomic scale in this attempt, direct observations of surface topography and particularly the dynamic changes of crystal surface due to adsorption/desorption and dissolution/growth processes become increasingly complicated or even infeasible. In this situation, theoretical approaches and molecular modeling techniques, such as molecular dynamics simulations, allow us, to some extent, understand the process at the molecular level. Particularly, by rapidly increasing the computer power, it has been possible to make substantial progress in this field. Therefore, in the recent decade, molecular modeling has become a powerful partner for the experimental/analytical studies. In 2001, Cygan and Kubicki <sup>3</sup> have assembled a comprehensive overview of the more recent modeling works. However, generally speaking, it is essential to decide at which level and size it is needed to investigate the system of interest.

Molecular dynamics modeling of the mineral-surface interactions makes a significant contribution to our understanding of these processes. In particular, the modeling technique can provide detailed mechanisms at the molecular scale. This approach includes information on: type of bonding, reaction pathways, non-equilibrium configurations, and the energetics, i.e., electrostatic potentials. If sufficiently coupled with our proposed experimentation, this information can play an important role in eliminating hypotheses, focusing on new phenomena and systematizing available experimental data.

## 2.2. CO<sub>2</sub> Emission

At the end of the 19th century, Arrhenius calculation showed a doubling of CO<sub>2</sub> concentration in the atmosphere would raise the average temperature by 5°C or 6°C <sup>41,42</sup>. Studies show that CO<sub>2</sub> concentration in the atmosphere is 112 parts per million more in 2011 (392 ppm)

than prior to the beginning of the industrial revolution (280 ppm) in late 1970<sup>42</sup>. CO<sub>2</sub> is the major human-produced greenhouse gas, over half of which derives from energy sector activities. Major contributors to the increased concentration of CO<sub>2</sub> in the atmosphere are power stations and the chemical and petrochemical industries. By increasing the concentration of the greenhouse gases in the atmosphere, heat-trapping capacity of the earth's atmosphere increases through the greenhouse effect which has led to the global warming<sup>43</sup>. Greenhouse gases include carbon dioxide (CO<sub>2</sub>), methane (CH<sub>4</sub>), water vapor (H<sub>2</sub>O), ozone (O<sub>3</sub>), nitrous oxide (N<sub>2</sub>O), and chlorofluorocarbons (CFCs)<sup>42,44</sup>. Emission of CO<sub>2</sub> as the largest contributor and the fastest growing emitted component leads to the highest concern. The nature (oceans, plants, and soil) cannot consume carbon produced by human activities fast enough to reduce CO<sub>2</sub> concentration in the atmosphere<sup>45</sup>. Thus, to constrain the CO<sub>2</sub> concentration in the atmosphere it is crucial to change the processes that humans produce and use energy. Dependence on the burning of the fossil fuels (petroleum, natural gas, and coal) for energy will lead to the rise in global temperatures between 1.4 and 5.8°C by 2100<sup>46</sup>. However, due to fossil fuels low cost, low investment, availability of the fuels, many industries will continue to use fossil fuels as main energy source. Therefore, any reasonable approach for controlling the global temperature must reduce greenhouse gas (GHG) emissions without shutting down a fossil fuel-based energy infrastructure. In this regard, carbon capture and storage (CCS) technology can offer the flexibility in achieving greenhouse gas emission reductions while we are switching to an energy infrastructure based on less carbon-intensive fuels and renewable energies<sup>47</sup>.

### 2.2.1. Carbon capture and storage (CCS)

Many methods are developed to separate CO<sub>2</sub> to a reasonable degree depending on the conditions of flue gas stream. The desired process for CO<sub>2</sub> separation should be cost effective at typical pressure, temperature and composition of the flue gas <sup>48</sup>. CO<sub>2</sub> capture can generally be attained in two main modes: post-combustion or pre-combustion. In the post-combustion mode, at fixed point sources CO<sub>2</sub> is separated from burning products containing N<sub>2</sub>, residual oxygen, water vapor, NO<sub>x</sub> and SO<sub>2</sub>. The capture process can be done at any stage of combustion stream from the combustor to the exhaust, but preferably after the removal of acid gases like SO<sub>x</sub> and NO<sub>x</sub> <sup>49,50</sup>. Pre-combustion capture comprises fuel gasification into carbon dioxide and hydrogen. Afterwards products go through a water-gas shift to a high-concentration stream of CO<sub>2</sub> and H<sub>2</sub>. The CO<sub>2</sub> is captured and the H<sub>2</sub> is reacted with air <sup>47,51</sup>.

### 2.2.2. Technologies for CO<sub>2</sub> Capture

- **Chemical and Physical Absorption**

In chemical and physical absorption, the CO<sub>2</sub> is absorbed by a liquid in a closed circuit through countercurrent contacting of a gas in either a packed or trayed tower. CO<sub>2</sub> can be regenerated either by thermal or pressure reduction equipment. According to Henry's law the physically absorbed CO<sub>2</sub> in the solvent can be regenerated using either or both heat and pressure reduction to produce a dry CO<sub>2</sub> stream. Due to the large amount of heat which is required to regenerate the solvent this process is not a desirable process. Breaking the chemical bond between the CO<sub>2</sub> and the chemical solvent is energy demanding process which significantly reduces the net efficiency of the power plant <sup>50,52</sup>.

- **Cryogenic Separation**

Cryogenic separation method separates the CO<sub>2</sub> from the waste gases by cooling the gases to a very low temperature so that the CO<sub>2</sub> can be liquefied and separated. The CO<sub>2</sub> separated by this method is ready for transportation by pipeline which means CO<sub>2</sub> purity after distillation can exceed 99.95%<sup>47</sup>. However, the amount of the energy needed to liquefy the CO<sub>2</sub> makes this process extremely energy intensive<sup>53</sup>.

- **Membrane Separation**

Membranes are thin barriers that allow selective permeation of certain gases. In the polymeric membrane the molecules interact with the membrane to diffuse across either by solution-diffusion or by absorption-diffusion<sup>47</sup>. Metallic membranes can be used for CO<sub>2</sub> recovery from gas stream<sup>53</sup>, in this membrane based on the membrane pores size, only gas molecules below a certain size are able to pass through the pores. Although simplicity, the compact and lightweight system, multi-stage operation and low maintenance make the membrane separation a desirable process<sup>53</sup>, the low purity of the CO<sub>2</sub> constrains the usage of this process. Actually, the very selective membranes are not permeable, while permeable membranes allow other gases besides CO<sub>2</sub> to permeate which results in a low purity stream of CO<sub>2</sub><sup>47</sup>.

- **Pressure Swing Adsorption (PSA)**

Pressure swing adsorption (PSA) is a gas separation process in which the adsorbent is regenerated by rapidly reducing the partial pressure of the adsorbed component. Adsorbents should have the ability to retain their adsorption capability upon releasing the adsorbed phase by changing the pressure or temperature. The central advantage of physical

adsorption methods is the potentially lower energy requirement to regenerate the sorbent material and the shorter regeneration time. Different adsorptive materials are used for PSA process such as a molecular sieve, zeolite and activated carbon <sup>54</sup>. These adsorbents have high capacity for CO<sub>2</sub> at ambient temperatures; however, they suffer from low CO<sub>2</sub> capacity at elevated temperature. Hydrotalcites have been used as adsorbents for several applications and their use in the carbon dioxide adsorption at high temperatures was reported <sup>55,56</sup>. HTlcs were found to be viable adsorbents for use in a high temperature PSA process for CO<sub>2</sub> capture <sup>57</sup>.

### 2.2.3. Hydrotalcite-like Compounds (HTlcs)

Hydrotalcite-like compounds (HTlcs), also known as mixed metal layered hydroxides or layered double hydroxides (LDHs), was initially found in Sweden in around 1842. This structure is composed of positively charged brucite-like layers in which trivalent cations partially substitute for divalent cations located at the center of octahedral sites in the hydroxide layer. Hydrotalcite is among the group of minerals referred to as “non-silicate oxide and hydroxides”. It has many physical and chemical properties that are similar to those of clay minerals. Their layered structure, wide chemical composition, variable layer charge density, ion-exchange properties, and rheological and colloidal properties make hydrotalcite behavior similar to clay minerals. Moreover, because of their anion exchange properties hydrotalcites were referred to as anionic clays <sup>58</sup>. Also, minerals such as hydrotalcite are good candidate to capture and storage CO<sub>2</sub> between their layers. The CO<sub>2</sub> adsorption capacity of Cl-hydrotalcite and interaction of CO<sub>2</sub> with the layers are studied by molecular dynamics simulation. The scanning electron microscopy image and the molecular structure of hydrotalcite are shown in Fig. 2-4.

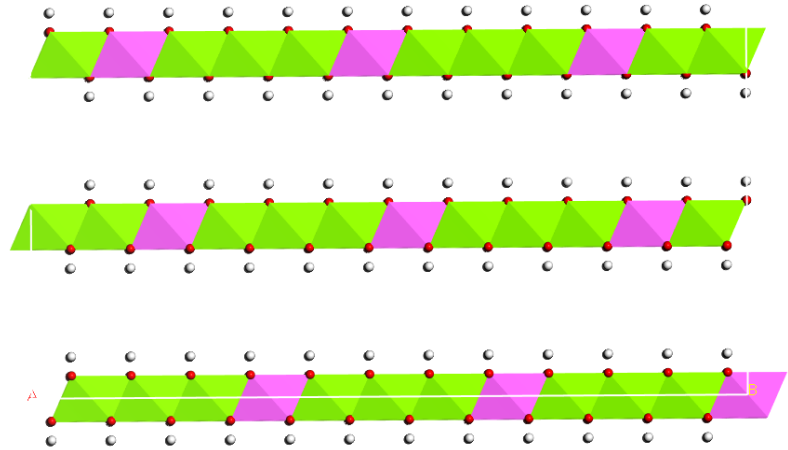
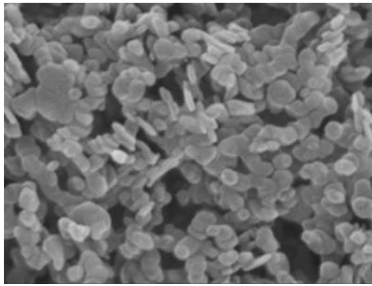


Figure 2-8 (a) Scanning electron microscopy of hydrotalcite<sup>59</sup> with Mg/Al = 3 and (b) its schematic structure.

### 2.3. Summary of the Literature

The environmental problems caused by the oil sands extraction and usage of oil and petroleum fuels have negatively affected human health and lives. To solve these problems, understanding the details of the molecular behavior involved can provide a good insight for their improvements. In this study, interaction between clay minerals, kaolinite in particular, and alkali solutions were studied. On the other hand, CO<sub>2</sub> adsorption capacity of hydrotalcite was examined as well.

# Chapter 3

## 3. Molecular Dynamics Simulation

### 3.1. Introduction

Molecular dynamics (MD) simulation is a technique whereby the Newton's equations of motion are solved for the trajectories of  $N$  particles interacting via prescribed potentials. The equations of motion for the  $N$  particles can be written as,

$$m\ddot{r}_i(t) = F_i(t) \quad (3.1)$$

where the force on particle  $i$  at time  $t$ ,  $F_i(t)$ , depends on the positions of all of the other particles of the system at that time. Integrating the equations of motion then yields a trajectory that describes the microscopic state of a system as it evolves with time. A microscopic state of a system is described by the summation of the kinetic (K) and the potential (U) energies defined as Hamiltonian (H).

$$H(r, p) = K(p) + U(r) = \sum_{i=1}^N \frac{p_i^2}{2m_i} + U(r) \quad (3.2)$$

where  $p = (p_1, \dots, p_N)$  and  $r = (r_1, \dots, r_N)$  are sets of atomic positions and momenta, while the  $m_i$  is the mass of the  $i_{th}$  atom. Potential energy is described as a combination of bonded and non-bonded interactions between particles. The expressions for the potential energy and the associated parameters constitute the force field. By integrating the Hamiltonian equations of motion written as following for each particle in the system,

$$\frac{dp_i}{dt} = -\frac{\partial H(r,p)}{\partial r_i} \quad (3.3)$$

$$\frac{dr_i}{dt} = \frac{\partial H(r,p)}{\partial p_i} \quad (3.4)$$

Molecular dynamics simulation will be conducted. According to the first equation, the force applied on each particle can be calculated which can be used for the calculation of the trajectory of each atom in the system by integrating Newton's equation of motion which requires an integration algorithm. Although many algorithms have been proposed, what is essentially the simplest algorithm, known as the Verlet algorithm, is still thought to be one of the best <sup>60</sup>. The Verlet algorithm <sup>61</sup> can be derived by considering the Taylor's series expansion about the coordinate of a particle at time  $t$ , which is,

$$r_i(t + \Delta t) = r_i(t) + v_i(t)\Delta t + \frac{F_i(t)}{2m}\Delta t^2 + \frac{\ddot{r}_i}{3!}\Delta t^3 + O(\Delta t^4). \quad (3.5)$$

Similarly,

$$r_i(t - \Delta t) = r_i(t) - v_i(t)\Delta t + \frac{F_i(t)}{2m}\Delta t^2 - \frac{\ddot{r}_i}{3!}\Delta t^3 + O(\Delta t^4) \quad (3.6)$$

Adding these equations gives,

$$r_i(t + \Delta t) \approx 2r_i(t) - r_i(t - \Delta t) + \frac{F_i(t)}{m}\Delta t^2 \quad (3.7)$$

which contains an error term of order  $(\Delta t^4)$ . Equation (3.7) can be used in an MD simulation to advance the positions of the particles. Velocity of each particle at the time  $t$  is calculated by 'velocity Verlet' algorithm. In this regard, the same Taylor's series expansion used in the original Verlet algorithm, Equation (3.5), is coupled to the following for the update of the velocities,

$$v_i(t + \Delta t) = v_i(t) + \frac{F_i(t+\Delta t)+F_i(t)}{2m} \Delta t \quad (3.8)$$

In the implementation of the velocity Verlet algorithm, the positions are first updated according to equation (3.7). From these new positions, the new forces can be calculated. Finally, the new velocities are computed according to the equation (3.8). It can be shown that this algorithm generates identical trajectories to the original Verlet algorithm <sup>60</sup>. However, it has the advantage that both the positions and velocities of the particles are defined at the same instant of time. Because of this latter property, all of the simulations that have been performed for this thesis use the velocity Verlet algorithm.

### 3.1.1. The quasi-ergodic hypothesis

Using MD simulations, one can measure the microscopic dynamics of a system in thermal equilibrium. From these dynamics, time averages of any given functions of the positions and velocities of the particles can be calculated. However, the quantities of principal interest of molecular dynamics simulations all been defined in terms of ensemble averages. Thus, to compute these quantities with MD the time averages computed in MD simulations need to be linked to the ensemble averages. This link is provided by the ergodic hypothesis that the time average of an observable physical quantity equals to its ensemble average.

$$\langle \dots \rangle_{\text{ens}} = \lim_{\tau \rightarrow \infty} \frac{1}{\tau} \int_0^\tau \dots dt \quad (3.9)$$

This means that to make a relation between MD results and experiments, it is necessary to let the simulated system, evolve in the phase space for a sufficiently long time and fulfill the quasi-ergodic theorem.

### 3.1.2. Simulation ensembles

Considering different thermodynamic parameters four different ensembles can be defined for MD simulation; however, the original MD ensemble is the micro canonical ensemble (with constant number of particles, volume and energy, NVE) which is energy conservative ensemble. Canonical ensemble (with constant number of particles, volume and temperature, NVT), isobaric isothermal ensemble (with constant number of particles, pressure and temperature NPT) and grand canonical ensemble (with constant chemical potential, pressure and temperature,  $\mu$ V T) are the other ensembles commonly used for MD simulation. There are several methods to control the temperature and pressure during MD simulation, However, the Nose-Hoover thermostat and barostat were used in this study.

### 3.1.3. Nosé-Hoover Thermostat

An algorithm was proposed by Nosé <sup>62</sup> to control the system temperature and later it was further improved by Hoover <sup>63</sup>, known as Nosé-Hoover thermostat. In this method, an additional degree of freedom is incorporated to the real physical system to represent the interaction of the system with a heat bath. The dynamic variable is defined with its own coordination ( $s$ ) and momentum ( $p_s$ ) in which the potential and kinetic energies are defined as Equations (3.10) and (3.11), respectively.

$$U_s = (N_f + 1)K_B T_0 \ln s \quad (3.10)$$

$$K_s = \frac{1}{2} Q \frac{ds}{dt} = \frac{p_s^2}{2Q} \quad (3.11)$$

where  $N_f$  is the degree of freedom in the system, and  $Q$  and  $T_0$  are effective mass of the thermostat and the temperature of the heat bath, respectively. Hamiltonian of the system could be written as follows,

$$H = K(p) + U(r) + \frac{p_s^2}{2Q} + (N_f + 1)k_B T_0 \ln s \quad (3.12)$$

The only problem of the Nosé thermostat was the scaling of velocity with  $s$  leading to scaling of time, which improved by Hoover modification. In fact, Hoover replaced  $s$  with the thermodynamic friction coefficient,  $\zeta = p_s/Q$ . In addition, Hoover removed the degree of freedom by taking the formulation back to the real time. The equations of motion of real variables can be recovered as,

$$\begin{aligned} \frac{dr_i}{dt} &= \frac{p_i}{m_i} \\ \frac{dp_i}{dt} &= f_i - \zeta p_i \\ \frac{d\zeta}{dt} &= \frac{1}{Q} \left( \sum_{i=1}^N \frac{p_i^2}{m_i} - N_f k_B T_0 \right) \end{aligned} \quad (3.13)$$

The effective mass of thermostat is usually defined as  $Q = N_f k_B T \tau_T^2$  where  $\tau_T$  is the time constant of thermostat. If  $Q$  is high, the flow of energy between the physical system and the reservoir will be too slow and consequently, infinite  $Q$  corresponds to a NVE MD system. On the other hand, if  $Q$  is too low, then the energy oscillates unphysically, causing equilibration problems. If the energy of the extended system is conserved, then the Nosé-Hoover thermostat reproduces the canonical ensemble of the real physical system in every respect. The corresponding Hamiltonian to the Hoover formulation is:

$$H = K(p) + U(r) + \frac{1}{2} Q \zeta^2 + N_f k_B T \int_0^t \zeta(\acute{t}) d\acute{t} \quad (3.14)$$

In this thesis, this formulation which is called Nosé-Hoover thermostat was used in all molecular dynamics simulation to control the temperature.

### 3.1.4. Nosé-Hoover Barostat

The idea of including constant pressure condition to the systems was initially introduced by Anderson <sup>64</sup>. In the original method, the size of the isotropic simulation cell was allowed to change; however, no change was in the shape to control the system pressure. Later, the Anderson method was extended by Parrinello-Rahman to allow the cell shape to change <sup>65</sup>. Similar to his thermostat, the new degree of freedom was added by Nosé to the Andersen dynamics generating NPT ensemble through scaling of time. Hoover proposed a straightforward method to extend his formulation for canonical ensemble to the isothermal-isobaric case <sup>63</sup>. This was done by introducing a new reduced coordinate  $x = \frac{r}{V^{1/D}}$  for D dimensional system. Accordingly, the equation of motion (Equation (3.13)) can be extended as,

$$\begin{aligned}
 \frac{dx_i}{dt} &= \frac{p_i}{m_i V^{1/D}} \\
 \frac{dp_i}{dt} &= f_i - (\eta + \zeta)p_i \\
 \frac{d\zeta}{dt} &= \frac{1}{\tau^2} \left( \frac{T(t)}{T_0} - 1 \right) \\
 \frac{d\eta}{dt} &= \frac{1}{Q} V(P(t) - P_0) \\
 \frac{dV}{dt} &= D\eta V
 \end{aligned} \tag{3.15}$$

Although the canonical case is well reproduced by Hoover formulation, the NPT simulation using Equation (3.15) results in a distribution function which does not represent

exactly the NPT ensemble. However, this problem was solved by Melchionna et al. <sup>66</sup> through introducing the effective mass of barostat to the formulation developed by Hoover:

$$\begin{aligned}
\frac{dr_i}{dt} &= \frac{p_i}{m_i} + \eta(r_i + R_0) \\
\frac{dp_i}{dt} &= f_i - (\eta + \zeta)p_i \\
\frac{d\zeta}{dt} &= \frac{1}{\tau^2} \left( \frac{T(t)}{T_0} - 1 \right) \\
\frac{d\eta}{dt} &= \frac{1}{\dot{Q}} V(P(t) - P_0) \\
\frac{dV}{dt} &= D\eta V
\end{aligned} \tag{3.16}$$

where  $\dot{Q} = N_f k_B T \tau_p^2$  is the effective mass of the barostat.  $\tau_p$  and  $R_0$  are the barostat time constant and the center of mass of the system, respectively. The corresponding Hamiltonian equivalent to Gibbs free energy is written as,

$$H = K(p) + U(r) + \frac{1}{2} Q \zeta^2 + \frac{1}{2} \dot{Q} \eta^2 + \int_0^t (N_f k_B T \zeta(\dot{t}) + k_B T_0) d\dot{t} \tag{3.17}$$

In this thesis, Melchionna modification of the Hoover algorithm which is called Nosé-Hoover barostat was used to control pressure in MD simulations.

### 3.1.5. Periodic boundary conditions

In order to perform an accurate MD simulation, a very large system should be designed because the effect of the box edges on the system properties should be minimized. However, only systems with a finite, and usually relatively small ( $N \approx 10^3 - 10^6$ ) number of particles can be simulated. This introduces the problem of surface effects. Periodic boundary conditions (PBC) should be applied to mitigate the problem of surface effects. In this regard, it is imagined that the simulation box is replicated throughout space to make translated

images of itself to form an infinite lattice. A two-dimensional representation of PBC is illustrated in Figure 3-1. Under the PBC condition, if a particle moves in the main simulation box, its periodic replicas in neighboring boxes move in the exact same way.

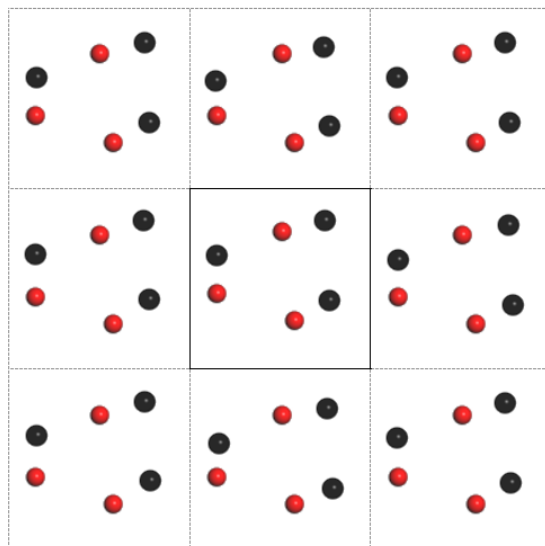


Figure 3-1 Periodic boundary conditions used in MD simulations.

However, due to replication of the simulation box the interaction of particles with its images especially non-bonded interaction, which is non-physical, can occur. To avoid this problem which is called the minimum image convention, the dimensions of the cell should be (at least) twice of the interatomic interaction cut-off distance.

### 3.2. Force Field

To calculate potential energy of the system, the interactions between atoms in the molecular dynamics simulation should be calculated. In this regard, for each system a reliable force field should be used. The force field uses a set of empirical formulas to mimic all interactions between atoms that are bonded as well as non-bonded interactions between atoms and molecules in molecular systems. In this thesis, all the simulations were done by using the

ClayFF force field which is defined to precisely model flexible clay minerals structures and their interaction with hydrated systems. In this force field, the total energy of the system is written as,

$$E_{total} = E_{Coul} + E_{VDW} + E_{bond\ stretching} + E_{Angle\ bend} \quad (3.18)$$

The formalization of each of this energy is described in next section.

### 3.2.1. Non-bonded Interaction

In the ClayFF force field, the interaction between metal and oxygen is just described by non-bonded parameters. Non-bond interaction is the summation of electrostatic interaction and Van der Waals interaction.

#### 3.2.1.1. Electrostatic Interaction

Most of the energy of the system is produced due to the existence of ionic species in the system which is calculated based on the Coulomb's law,

$$E_{Coul} = \frac{e}{4\pi\epsilon_0} \sum_{i \neq j} \frac{q_i q_j}{r_{ij}} \quad (3.19)$$

where,  $e$  is the charge of the electron,  $\epsilon_0$  is the dielectric permittivity of vacuum ( $8.85419 \times 10^{-12}$  F/m),  $q_i$  and  $q_j$  are partial atomic charges on atoms  $i$  and  $j$  and  $r_{ij}$  is their distance.

Despite the simple form of the Coulomb energy, it is in fact the most complicated atomic interaction to evaluate in an atomistic simulation. It is because Coulomb energy shows a slow decay in respect to separation distance of atoms due to the  $\frac{1}{r}$  term, which makes it the long-range component of the interatomic potential. The most applied solution to overcome the Coulomb energy problem is proposed by Ewald [55].

- **The Ewald summation and the PPPM algorithm**

The Ewald summation is basically used to evaluate the total potential energy of a system of interest including  $N$  interacting particles under periodic boundary conditions. Although Ewald summation was primarily developed for ionic systems <sup>67</sup>, the Ewald method can be principally applied for any interaction potential.

$$V = \frac{1}{2} \sum_{i,j=1}^N \sum'_{m \in \mathbb{Z}} v(r_{ij} + mL) \quad (3.20)$$

where  $r_{ij} = r_i - r_j$ . The periodic images of the particles are taken into account by the sum over  $m$  and the prime indicates that for  $m = 0$ , the case  $i = j$  must be omitted. However, Equation (3.20) turns into Equation (3.21) in the case of the Coulomb Potential,

$$V = \frac{1}{2} \sum_{i,j}^N \sum'_{m \in \mathbb{Z}} \frac{(Ze)^2}{4\pi\epsilon_0 |r_{ij} + mL|} \quad (3.21)$$

Direct evaluation of the above summation is problematic due to the difficulty of its evaluation as it is being merely conditionally convergent <sup>68</sup>, and practically due to the slowly decaying long-range part of the Coulomb potential. The essential step in the Ewald method is to separate the Coulomb term into two components,

$$\frac{1}{r} = \frac{f(r)}{r} + \frac{1-f(r)}{r} \quad (3.22)$$

The idea behind this splitting is as follows:  $f(r)$  can be chosen so that the first part of Equation (3.22) is negligible beyond some (small) cutoff radius  $r_{\max}$ , and so that the second part is a slowly varying function for all  $r$ , which means that its Fourier transform is well represented by only a few wave-vectors  $k$ . This allows the first short range part to be readily evaluated in real space, and the second-long range part in reciprocal space. The usual selection for  $f(r)$  is the complementary error function,

$$\operatorname{erfc}(r) = \frac{2}{\sqrt{\pi}} \int_r^\infty \exp(-t^2) dt \quad (3.23)$$

which leads to the well-known Ewald formula for the total potential energy of the system <sup>68</sup>,

$$V = V^{(r)} + V^{(k)} + V^{(s)} + V^{(d)} \quad (3.24)$$

where the contributions from real space ( $V^{(r)}$ ), reciprocal space ( $V^{(k)}$ ), self-energy ( $V^{(s)}$ ) and dipole correction ( $V^{(d)}$ ) are given by,

$$V^{(r)} = \frac{1}{2} \sum_{i,j}^N \sum_{m \in \mathbb{Z}}' \frac{(Ze)^2 \operatorname{erfc}(\alpha|r_{ij+mL}|)}{4\pi\epsilon_0 |r_{ij+mL}|} \quad (3.25)$$

$$V^{(k)} = \frac{1}{2L^3} \sum_{k \neq 0} \frac{(Ze)^2}{\epsilon_0 k^2} \exp(-k^2/4\alpha^2) |n(k)|^2 \quad (3.26)$$

$$V^{(s)} = -\frac{\alpha}{\sqrt{\pi}} \sum_{i=1}^N \frac{(Ze)^2}{4\pi\epsilon_0} \quad (3.27)$$

$$V^{(d)} = \frac{1}{2\pi\epsilon_0(1+2\epsilon)L^3} (\sum_{i=1}^N Zer_i)^2 \quad (3.28)$$

In Equations (3.25) and (3.26), the parameter  $\alpha$  can be tuned so that the evaluation is as efficient as possible <sup>68</sup>. In Equation (3.26),  $n(k)$  is the Fourier transform of the particle density, and the summation is over wave-vectors at the discrete values of  $k$  consistent with the periodic boundary conditions.

From Equations (3.24)-(3.28), the force on each particle  $i$  in the simulation box can be calculated as,

$$F_i = -\nabla_i V = -\frac{\partial}{\partial r_i} V \quad (3.29)$$

This final equation, in principle, completes the specification of the force calculation part of an MD program dealing with Coulomb interactions. In this force calculation, the real space

part of the force resulting from  $V(r)$  is directly evaluated, using some cutoff radius, and the reciprocal space sum resulting from  $V(k)$  is truncated at some maximum wave-vector.

While the direct evaluation of the Ewald summation as outlined above in principle solves the problem of including long range interactions in an MD simulation, it has one main drawback: poor computational efficiency. This is mainly a result of the fact that direct evaluation scales with particle number  $N$  approximately as  $N^2$ . In order to improve this scaling, a number of methods based on evaluating the long-range part of the potential on a grid have been developed. The idea behind these methods is that they allow the reciprocal space part of the Ewald summation to be evaluated using the fast Fourier transform, which itself scales as  $N \log(N)$  (a significant improvement on  $N^2$ ). By choosing the real space cut-off to be sufficiently small, this improved scaling then essentially applies to the complete Ewald sum<sup>68</sup>.

One of the various mesh implementations is the so-called particle-particle-particle mesh (PPPM) algorithm<sup>69</sup>. For details of this algorithm, the reader is referred to<sup>68</sup>. All of the MD simulations performed by the author for this thesis used the PPPM algorithm for the Ewald summation.

#### 3.2.1.2. Van der Waals Interaction

Van der Waals interaction includes the short-range repulsion associated with the increase as two atoms approach each other and attractive dispersion energy. Lennard-Jones 6-12 function is the model commonly used for describing Van der Waals energy which is written as follows:

$$E_{LJ} = \sum_{i \neq j} D_{0,ij} \left[ \left( \frac{R_{0,ij}}{r_{ij}} \right)^{12} - 2 \left( \frac{R_{0,ij}}{r_{ij}} \right)^6 \right] \quad (3.30)$$

where  $D_{0,ij}$  and  $R_{0,ij}$  are empirical parameters .  $D_{0,ij}$  is the depth of the potential well (potential value at the equilibrium atomic distance) and  $R_{0,ij}$  is the distance at which the potential equals to zero. In the ClayFF force field, interaction parameters between the unlike atoms are calculated by arithmetic mean rule for  $R_{0,ij}$  and the geometric mean rule for  $D_{0,ij}$ ,

$$R_{0,ij} = \frac{1}{2}(R_{0,i} + R_{0,j}) \quad (3.31)$$

$$D_{0,ij} = \sqrt{D_{0,i}D_{0,j}}$$

### 3.2.2. Bonded Interaction

#### 3.2.2.1. Bond stretching

Phases containing hydroxyl groups require the stretch energy associated with each of the O-H bonds. This bond energy similar to SPC water model is described by harmonic term written as follows:

$$E_{bond\ stretch} = k_1(r_{ij} - r_0)^2 \quad (3.32)$$

where  $k_1$  is a force constant and  $r_0$  is the equilibrium bond length.

#### 3.2.2.2. Angle bending

To improve the vibrational behavior of hydroxyl groups, the angle bend term between a triplet of atoms  $i - j - k$  is represented by a harmonic potential,

$$E_{angle\ bend\ ijk} = k_2(\theta_{ijk} - \theta_0)^2 \quad (3.33)$$

where  $k_2$  is a force constant and  $\theta_{ijk}$  is the bond angle for the metal-oxygen-hydrogen and  $\theta_0$  represents the equilibrium bond angle.

## Chapter 4

### 4. Molecular Dynamics Study of the Dissolution Mechanism of Kaolinite Basal Surfaces in Alkali Media

#### 4.1. Introduction

Over the past few decades, geopolymerization has attracted tremendous interests to alter the industrial wastes to geopolymers which can be used as construction materials. Properties of these materials are comparable to those of the Portland cement. One major advantage of the geopolymerization process, compared with the Portland cement production process, is that the process requires much less energy, thereby less greenhouse gases emission. Studies showed that the geopolymerization process reduces CO<sub>2</sub> emission by about 80%<sup>70,71</sup>. A geopolymer is essentially formed by the initial dissolution of the aluminosilicate source material in an alkali solution followed by the reaction of the dissolved aluminate and silicate oligomers to form a three-dimensional, amorphous structure interlinked tetrahedrally, alternatively sharing all oxygen atoms<sup>72</sup>. The tetrahedrally coordinated aluminum carries a negative charge that is balanced by an alkali cation (e.g., sodium (Na<sup>+</sup>))<sup>72,73</sup>.

In the dissolution step, it is believed that the alkali solution (i.e., high pH) activates octahedral surfaces of the aluminosilicate source material by deprotonation<sup>74</sup>. This surface activation is considered as a necessary step for the subsequent dissolution of the aluminum (Al) and silicon (Si) containing species (oligomers)<sup>33,75</sup>. According to Xu *et al.*<sup>76</sup> the final

strength of a geopolymer highly depends on the Si/Al ratio of the gel phase (i.e., the oligomer solution) that is formed during the dissolution process. It is worth noting that Si/Al ratios in the range of 2 to 3 generally yield geopolymers with higher compressive strengths. Therefore, understanding the dissolution process is essential for optimizing the geopolymerization processes and the resultant geopolymers <sup>29,77,78</sup>.

Researchers have evaluated the dissolution process of aluminosilicate source materials under different conditions in terms of alkali type, concentration, pH and temperature. In most studies, kaolinite was used as the aluminosilicate source material. Kaolinite,  $\text{Al}_4\text{Si}_4\text{O}_{10}(\text{OH})_8$ , is a typical mineral with a 1:1 type layered structure, which comprises aluminum octahedral sheet and silicon tetrahedral sheet. These two sheets are connected together by bridging oxygens (Al-O-Si). For the tetrahedral sheet, a silicon atom is bound to three other silicon atoms through bridging oxygens (Si-O-Si) leading to the formation of the tetrahedral surface. This arrangement of tetrahedral silicones forms six-membered silica ring on the surface that is called tetrahedral cavity. For the octahedral sheet, each aluminum atom is connected to two oxygens of the tetrahedral sheet and shares four hydroxyl moieties with adjacent aluminum atoms. Three of these hydroxyl moieties are oriented toward the external surface giving rise to the octahedral surface while the fourth one is oriented inward in the direction of the tetrahedral cavity <sup>74,79</sup>. All layers in kaolinite structure are kept together by weak hydrogen bonds between hydroxyl moieties extending from the octahedral surface of a layer to the basal oxygen atoms on the tetrahedral surface of the adjacent layer. Studies have shown that the bridging oxygen atoms on silicate surface tend to be highly hydrophobic <sup>80,81</sup>. Blum *et al.* <sup>82</sup> showed that adsorption of proton at the silicate surface of kaolinite is very weak and the  $(\text{Si-OH-Si})^+$  sites at the tetrahedral layer will not be detectable

by surface titration in the pH range studied. Huertas *et al.* <sup>74</sup> studied the dissolution of kaolinite at ambient temperature and pressure over the pH range of 1 to 13. Their findings confirm that the adsorption of protons at the Si sites of the kaolinite surface and edges is negligible and the limiting step for the dissolution of kaolinite in an alkali solution is the formation of an  $\text{AlO}^-$  surface complex and the detachment of the Al atom from the structure. In fact, the octahedral surface becomes deprotonated at high pH (> 9). Bauer and Berger <sup>83</sup> studied the kinetics of the kaolinite dissolution in a solution containing  $\text{K}^+$  cations ranging from 0.1 to 4 M at various solid-solution ratios. It was reported that the rate-limiting step is the dissolution of the octahedral layer of kaolinite. Carroll and Walther <sup>84</sup> studied the dissolution of kaolinite at 25, 60 and 80°C at various pH ranging from 1 to 12. They found that at high pH, the detachment of Si from the kaolinite structure is slower than that of Al. On the other hand, Walther's studies showed that under alkali conditions, formation of  $\text{SiO}^-$  complexes controls the rate of the dissolution of kaolinite <sup>85,86</sup>. Panagiotopoulou *et al.* <sup>87</sup> studied the dissolution of different industrial aluminosilicate minerals and by-products in the alkali media. The experimental results showed that the extent of dissolution of Al and Si atoms of the reactive materials, such as metakaolin, in the sodium hydroxide (NaOH) solution was ~40% higher than the KOH solution. However, in the case of kaolin, the KOH solution yielded ~10% more dissolution of Al and Si atoms than the NaOH solution. Nevertheless, in both cases, more Si atoms were released to the solution. Xu and Van Deventer <sup>29</sup> investigated the extent of dissolution of 16 different minerals in the alkali solutions and the subsequent geopolymerization processes. It was concluded that in the presence of  $\text{K}^+$  and calcium ( $\text{Ca}^{+2}$ ) cations, the Si/Al ratio reached to 2. Hajimohammadi *et*

al. <sup>88</sup> have found that the release of alumina in the early stage of the reaction leading to a more homogeneous geopolymer gel.

In view of the apparent conflicting results of the interaction/dissolution of kaolinite in alkali media reported in the literature, in the present research, molecular dynamics (MD) simulation was utilized to study the interaction/dissolution mechanism of two basal surfaces of kaolinite at low (1 M) and medium (5 M) concentrations of three different alkali solutions at ambient condition (i.e., 298 K and 1 atm). Here, it should be noted that alkali solutions with concentrations greater than 1 M have a pH close to 14 at room temperature. Since NaOH and KOH solutions are widely used in the geopolymerization process <sup>29,89</sup>, in this study, alkali media containing Na<sup>+</sup>, K<sup>+</sup> and a mixture of 50/50 Na<sup>+</sup>/K<sup>+</sup> were studied.

#### 4.2. Simulation Method

Interactions between kaolinite's basal surfaces and the alkali solutions were modeled using the CLAYFF force field. The CLAYFF force field is commonly used to model structural and dynamical properties of hydrated clay systems and their interfaces with fluid phases by other researchers <sup>90-92</sup>. The force field treats clay minerals made up of flexible structures. In particular, interactions between the oxygen and metal atoms in the clay lattice are described by short-range 12-6 Lennard-Jones (LJ) potentials and long-range Coulombic potential using *ab initio* atomic partial charges <sup>93</sup>. Therefore, interaction energy between metal and oxygen atoms is given by the sum of LJ and Coulombic potentials,

$$E_{total} = E_{coul} + E_{LJ} = \frac{e^2}{4\pi\epsilon_0} \sum_{i \neq j} \frac{q_i q_j}{r_{ij}} + \sum_{i \neq j} D_{0ij} \left[ \left( \frac{R_{0ij}}{r_{ij}} \right)^{12} - 2 \left( \frac{R_{0ij}}{r_{ij}} \right)^6 \right] \quad (4.1)$$

where  $e$  is the charge of the electron,  $\epsilon_0$  is the permittivity of vacuum,  $q_i$  and  $q_j$  are *ab initio* partial atomic charges,  $r_{ij}$  is the distance between atoms  $i$  and  $j$ .  $D_{0ij}$  and  $R_{0ij}$  are empirical parameters. All non-bonded and bonded parameters for the CLAYFF force field<sup>90</sup> used in this study are presented in Tables 1 and 2.

Table 4-1 Nonbonded parameters used in the CLAYFF force field<sup>23</sup>

Force field type	Symbol	Charge (e)	$D_0$ (kcal/mol)	$R_0$ (Å)
water hydrogen	h*	0.410		
water oxygen	o*	-0.820	0.1554	3.5532
hydroxyl hydrogen	ho	0.425		
hydroxyl oxygen	oh	-0.950	0.1554	3.5532
bridging oxygen	ob	-1.050	0.1554	3.5532
tetrahedral silicon	st	2.100	$1.8405 \times 10^{-6}$	3.7064
octahedral aluminum	ao	1.575	$1.3298 \times 10^{-6}$	3.7064
aqueous sodium ion	Na	1.000	0.1301	2.6378
aqueous potassium ion	K	1.000	0.1000	3.7423

Table 4-2 Bonded parameters used in the CLAYFF force field<sup>23</sup>

<b>Bond Stretching</b>				
<i>Species i</i>	<i>Species j</i>	$K_a$ (kcal/mol Å <sup>2</sup> )	$r_0$ (Å)	
o*	h*	554.1349	1.0000	
oh	ho	554.1349	1.0000	
<b>Bond Angle</b>				
<i>Species i</i>	<i>Species j</i>	<i>Species k</i>	$K_b$ (kcal/mol rad <sup>2</sup> )	$\theta_0$ (deg)
h*	o*	h*	45.7696	109.47

In the CLAYFF force field, interactions between water molecules are described by the simple point charge (SPC) water model, which has been used to study properties of bulk water and aqueous systems<sup>94-97</sup>. The atomic structure of kaolinite was taken from the crystal structure refinement data determined from neutron diffraction studies performed at 1.5 K with well-characterized hydrogen position data<sup>98</sup>. According to reference<sup>98</sup> kaolinite has triclinic lattice structure with C1 symmetry and the lattice parameters are  $a = 5.1535 \text{ \AA}$ ,  $b = 8.9419 \text{ \AA}$ ,  $c = 7.3906 \text{ \AA}$ , and  $\alpha = 91.926^\circ$ ,  $\beta = 105.046^\circ$ ,  $\gamma = 89.797^\circ$ . Three-dimensional periodic boundary conditions were employed to all simulations reported here and all dimensions of the cell were free to vary independently. The simulation cell was built by repeating the kaolinite unit cell along the three axes ( $12 \times 12 \times 6$  units in  $a$ ,  $b$ , and  $c$  dimensions) which led to the formation of contained 864 kaolinite unit cells. The aqueous part of simulation cells in this study contained 4,020 water molecules and 84 and 420 cations for 1 M and 5 M solutions, respectively. First, the cell of 4,020 water molecules with the dimension of  $61.7 \text{ \AA} \times 107.2 \text{ \AA} \times 18.6 \text{ \AA}$  was built based upon the density of water at ambient condition and was assembled with the basal surface of kaolinite (the  $ab$  plane) to create the solid-aqueous solution interface with the dimension of  $61.7 \text{ \AA} \times 107.2 \text{ \AA} \times 65.1 \text{ \AA}$ . It is worth noting that kaolinite has two different (001) basal surfaces and building a simulation cell in this way allowed us to simultaneously study the interactions at both interfaces using molecular dynamics (MD) simulation. Afterwards, cations were inserted in the solution region of the simulation cell in three different initial configurations, i.e., i. random distribution of cations in the solution region, ii. positioning of cations in the middle region of the solution and iii. Positioning of cations close to the octahedral surface in the solution.

We deprotonated the octahedral surface simply by manually removing (deleting) the hydrogen atoms from randomly selected hydroxyl groups on the octahedral surface before the MD simulations. This led to an octahedral surface with both  $-OH$  and  $-O^-$  moieties. To ensure charge neutrality, a different number of hydrogen atoms (charge of hydrogen differs from those of the cations added) was removed on the octahedral surface so that a partially deprotonated octahedral surface was created. Similar study of the deprotonated surface (charged surface) of amorphous silica in contact with Lithium and Cesium cations was studied by Hocine *et al.*<sup>99</sup>.

It is worth noting that the distance between the two layers of de-protonated octahedral surfaces was actually 62.9 Å (18.6 Å solution plus 44.3 Å of kaolinite). Furthermore, water molecules (with a high dielectric constant of 78.54 at 25 °C) in between the kaolinite layers exhibit high screening effects, thereby substantially shortening the Bjerrum length ( $< 10$  Å). Therefore, there are no significant interactions between the interfaces. The degree of deprotonation was dependent on the solution concentration used in the model<sup>74,79</sup>. In the case of mixed  $Na^+$  and  $K^+$  solution, equal number of both cations was used. For instance, in the 1 M solution containing the total number of 84 cations, there were 42  $Na^+$  and 42  $K^+$  cations dispersed within 4,020 water molecules. It was assumed that most of the protons released into the solution in the vicinity of octahedral surface would react with the hydroxide ions to form water. Therefore, we feel justified not to include both protons and hydroxide ions in the simulations. In addition, there are no reliable force field parameters available for protons.

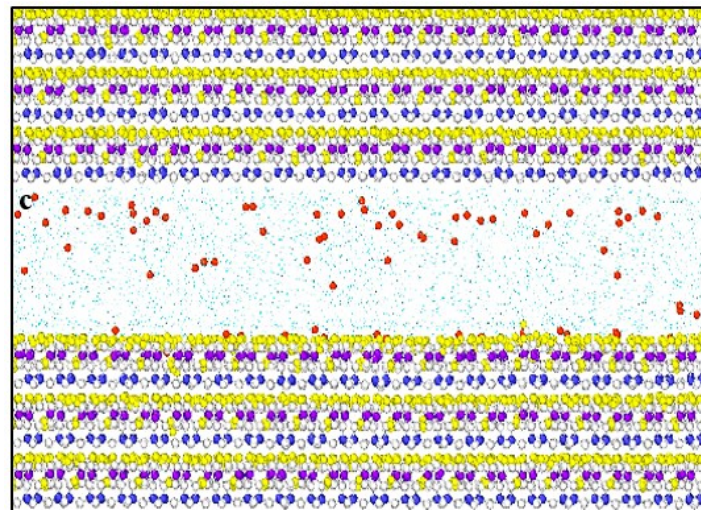
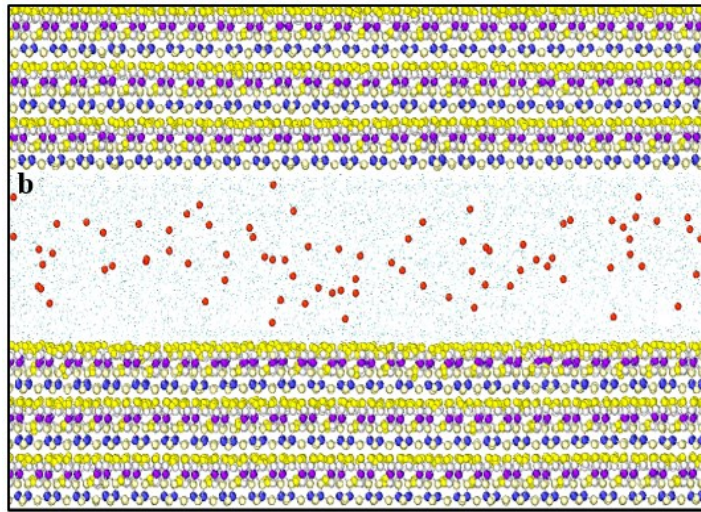
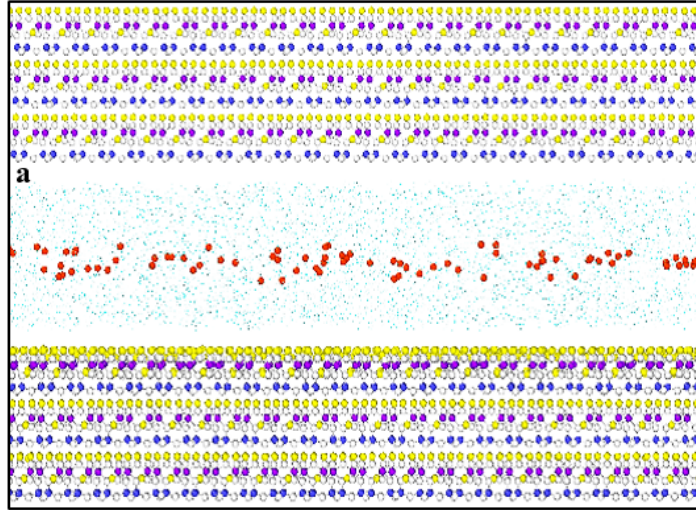
All MD simulations were performed in isothermal-isobaric (i.e., NPT) ensemble<sup>63,100</sup> at 298 K and 1 atm, using the Nose-Hoover thermostat and barostat<sup>101,102</sup> with relaxation times

of 0.1 and 1 ps, respectively. Velocity Verlet's algorithm <sup>61,103</sup> was used to integrate the equations of motion of atoms in every 1 fs and long-range electrostatic interactions were evaluated every 1.0 fs with the particle-particle particle-mesh (PPPM) summation algorithm <sup>104</sup>. At the early stage of performing all simulations, the system went through 100 ps NPT MD simulation to relax the structure and afterward 1,000 ps (i.e., 1 ns) of NPT MD simulation was run for data collection. The cutoff distance of the CLAYFF force field is 8.5 Å meaning that once two atoms in the kaolinite structure is beyond such distance, the force field is not able to describe their interaction. In our study, it was found that for the long simulations (e.g., > 1 ns simulation), such situations occurred. Therefore, the simulation time was chosen to be 1 ns. It is worth noting that the systems were still stable for a longer time of simulation (i.e., 10 ns) which confirms the stability of the simulation systems; however, due to the force field cutoff distance, the results were studied within 1 ns of simulation. Radial distribution functions and atomic density profiles <sup>61,102</sup> in the [001] direction were utilized to analyze the structural changes. All the simulations were carried out by using the LAMMPS (Large-scale Atomic/Molecular Massively Parallel Simulator) program <sup>105</sup> on Linux cluster and Materials Studio 8.0 software (Biovia Inc., San Diego, CA, USA) was used to create the simulation cells and visualize the results.

### 4.3. Results and Discussion

The initial configuration of the 1 M Na<sup>+</sup> solution sandwiched between the two basal surfaces of kaolinite (tetrahedral and partially deprotonated octahedral surfaces are below and above the solution, respectively) and Na cations positioned in the middle of the solution region is shown in Fig. 4-1a. As stated earlier, the simulations were conducted for different configurations of cations in the solution; however, we observed same results for different

initial positions of cations in the systems containing different cations, i.e., Na<sup>+</sup>, K<sup>+</sup> and 50/50 Na<sup>+</sup>/K<sup>+</sup> solutions. Accordingly, due to the similarity, the results of the simulations with one of the cations configuration are shown (i.e., cations positioned in the middle of solution). To statistically increase the accuracy of the results, each system with different cations configuration was studied three times. Figs. 4-1b and 1c depict snapshots of the same system after 10 ps and 1 ns of NPT MD simulation, respectively. Fig. 4-1d shows the configuration of the basal surfaces exposed to a 5 M Na<sup>+</sup> solution after 1 ns of NPT MD simulation. It should be noted that at 5 M, compared with the 1 M solution, more surface hydroxyl groups of the initial partially deprotonated octahedral surface were further deprotonated. Thus, as shown in Fig. 4-1d, there is much distortion occurred in the octahedral surface in the 5 M system than that in the 1 M system after the MD simulation. However, in both cases, there was not much distortion occurred to the tetrahedral surface. However, detailed analysis of the data discussed later in this section indicates that the solutions containing Na<sup>+</sup> and K<sup>+</sup> cations behaved differently in their interactions (dissolution) with the kaolinite basal surfaces.



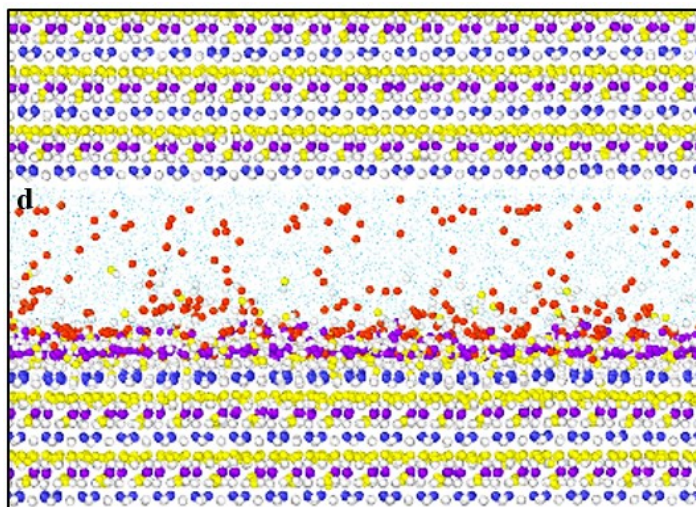


Figure 4-1 The two basal surfaces of kaolinite in contact with a 1 M Na<sup>+</sup> solution: (a) initial configuration, (b) a snapshot of the system described after 10 ps of NPT MD simulation, (c) a snapshot of the system after 1 ns of NPT MD simulation, and (d) a snapshot of the system in a 5 M Na<sup>+</sup> solution after 1 ns of NPT MD simulation. All NPT MD simulations were carried out at 298 K and 1 atm. The color scheme is: violet for aluminum, navy for silicon, white for oxygen, yellow for hydrogen, red for Na<sup>+</sup> (a – c) and K<sup>+</sup> (d) and blue dots are water.

The results shown in Fig. 4-1 suggest that the interaction (dissolution) process started with the diffusion of Na<sup>+</sup> (or K<sup>+</sup>) cations toward the octahedral and tetrahedral surfaces (mostly octahedral) at the early stage of the simulation (< 100 picoseconds). Once the cations “adsorbed” on the deprotonated sites (i.e., Al-O-Al) on the octahedral surface, it started to distort the surface structure (see detailed discussion on the mechanisms later) and eventually led to the dissolution of hydroxyl and aluminate groups into the solution.

Let’s define dissolution computationally at the outset. Atoms (e.g., aluminum) that belong to the octahedral surface (initially in the crystalline phase) tend to have more neighboring atoms than those in the solution. And this difference leads to the difference in their order parameters as defined by Lanaro and Patey in their work of quantifying the dissolution of sodium chloride in water<sup>41</sup>. The order parameter is simply calculated by selecting an atom

of interest and counting the number of neighboring atoms of the same type or different type within a specified radius of the selected atom. And this process is repeated for all atoms initially present in the octahedral surface as well as at different times during the MD simulation. According to Lanaro and Patey<sup>106</sup>, the value of the radius used does not greatly affect the resultant order parameters. Given that the cutoff distance of the CLAYFF force field is 8.5 Å, a radius of 8 Å was used to calculate the order parameters. The results showed that aluminum atoms associated with the octahedral surface had an average of 21.2 neighboring aluminum atoms, while those exhibited order parameters less than 12 were considered dissociated. For oxygen atom in the hydroxyl groups on the octahedral surface, it had 16.7 neighboring aluminum atoms but those with less than 4 were considered dissociated. In other words, if order parameters of aluminum and oxygen atoms initially present in the octahedral surface are less than 12 and 4, respectively, the atoms are considered to be part of the solution (i.e., dissociated), not that of the octahedral surface.

Fig. 4-2 shows the dissociation of the hydroxyl and aluminate groups schematically. As shown in Fig. 4-2a, at the early stage of simulation, a cation ( $\text{Na}^+$  in this particular case) adsorbs onto a deprotonated site on the surface. This interaction leads to the continued increase in the interatomic distance between the neighboring hydroxyl group and the aluminum atom to which the hydroxyl group attached over the course of the simulation. When the order parameter of the oxygen atom is below 4.0, the hydroxyl group is considered dissociated. On the other hand, as shown in Fig. 4-2b, interaction between the adsorbed cation and the deprotonated site can shift the positions of the aluminum atoms that are attached to the deprotonated site and consequently increases the interatomic distance between one of the aluminum atoms and its two bridging oxygen ( $\text{O}_b$ ). The interaction also

increases the interatomic distance between the oxygen atom that is shared between two aluminum atoms and one of those two aluminum atoms (see light blue lines in Fig. 4-2b). When the order parameter of the aluminum atom adjacent to the deprotonated is below 0.5, the aluminum atom and all the groups attached to it (see dark blue lines in Fig. 4-2b) are considered dissociated. If there are additional neighboring deprotonated group(s) involved, different numbers of oxygen and hydrogen attached to the aluminum atom in question could dissociate in the form of aluminates, i.e.,  $(\text{AlO}_m\text{H}_n)^{(m-n)-}$  where  $m$  was observed to be 3 or 4. In the case shown in Fig. 4-2b, the aluminate dissociated is  $\text{AlO}_4\text{H}_3^-$ . The dissociation of the hydroxyl and aluminate groups led to the change in the coordination number of surface aluminum atoms from 6-fold ( $\text{AlO}_6$ ) to 5-fold ( $\text{AlO}_5$ ) and 4-fold ( $\text{AlO}_4$ ). In both cases, this caused distortion to the octahedral surface structure. The results are in agreement with previous experimental observation of Huertas *et al.* <sup>74</sup> in which the authors suggested that dissolution of kaolinite in alkali solution started with the de-protonation of the octahedral surface followed by the interaction between the cations and aluminum atoms presented in the octahedral surface.

Fig. 4-3 summarizes the top views of a part of the octahedral surface exposed to various alkali solutions. To show the structural distortion more clearly, all other types of atoms are removed except the aluminum atoms along with the hydroxyl groups on the octahedral surface. Snapshots of the distortion of the octahedral surface in the presence of 1M and 5 M alkali solutions (after 1 ns of NPT MD simulation) are shown in Fig. 4-3 b, 4-3 d and 4-3 f and 4-3 c, 4-3 e and 4-3 g, respectively. It was observed that a dissociated hydroxyl group affected the surface structure in two ways. Firstly, it changed the position of the connected aluminum atom, leading to a minor distortion to the surface structure. Secondly, it caused

the formation of a vacancy in the structure. As such, some neighboring aluminum atoms would tend to migrate to that vacancy leading to more distortion to the octahedral surface.

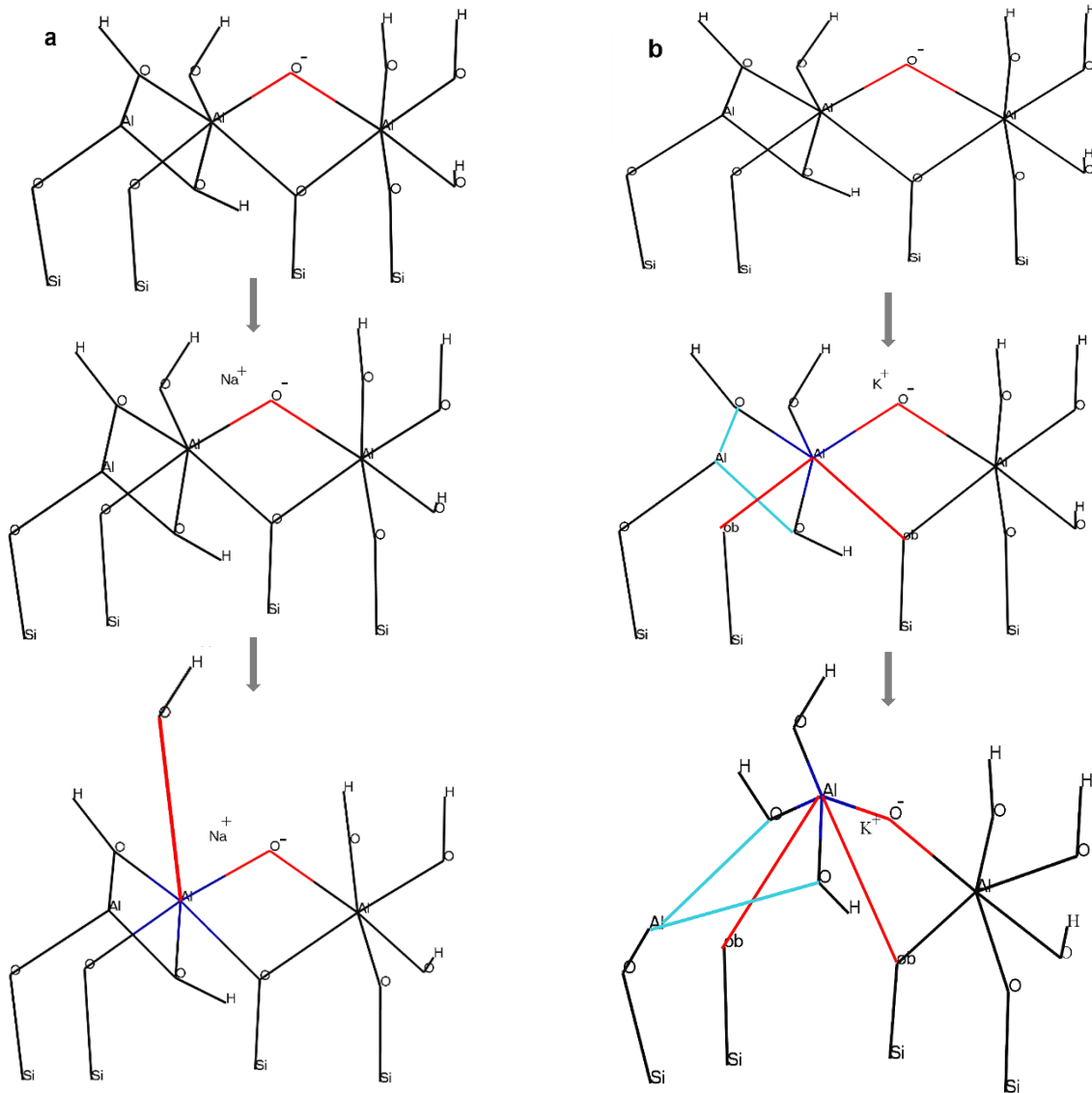
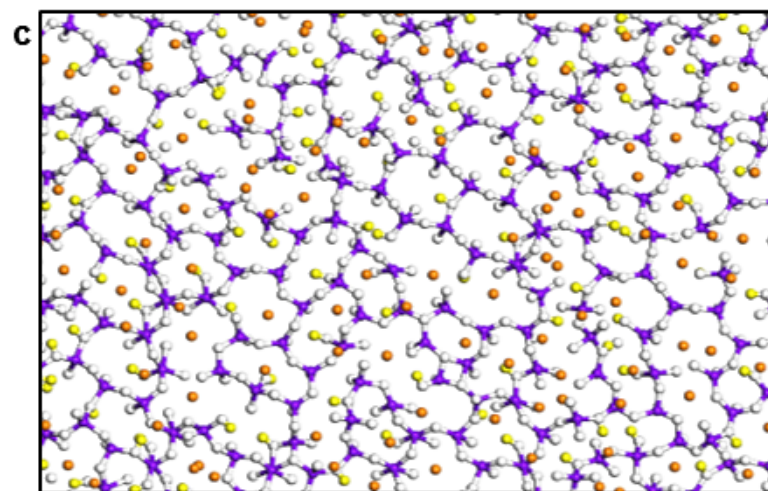
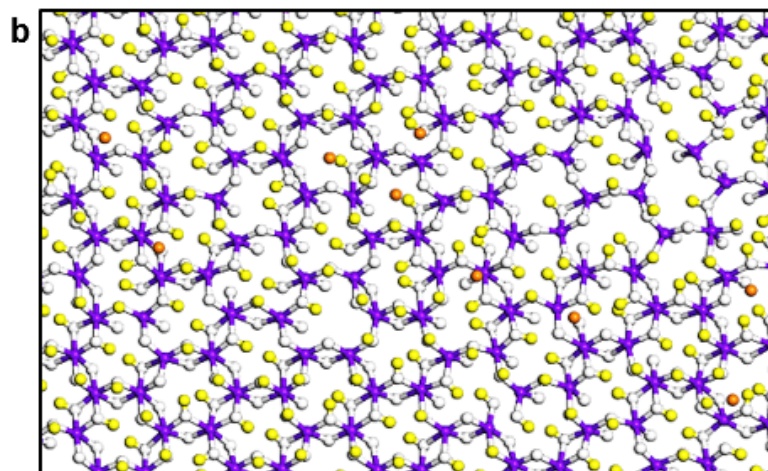
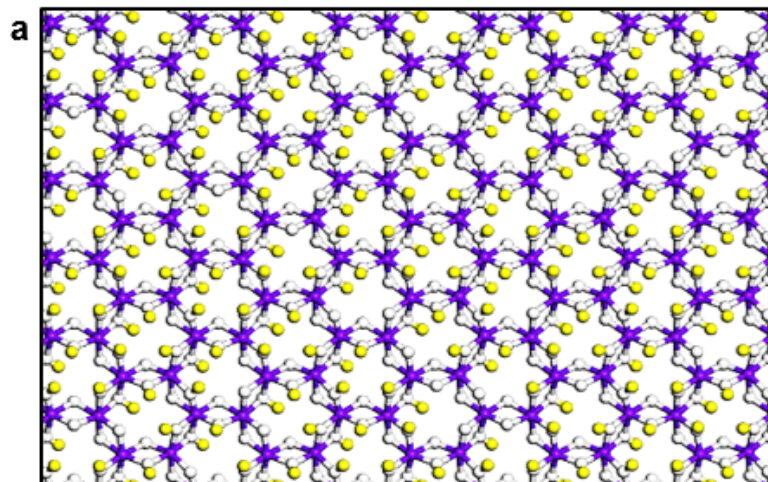
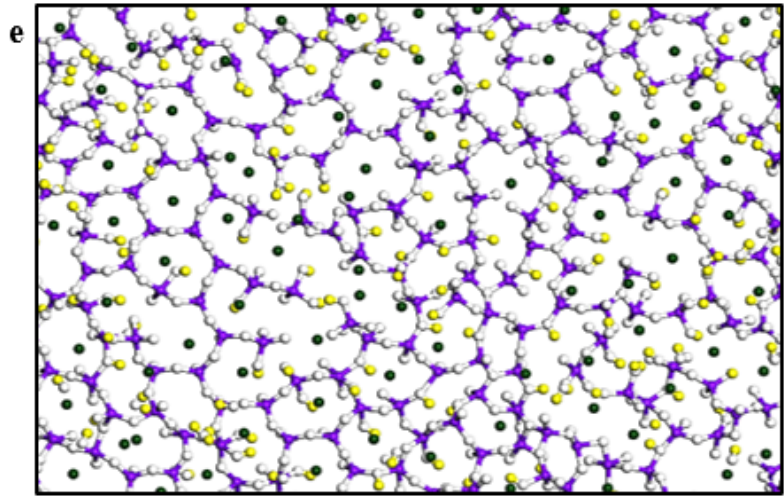
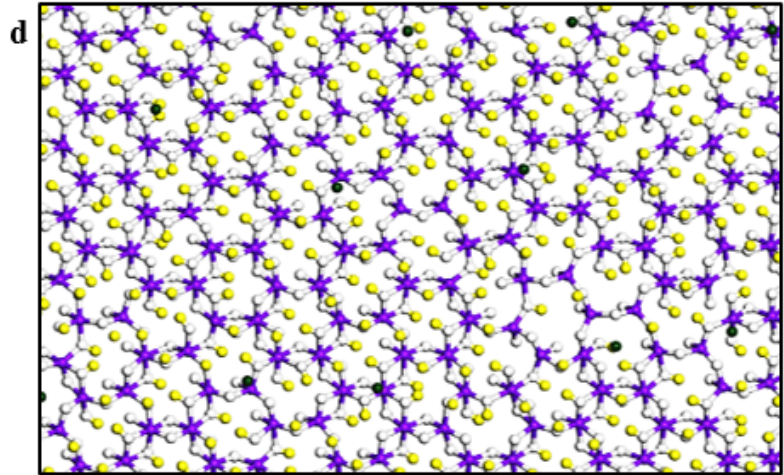


Figure 4-2 Schematic illustrations of the sequences of the dissociation (a) the OH group and (b) the aluminate group in the solutions containing Na<sup>+</sup> and K<sup>+</sup>, respectively, as a result of interaction between a deprotonated site on the octahedral surface and the cations.





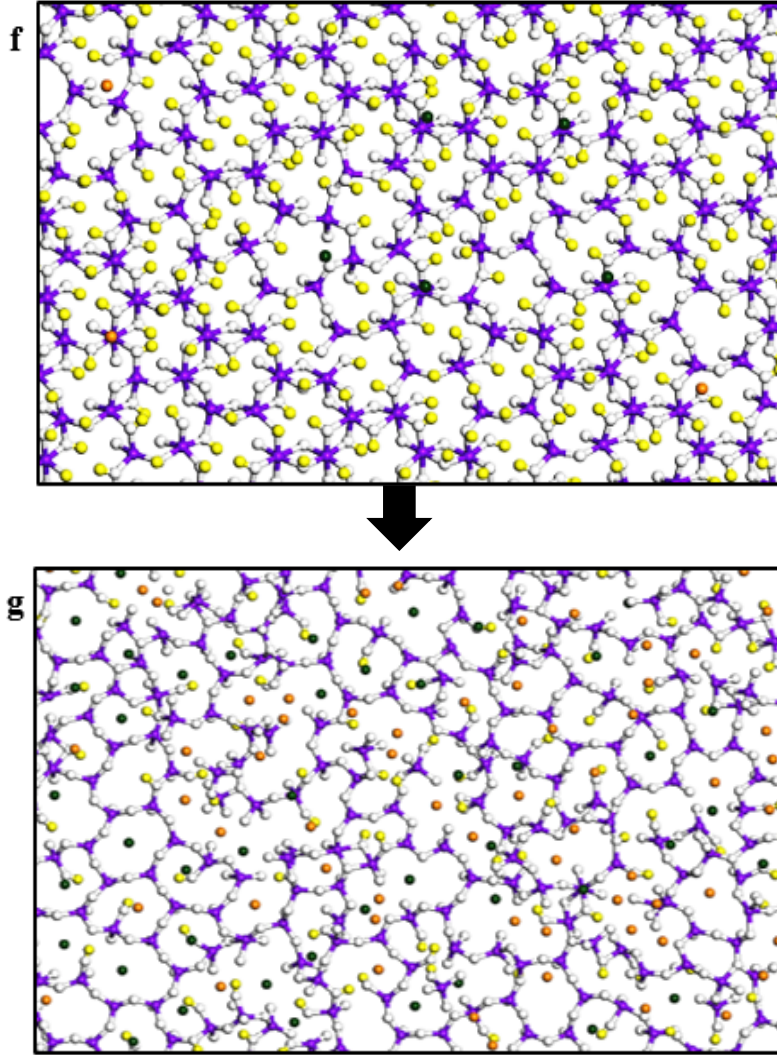


Figure 4-3 Part of the octahedral surface (top view) upon 1 ns NPT MD simulation at 298 K and 1 atm (a) initial structure, (b) 1 M Na<sup>+</sup>, (c) 5 M Na<sup>+</sup>, (d) 1 M K<sup>+</sup>, (e) 5 M K<sup>+</sup>, (f) 1 M 50/50 Na<sup>+</sup>/K<sup>+</sup>, (g) 5 M 50/50 Na<sup>+</sup>/K<sup>+</sup>. The color scheme here is violet, white, yellow, orange and dark green for Al, O, H, Na<sup>+</sup> and K<sup>+</sup>, respectively.

The aforementioned distortion was also confirmed by the radial distribution functions (RDFs) of the aluminum and oxygen atoms in the structure of the octahedral surface (see Fig. 4-4). In particular, the octahedral surface lost its crystallinity and turned to amorphous structure. In the 1 M solution, the distortion on the surface is mostly due to the dissociation

of OH<sup>-</sup> groups. As a result, most of aluminum atoms are still in 6-fold position (Fig. 4-4a). In the cases of 5 M solutions, the change in the first peak position indicates that aluminum atoms in the octahedral surface changes from the octahedral to tetrahedral positions after 1 ns NPT simulation <sup>107</sup>.

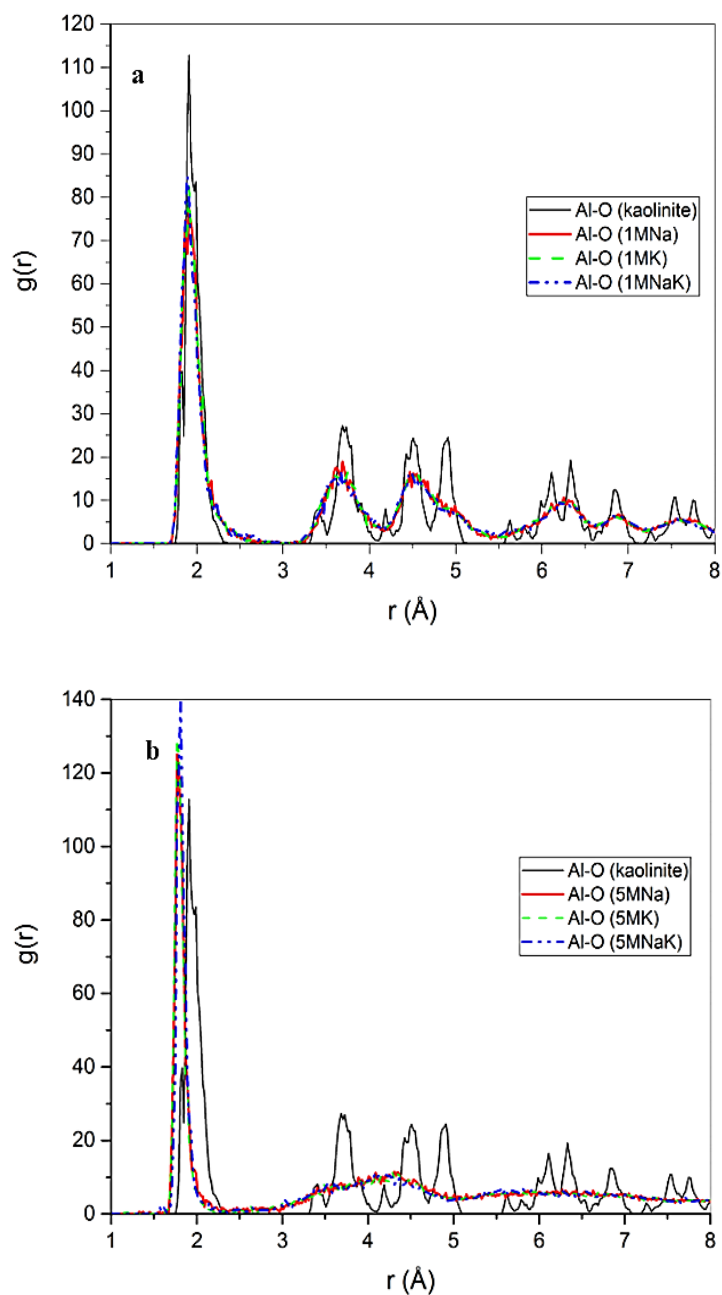
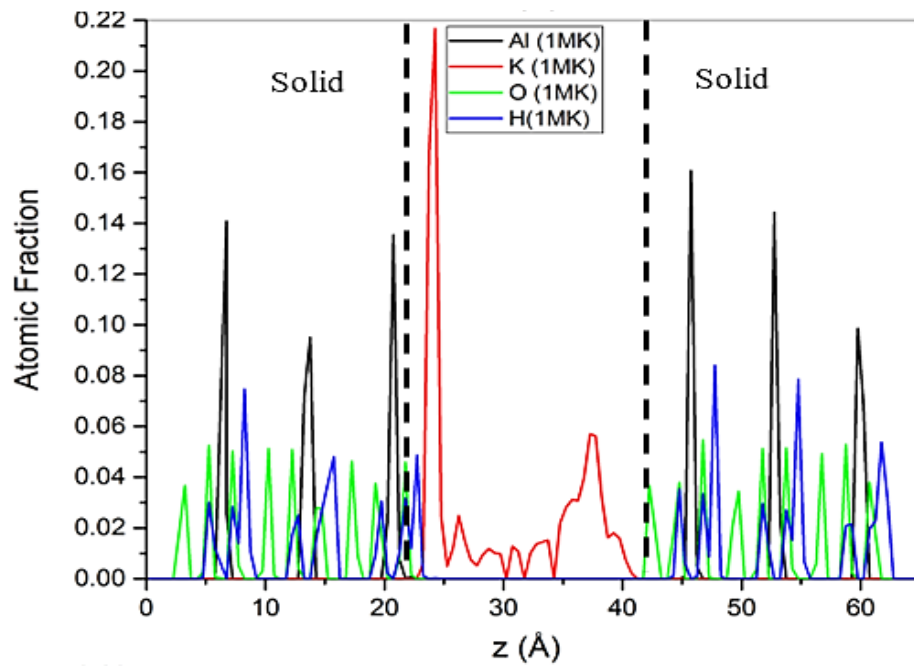
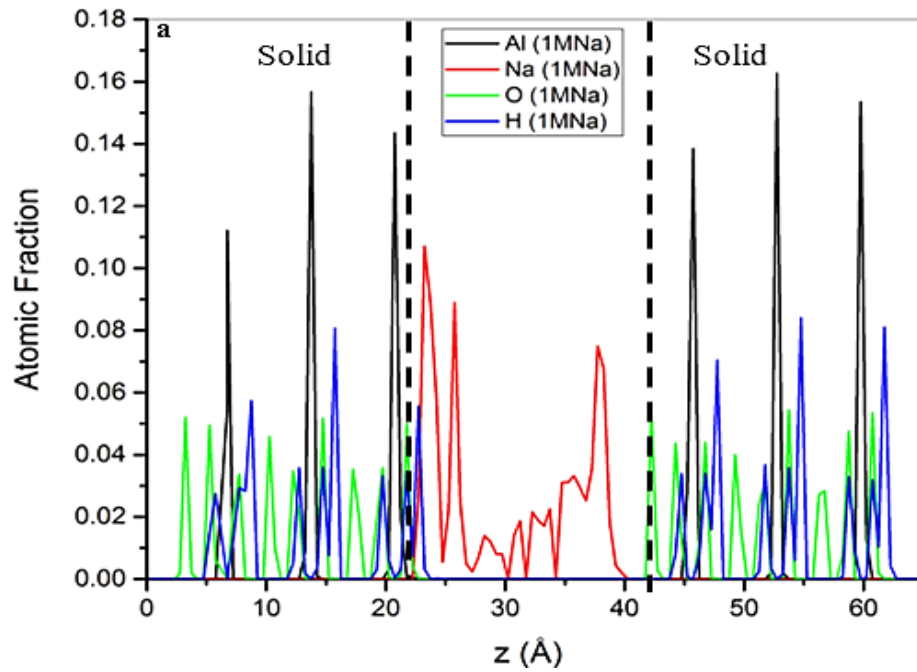


Figure 4-4 Radial distribution functions of Al–O of the octahedral surface: (a) 1 M solutions and (b) 5 M solutions.

The atomic density profiles (Fig. 4-5) clearly support the aforementioned dissolution process. Owing to the similarity of the profiles of 1 M and 5 M solutions, we only show the profiles of the 1 M solutions here. The atomic density profiles were calculated by averaging

the  $z$  coordinates of each atomic species during last 300 ps of the corresponding NPT MD simulation. The number of specific atomic species at specific distance, i.e.,  $\Delta z$ , can be calculated by integration of atomic density profile over the slab of interest. There are three distinct regions in the  $z$  direction as shown in Fig. 4-5. Starting from the bottom, over the length of 0 - 22.2 Å, the cell is occupied by three layers of kaolinite (each layer contains one octahedral sheet and one tetrahedral sheet). Over the length of 22.2 - 42 Å, it is the alkali solution. And above 42 Å, there are another three layers of kaolinite.

As shown in Fig. 4-5, in all three cases, both  $\text{Na}^+$  and  $\text{K}^+$  cations mostly adsorbed on the octahedral surface rather than the tetrahedral surface. Comparison of the peak heights of the cations shows that there are more  $\text{K}^+$  cations adsorbed on the octahedral surface than  $\text{Na}^+$  cations at the same concentration. In fact,  $\text{K}^+$  cations exhibited one peak (single layer) near the octahedral surface, whereas,  $\text{Na}^+$  cations showed two peaks (two layers). All three atomic density profiles clearly show that  $\text{Na}^+$  cations are closer to the octahedral surface than  $\text{K}^+$  cations, which is attributed to smaller size of  $\text{Na}^+$  cations relative to  $\text{K}^+$  cations and consequently higher charge density of  $\text{Na}^+$  than  $\text{K}^+$  (see second and fourth columns in Table 1). Accordingly,  $\text{Na}^+$  cations can diffuse more into the octahedral surface, leading to the formation of first layer.



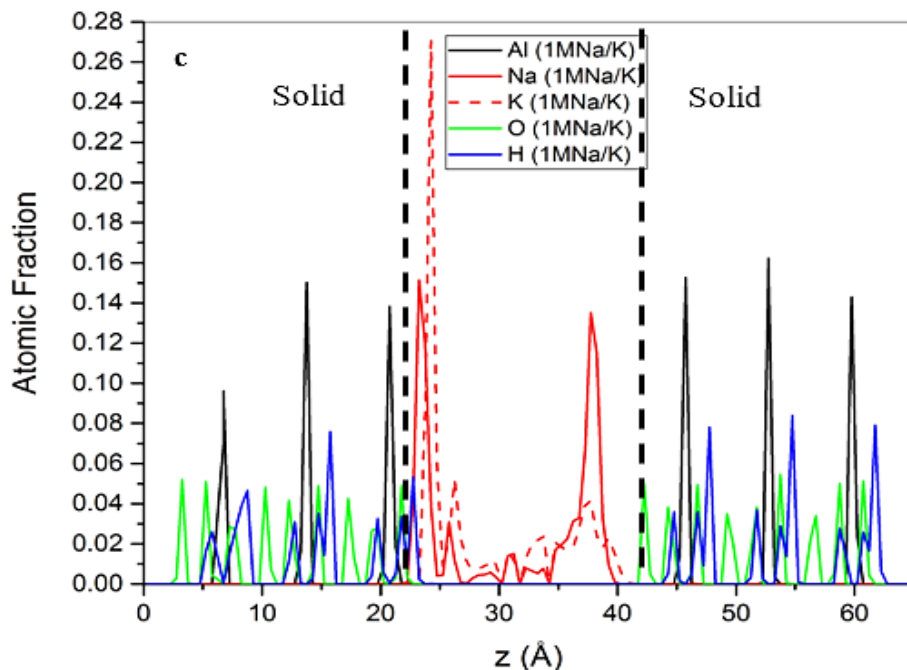


Figure 4-5 Atomic density profiles of aluminum atoms (black), cations (red), oxygen atoms (green) and hydrogen atoms (blue) after 1 ns of NPT MD simulations: (a) 1 M Na<sup>+</sup> solution, (b) 1 M K<sup>+</sup> solution and (c) 1 M Na<sup>+</sup>/K<sup>+</sup> solution.

As stated earlier, the area under the peak of an atomic density profile for a specific type of atom at any specific  $z$  region signifies the number of such atom in that region. Based upon the peaks of the hydrogen atoms before (not shown here) and after the MD simulation for both 1 M and 5 M solutions, it was found that more hydroxyl groups dissociated in the presence of Na<sup>+</sup> compared to the other two cases (i.e., K<sup>+</sup> and 50/50 Na<sup>+</sup>/K<sup>+</sup>) as depicted in Fig. 4-6. It seems that Na<sup>+</sup> cations with a higher charge density which leads to the formation of a stronger hydration shell, triggered more hydroxyl groups to dissociate. The number of aluminum atoms (in the form of dissociated aluminate groups) that dissociated from the octahedral surface was also determined using the aluminum peaks over the  $z$  range of 20 to

22 Å for all systems. The results showed that the number of dissociated aluminate groups is higher in the presence of K<sup>+</sup>.

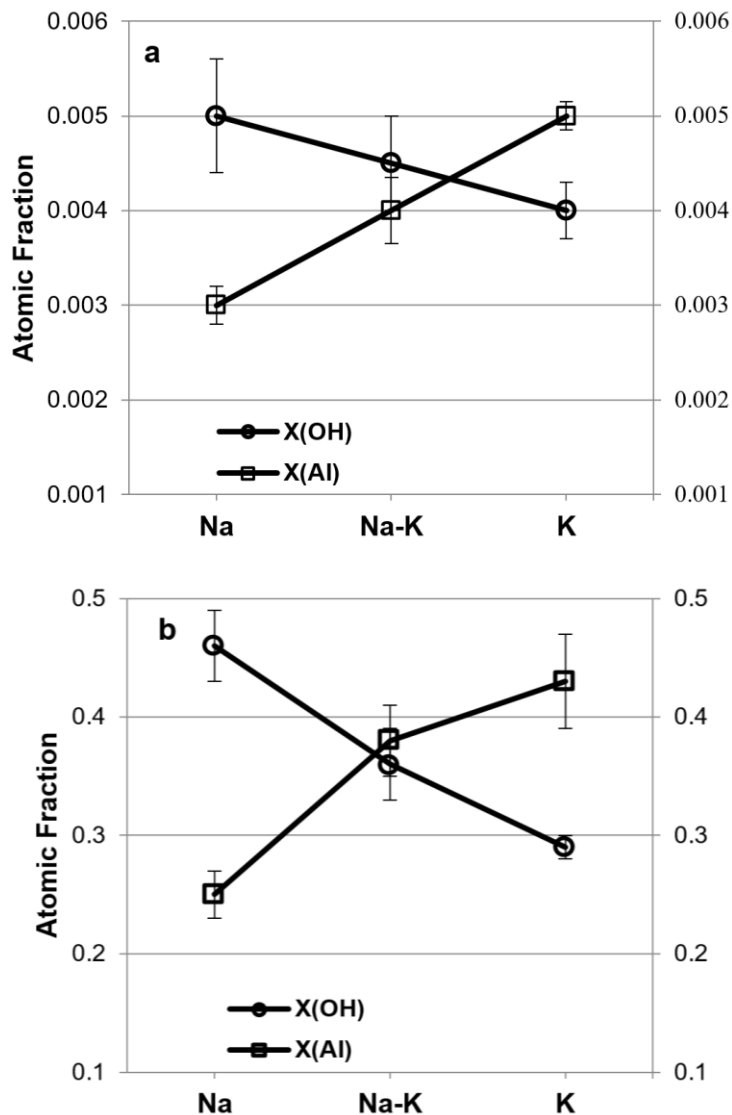


Figure 4-6 Relative atomic fractions of hydroxyl groups released into the alkali solution and aluminum atoms (in the form of aluminates) drifted away from their initial positions for the systems containing different cations at different concentrations: (a) 1 M and (b) 5 M.

As shown in Fig. 4-6, the two cations affect the octahedral surface differently. The cation with high charge density, i.e., Na<sup>+</sup>, caused more dissociation of hydroxyl groups from the

octahedral surface. As shown in Fig. 4-7a, the number of hydroxyl groups released to the solution containing 5 M Na<sup>+</sup> cation was ~30 after 1 ns simulation; however, relatively fewer number of hydroxyl groups left the octahedral surface to the K<sup>+</sup> and Na<sup>+</sup>/K<sup>+</sup> solutions. In contrast, the cation with low charge density, i.e., K<sup>+</sup>, encouraged more dissociation of the aluminate groups, which consequently led to a significant distortion to the surface. In the presence of 5 M K<sup>+</sup> solution, the interaction of solution with the kaolinite octahedral surface led to the release of 15 aluminate groups to the solution after 1 ns simulation; however, 10 and 4 aluminate groups were released for the Na<sup>+</sup>/K<sup>+</sup> and Na<sup>+</sup> solutions, respectively (Fig. 4-7b).

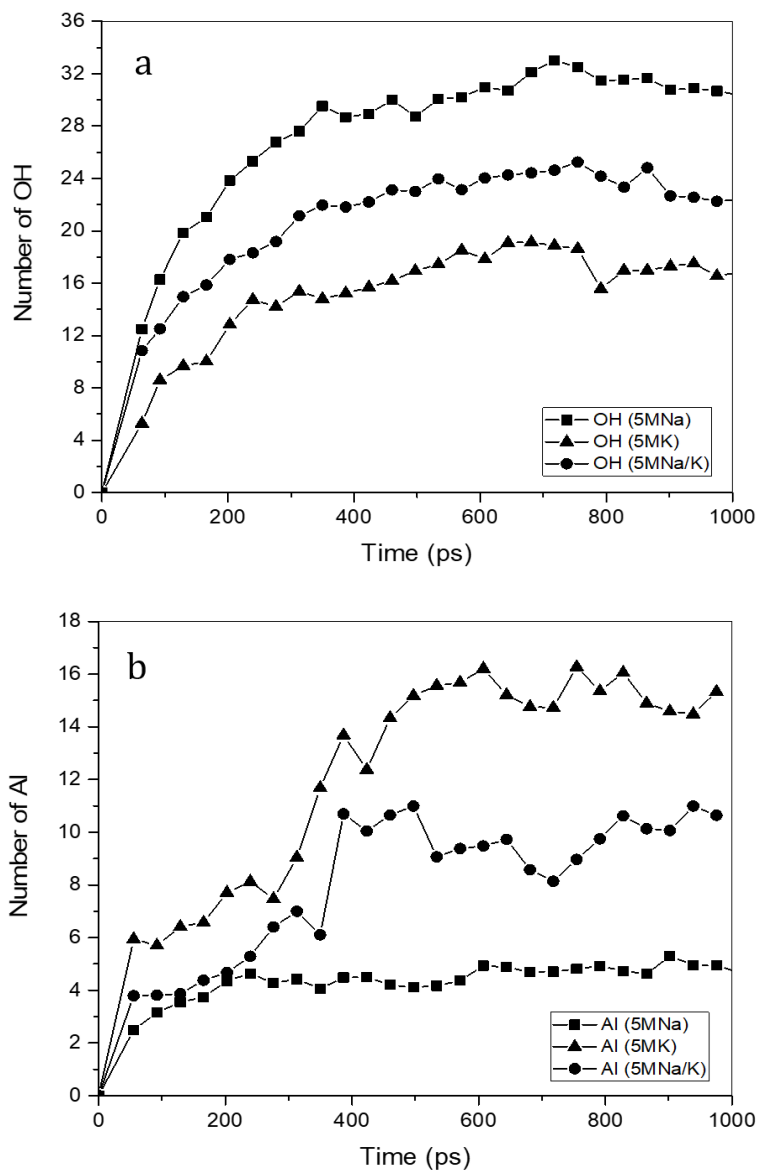
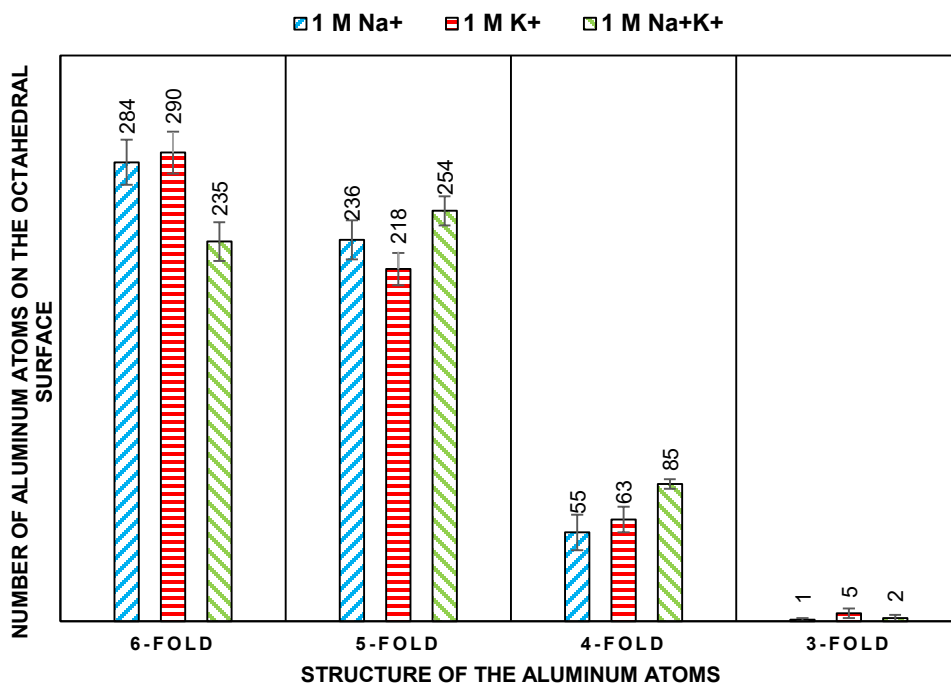


Figure 4-7 Number of (a) hydroxyl groups and (b) aluminum atoms dissociated from the octahedral surface and entered into the alkali solution versus simulation time for 5 M solutions containing different cations (i.e., Na<sup>+</sup>, K<sup>+</sup>, Na<sup>+</sup>/K<sup>+</sup>).

Fig. 4-8 indicates the number of 6-, 5-, 4- and 3-fold aluminum atoms for the systems containing different cations after 1 ns NPT MD simulation. The original octahedral surface comprises 576 aluminum atoms individually connected to 6 oxygen atoms. For the 1 M solutions after the MD simulation,  $55 \pm 7$  and  $63 \pm 4$  aluminum atoms turned to 4-fold

position in the presence of Na<sup>+</sup> and K<sup>+</sup>, respectively. However, in the presence of a 50/50 mixture of Na<sup>+</sup> and K<sup>+</sup>, more than 35% aluminum atoms became 4-fold (85 ± 2) compared with the solutions containing only Na<sup>+</sup> or K<sup>+</sup>. Likewise, relatively more aluminum atoms turned to 4-fold position (520 ± 6) in the 5 M Na<sup>+</sup>/K<sup>+</sup> solution relative to the Na<sup>+</sup> (463 ± 11) or K<sup>+</sup> (490 ± 9) solutions. A synergistic effect of both Na<sup>+</sup> and K<sup>+</sup> cations resulted in more aluminum atoms to lose their hydroxyl groups (caused by Na<sup>+</sup>) and bridging oxygen atoms (caused by K<sup>+</sup>), which led to slightly more distortion to the octahedral surface compared with the systems with Na<sup>+</sup> or K<sup>+</sup> alone.



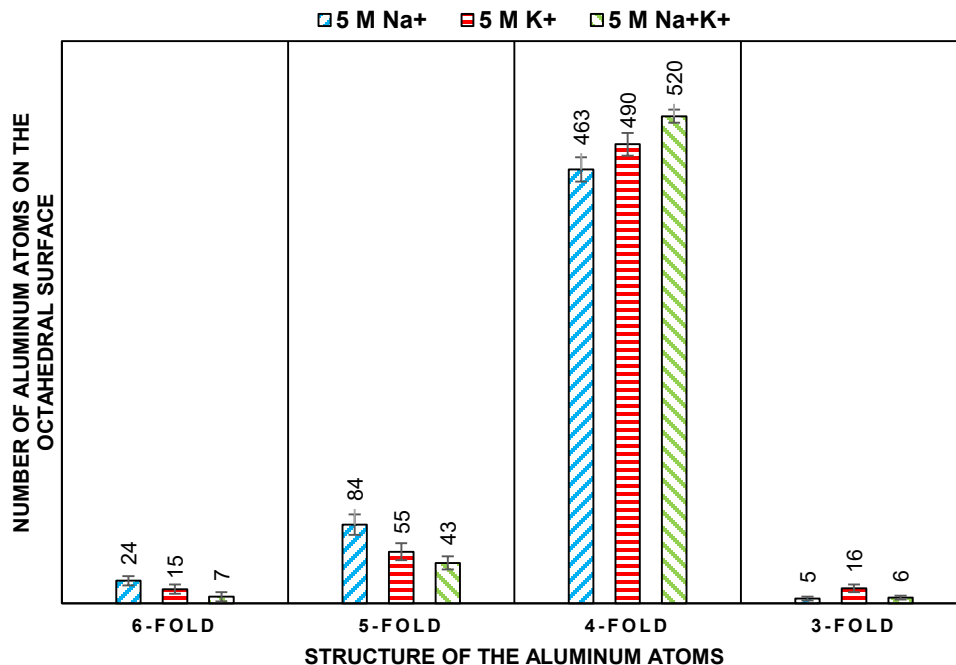


Figure 4-8 Coordination numbers of the aluminum atoms on the octahedral surface of kaolinite, (a) 1 M solutions, (b) 5 M solutions.

#### 4.4. Conclusions

In the present research, the dissolution of the basal surfaces of kaolinite in the alkali solutions containing  $\text{Na}^+$ ,  $\text{K}^+$  and 50/50  $\text{Na}^+/\text{K}^+$  cations was studied at low (1 M) and medium (5 M) concentrations at 298 K and 1 atm, using molecular dynamics (MD) simulation along with the CLAYFF force field. The adsorption of the cations on the partially deprotonated octahedral surface resulted in the dissolution of the surface hydroxyl groups near the adsorption sites and the aluminum atoms (in the form of aluminates) associated with them. The MD simulation results are in agreement with the experimental observations performed by Huertas *et al.* (1999) in which the authors suggested that dissolution of kaolinite in alkali solution started with the de-protonation of the octahedral surface followed by the interaction of solution with the octahedral surface. The MD results showed that the  $\text{Na}^+$

solution triggered more surface hydroxyl groups to dissociate from the octahedral surface than the  $K^+$  solution. In contrast, the  $K^+$  solution resulted in more dissociation of the aluminate groups than the  $Na^+$  solution. The different dissolution mechanism of the two cations was attributed to the difference in the charge density of the two cations. However, when the octahedral surface was exposed to a 50/50  $Na^+/K^+$  solution, more distortion to the surface occurred, suggesting that there was a synergistic effect of both  $Na^+$  and  $K^+$  cations. Dissolution of the tetrahedral surface was not observed in the present work.

## Chapter 5

### 5. Influence of Structural Al and Si Vacancies on the Interaction of Kaolinite Basal Surfaces with Alkali Cations: A Molecular Dynamics Study

#### 5.1. Introduction

Geopolymers are amorphous aluminosilicate polymer networks that are synthesized using aluminosilicate source materials in a high concentrated alkali media at ambient or slightly elevated temperatures <sup>15,16,108</sup>. In general, it is believed that the geopolymerization reaction involves two steps. The first step is the dissolution of the source material, a crystalline aluminosilicate material, into aluminate and silicate monomers. The second step is the reaction of the dissolved aluminate and silicate monomers to form amorphous geopolymer networks <sup>29,77</sup>. The dissolution step determines the resultant structures of the monomers, thereby determining how does the geopolymerization reaction proceed and properties of the final products.

Kaolinite is an aluminosilicate source material which is abundantly found in nature and industrial waste such as oil sand tailings <sup>74,79,109</sup>. Kaolinite possesses a layered structure containing aluminum and silicon in its octahedral sheet and tetrahedral sheet, respectively. And it is commonly used as the source material for the geopolymerization process <sup>110,111</sup>. It has been observed that the type and concentration of alkali cation significantly affect the

geopolymerization process <sup>110,111</sup>. The effect of the type and concentration of alkali cation on the dissolution process of kaolinite has been studied experimentally extensively. And most of the studies used kaolinite with imperfect crystalline structure <sup>112</sup>. Defects, particularly point defects, have been commonly found in natural kaolinite <sup>113-115</sup>. As a result, many of the physical and chemical properties of kaolinite may be fundamentally changed by the presence of point defects. Several studies have been devoted to understand the structure of kaolinite and to identify the typical types of defects present in its structure <sup>115-122</sup>. In kaolinite, these point defects may take the form of impurity atoms or ions, in interstitial or interlayer sites or directly replace the normal lattice ions. Additional possibilities include lattice vacancies which are present at different concentrations in all crystalline materials <sup>112,113</sup>. Vacancies present in the octahedral surface hydroxyl groups and Al and Si vacancies in the octahedral and tetrahedral layers, respectively, are the most common types of vacancies in the kaolinite crystal structure <sup>114</sup>. However, systematic investigation on the effect of vacancies on the dissolution of kaolinite with various alkali cations are scanty. Li et al. <sup>120</sup> studied the effect of Si vacancy on the tetrahedral surface on the adsorption capability of kaolinite tetrahedral surface by molecular dynamics simulation method. They found that, in the presence of vacancy, more Na<sup>+</sup> and Pb<sup>2+</sup> cations can adsorb onto the surface. Since any further processing of kaolinite essentially takes place through dissolution and re-formation of the Al and Si groups (such as the geopolymerization process of kaolinite), the study of the influence of vacancies on the dissolution of kaolinite is of special interest.

The (001) plane is the cleavage plane of kaolinite as well as the main exposed surface of kaolinite crystals and the -OH groups in the aluminum octahedral (001) plane have been shown to be the most active sites of the kaolinite <sup>114,123</sup>. Accordingly, this plane has been

extensively used in various studies <sup>79,124</sup> of kaolinite. In this work, the effect of two typical vacancy defects in the (001) plane of kaolinite on the dissolution of kaolinite with solutions containing Na<sup>+</sup> and K<sup>+</sup> cations was investigated. In all systems of interest, H vacancies were initially created on the octahedral side. This phenomenon is known as surface deprotonation <sup>74,125</sup>, which take places when kaolinite is exposed to the alkali solution. The work done by Šolc et al. <sup>124</sup> showed that kaolinite tetrahedral surface is hydrophobic while defect silanol (Si-OH) is hydrophilic <sup>115</sup>. As such, the Si vacancy can regulate the hydrophobic/hydrophilic property of tetrahedral surface of kaolinite and consequently it may influence the tetrahedral surface dissolution in alkali medium.

In general, the study of dissolution of kaolinite in the presence of different vacancies is extremely complicated experimentally. As such, molecular dynamics (MD) simulation provides an effective alternative for evaluating the influence of the surface vacancies on the dissolution of two basal surfaces of kaolinite in the presence of different Al and Si vacancies exposed to an alkali medium. The two typical alkali solutions (i.e., Na<sup>+</sup> and K<sup>+</sup>) at 3 M and 5 M concentrations at ambient condition (i.e., 298 K and 1 atm) were studied.

## 5.2. MD Simulation Method

Kaolinite (Al<sub>4</sub>Si<sub>4</sub>O<sub>10</sub>(OH)<sub>8</sub>) structure was taken from neutron diffraction studies performed at 1.5 K <sup>126</sup>. Kaolinite is 1:1 layer clay mineral that each layer contains one octahedral sheet and one tetrahedral sheet. The simulation cell in this study contains 6 layer of kaolinite which obtained by iterating kaolinite unit cell along the three axes (12×12×6 units in a, b, and c dimensions) resulted in the 864 kaolinite unit cells. Afterwards, a series of defect sites were created manually on the octahedral surface as shown in Fig. 5-1; two Al vacancies by removing two aluminum atoms of an aluminate ring on the octahedral surface (blue atoms

in Fig. 5-1a), four Al vacancies by removing two aluminum atoms of three aluminate rings (two of them are shared between two rings) connected together (blue atoms in Fig. 5-1b) and six Al vacancies by removing three aluminum atoms of two close aluminate rings (blue atoms in Fig. 5-1c). Fig. 5-1d, 5-1e and 5-1f show the top view of the corresponding octahedral surfaces after the removal of aluminum atoms.

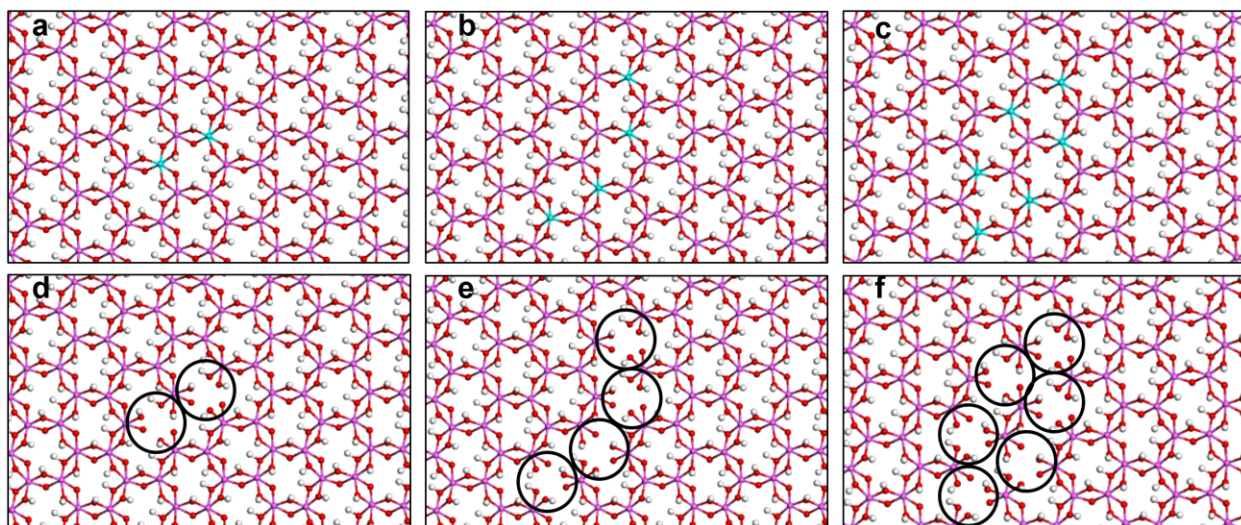


Figure 5-1 Top view of the kaolinite's octahedral surface before the removal of Al atoms for the cases (a) 2, (b) 4 and (c) 6 Al vacancies. Here, Al atoms shown in blue were removed. Figures 1(d), 1(e) and 1(f) show the structures after the removal of the Al atom (atoms colored in blue in Figures 1(a), 1(b) and 1(c)) but before the molecular dynamics simulation. The color scheme here is purple, red and white for Al, O and H, respectively. For easy viewing, only surface Al, O and H atoms are shown.

In addition, 24 lattice aluminum atoms (a combination of 2 and 4 Al vacancies) which were randomly distributed throughout the octahedral surface were removed to construct the system with high concentration of Al vacancies. To maintain the neutrality of the systems, adequate numbers of  $\text{Na}^+$  or  $\text{K}^+$  cations (same as cation in the solution) relative to the number of Al vacancies were added below the tetrahedral sheet (to the hexagonal cavity below the octahedral surface). The motivation for using these particular defect types stems

from the electron microscopy studies of the kaolinite structural defects <sup>116,127-129</sup>. Accordingly, the defects found on the tetrahedral and octahedral surfaces were greater than the size of one missing atom (i.e., in the size of few nanometers) <sup>129-132</sup>, which indicates that several atoms close together were missing on the surfaces. In addition, Croteau *et al.* <sup>130</sup> showed that the defects in the kaolinite structure have a trench shape which is formed by the absence of connected Al and Si atoms on the tetrahedral and octahedral surfaces, respectively. As such, this suggests the necessity of removing nearby atoms to create kaolinite structural defects. However, due to the computational limitations, high number of vacancies on the surfaces similar to what observed by electron microscopy cannot be simulated. However, removing specific number of atoms performed on this work is within the limits of current computational power. Similar to Al vacancies, the same pattern and number of Si atoms were removed from the tetrahedral surface (Fig. 5-2 a, 5-2 b and 5-2 c for 2, 4 and 6 Si vacancies, respectively). In addition, 24 Si vacancies were created in the same way as in the case of 24 Al vacancies. The dangling O atoms of the defect sites on the tetrahedral surface were saturated by hydrogen atoms to fulfil charge neutrality of the system. Note that all these defect sites are smaller than the previous studies <sup>120,130</sup>.

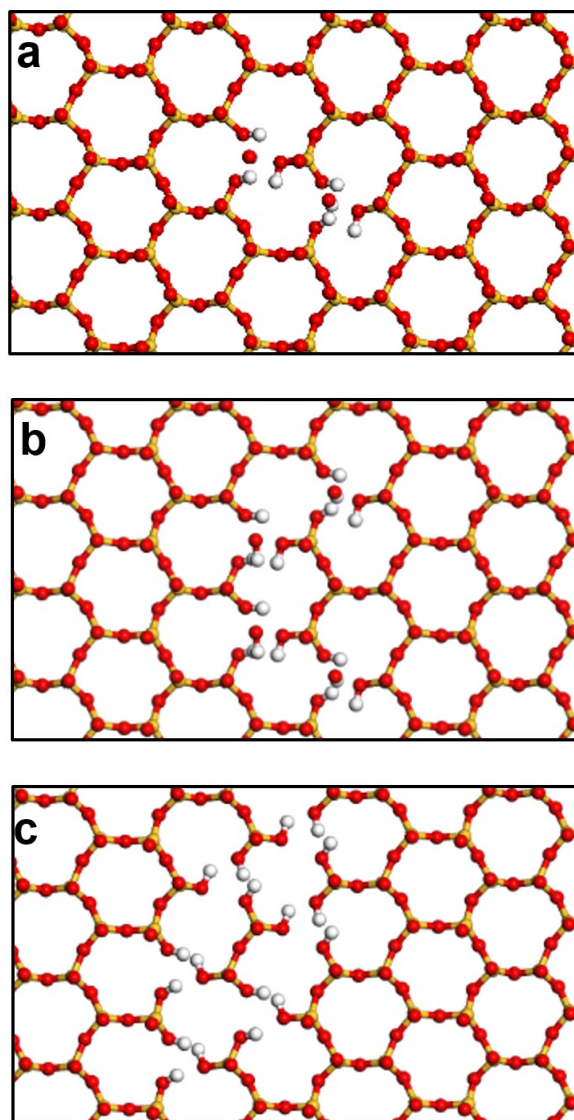


Figure 5-2 Top view of vacancies on the kaolinite tetrahedral surface before running simulation for (a) two, (b) four and (c) six Si vacancies. The color scheme here is yellow, red and white for Si, O and H, respectively.

For clarification, solely surface Si, O and H atoms are shown.

We created the aqueous part of the simulation cell with the dimension of  $61.7 \text{ \AA} \times 107.2 \text{ \AA} \times 18.6 \text{ \AA}$  in  $a \times b \times c$  directions containing 4,020 water molecules and then located this fluid part adjacent to the kaolinite (001) basal plane. In fact, due to the periodic boundary condition, aqueous part was inserted between octahedral and tetrahedral surfaces of

kaolinite. Then, different numbers of cations, i.e., 252 for 3 M and 420 for 5 M, in three different initial configurations were placed in the solution region of the simulation cell, i.e., i. cations were randomly distributed in the solution, ii. cations were positioned in the middle region of the solution and iii. cations were placed close to the octahedral surface in the solution. Afterward, adequate number of hydrogen atoms were randomly selected and manually removed from the octahedral surface before performing any simulation to fulfil the charge-neutrality of the system. In fact, it was assumed that proton and hydroxide ions react near the surface and form water. Therefore, these ions were manually removed. Nevertheless, the reaction of hydroxide ions and surface protons and formation of water cannot be modeled by classical force field in MD simulation. The degree of deprotonation was dependent on the solution concentration resulted in the formation of both  $-OH$  and  $-O^-$  groups on the octahedral surface. It is believed that high screening effects of water molecules inhibit significant interactions between the interfaces in between the kaolinite surfaces by shortening the Bjerrum length ( $< 10 \text{ \AA}$ ).

The CLAYFF force field<sup>133</sup>, which has been widely used to model clay minerals<sup>79,92,120,124,134</sup>, was used to model kaolinite-alkali solution interaction. Non-bonded terms, particularly interactions between the oxygen and metal atoms in the clay lattice, are only defined through the short-range 12-6 Lennard-Jones (LJ) potentials and long-range Coulombic potential, using *ab initio* atomic partial charges<sup>133</sup>, which allow the atoms to move freely in the structure. Due to the flexibility of the clay structure in this force field and also the conjunction with SPC water model, CLAYFF has been demonstrated to be accurate to simulate hydrated minerals and aqueous-mineral interfaces<sup>95-97,135</sup>. LAMMPS (Large-scale Atomic/Molecular Massively Parallel Simulator) program<sup>105</sup> was used to perform all the

simulations on Linux cluster. Materials Studio 8.0 software (Biovia Inc., San Diego, CA, USA) and VMD <sup>136</sup> software were used to create the simulation cells and visualize the results, respectively. All MD simulations were conducted in isothermal-isobaric (i.e., NPT) ensemble <sup>102,137</sup> at 298 K and 1 atm, and Nose-Hoover thermostat and barostat <sup>63,101</sup> were used with respective relaxation times of 0.1 and 1 ps. During the simulation, all dimensions of the cell fluctuate independently. The Verlet's algorithm <sup>61,103</sup> was used to update positions by integrating the equations of motion of atoms every 1fs. The simulations were performed under periodic boundary conditions in three dimensions, with the long-range electrostatics treated by the particle-particle particle-mesh (PPPM) summation algorithm <sup>138</sup>. The cutoff radii for the non-bonded van der Waals interactions and the Ewald summation of the electrostatics was chosen to be 8.5 Å. All simulation systems initially went through 100 ps NPT MD simulation to relax the structure followed by 1,000 ps (i.e., 1 ns) simulation run for data collection. Each simulation was conducted three times with different initial configurations of Al and Si vacancies to statistically increase the accuracy of the results. Radial distribution function (RDF) <sup>139</sup> was utilized to study the degree of crystallinity of the octahedral surface. In addition, the release of the atoms from kaolinite structure as a function of simulation time was analyzed.

The order parameter, similar to which defined by Lanaro and Patey <sup>106</sup>, was utilized to determine if the atom is a part of the surface or released in the solution. The order parameter is calculated by counting the number of atoms surrounding a selected atom of interest within a specified radius from the selected atom. Due to the cutoff distance of the CLAYFF force field (8.5 Å), the radius of 8 Å was chosen in this study. To calculate the average, this process was repeated for all atoms initially presented in the octahedral surface at different times during

the MD simulation. It is worth noting that the atoms (e.g., aluminum) that belong to the octahedral surface (solid) have more neighboring atoms than those in the solution. The aluminum atoms connected to the octahedral surface had an average of 19.5 neighboring aluminum atom within 8 Å for the system containing twenty-four Al vacancies, whereas those exhibited order parameters less than 14 were considered dissociated. In addition, in the system with twenty-four Al vacancies, each oxygen atom in the hydroxyl group on the octahedral surface had 16.7 neighboring aluminum atoms, however; after simulation those oxygen atoms with 5 neighboring aluminum atoms were considered dissociated. In the other words, if order parameter of aluminum and oxygen atoms (which were initially belonging to the octahedral surface) was less than 14 and 5, respectively, during the simulation, atoms were considered to be a part of the solution (dissociated and dissolved into the solution). For the cations, based on the order parameter definition, if the number of aluminum atoms around a cation is greater than 13.6, that cation is considered as diffused within the octahedral surface.

### 5.3. Results and Discussion

The structures of the octahedral surface containing 2, 4, and 6 Al vacancies in contact with a 5 M Na<sup>+</sup> solution after 1 ns NPT MD simulation are shown in Fig. 5-3 a, 5-3 b and 5-3 c, respectively. As shown, the spatial arrangement of the atoms on the octahedral surface was distorted (such atoms surrounding the Al vacancies are highlighted for easy viewing). The octahedral surface lost its crystallinity and the Al atoms remaining on the surface mostly turned into 4-fold position. And it seems that more vacancies created long chains of 4-fold Al atoms. As mentioned earlier, for each concentration of vacancies, simulations were

repeated using three different initial configurations of cations in the solution and similar results were obtained. Therefore, only one set of results is shown here.

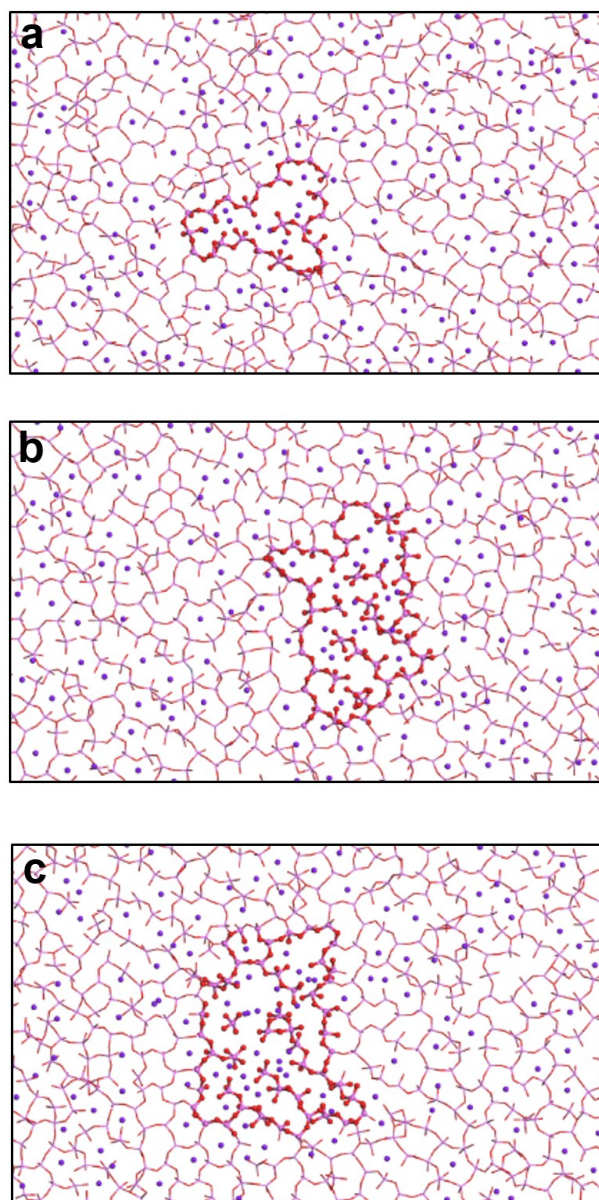
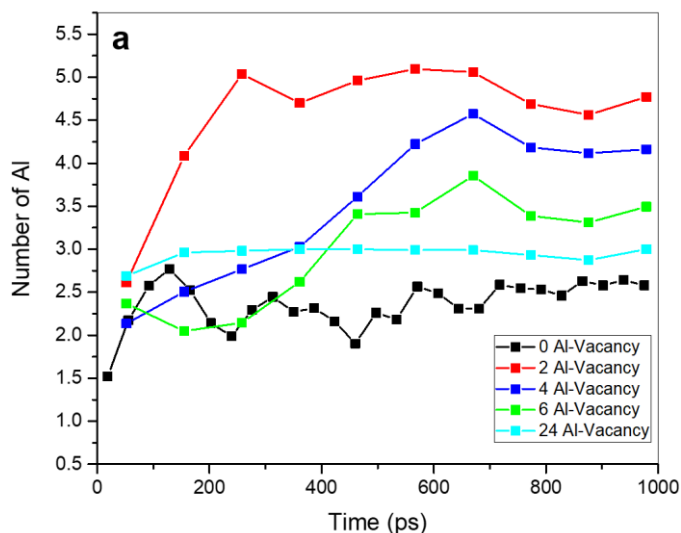


Figure 5-3 Top view of the kaolinite's octahedral surface with (a) 2, (b) 4 and (c) 6 Al vacancies in contact with a solution containing 5 M Na<sup>+</sup> after 1 ns of NPT MD simulation. The color scheme here is purple, red, white and navy for Al, O, H and Na<sup>+</sup>, respectively. For ease viewing, only surface Al, O and H atoms along with Na<sup>+</sup> are shown.

Numbers of aluminate groups dissociated from the octahedral surface in the cases of 3 M and 5 M Na<sup>+</sup> systems are shown in Fig. 5-4 a and 5-4 b, respectively. Overall, it is clear from the figures that Al vacancies led to higher levels of dissociation of moieties containing Al atoms in comparison with the system with no vacancies. In the system without vacancies (the reference system), only 2.5 and 4 aluminate groups dissociated into the 3 M and 5 M Na<sup>+</sup> solutions, respectively. However, the system with 2 vacancies exhibits the highest number of dissociated Al atoms and interestingly, when the number of vacancies is above 2, the number of dissociated Al atoms decreases with increasing number of vacancies but it is still higher than those of the reference system. It is obvious that the number of dissociated Al atoms increases with increasing Na<sup>+</sup> concentration.



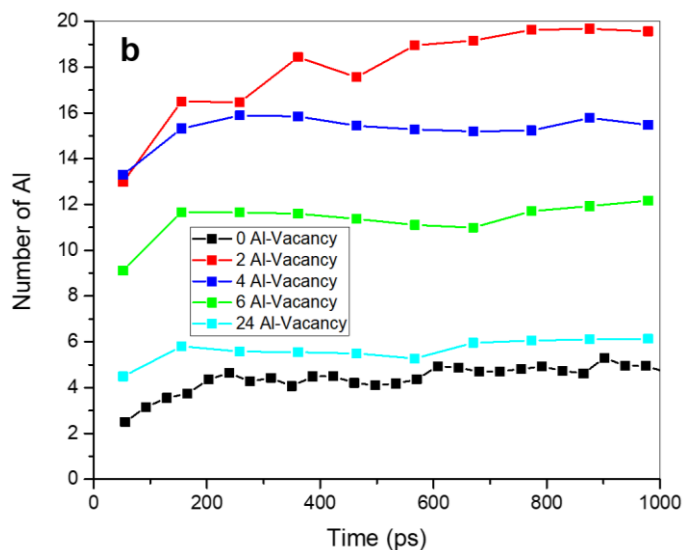


Figure 5-4 Mean numbers of Al atoms in the kaolinite's octahedral surface containing different amounts of Al vacancies completely dissociated into the Na<sup>+</sup> solutions as a function of simulation time (a) 3 M and (b) 5 M.

This above observation can be explained in terms of the interaction of Na<sup>+</sup> with the atoms in the region of the surface containing Al vacancies. In the reference system, cations initially attracted to the O<sup>-</sup> (or OH groups) on the partially deprotonated octahedral surface lengthen the distances (weaken the interatomic forces) between the O<sup>-</sup> (or OH groups) and the atoms attached to them. As a result, some O<sup>-</sup> (or OH groups) dissociated into the solution. This process is schematically shown in Fig. 5-5 a and 5-5 b for the dissociation of OH groups from the octahedral surface. As shown in Fig. 5-5 c, if two or more cations simultaneously attract to the two or more O<sup>-</sup> (or OH groups) that are parts of an aluminate group, the interaction leads to an increase in the distances of the Al atom and its bridging oxygen atoms (Obs). When an Al atom loses its two Ob atoms, the aluminate group (Al atom along with 4 OH groups (or O<sup>-</sup>) dissociates from the octahedral surface (see Fig. 5-5 d) and dissolves into the solution in the form of (AlO<sub>m</sub>H<sub>n</sub>)<sup>(m-n)-</sup>. Here, m was observed, from our simulations, to be 3 or 4 and m > n. And the number of hydrogen atoms dissociated along with the aluminate

group depends on the degree of deprotonation on the surface. It is worth mentioning that based on the study of Sperinck *et al.*<sup>107</sup> and the current study, the remaining Al atoms on the octahedral surface turn into 5- and 4- fold from their initial 6- fold coordination due to the loss of the OH and/or aluminate groups. It was observed that the cations, which diffused into the surface, balanced the negative charge of the remaining aluminate groups in the surface.

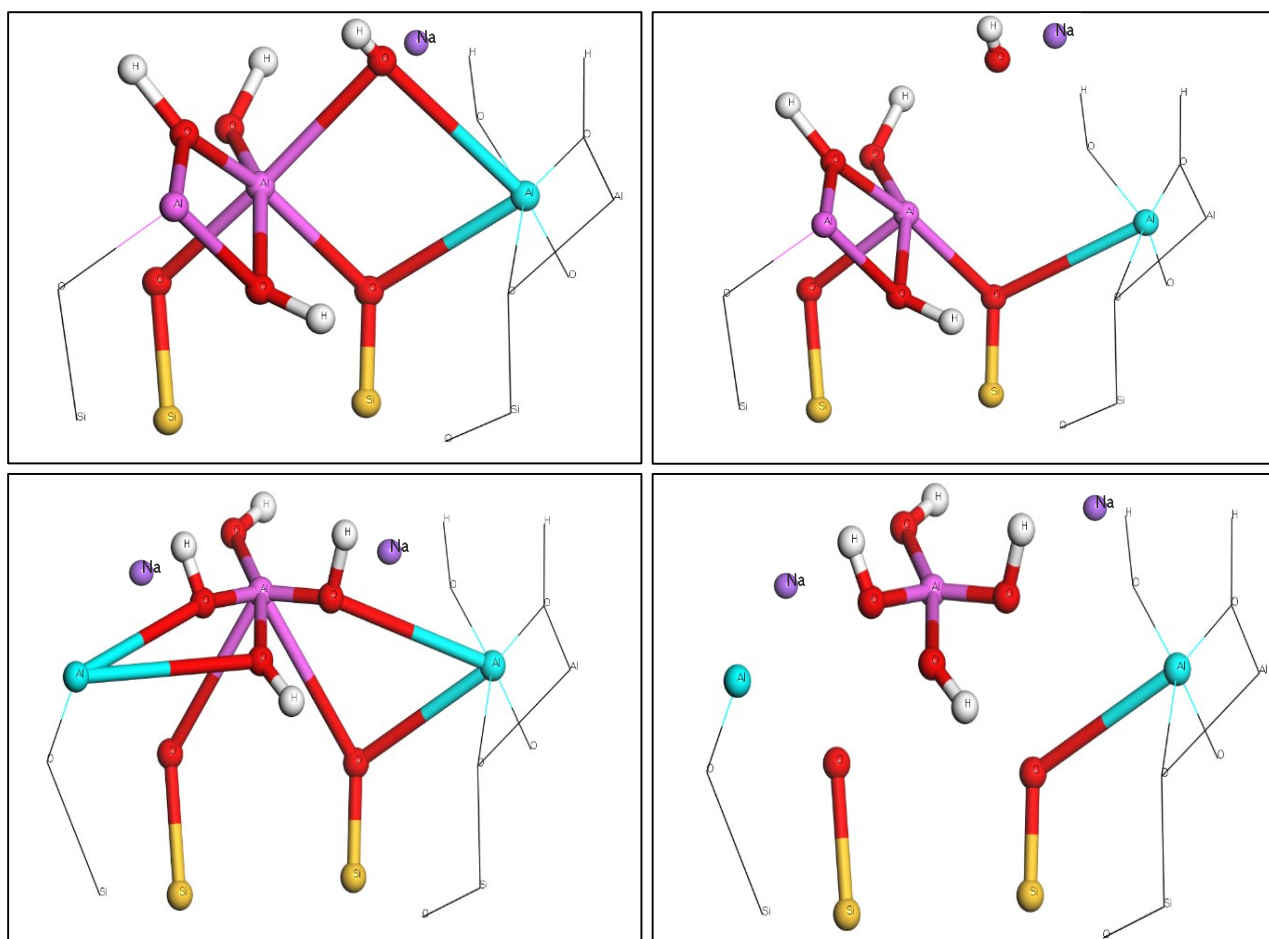


Figure 5-5 Dissociation mechanisms of (a, b) an OH group and (c, d) an aluminate group from the NPT MD simulations.

Let us examine the octahedral surfaces with Al vacancy. Fig. 5-6 shows the difference between the structures of the octahedral surface without and with vacancies. Fig. 5-6 a shows the position of Al atom (blue) in the octahedral surface that will be removed prior to the simulation to generate an Al vacancy (Fig. 5-6 b). In the structure without vacancies (Fig. 5-6 a), each oxygen atom is connected to 3 other atoms. However, once a vacancy is created (i.e., the Al atom (blue) is removed), the surface oxygen atoms (red circles) were connected to only one Al atom (green) as shown in Fig. 5-6 b. This will in turn lead to stronger interaction between these oxygen atoms with the Al atom (green atom in Fig. 5-6 b) as charges of the oxygen atoms are more negative. Accordingly, the interaction of the surface oxygen atoms with the cations resulted in weakening the interaction between the Al atom (green) and the bridging oxygen atoms, thereby facilitating the dissociation of the Al atom along with the OH groups associated with it. In addition, considering the situation in which the surface hydroxyl group is deprotonated, the oxygen atom will become more negative (i.e., stronger interaction with the cations), which helps the dissolution of the Al atom.

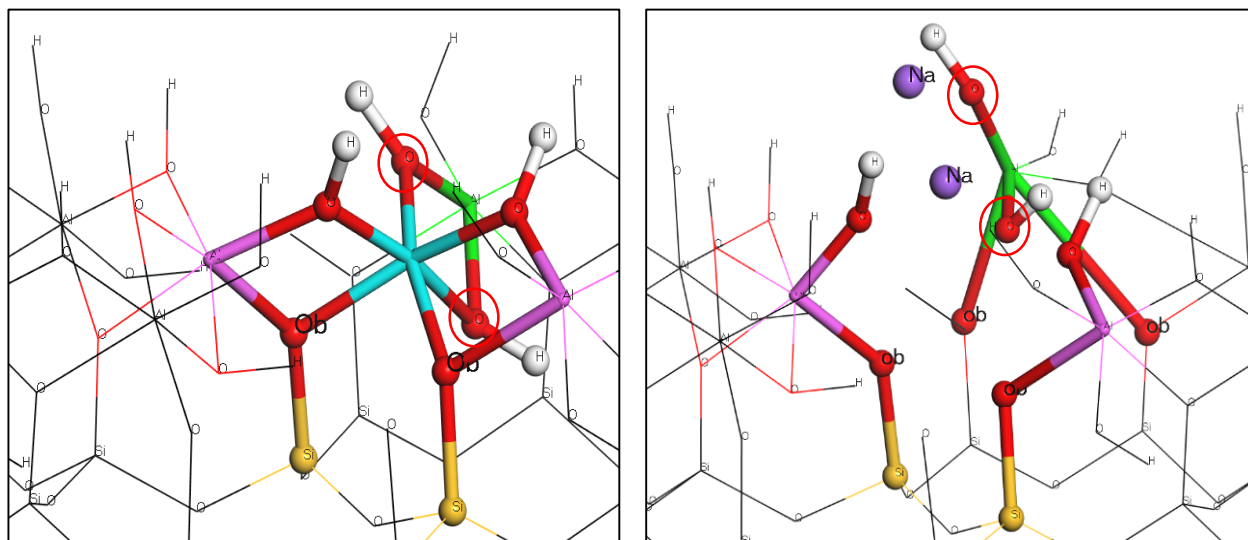


Figure 5-6 Configuration of the Al atoms on the octahedral surface (a) in the reference system and (b) in the system containing Al vacancies during a NPT MD simulation.

Given the above described dissolution mechanism involving an Al vacancy, it is expected that more Al vacancies would provide more highly negatively charged oxygen atoms to interact with the cations, thereby increasing the dissociation amount of the Al atoms. Given this reasoning, it was totally unexpected that there existed a maximum amount of Al atoms dissociated when the octahedral surface contained 2 Al vacancies. This was because cations were not able to diffuse into the octahedral surface with only 2 Al vacancies as much as in the systems with 4 or 6 Al vacancies (more free volume). As mentioned earlier, the dissolution process that took place at regions without or with Al vacancies, would change the 6-fold Al to negatively charged 5- and 4-fold Al. If a cation can diffuse into the octahedral surface, it will be attracted to such Al atoms. This will in turn stop the attack of the cation to the 6-fold Al. In the systems containing 24 Al vacancies, a decrease in the tendency of Al atoms to dissociate from the octahedral surface was more evident.

The RDFs of the octahedral surface Al and O atoms exposed to a 5 M Na<sup>+</sup> solution upon a 1 ns NPT MD simulation are shown in Fig. 5-7. As shown, by increasing the number of Al vacancies on the octahedral surface, the height of the first peak in the RDF decreases, suggesting that more Al vacancies lead to more distortion of the surface. Similar behavior was also observed for the 3 M Na<sup>+</sup> solution (not shown here).

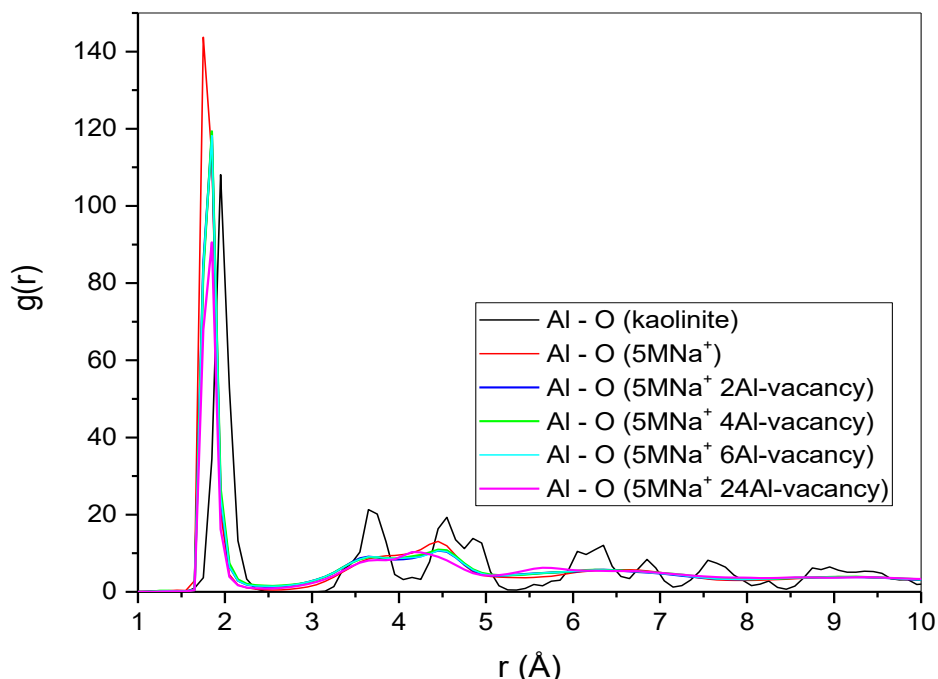
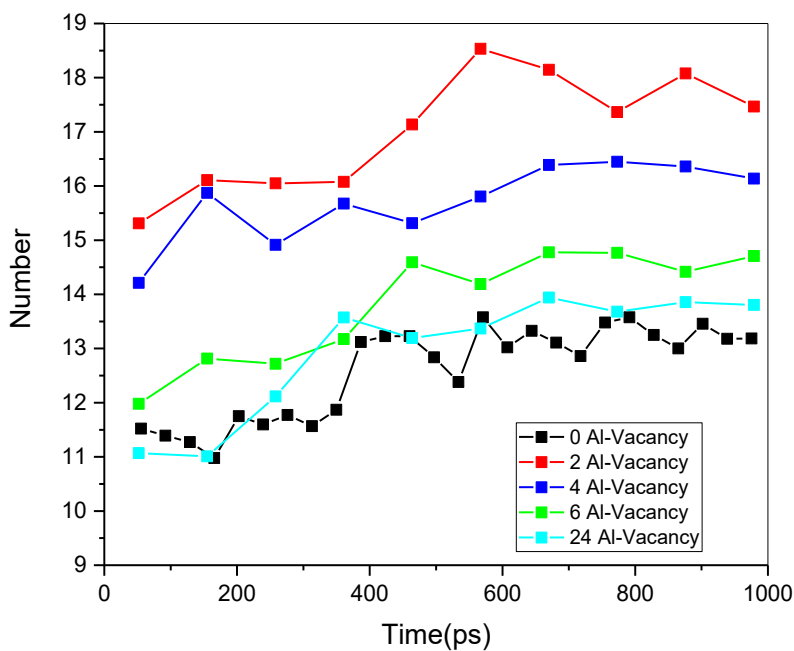


Figure 5-7 Radial distribution functions derived from the NPT MD simulations for Al atoms and structural O atoms on the kaolinite's octahedral surface in contact with a 5 M Na<sup>+</sup> solution without and with different amounts of Al vacancies.

The results of the systems containing K<sup>+</sup> cations (Fig. 5-8) are similar to those of the systems containing Na<sup>+</sup>. However, more Al atoms dissociated in both 3 M and 5 M K<sup>+</sup> solutions compared to the corresponding Na<sup>+</sup> solutions. This is attributed to the difference in their sizes. Owing to the smaller size of Na<sup>+</sup> (i.e., higher charge density), Na<sup>+</sup> exhibits

interaction with  $O^-$  (or OH groups) on the partially deprotonated octahedral surface and therefore, increases the tendency of the dissociation of  $O^-$  (or OH groups), not the moieties containing Al atom. Also, due to its smaller size of  $Na^+$ , it can easily diffuse into the kaolinite surface and interact with the negatively charged 5-fold and 4-fold aluminum atoms.  $Na^+$  does not attack the 6-fold aluminum atoms. On the other hand, the  $K^+$  cations tended to interact with the 6-fold Al atoms. As a result, it triggered more dissociation of moieties containing Al atoms.



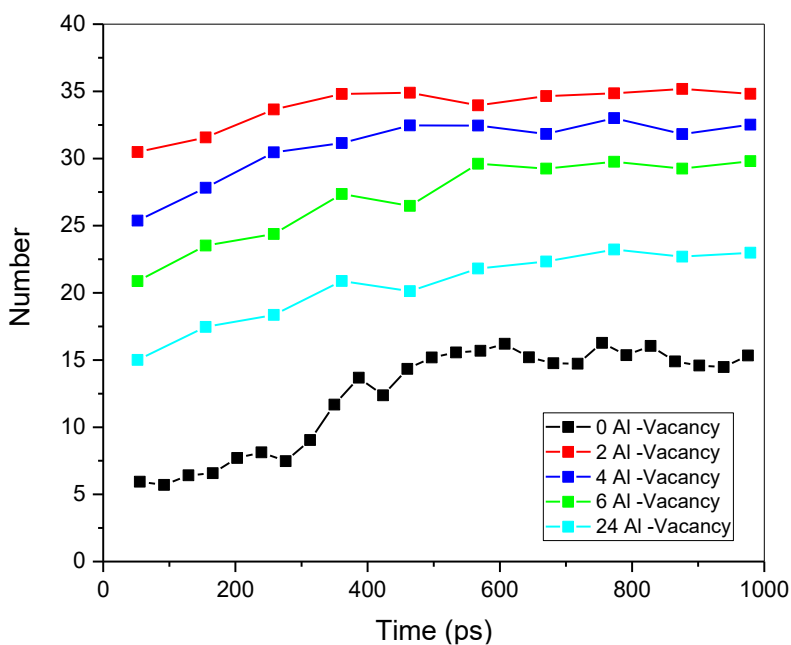


Figure 5-8 The average number of Al atoms in kaolinite structure completely released to the solution area as a function of time in the existence of Al vacancies for K<sup>+</sup> solution at concentrations of (a) 3 M, (b) 5 M.

Average numbers of Na<sup>+</sup> and K<sup>+</sup> cations diffused into the octahedral surface after 1 ns NPT MD simulation are shown in Fig. 5-9. It is clear from the figure that numbers of Na<sup>+</sup> and K<sup>+</sup> cations presented in the octahedral surface increase with increasing cation concentration and surface Al vacancies.

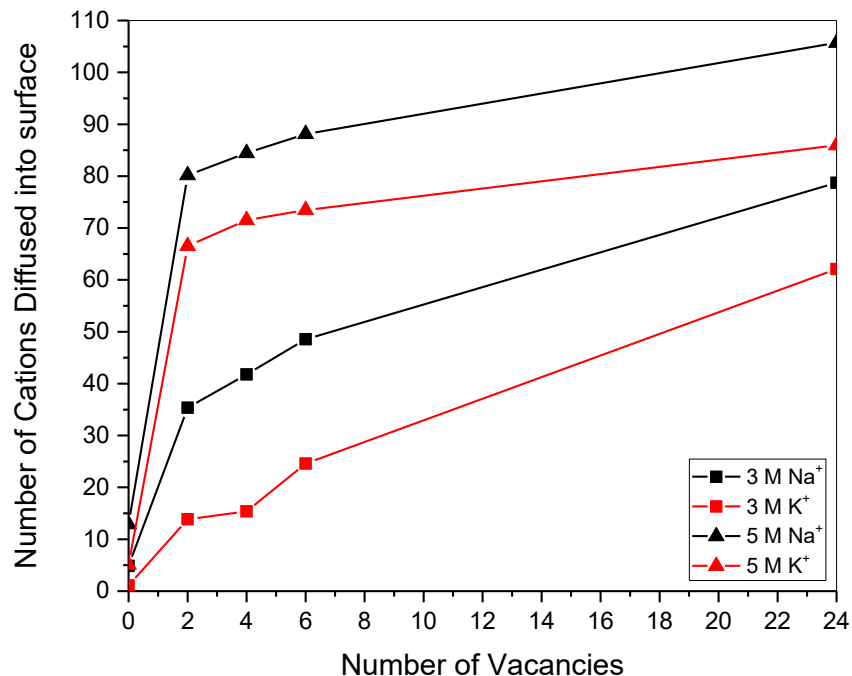


Figure 5-9 Plot of the average number of cations (Na<sup>+</sup> and K<sup>+</sup>) diffused into the octahedral surface against the number of Al vacancies for the 3 M and 5 M solutions.

The effect of Si vacancies in the tetrahedral surface on the dissociation of Si atoms were also examined. Top views of the tetrahedral surfaces with 2, 4 and 6 Si vacancies exposed to a 5 M Na<sup>+</sup> solution after 1 ns NPT MD simulation are shown in Fig. 5-10 a, 5-10 b and 5-10 c, respectively. Compared to the octahedral surfaces, there are minimal structural changes occurred to the tetrahedral surfaces. Fig. 5-11 shows the corresponding RDFs. Reduction in height of the first peak shows that the number of O atoms around each Si atom on the tetrahedral surface decreased as some Si and O atoms changed their positions especially for the system with 24 Si vacancies. However, slight decreases in the heights of the other peaks demonstrate that the tetrahedral surface more or less preserves its crystalline structure. Moreover, no Si groups dissolved into the solution. The same behavior was observed for the system containing K<sup>+</sup> cations.

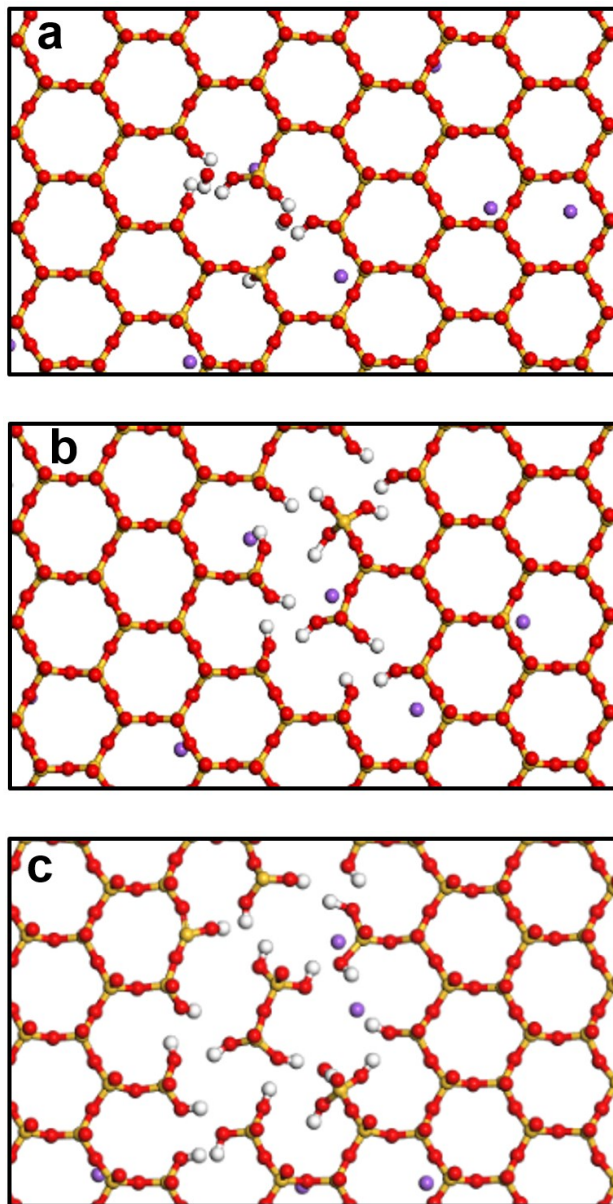


Figure 5-10 Top view of vacancies on the kaolinite's tetrahedral surface after 1 ns NPT MD simulation run for 5 M Na<sup>+</sup> solution for the systems containing (a) two, (b) four and (c) six Si vacancies. The color scheme here is yellow, red, white and navy for Si, O, H and Na<sup>+</sup>, respectively. For easy viewing, only surface Si, O and H atoms along with Na cations are shown.

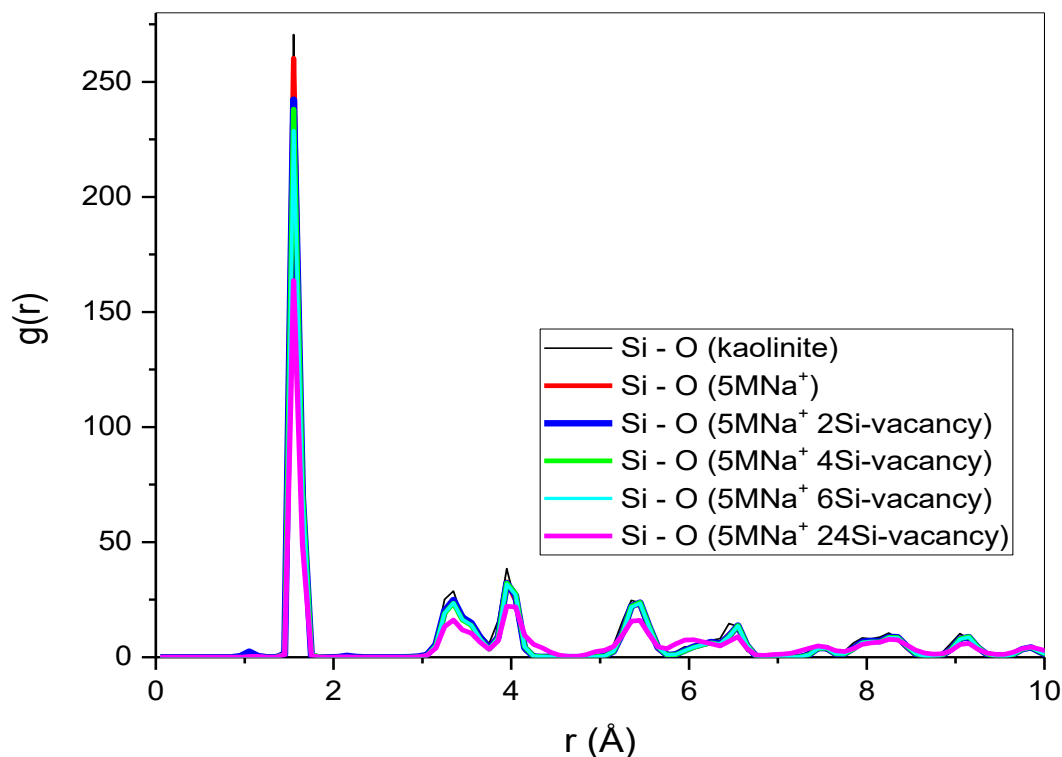


Figure 5-11 Radial distribution functions derived from MD simulations for Si atoms and structural O atoms on the tetrahedral surface of kaolinite in contact with a 5 M Na<sup>+</sup> solution without vacancies and kaolinite with different numbers of Si vacancies.

#### 5.4. Conclusions

In this work, the dissolution of the two basal surfaces of kaolinite (i.e., tetrahedral and partially deprotonated octahedral surfaces) with different amounts of Al and Si vacancies exposed to two alkali solutions, one with Na<sup>+</sup> cations only while the other K<sup>+</sup> cations only, at concentrations of 3 M and 5 M and ambient conditions was studied using molecular dynamics (MD) simulation along with the CLAYFF force field. The existence of Al vacancies on the partially deprotonated octahedral surface resulted in more dissociation of Al groups compared with the octahedral surface with no Al vacancies. However, the dissolution amount exhibited a maximum at a relatively low vacancy concentration (2 vacancies per 576

Al atoms), above which the dissolution amount decreased with increasing concentration of Al vacancy. However, increasing the number of Al vacancies led to more distortion to the octahedral surface, thereby decreasing its crystallinity as confirmed by the corresponding radial distribution functions. And such observations took place in both Na<sup>+</sup> and K<sup>+</sup> solutions. Si vacancies in the tetrahedral surface of kaolinite increased the interaction of cations with the surface; however, no Si groups dissociated from the surface even at the existence of high numbers of vacancies, thereby retaining its crystallinity.

## Chapter 6

### 6. Effect of Inorganic Salt Contaminants on the Dissolution of Kaolinite Basal Surfaces in Alkali Media: A Molecular Dynamics Study

#### 6.1. Introduction

Geopolymers are alkali-activated aluminosilicate gels with a highly cross-linked amorphous network<sup>16</sup>. These materials have shown significant potential in construction applications and can be considered as an alternative to Portland cement. Geopolymers are acid-, heat- and fire- resistant. Owing to the possibility of considerable savings in greenhouse gas emissions<sup>24,140,141</sup>, these materials have attracted scientific interest in recent years. Generally speaking, a geopolymer is made by dissolving a solid aluminosilicate source material (e.g., kaolinite, one form of clay minerals) in highly concentrated alkali solutions and subsequently reacting such dissolved monomers to form a three-dimensional network structure<sup>16</sup>. The effect of alkali solution on clay minerals has been the subject of studies for a number of years<sup>83,142-147</sup>. It is generally agreed that the quality and properties of the final product are greatly dependent on the dissolution process (i.e., the monomers formation process)<sup>88</sup> and the availability of aluminate in the starting materials controls geopolymer gel properties<sup>148,149</sup>. However, the first stage of the dissolution of the clay mineral is less documented under highly alkali conditions. The dissolution process is assumed to be surface controlled at ambient temperature and pressure<sup>29,142,143,150,151</sup>, which means that the dissolution is limited by the basic molecular processes that finally lead - in the case of crystal

dissolution - to the detachment of segments from the bulk crystal structure into the solution<sup>150</sup>. The dissolution of kaolinite in an alkali solution involves the initial interaction between the OH<sup>-</sup> anions and the octahedral surface which contains a high number of hydroxyl moieties, leading to the deprotonation of the surface<sup>74,150</sup>. Following the deprotonation, the surface exhibits a high affinity for the cations present in the alkali solution. Consequently, owing to the interaction between the cations and the deprotonated octahedral surface, hydroxyl moieties and aluminate groups dissociate from the surface and release into the solution. The mechanism of interactions of Na<sup>+</sup> and K<sup>+</sup> alkali cations with the kaolinite basal surfaces was discerned in detail in our previous work<sup>152,153</sup>. However, there are some factors which may affect the interaction of alkali cations with the surfaces such as structural defects of source material and contaminants present in the source material or in the aqueous medium. The interaction of the alkali cations (i.e., Na<sup>+</sup> and K<sup>+</sup>) with the kaolinite basal surfaces in the presence of different concentrations of Al and Si vacancies on the octahedral and tetrahedral surfaces was studied previously and it was found that the structural vacancies affect the number of moieties dissociated from the octahedral surface<sup>153</sup>.

Chloride salts such as CaCl<sub>2</sub> and MgCl<sub>2</sub> are believed to be always present in water varied from 250 mg/L to more than 60,000 mg/L for intake water and basin brines, respectively<sup>154</sup>. However, the concentration of these salts in the solution is usually high enough to influence the geopolymerization process due to the usage of waste disposals as source materials as well as the re-usage of the water concentrated by the salts in further processing. Lee *et al.*<sup>155</sup> investigated the effect of inorganic salts on the strength of the final geopolymer by adding 0.4 M of KCl, MgCl<sub>2</sub> and CaCl<sub>2</sub> individually to the alkali solution. They suggested that the presence of these chloride salts in the solution led to the formation of new phase in

final geopolymer product which affected the strength of the geopolymer. In addition, it was reported by Kucche *et al.* <sup>156</sup> that the presence of contaminants at 0.1 M concentration resulted in some beneficial effect on the properties of final product with no deterioration in its comprehensive strength. However, no detailed evaluation was carried out on any changes in the dissolution process of the source material in the existence of salt contaminants. Further literature surveying overall indicated a lack of documented studies on the dissolution of kaolinite in the alkali media in the presence of salt contaminants.

Since the properties of the final geopolymer product is highly dependent on the initial dissolution of the source material and the dissolution process is greatly affected by the type and concentration of alkali cations and contaminants, the present work focused on the study of the influence of the inorganic salts (i.e., CaCl<sub>2</sub> and MgCl<sub>2</sub>), which can be ionized in the aqueous medium, on the dissolution process of kaolinite in different alkali media. In particular, molecular dynamics (MD) simulation was utilized to study the dissolution of the two basal surfaces of kaolinite in the alkali solutions containing different aqueous contaminants. Systems containing 3 M and 5 M of two neat alkali solutions widely used in geopolymerization process (i.e., Na<sup>+</sup> and K<sup>+</sup>) <sup>29,89</sup> with different concentrations of MgCl<sub>2</sub> and CaCl<sub>2</sub> contaminants were studied. For this purpose, the amount of salt contaminants was selected at a relatively low concentration of 0.1 M to moderate and relatively high concentrations of 0.3 M and 0.5 M. All MD simulations were conducted at ambient condition, i.e., 298 K and 1 atm.

## 6.2. MD Simulations Methodology

Initial atomic coordinates of kaolinite were taken from the Bish <sup>98</sup> neutron diffraction studies. The unit cell formula is (Al<sub>4</sub>Si<sub>4</sub>O<sub>10</sub>(OH)<sub>8</sub>) and the silicon and aluminum atoms are

positioned at the tetrahedral and octahedral coordination, respectively. The unit cell is neutral. A supercell containing  $12 \times 12 \times 6$  unit cells in the x, y, and z directions with an approximate dimension in the xy plane of  $62 \text{ \AA} \times 107 \text{ \AA}$  was created. Subsequently, a bulk water phase containing 4,020 water molecules with the dimensions of  $61.7 \text{ \AA} \times 107.2 \text{ \AA} \times 18.6 \text{ \AA}$  in x  $\times$  y  $\times$  z directions was created and brought into contact with the kaolinite (001) basal plane (i.e., the octahedral surface). The entire system was subjected to three-dimensional periodic boundary conditions. This led to the situation that the water phase is in contact with both the octahedral and tetrahedral surfaces. To build 3 M and 5 M NaOH or KOH solutions, 252 and 420 of the corresponding cations were added to the water phase. Cations were placed in three different initial configurations: random distribution in the solution, the middle region of the solution and close to the octahedral surface in the solution. Experimentally, it was observed that the octahedral surface is deprotonated in an alkali environment. Therefore, we manually deprotonated certain number of hydroxyl moieties on the model octahedral surface to maintain the neutrality of the systems. The number of hydrogen atoms removed from the octahedral surface was dependent on the solution. Here, it was assumed that hydroxide ions were not present in the solution as they were consumed in the deprotonation reaction. Similar approach of modeling the deprotonated surface (i.e., charged surface) of the amorphous silica was used by Hocine *et al.*<sup>99</sup>. Also, it is worth noting that water molecules exhibit high screening effects (i.e., short Bjerrum length ( $< 10 \text{ \AA}$ )), thereby significantly reducing the interactions between the interfaces that sandwiched the solution. Effect of salt contaminants on the dissolution process was studied by adding different numbers of  $\text{CaCl}_2$  and  $\text{MgCl}_2$  molecules to the solution part of the simulation cell that contained either  $\text{Na}^+$  or  $\text{K}^+$  cations. Concentrations of contaminants were 0.1 M, 0.3 M

and 0.5 M. Systems containing one type of contaminant (i.e., CaCl<sub>2</sub> or MgCl<sub>2</sub>) and a 50/50 mol/mol mixture of two contaminants (i.e., CaCl<sub>2</sub> + MgCl<sub>2</sub>) were used. For instance, a system containing 0.1 M contaminants includes 8 CaCl<sub>2</sub> or MgCl<sub>2</sub> molecules or a mixture of 4 CaCl<sub>2</sub> molecules and 4 MgCl<sub>2</sub> molecules. It should be noted that the contaminant molecules would dissociate in the ion form in water.

All interaction parameters were taken from the ClayFF force field <sup>90</sup> and will be briefly defined here. ClayFF allows flexibility of clay layers which has been demonstrated by several previous researches <sup>79,90,92,120,124,134</sup> to accurately reproduce structural and spectroscopic properties of clays as well as dynamical and energetic properties of clay layers and aqueous interfaces <sup>157-160</sup>. Other than bonded interactions required for kaolinite hydroxyl groups and water molecules, potential energies were calculated from pairwise non-bonded, i.e., electrostatic and van der Waals, interactions. The flexible SPC water model was used for Van der Waals parameters of oxygen atoms in ClayFF <sup>135</sup>. MD simulations were performed with the LAMMPS code <sup>105</sup> at a temperature of 298 K and pressure of 1atm for all systems. Interactions were evaluated every 1 fs with a real-space cutoff distance of 8.5 Å. The long-range electrostatic interactions were evaluated with the particle-particle particle-mesh (PPPM) summation algorithm <sup>104</sup> and a precision of  $1.0 \times 10^{-5}$ . Model systems were thermally equilibrated using an initial 100 ps simulation in the isothermal-isobaric (i.e., NPT) ensemble <sup>100,102</sup>, followed by an additional 1,000 ps simulation in the same ensemble. Temperature and pressure were controlled by Nose-Hoover thermostat and barostat <sup>63,101</sup> with respective relaxation times of 0.1 and 1 ps while all dimensions of the unit cells were allowed to fluctuate freely. All the simulation unit cells were built by Materials Studio 8.0 software (Biovia Inc., San Diego, CA, USA) software and OVITO <sup>161</sup> and VMD <sup>136</sup> software were

used to visualize the results. As mentioned, each simulation was conducted three times with three different initial configurations of cations in the solution to statistically increase the accuracy of the results. Radial distribution function (RDF) <sup>139</sup> was utilized to study the degree of crystallinity of the octahedral surface. In addition, the release of the atoms from kaolinite structure as a function of simulation time was analyzed.

Similar to Lenaro *et al.* work <sup>106</sup>, an order parameter was defined to determine if an atom belonging to the surface dissolved in the solution or not. Accordingly, the order parameter is calculated by counting the number of Al atoms surrounding a selected atom of interest within a specified radius from the selected atom. Owing to the cutoff distance of 8.5 Å used in the ClayFF force field, a radius of 8 Å was chosen in this study to calculate the order parameter. To calculate the average, this process was repeated for all atoms initially presented in the octahedral surface at different MD simulation times. The number of aluminum atoms around an aluminum atom on the octahedral surface within 8 Å is ~21.2. If this number for any aluminum atom in the simulation cell becomes  $\leq 12$ , the aluminum atom is considered as a dissociated one from the surface. Likewise, if the number of aluminum atoms surrounding oxygen atom of the octahedral surface hydroxyl groups, which is ~16.7 - within 8 Å - when the atom belongs to the surface, reaches to  $\leq 4$ , the oxygen atom is no longer considered as a part of the surface structure. In the other words, during the simulation, if the order parameter of aluminum and oxygen atoms of kaolinite octahedral surface became less than 12 and 4, respectively, these atoms were considered to be a part of the solution.

### 6.3. Results and Discussion

We carried out a total of 108 molecular dynamics simulations (2 alkali cation types  $\times$  2 alkali cation concentrations  $\times$  3 contaminant types  $\times$  3 contaminant concentrations  $\times$  3 initial

configurations). To illustrate what typically would take place during these simulations, we use the solutions containing 3 M Na<sup>+</sup> cations and 0.1 M, 0.3 M and 0.5 M CaCl<sub>2</sub> with all species initially placed in the middle of the solutions as examples (see Fig. 6-1). It was observed that both Na<sup>+</sup> and Ca<sup>2+</sup> cations in the solution tended to migrate towards both octahedral and tetrahedral surfaces just after 100 ps of 1 ns simulations. However, more cations adsorbed onto the octahedral surface due to the presence of the deprotonated sites. On the other hand, although some Cl<sup>-</sup> were attracted by the adsorbed cations, a considerable amount of such anions remained dispersed in the solution. The adsorption of Cl<sup>-</sup> to cations was more evident at higher salt contaminant concentrations due to the presence of higher number of Cl<sup>-</sup> in the system. As a result, upon 1 ns simulations of the model solutions, some aluminate groups and OH<sup>-</sup> moieties dissociated from the octahedral surface and migrated into the solutions leading to the local distortion of the octahedral surface. The dissolution is not easily seen at the scale shown in Fig. 6-1. The dissolution mechanism was primarily dominated by the interaction of the cations in the solution with the deprotonated sites on the octahedral surface of kaolinite similar to what presented and discussed in our previous work<sup>152,153</sup> for the systems with no salt contaminants. However, due to the presence of cations with higher charge densities (i.e., Ca<sup>2+</sup> and Mg<sup>2+</sup>) as a result of the existence of salt contaminants in the solution, stronger interactions took place between the cations and the surface deprotonated sites. Such dissolution processes did not occur on the tetrahedral surface.

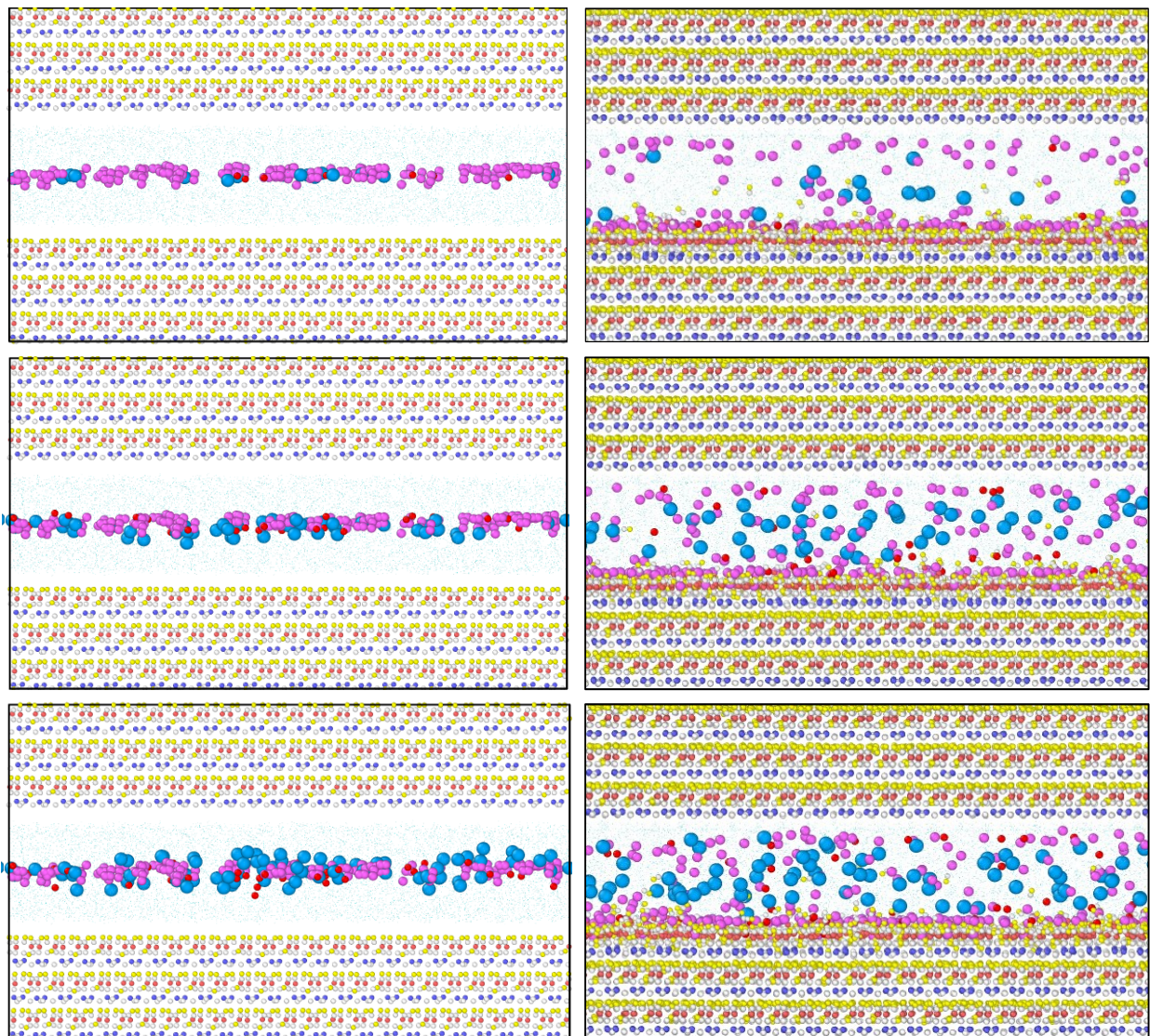
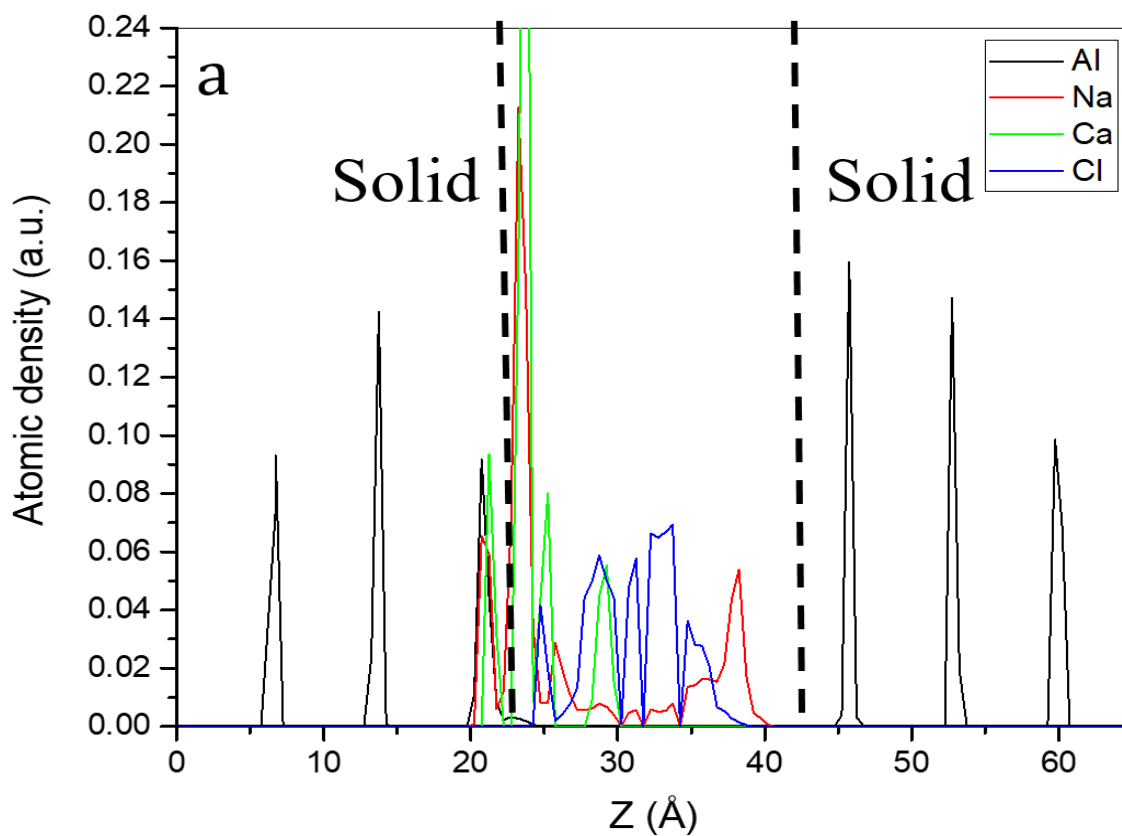


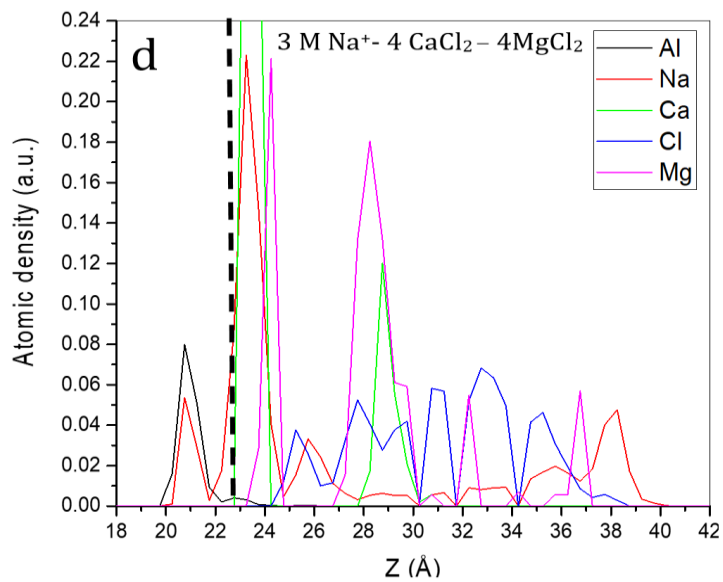
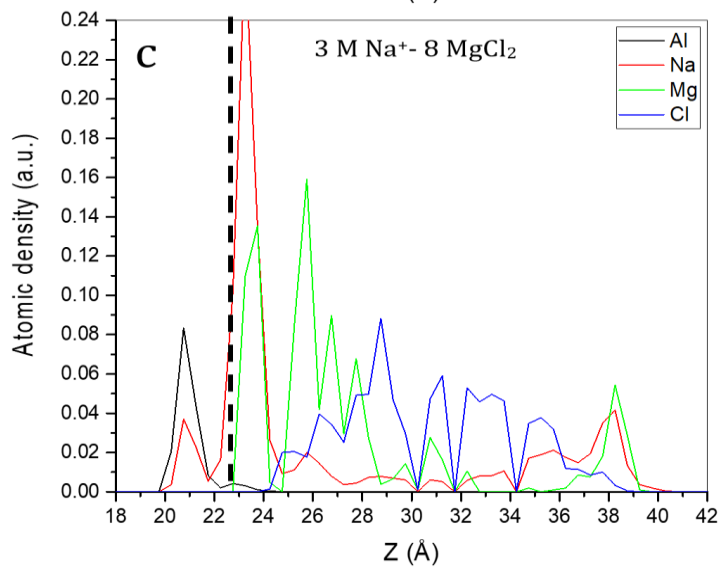
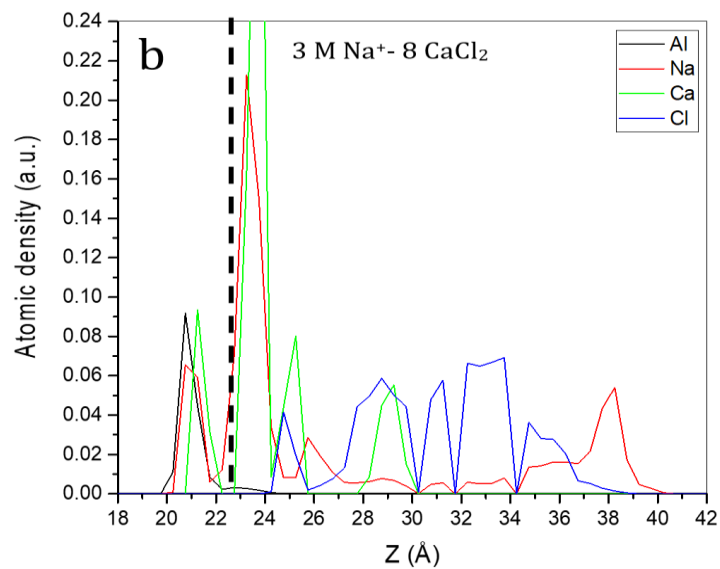
Figure 6-1 Initial configurations of the 3 M Na<sup>+</sup> systems (all species initially placed in the middle of the solutions) containing (a) 0.1 M CaCl<sub>2</sub>, (c) 0.3 M CaCl<sub>2</sub> and (e) 0.5 M CaCl<sub>2</sub>, and the corresponding final configurations of the systems of (b) 3 M Na<sup>+</sup>-0.1 M CaCl<sub>2</sub>, (d) 3 M Na<sup>+</sup>-0.3 M CaCl<sub>2</sub>, (f) 3 M Na<sup>+</sup>-0.5 M CaCl<sub>2</sub>, after 1 ns NPT simulation. The color scheme is: orange for aluminum, navy for silicon, white for oxygen, yellow for hydrogen, pink for Na<sup>+</sup>, blue for Cl<sup>-</sup>, red for Ca<sup>2+</sup> and tiny blue dots are water.

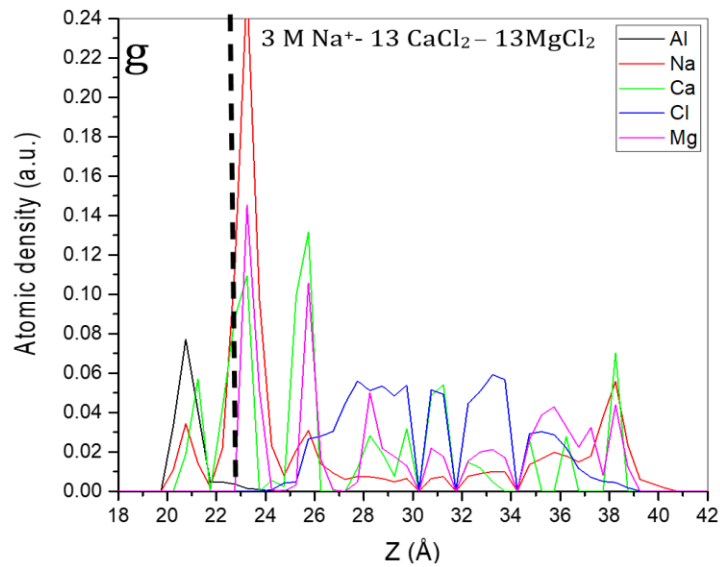
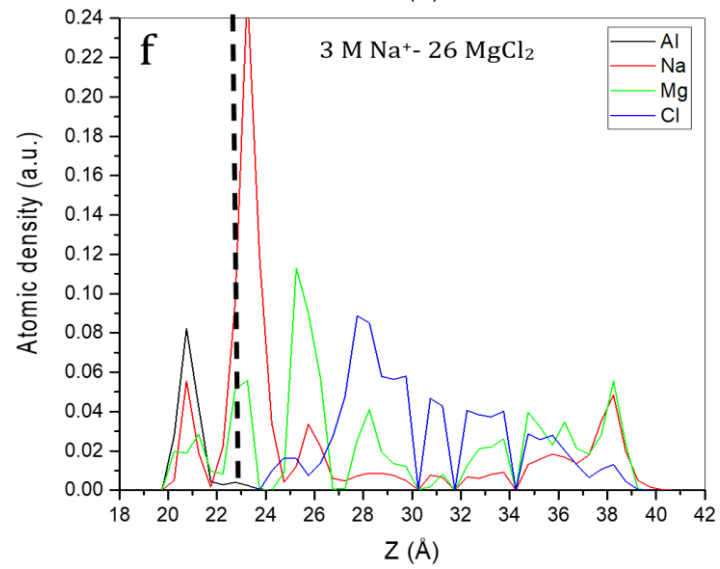
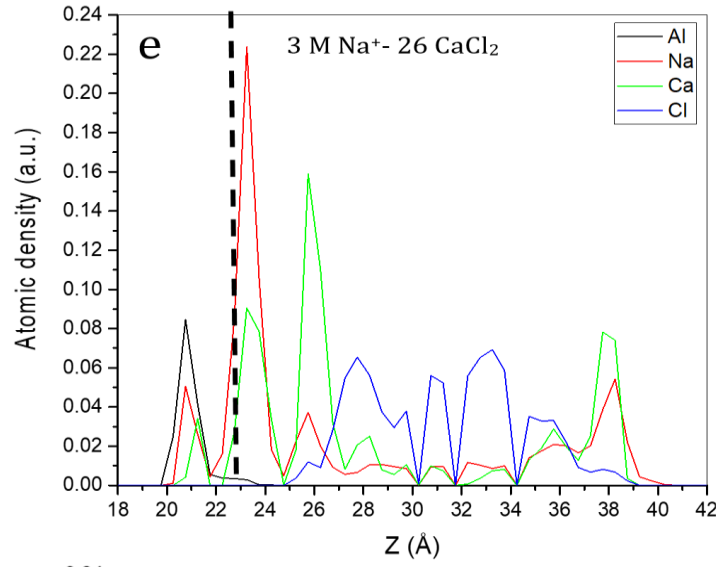
The atomic density profiles of Al atoms and ions in the 3 M Na<sup>+</sup> solutions containing 8, 26 and 42 CaCl<sub>2</sub> molecules (i.e., 0.1, 0.3 and 0.5 M) are shown in Figs. 6-2 a-c. As indicated, some of the cations adsorbed onto the octahedral surface while some of them diffused within the

surface, one peak above the surface while one below the surface. In the system containing 3 M Na<sup>+</sup> and 8 CaCl<sub>2</sub>, both Na<sup>+</sup> and Ca<sup>2+</sup> cations diffused into the surface. In the Na<sup>+</sup> and Ca<sup>2+</sup> systems, the Ca<sup>2+</sup> cations behaved somewhat similar to Na<sup>+</sup> cations on the octahedral surface. However, Mg<sup>2+</sup> cations in the 3 M Na<sup>+</sup> and 8 MgCl<sub>2</sub> system behaved differently (Fig. 6-2d). In particular, Mg<sup>2+</sup> cations did not diffuse into the octahedral surface and only a layer of adsorbed cations was formed on the surface. By increasing the MgCl<sub>2</sub> concentration in the solution from 8 molecules to 26 and then to 42 molecules (Figs. 6-2e and 6-2f), some of the Mg<sup>2+</sup> cations started to diffuse into the octahedral surface. Overall, both Na<sup>+</sup> and Ca<sup>2+</sup> cations showed stronger adsorption to the octahedral surface in comparison with Mg<sup>2+</sup> cations. In addition, in the concurrent presence of Ca<sup>2+</sup> and Mg<sup>2+</sup> in the solution, at the low contaminant concentration, a strong peak of Ca<sup>2+</sup> was observed adjacent to octahedral surface indicating a stronger interaction between the surface and Ca<sup>2+</sup> cations in comparison with Mg<sup>2+</sup> (Fig. 6-2g). By increasing the contaminant concentration (Fig. 6-2h-i), although sharp peak of Mg<sup>2+</sup> close to the octahedral surface revealed its strong affinity to interact with the surface, more Ca<sup>2+</sup> cation diffused through the surface compared with Mg<sup>2+</sup>. Difference in the adsorption behavior could be explained in terms of the differences in their charge density. The higher charge density of Mg<sup>2+</sup> cations (leading to the formation of stronger hydration shell around it) led to stronger interaction with the anions, i.e., Cl<sup>-</sup>, in the solution, thereby reducing its tendency to adsorb onto the octahedral surface. In fact, there seems more Mg<sup>2+</sup> and Cl<sup>-</sup> density peak overlaps than those of Ca<sup>2+</sup> and Cl<sup>-</sup> or Na<sup>+</sup> and Cl<sup>-</sup>. The ionic charge density (C•mm<sup>-3</sup>) was calculated using the formula  $ne/(1.33\pi r^3)$ , where  $r$  is the ionic radii value by Shannon-Prewitt in mm<sup>161</sup> and  $e$  and  $n$  are the electron charge ( $1.6 \times 10^{-19}$  C) and the ion charge, respectively. According to the formula, the charge density of Mg<sup>2+</sup> cations was

calculated to be  $120 \text{ C}\cdot\text{mm}^{-3}$ . The charge density values of  $\text{Ca}^{2+}$  and  $\text{Na}^+$  cations were calculated to be  $52 \text{ C}\cdot\text{mm}^{-3}$  and  $24 \text{ C}\cdot\text{mm}^{-3}$ , respectively. Due to the similarity of ADP graphs of other studied system just 3 M  $\text{Na}^+$  system is shown here. The ADP graphs for 5 M  $\text{Na}^+$  solutions can be found in the supplementary information file.







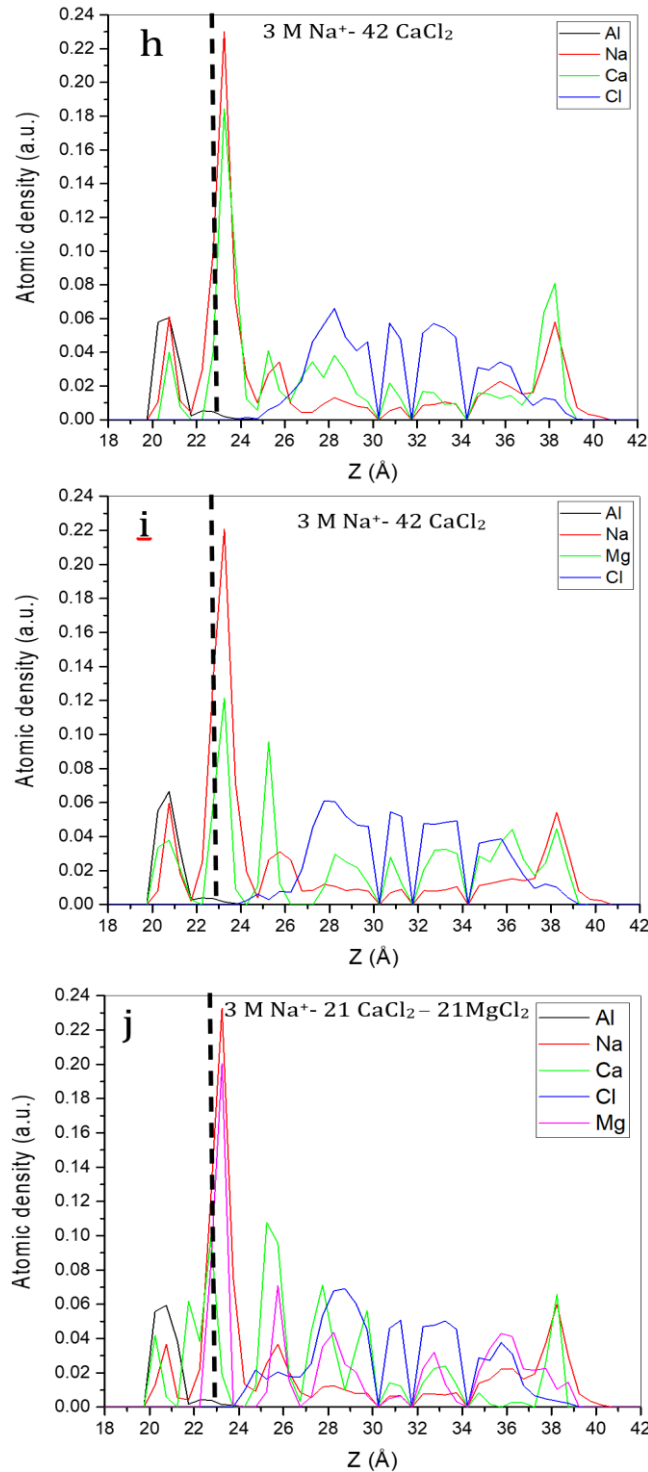
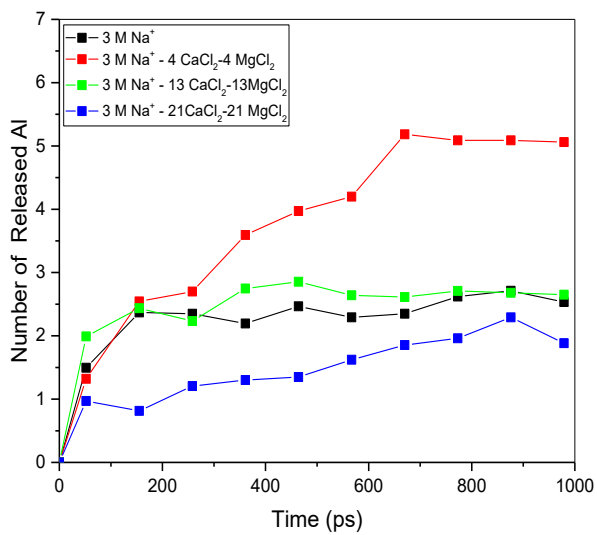
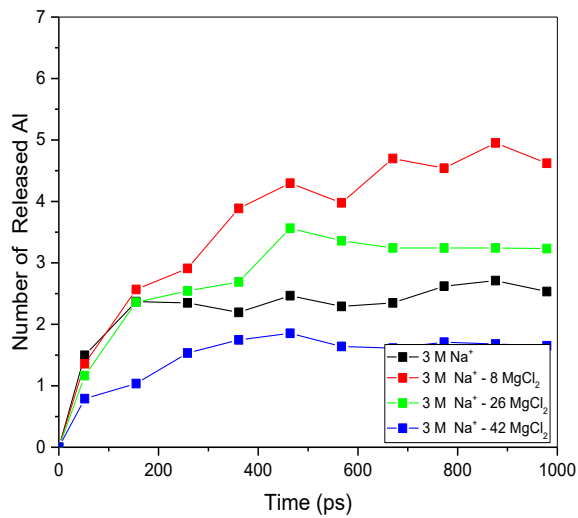
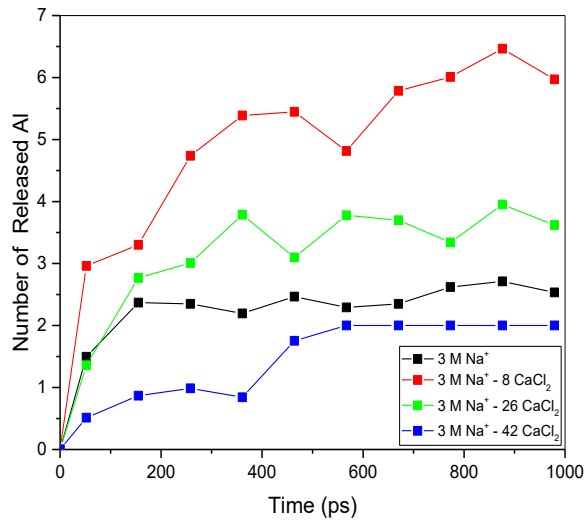


Figure 6-2 Atomic density profile of the 3 M Na<sup>+</sup> system containing (a) and (b) 8 CaCl<sub>2</sub> molecules, (c) 8 MgCl<sub>2</sub> molecules and (d) 4 CaCl<sub>2</sub> and 4 MgCl<sub>2</sub> molecules, (e) 26 CaCl<sub>2</sub> molecules, (f) 26 MgCl<sub>2</sub> molecules, (g) 13 CaCl<sub>2</sub> and 13 MgCl<sub>2</sub> molecules, (h) 42 CaCl<sub>2</sub> molecules, (i) 42 MgCl<sub>2</sub> molecules and (j) 21 CaCl<sub>2</sub> and 21 MgCl<sub>2</sub> molecules.

The number of dissociated aluminate groups from the octahedral surface in the presence of 3 M Na<sup>+</sup> and 5 M Na<sup>+</sup> solutions and different contaminant type and concentrations is shown in Fig. 6-3. In the 3 M Na<sup>+</sup> solution, the number of aluminate groups dissociated from the octahedral surface was around 2.5 upon 1 ns NPT MD simulation (the black curves in Figs. 6-3a, 6-3b and 6-3c). However, presence of low concentrations of contaminants in the solution (either type) increased the number of aluminate groups dissociating from the octahedral surface (red and green curves in Figs. 6-3a, 6-3b and 6-3c). Nonetheless, owing to the difference in the charge density values of Ca<sup>2+</sup> and Mg<sup>2+</sup> cations, the number of dissociated aluminate groups of solutions containing CaCl<sub>2</sub> and MgCl<sub>2</sub> differ slightly. The system containing 50/50 CaCl<sub>2</sub> and MgCl<sub>2</sub> contaminant mixture showed similar behavior to those solutions containing only one type of contaminant. On the other hand, at 0.5 M of contaminants (blue curves in Figs. 6-3a, 6-3b and 6-3c), owing to the presence of a high number of anion (Cl<sup>-</sup>) in the solution, such anions tended to adsorb on the cation layer adsorbed to the octahedral surface, weakening the interaction between the adsorbed cations and the surface which in turn reduced the number of dissociated aluminate groups. In the cases of 5 M Na<sup>+</sup> solution (Figs. 6-3d, 6-3e and 3f), the effect of contaminants on the dissolution of aluminate groups is similar to that of the 3 M Na<sup>+</sup> solutions except that the number of dissociated aluminate groups is much higher at low contaminant concentrations but not at 0.5 M.



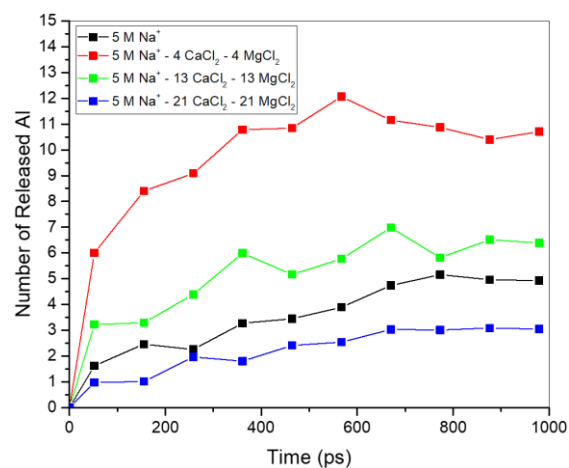
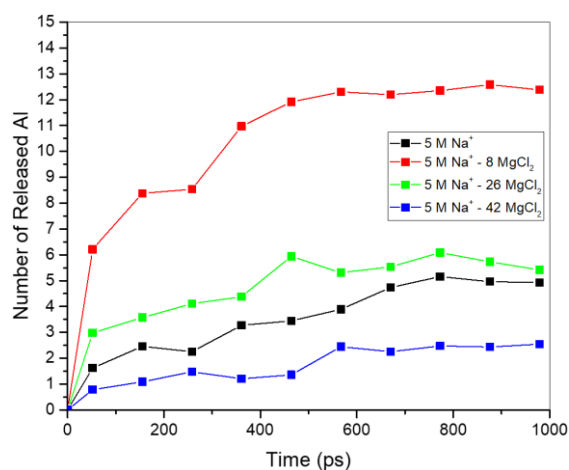
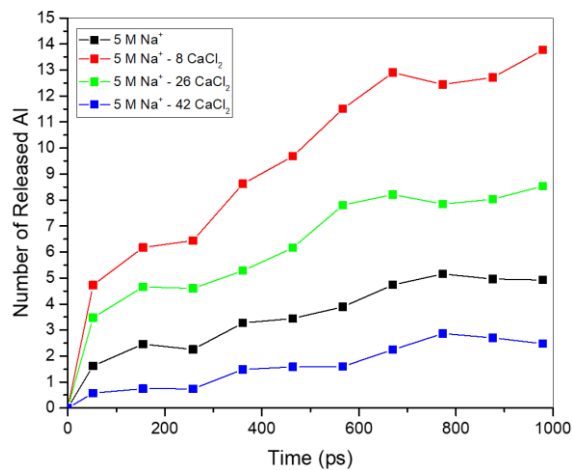
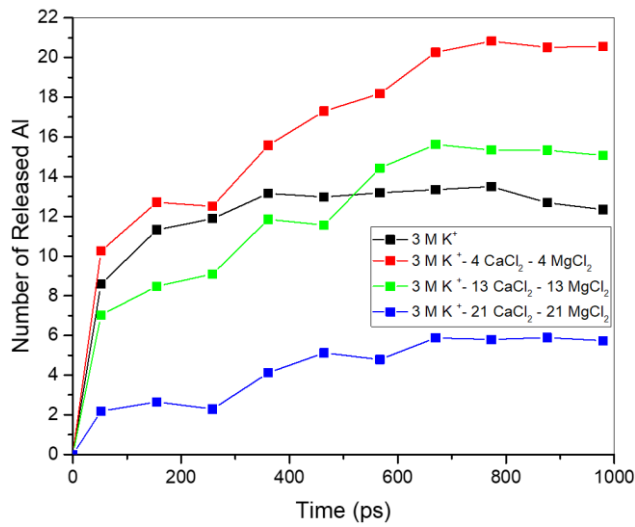
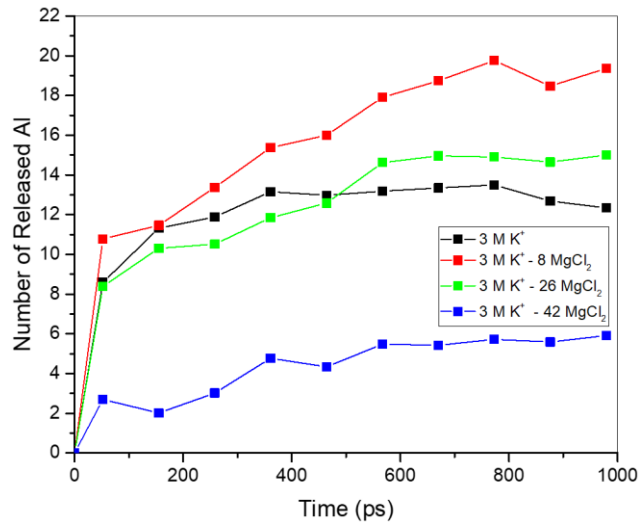
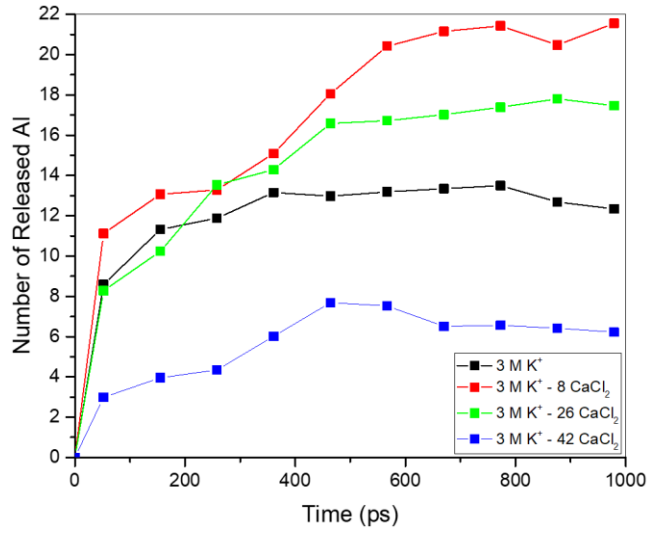


Figure 6-3 The number of aluminate groups dissociated from the octahedral surface as a function of simulation time in the presence of (a) 3 M Na<sup>+</sup> and different concentrations of CaCl<sub>2</sub>, (b) 3 M Na<sup>+</sup> and different concentrations of MgCl<sub>2</sub> molecules, (c) 3 M Na<sup>+</sup> and different concentrations of 50/50 CaCl<sub>2</sub> and MgCl<sub>2</sub> mixture, (d) 5 M Na<sup>+</sup> and different concentrations of CaCl<sub>2</sub>, (e) 5 M Na<sup>+</sup> and different concentrations of MgCl<sub>2</sub> and (f) 5 M Na<sup>+</sup> and different concentrations of 50/50 CaCl<sub>2</sub> and MgCl<sub>2</sub> mixture.

The simulation results suggest that the presence of low concentration of cations with higher charge density (i.e.,  $\text{Ca}^{2+}$  and  $\text{Mg}^{2+}$ ) in comparison with  $\text{Na}^+$  and  $\text{K}^+$  (discussed in the next section) facilitated the dissociation of the aluminate groups from the octahedral surface. Our previous studies <sup>152</sup> showed that the dissociation of an aluminate group from the octahedral surface occurred while two or more alkali cations (i.e.,  $\text{Na}^+$  and  $\text{K}^+$ ) simultaneously adsorbed and interacted with a locally deprotonated site on the octahedral surface; therefore, interaction of aluminate group with the cations with higher charge density (i.e.,  $\text{Ca}^{2+}$  and  $\text{Mg}^{2+}$ ) resulted in more easily dissociation of the aluminate group from the surface.

The number of aluminate groups dissociated from the octahedral surface in the presence of  $\text{K}^+$  cation at concentrations of 3 M and 5 M and different type and concentration of contaminants is shown in Fig. 6-4. Similar dissolution trends (i.e., high dissolution amounts at low contaminant concentrations but low dissolution amount at high contaminant concentration) were obtained but the results of  $\text{K}^+$  cation showed that there were much more dissolution taking place on the octahedral surface compared to the solutions containing  $\text{Na}^+$ . In fact, due to the higher charge density of  $\text{Na}^+$  relative to  $\text{K}^+$ ,  $\text{Na}^+$  has higher ability to dissociate the  $\text{O}^-$  or  $\text{OH}^-$  moieties from the octahedral surface rather than aluminate groups in comparison with  $\text{K}^+$ . The mechanisms involved in the dissociation of aluminate groups and  $\text{O}^-$  or  $\text{OH}^-$  moieties from the octahedral surface in the presence of  $\text{Na}^+$  or  $\text{K}^+$  solutions are discussed elsewhere <sup>152</sup>.



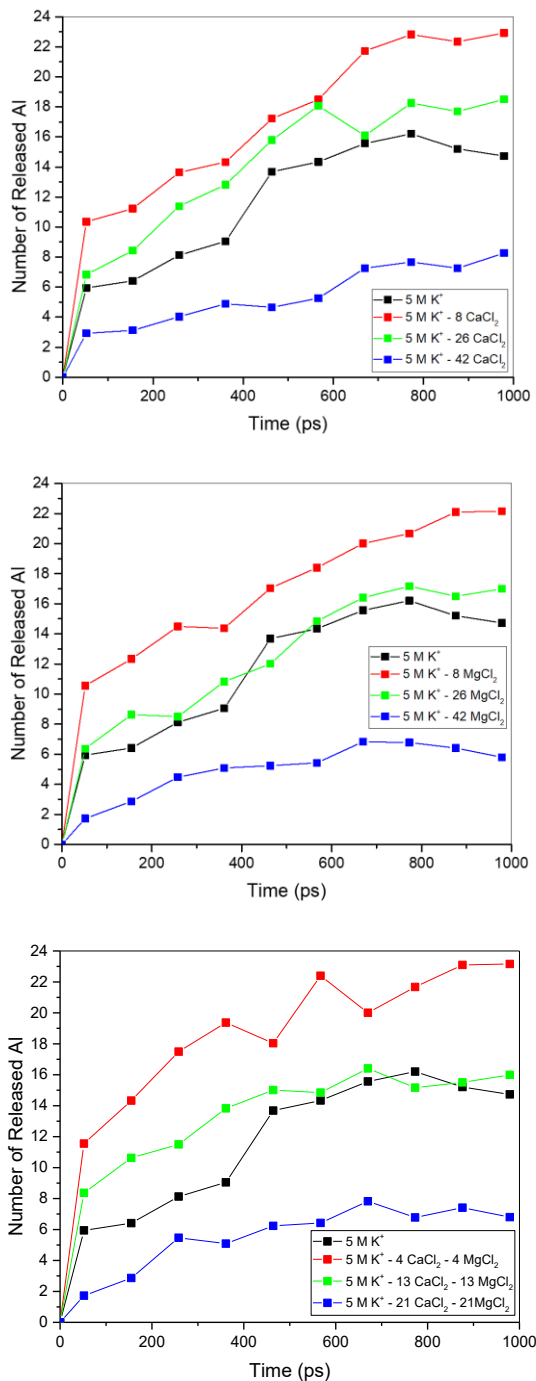


Figure 6-4 The number of aluminate groups dissociated from the octahedral surface as a function of simulation time in the presence of (a) 3 M K<sup>+</sup> and different concentrations of CaCl<sub>2</sub>, (b) 3 M K<sup>+</sup> and different concentrations of MgCl<sub>2</sub>, (c) 3 M K<sup>+</sup> and different concentrations of a 50/50 mol/mol mixture of CaCl<sub>2</sub> and MgCl<sub>2</sub>, (d) 5 M K<sup>+</sup> and different concentrations of CaCl<sub>2</sub>, (e) 5 M K<sup>+</sup> and different concentrations of MgCl<sub>2</sub> and (f) 5 M K<sup>+</sup> and different concentrations of a 50/50 mol/mol mixture of CaCl<sub>2</sub> and MgCl<sub>2</sub>.

The crystalline structures of the octahedral surface after 1 ns NPT MD simulation were compared with that of the initial structure using the radial distribution functions (RDFs) of the aluminum and oxygen atoms of the octahedral surface (see Fig. 6-5). Obviously, the octahedral surface lost its crystallinity to some extent in the systems containing 3 M Na<sup>+</sup> and aqueous contaminants, as the number of peaks and the heights of the peaks (except the first peak) decrease. There also exists a shift in the position of the first peak to the left, indicating that aluminum atoms in the octahedral surface changed their positions from octahedral to tetrahedral positions. Although at high concentration of contaminants, the number of dissociated aluminate groups decreased, adsorption of cations on the surface caused change in aluminum coordination and consequently distortion of the surface structure. As shown in Fig. 6-5, regardless of the type of aqueous contaminants, similar crystallinity decreasing trends were observed for the systems containing Ca<sup>2+</sup> and Mg<sup>2+</sup> cations. Furthermore, similar to the 3 M Na<sup>+</sup> systems shown here, the octahedral surface structure was altered when the surface was exposed to 5 M Na<sup>+</sup> as well as 3 M and 5 M K<sup>+</sup> alkali solutions with/without aqueous contaminants. The RDF graphs of the other systems are shown in Appendix A.

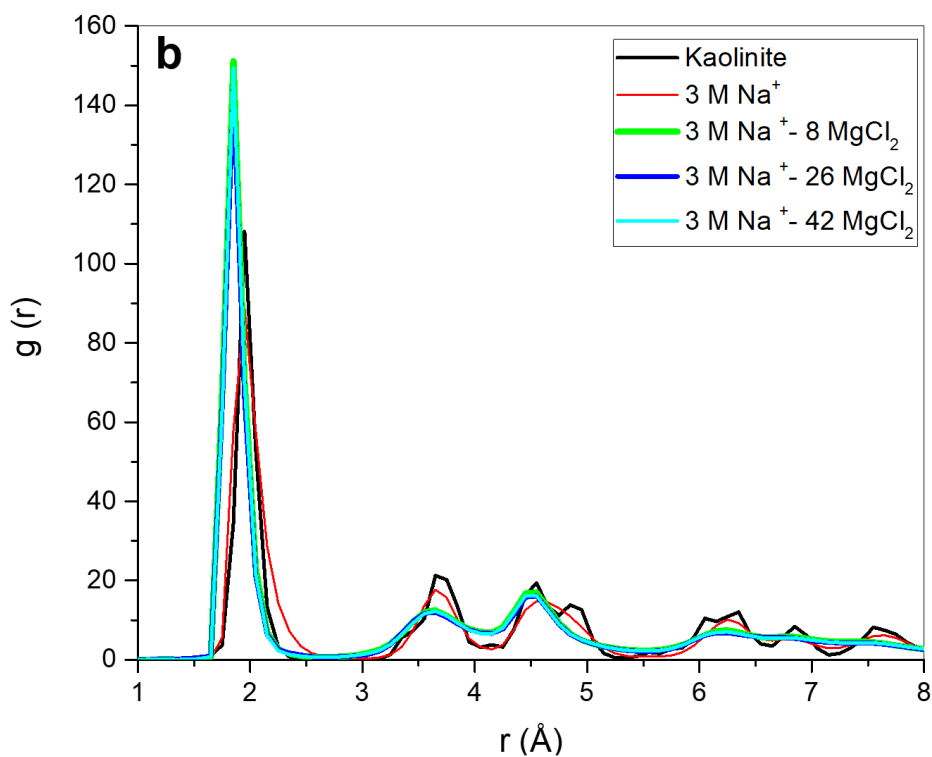
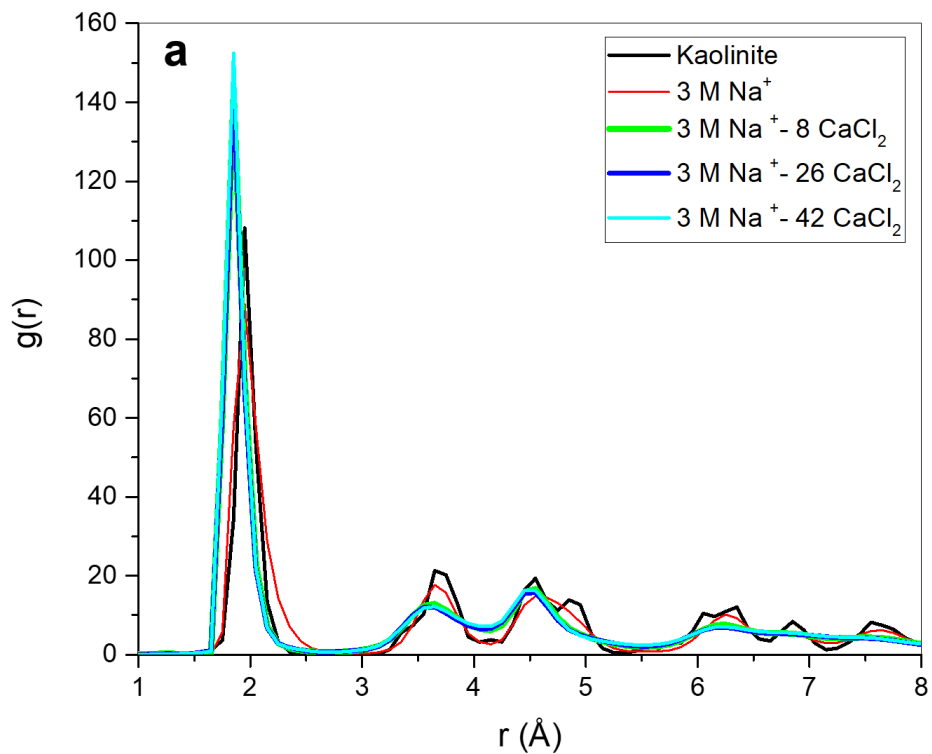


Figure 6-5 Radial distribution functions of Al - O of the octahedral surface for 3 M Na<sup>+</sup> alkali solutions containing (a) CaCl<sub>2</sub> at different concentrations and (b) MgCl<sub>2</sub> at different concentrations.

On the other hand, some of the  $\text{Na}^+$ ,  $\text{K}^+$ ,  $\text{Ca}^{2+}$  and  $\text{Mg}^{2+}$  cations were adsorbed to the tetrahedral surface of kaolinite. Atomic density profile graphs show that more  $\text{Ca}^{2+}$  cations adsorbed to the tetrahedral surface in comparison with  $\text{Mg}^{2+}$ , which could be due to the strong interaction between  $\text{Mg}^{2+}$  and  $\text{Cl}^-$  as mentioned before. However, there was essentially no change in the crystallinity of the tetrahedral surface and no dissociation of species from the such a surface was observed.

#### 6.4. Conclusion

The surface dissolution of kaolinite's basal surfaces in neat  $\text{Na}^+$  or  $\text{K}^+$  alkali solutions with inorganic salt contaminants at room temperature and pressure was studied.  $\text{MgCl}_2$  and  $\text{CaCl}_2$ , the two typical contaminants present in industrial water, were used in this work. In general, in the case of  $\text{K}^+$  cations, more aluminate groups dissociated from the kaolinite octahedral surface in comparison with the  $\text{Na}^+$  solution due to the lower charge density of  $\text{K}^+$  than that of  $\text{Na}^+$ . It was observed that aqueous contaminants such as  $\text{MgCl}_2$  and  $\text{CaCl}_2$  influenced the amount of the aluminate groups dissociated from the octahedral surface. Low concentration of contaminants in both neat  $\text{Na}^+$  and  $\text{K}^+$  solutions triggered more dissolution of aluminate group from the octahedral surface due to the higher charge density values of  $\text{Ca}^{2+}$  and  $\text{Mg}^{2+}$  cations relative to those of  $\text{Na}^+$  and  $\text{K}^+$  cations. However, at highest concentration of contaminants used (i.e., 0.5 M), a considerable amount of  $\text{Cl}^-$  anions clustered around the cations nearby the octahedral surface and screened the interaction between such cations and the octahedral surface, decreasing the number of aluminate groups dissociated from the surface. In all systems, the crystallinity of the octahedral surface decreased as a result of the surface aluminate groups changing their 6-fold position to 4-fold. Nonetheless, there was no dissolution taking place on the tetrahedral surface, at least within the simulation time used.

## Chapter 7

### 7. Molecular Dynamics Study of the Role of Water in the Carbon Dioxide Intercalation in Chloride Ions Bearing Hydrotalcite

#### 7.1. Introduction

According to a recent report of the Intergovernmental Panel on Climate Change (IPCC), a significant reduction in worldwide greenhouse gas emissions is needed in order to alleviate the global warming situation<sup>162,163</sup>. It is generally believed that carbon dioxide (CO<sub>2</sub>) emissions as a result of the consumption of fossil fuels are the major cause of global warming<sup>162,164,165</sup>. One of the most promising short term solutions for the mitigation of the problem is carbon capture and storage (CCS) as a substantial reduction in the consumption of fossil fuels, at least in the near future, is not pragmatic<sup>51,166,167</sup>. In this regard, technologies have been developed to capture CO<sub>2</sub> and to transport the captured CO<sub>2</sub> to a permanent storage location<sup>51</sup>. The technology of CO<sub>2</sub> storage comprises the injection of CO<sub>2</sub> into deep geological formations such as traps formed by clays that are expected to inhibit CO<sub>2</sub> from escaping. Geological clays or synthetic minerals can be considered as potential materials for long-term storage of industrially generated CO<sub>2</sub><sup>168</sup>. The ability of minerals to retain CO<sub>2</sub> depends on their permeability and geo-mechanical property evolution<sup>168,169</sup>.

Hydrotalcites, a class of anionic clays, have attracted attention in recent years due to their desirable properties such as lower energy of regeneration, retention of capacity after multiple cycles and suitable kinetics of CO<sub>2</sub> adsorption at ambient conditions<sup>51,170</sup>.

Hydrotalcite is a layered double hydroxide (LDH) with a crystal structure similar to that of brucite.

The general form of hydrotalcite-like materials is  $[M_{(1-x)}^{II}M_x^{III}(OH)_2]^{x+}(x/m)A^{m-} \cdot nH_2O$ , where  $M^{II}$  is the divalent metal cation (typically,  $Mg^{2+}$ ,  $Fe^{2+}$ ,  $Mn^{2+}$ ,  $Ni^{2+}$  and  $Zn^{2+}$ ) and  $M^{III}$  is the trivalent metal cation (typically,  $Al^{3+}$ ,  $Fe^{3+}$ ,  $Cr^{3+}$  and  $Co^{3+}$ ) and  $x$  is the fraction of trivalent cations in the structure and  $m$  is the charge of the anion. Owing to the cation substitution, hydrotalcites contain positive charges which are neutralized by positioning anions between layers<sup>171-173</sup>. Each  $Mg^{2+}$  in the brucite-like structure is in the octahedral position and coordinated to six  $OH^-$  groups<sup>51,174</sup>. The hydrotalcite layers are stacked on top of each other and are held together by hydrogen bonding<sup>175</sup>. Measurement of  $CO_2$  adsorption isotherms at 298 K on various hydrotalcite samples with different combinations of trivalent and divalent cations, including Ni-Al, Co-Al, Cu-Al, Zn-Al, and Mg-Al revealed that the framework made up of  $Mg^{2+}$  and  $Al^{3+}$  cations showed the best performance for carbon capture and storage<sup>167,170</sup>. In such a system, positive charges of the layers are counterbalanced by interlayer anions (e.g., chloride ions  $Cl^-$ ) that are usually hydrated allowing for expansion or contraction of the interlayer distances of the material depending on the relative humidity<sup>176</sup>. The water concentration between hydrotalcite layers determines the c-dimension of the hydrotalcite unit cell. And experimental results revealed that the c-dimension of the  $Cl^-$  bearing hydrotalcite does not expand beyond 23.9 Å at high relative humidity and ambient pressure<sup>175,177</sup>.

Rodrigues *et al.* compared  $CO_2$  adsorption capacities of a hydrotalcite at three different temperatures (293, 473, and 573 K) and showed that  $CO_2$  adsorption was maximum at 573 K and lowest at 473 K<sup>165</sup>. They suggested that the main reason for lower  $CO_2$  adsorption

capacity of hydrotalcite at 473 K compared to 293 K is a decrease in the interlayer spacing of the hydrotalcite by heating. However, it was observed that removal of water (H<sub>2</sub>O) molecules at higher temperatures caused an increase of void space which increased the capacity of CO<sub>2</sub> adsorption<sup>165,167</sup>. Presence of water between hydrotalcite layers at low temperatures leads to the hydration of dry CO<sub>2</sub> injected into hydrotalcite. The experimental data of CO<sub>2</sub> adsorption capacity of hydrotalcite in wet and dry conditions showed that under dry conditions, maximum adsorption was 0.61 mmol g<sup>-1</sup>, while under wet conditions, the adsorption capacity increased to 0.71 mmol g<sup>-1</sup><sup>178</sup>. Also, Alpay *et al.* found a 10% increase in the adsorption capacity of hydrotalcite under humid conditions<sup>56,167</sup>.

Modifying hydrotalcite structure by incorporating alkali metal cations improves its CO<sub>2</sub> adsorption capacity. Oliveira *et al.*<sup>179</sup> reported that hydrotalcites promoted by cesium or potassium exhibit significant improvements in adsorption capacity compared to those without modification. They suggested that the reason for the CO<sub>2</sub> adsorption in the alkali-modified hydrotalcites is the presence of additional interactions with the alkali cations. Sircar *et al.*<sup>180</sup> reported 0.52 mmol g<sup>-1</sup> of CO<sub>2</sub> capacity for a potassium carbonate promoted hydrotalcite at 673 K when dry gas mixture containing 70% CO<sub>2</sub> and 30% N<sub>2</sub> at a total gas pressure of 1 bar was injected<sup>181</sup>. They also reported that exposure of hydrotalcite to a wet gas stream increased the CO<sub>2</sub> adsorption capacity considerably to 0.76 mmol g<sup>-1</sup> at the same operating temperature<sup>181</sup>.

In order to optimize the storage capacity of hydrotalcites, understanding the interactions between captured CO<sub>2</sub> and the mineral in the presence of water is crucial as these molecules between layers can alter some of minerals properties such as porosity and permeability. Also, the long term storage of CO<sub>2</sub> in minerals can lead to the formation of cracks and fracture

in such minerals <sup>168,182</sup>. In the present work, molecular dynamics (MD) simulation was carried out to study the role of water in the CO<sub>2</sub> storage capacity of a model Cl<sup>-</sup> bearing hydrotalcite at room temperature and pressure. The CO<sub>2</sub> diffusion coefficients were also calculated at different CO<sub>2</sub> and water concentrations.

## 7.2. Molecular Models and Simulation Details

MD simulations were carried out using the Large-scale Atomic/Molecular Massively Parallel Simulator (LAMMPS) package <sup>105</sup>. The ClayFF force field<sup>90</sup> which comprises non-bonded (electrostatic and van der Waals) terms for metal and oxygen interaction parameterized to model layered minerals such as hydrotalcite was used. In ClayFF, the pairwise energy between atoms  $i$  and  $j$  is given by:

$$E_{total} = E_{coul} + E_{VDW} = \frac{e^2}{4\pi\epsilon_0} \sum_{i \neq j} \frac{q_i q_j}{r_{ij}} + \sum_{i \neq j} D_{0ij} \left[ \left( \frac{R_{0ij}}{r_{ij}} \right)^{12} - 2 \left( \frac{R_{0ij}}{r_{ij}} \right)^6 \right] \quad (7.1)$$

where  $e$  is the charge of the electron,  $\epsilon_0$  is the permittivity of vacuum,  $q_i$  and  $q_j$  are *ab initio* partial atomic charges,  $r_{ij}$  is the distance between atoms  $i$  and  $j$ .  $D_{0ij}$  and  $R_{0ij}$  are empirical parameters. The flexible single point charge (SPC) <sup>135</sup> model was used for the water molecules and the layer hydroxyl groups. For CO<sub>2</sub>, a recently developed flexible potential including intramolecular bond stretching and angle bending was used <sup>183</sup>. The general expression for the total potential energy is:

$$E_{total} = E_{coul} + E_{VDW} + E_{Stretch} + E_{Bend} \quad (7.2)$$

where harmonic potentials are used for the bond stretching and angle bending terms. The Lennard-Jones parameters for interaction of unlike atoms was calculated using the Lorentz–Berthelot mixing rule <sup>184</sup>. The simulations were performed under periodic

boundary conditions, and the particle–particle particle–mesh (PPPM) Ewald method<sup>138,184</sup> was used to ensure convergence of the long-range electrostatic energy. The cutoff distance for the van der Waals interactions was set at 8.5 Å and the velocity Verlet algorithm<sup>61,103</sup> was used to integrate Newton’s equations of motion with a time step of 1 fs.

Hydrotalcite-like materials in general have a three-layer rhombohedral lattice with the hexagonal unit-cell parameters of  $a = 3.054 \text{ \AA}$ ,  $c = 22.81 \text{ \AA}$ ; space group  $R\bar{3}m$ <sup>185</sup>. To simulate the structure of layered double hydroxide, 3D orthogonal models with the dimension of  $73.98 \text{ \AA} \times 64.55 \text{ \AA} \times 22.91 \text{ \AA}$  ( $x \times y \times z$ ) were generated. The Mg : Al ratio in the structure was retained as 3 : 1 as this ratio is considered to be optimum for carbon dioxide capture<sup>167,170</sup>. On account of the substitution, mineral layers gain positive charges which are counter-balanced by 290 chloride ions in total positioning in the interlayer regions of the simulation cell. The stoichiometry of the system is  $\text{Mg}_3\text{Al}(\text{OH})_8 \cdot 0.67 \text{ Cl} \cdot n \text{ H}_2\text{O}$ . The number of water molecules per unit cell in hydrotalcite materials can broadly vary depending on the nature of the anion, relative humidity and sample history<sup>172</sup>. The simulation cell used here contained 432 unit cells of hydrotalcite and overall 5,474 atoms in the structure before the addition of  $\text{H}_2\text{O}$  or  $\text{CO}_2$  molecules. The amount of  $\text{CO}_2$  in the mineral interlayer space was varied from 0.08 to 1 molecule per unit cell that corresponded to storage capacities over the range of 0.32 to 3.85  $\text{mmol g}^{-1}$  while the water concentration from 0 to 2  $\text{H}_2\text{O}$  molecules per unit cell. All of the systems studied in this work are shown in Table 1. The total number of  $\text{H}_2\text{O}$  molecules in each simulation cell is shown in the same table.

Table 7-1 Numbers of H<sub>2</sub>O and CO<sub>2</sub> molecules used in the interlayer spacing of the model hydrotalcite.

<b>H<sub>2</sub>O content</b>	<b>Concentration of CO<sub>2</sub></b>				
	<b>36 CO<sub>2</sub> (0.08/unit cell) (0.32 mmolg<sup>-1</sup>)</b>	<b>84 CO<sub>2</sub> (0.2/unit cell) (0.75 mmolg<sup>-1</sup>)</b>	<b>120 CO<sub>2</sub> (0.27/unit cell) (1.12 mmolg<sup>-1</sup>)</b>	<b>216 CO<sub>2</sub> (0.5/unit cell) (1.92 mmolg<sup>-1</sup>)</b>	<b>432 CO<sub>2</sub> (1/unit cell) (3.85 mmolg<sup>-1</sup>)</b>
<b>0 H<sub>2</sub>O</b>	A0	B0	C0	D0	E0
<b>36 H<sub>2</sub>O 0.084/unit cell</b>	A1	B1	C1	D1	E1
<b>72 H<sub>2</sub>O 0.167/unit cell</b>	A2	B2	C2	D2	E2
<b>144 H<sub>2</sub>O 0.334/unit cell</b>	A3	B3	C3	D3	E3
<b>432 H<sub>2</sub>O 1.00/unit cell</b>	A4	B4	C4	D4	E4
<b>864 H<sub>2</sub>O 2.00/unit cell</b>	A5	B5	C5	D5	E5

For each system, 100 ps MD simulation was performed using the NPT ensemble at T = 300 K and P = 1 atm to relax the structure. An equilibration run of 5 ns was carried out followed by a 5 ns production run, also in the NPT ensemble, with pressure coupling permitting each dimension of the cell to fluctuate independently. Pressure and temperature were controlled by N ose-Hoover barostat and thermostat<sup>63,101</sup> with a relaxation time of 1 and 0.1 ps, respectively. The radial distribution functions (RDF) and CO<sub>2</sub> diffusion coefficients were calculated to analyze the structure and dynamics of H<sub>2</sub>O and CO<sub>2</sub> in the mineral interlayer spacing. The Materials Studio 8.0 software (Biovia Inc., San Diego, CA, USA) was used to create the structure and VMD<sup>136</sup> software was used for visualization.

### 7.3. Results and Discussion

Figure 7-1 shows the front view of the two layers of hydrotalcite and the interlayer species (H<sub>2</sub>O, CO<sub>2</sub>, Cl<sup>-</sup>) used in the present work.

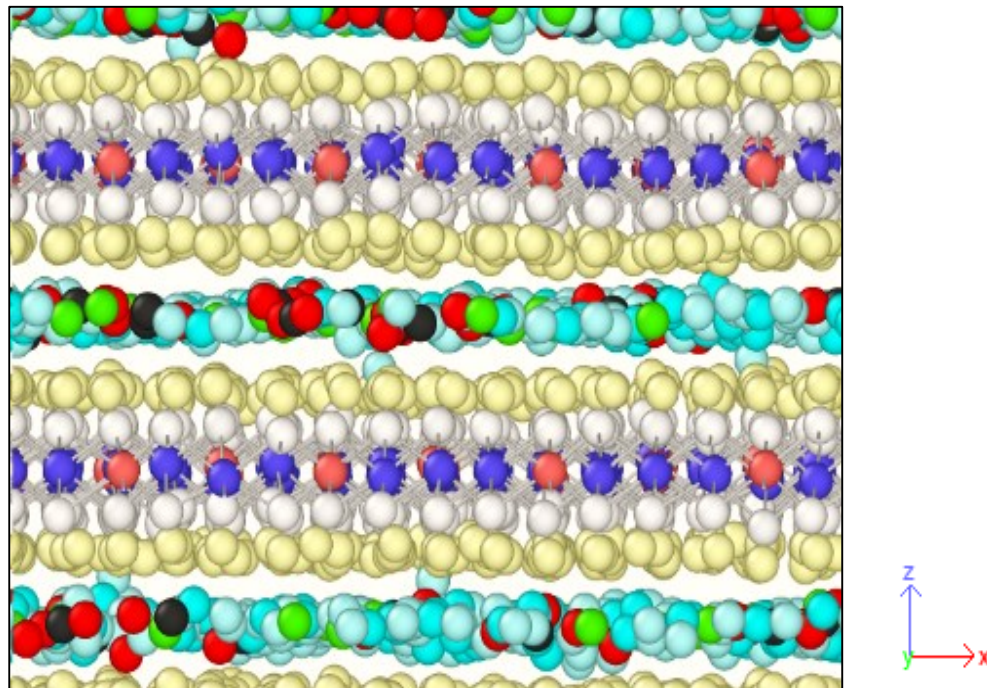


Figure 7-1 Schematic representation of the front view of the Cl-hydroxalcite/H<sub>2</sub>O/CO<sub>2</sub> system used in the present work. Color scheme: H<sub>2</sub>O molecules are shown in light blue, CO<sub>2</sub> molecules are shown in black (C) and red (O), green balls are chlorine ions, Mg, Al, O, and H atoms that make up of hydroxalcite are shown in navy, light red, white, and light yellow, respectively.

All dimensions of the simulation cell were allowed to change independently during the NPT MD simulations. However, it was observed that changes in the x and y dimensions were negligible. The expansion of the z dimension of the simulation cell intercalated by water at different concentrations (no CO<sub>2</sub>) is shown in Figure 2. Obviously, by increasing the amount of water (i.e., increasing the H<sub>2</sub>O/Cl<sup>-</sup> ratio), the total z dimension of the cell (containing three layers) increased and reached 23.7 Å which is consistent with the experimental results obtained from previous studies<sup>175,177</sup>. Figure 7-2 seems to suggest that the interlayer spacing could increase with increasing H<sub>2</sub>O/Cl<sup>-</sup> ratio beyond 3. However, this was not observed experimentally. Therefore, we used systems with H<sub>2</sub>O/Cl<sup>-</sup> ratios over the range of 0 to 3 in the subsequent NPT MD simulations. Nonetheless, the increase in z dimension was small

(23.0 to 23.75 Å), suggesting that z dimension may level off at the H<sub>2</sub>O/Cl<sup>-</sup> ratio of 3 in practice. It is worth noting that, a H<sub>2</sub>O/Cl<sup>-</sup> ratio corresponds to 2 H<sub>2</sub>O molecules per hydrotalcite unit cell (or 864 H<sub>2</sub>O molecules in the model hydrotalcite used).

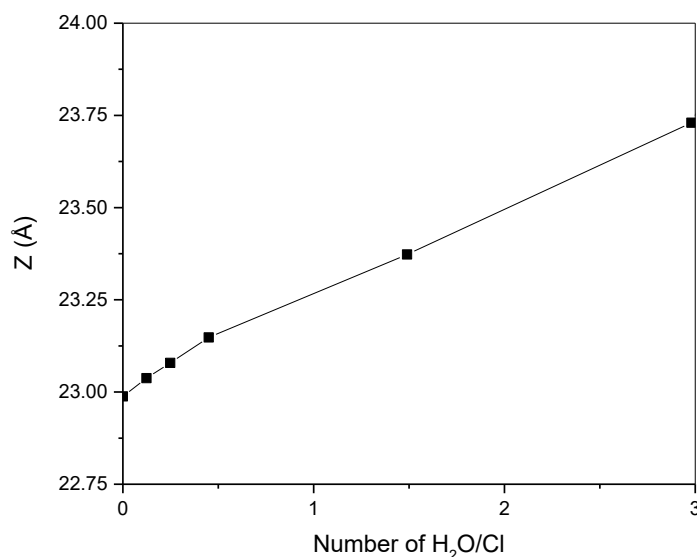


Figure 7-2 Change in the z dimension of the simulation cell as a function of the H<sub>2</sub>O/ Cl<sup>-</sup> ratio.

To understand the behavior of the CO<sub>2</sub> in the interlayer regions, atomic density profiles (ADP) of CO<sub>2</sub> in the interlayer regions were calculated for different CO<sub>2</sub> hydration states. The ADPs show that regardless of concentrations of CO<sub>2</sub> and H<sub>2</sub>O, the interlayer species form a single layer in the interlayer regions. This result is in good agreement with the results of Wang *et al.*<sup>177</sup> that a complete single layer of H<sub>2</sub>O and Cl<sup>-</sup> formed in the interlayer regions of hydrotalcite. Owing to the similarity of the ADPs of all the systems shown in Table 1, only the ADP of the C5 system which contained 120 CO<sub>2</sub> and 864 H<sub>2</sub>O is shown in Figure 7-3. The ADP graphs for other systems can be found in the supplementary information file.

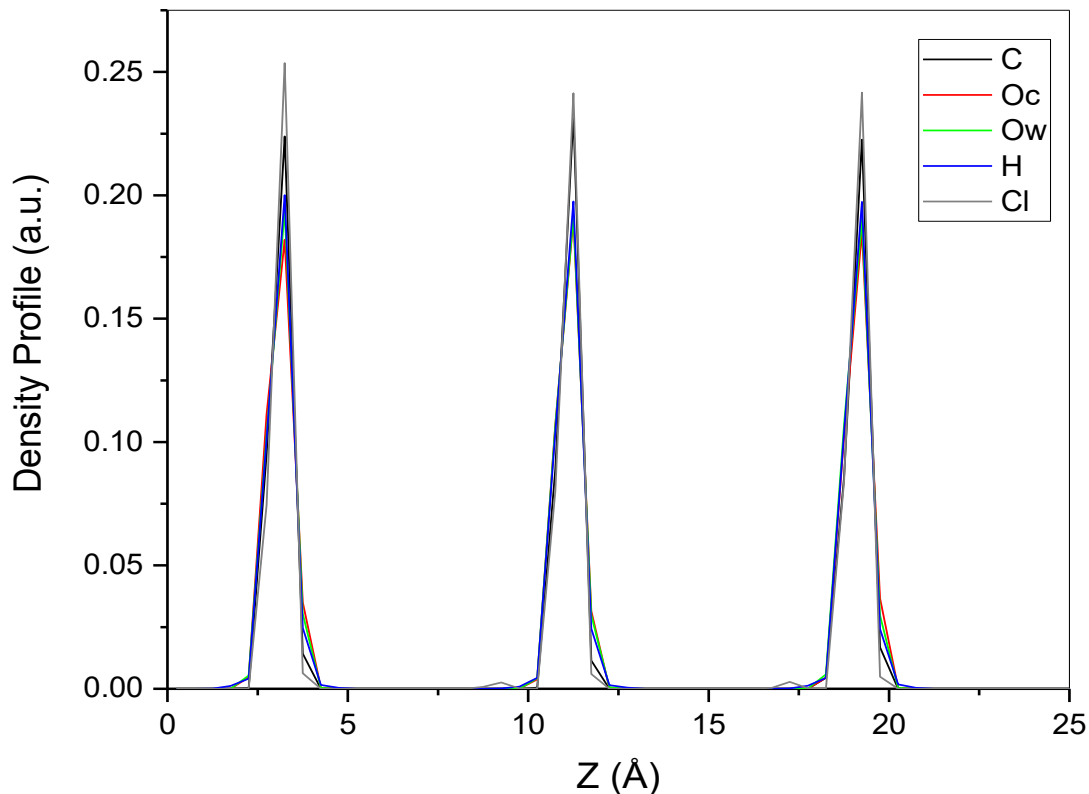


Figure 7-3 Atomic density profiles of interlayer H<sub>2</sub>O and CO<sub>2</sub> in the simulation cell along the z dimension (perpendicular to the mineral surface) for the system containing 120 CO<sub>2</sub> and 864 H<sub>2</sub>O.

Figure 7-4 shows the calculated simulation cell z dimension as a function of the number of H<sub>2</sub>O molecules per hydroxalite unit cell with different numbers of intercalated CO<sub>2</sub> molecules. The intercalation of CO<sub>2</sub> caused expansion of the interlayer spacing but magnitudes of the expansion were small and comparable to that caused by water alone (see Figure 7-2), especially at low CO<sub>2</sub> concentrations (i.e., A, B and C series in Table 1), the simulation cell expansion is less than 0.5 Å regardless of the water concentration; however, by increasing the number of CO<sub>2</sub> molecules to 216 (i.e., 1.92 mmol g<sup>-1</sup>), the cell expanded drastically (1.5 Å in system D5 (1.92 mmol g<sup>-1</sup>) and 5 Å in system E5 (i.e., 3.85 mmol g<sup>-1</sup>)). The results suggest that high H<sub>2</sub>O and CO<sub>2</sub> concentrations yielded interlayer spacing expansion.

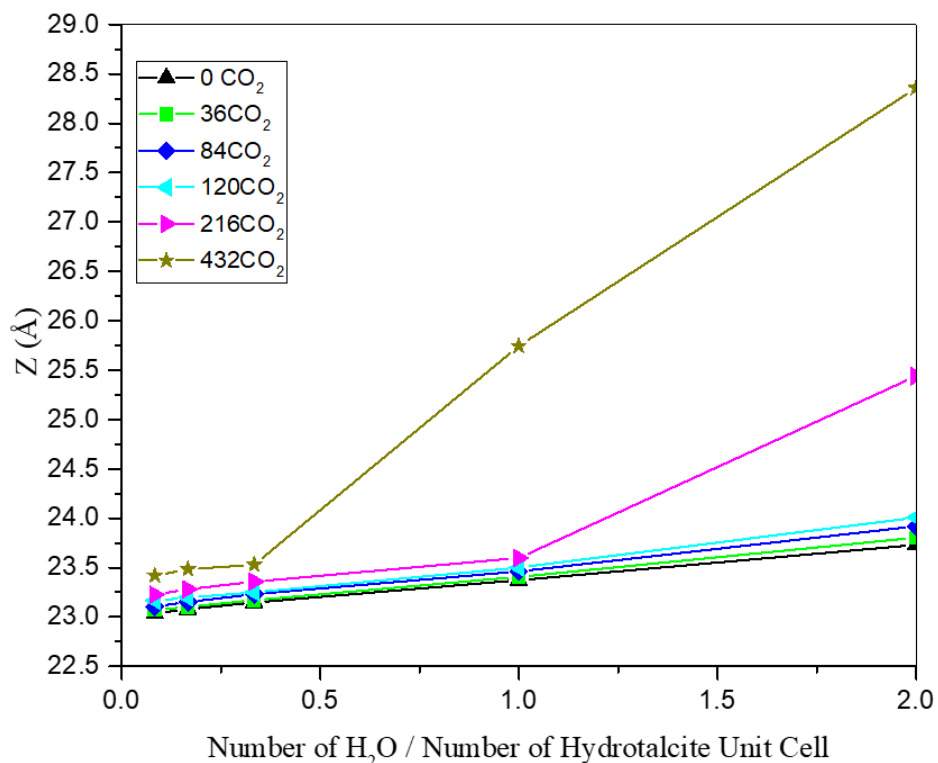
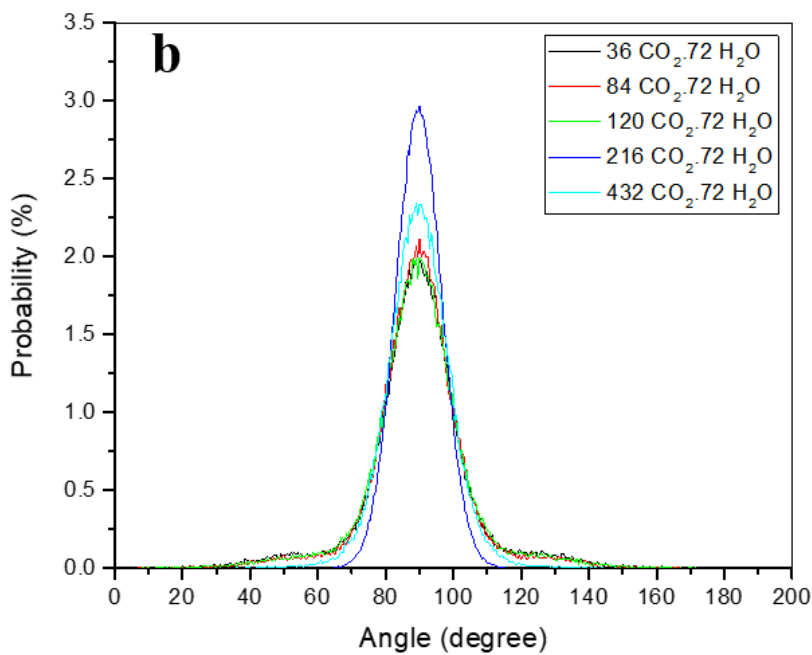
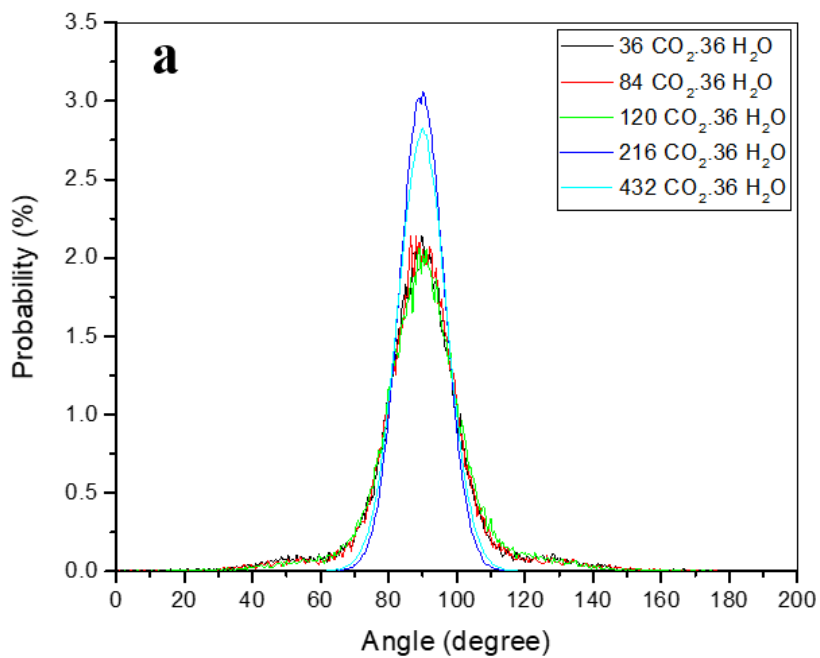
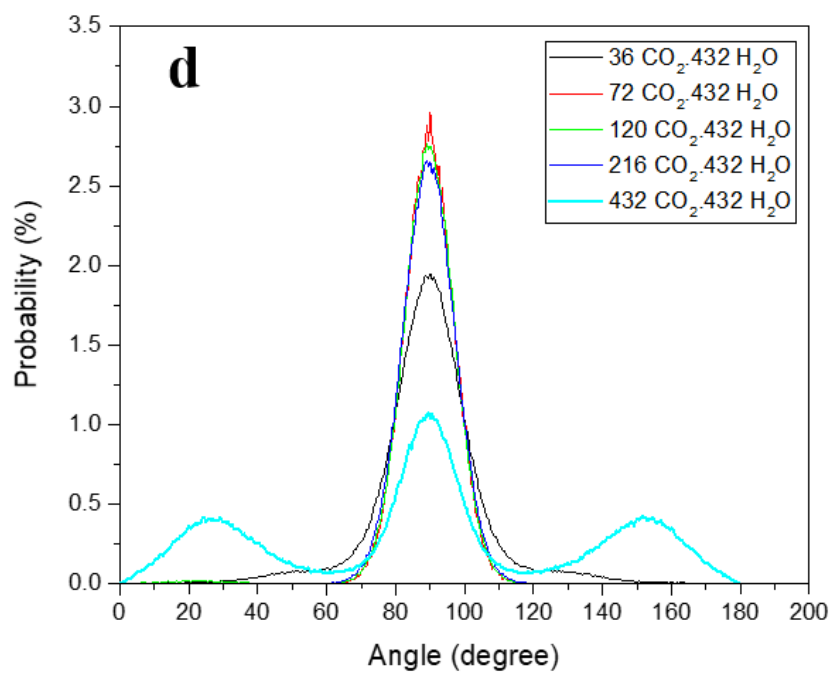
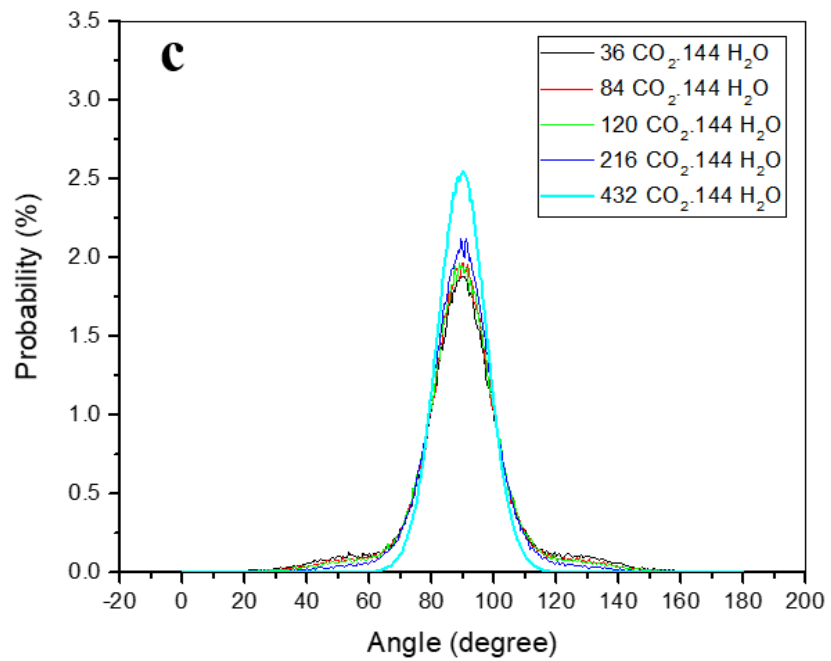


Figure 7-4 The z dimension of simulation cell as a function of number of water molecules per number of hydrotalcite unit cell at fixed numbers of CO<sub>2</sub> molecules.

Ability of water molecules to form an extended hydrogen bonding network and orientation of CO<sub>2</sub> molecules are believed to be the two key factors causing the expansion of the hydrotalcite minerals<sup>56,168</sup>. Due to the non-swelling nature of Cl<sup>-</sup>hydrotalcite in water<sup>177</sup>, orientations of CO<sub>2</sub> molecules may be the reason for the observed expansion. In this regard, we determined orientations of CO<sub>2</sub> molecules in the interlayer regions of Cl<sup>-</sup>hydrotalcite and the results are shown in Figure 7-5. As indicated in Figures 5a, 5b and 5c, at low water concentrations, orientations of CO<sub>2</sub> molecules, quantified by the angle between their molecular axes and the normal of the mineral surface, at various CO<sub>2</sub> concentrations were parallel to the mineral surface (i.e., 90°), especially at high CO<sub>2</sub> concentrations. However, at high H<sub>2</sub>O concentrations (i.e., systems D5, E4, and E5), CO<sub>2</sub> molecules tended to

adopt a wider range of angles with a significant fraction of them at 20° and 160° (i.e., parallel to the normal of the surface) as shown in Figures 5d and 5e. It seems that such orientation led to the expansion of the interlayer spacing observed in Figure 7-4.





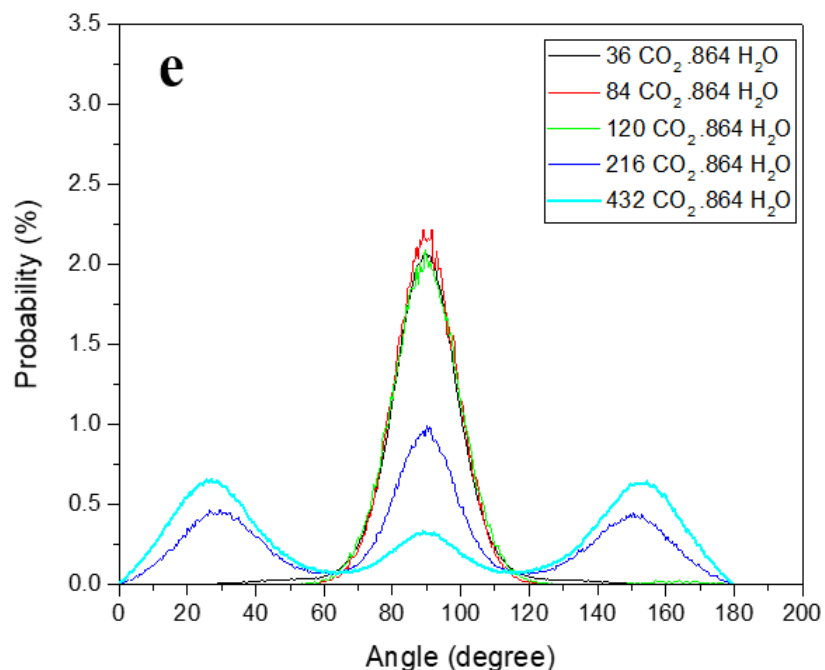
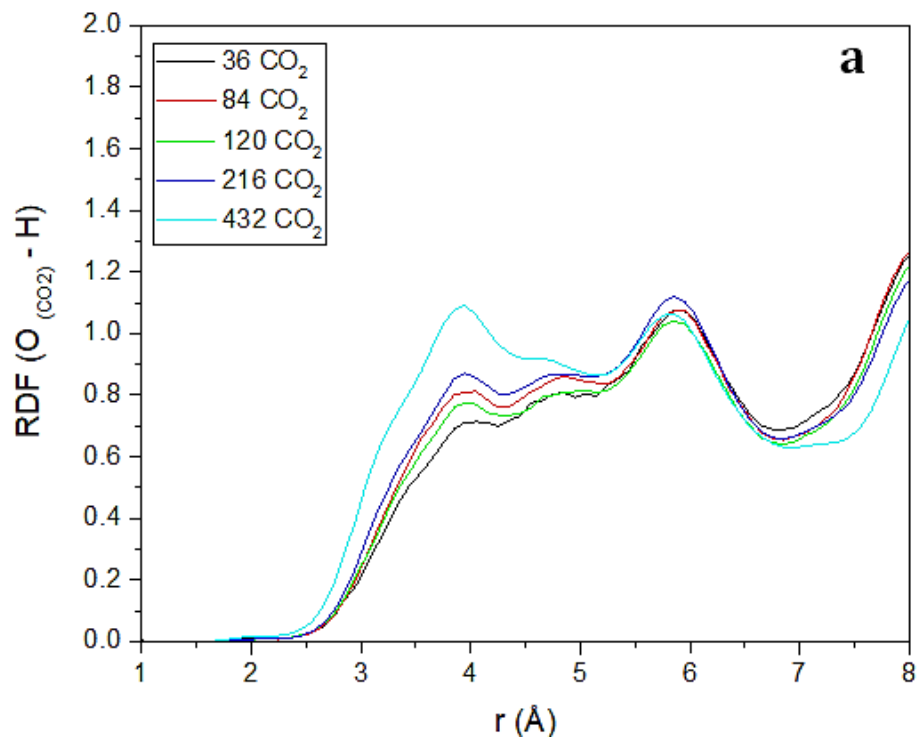
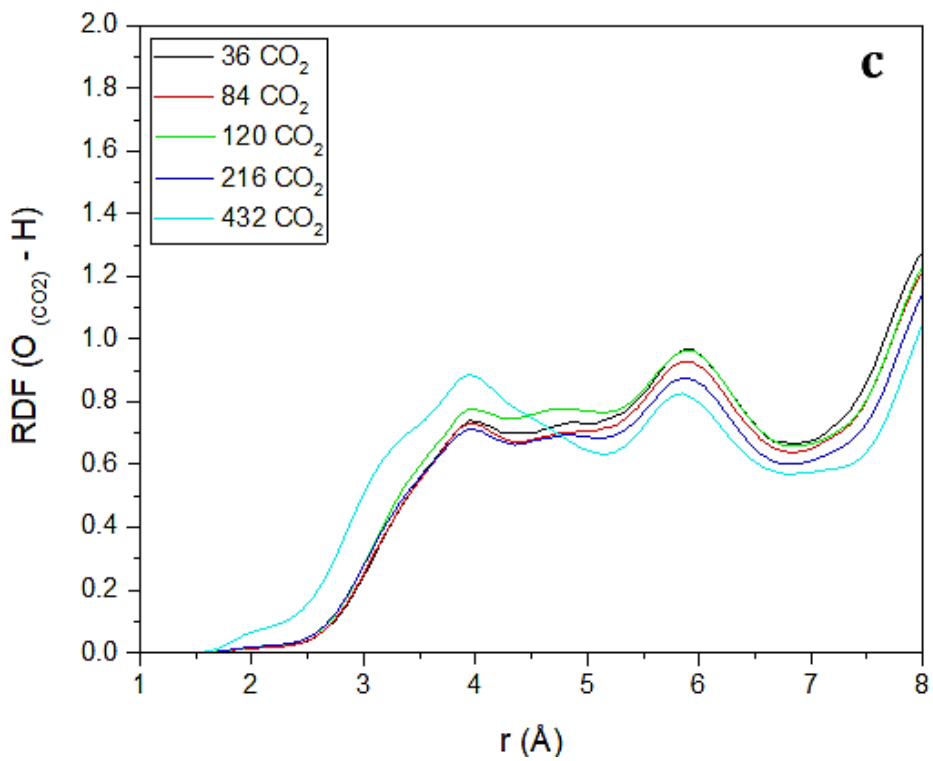
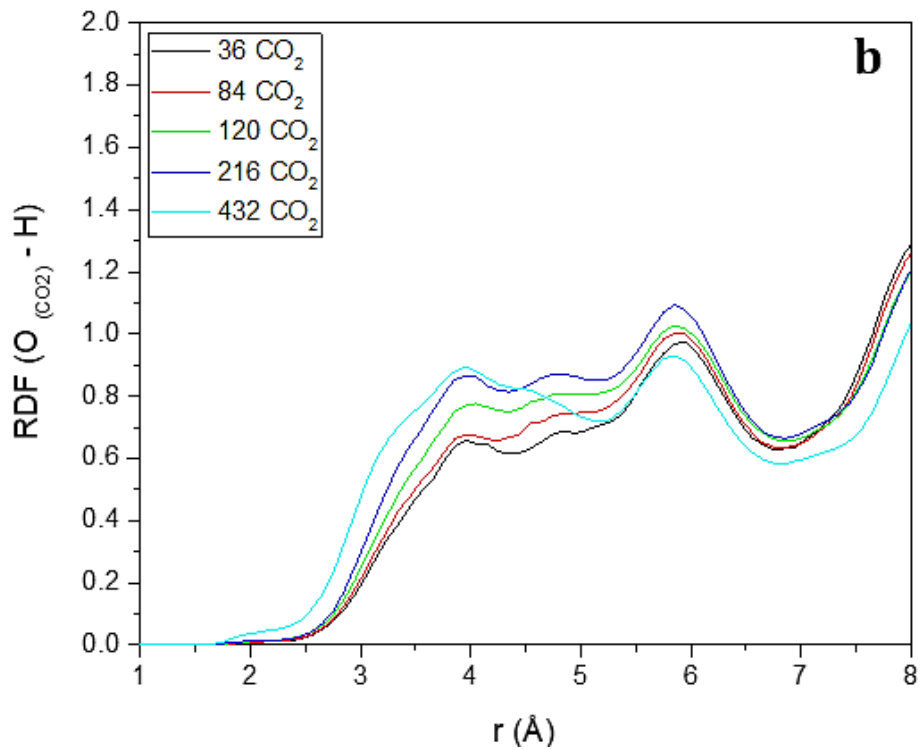


Figure 7-5 Histograms of angular distribution for CO<sub>2</sub> orientation relative to the axis normal to mineral surface at different water concentrations: (a) 36 H<sub>2</sub>O, (b) 72 H<sub>2</sub>O, (c) 144 H<sub>2</sub>O, (d) 432 H<sub>2</sub>O, and (e) 864 H<sub>2</sub>O.

Figure 7-5 suggests that structure of the first layer of water molecules adjacent to the CO<sub>2</sub> molecules may have changed from low to high water concentration to allow the CO<sub>2</sub> molecules to adopt a wider range of orientations. We therefore determined the RDF graphs of H (H<sub>2</sub>O) – O (CO<sub>2</sub>) and the results are shown in Figure 7-6. As the figure shows, when the water concentration increases, the first peak becomes more pronounced and shifts to the left (from 4 to 3.5 Å), indicating that there are more water molecules with their hydrogen atoms pointing towards the oxygen atoms of the CO<sub>2</sub> molecules and their interatomic distances are also reduced. This was attributed to the dipole-quadrupole interactions between the H<sub>2</sub>O and CO<sub>2</sub>. Please note that the oxygen atoms in the CO<sub>2</sub> model carried a charge of -0.35 while the hydrogen atoms of H<sub>2</sub>O model carried a charge of +0.41. Table 7-2 shows the number of such close, oriented contacts between the hydrogen of water and oxygen of the CO<sub>2</sub> molecules. As shown, systems with high water concentrations (i.e., C4, D4, E4, A5, B5, C5, D5

and E5) show high number of such contacts. And within these systems, the ones with high CO<sub>2</sub> concentrations exhibit high swelling (i.e., systems D5, E4, and E5).





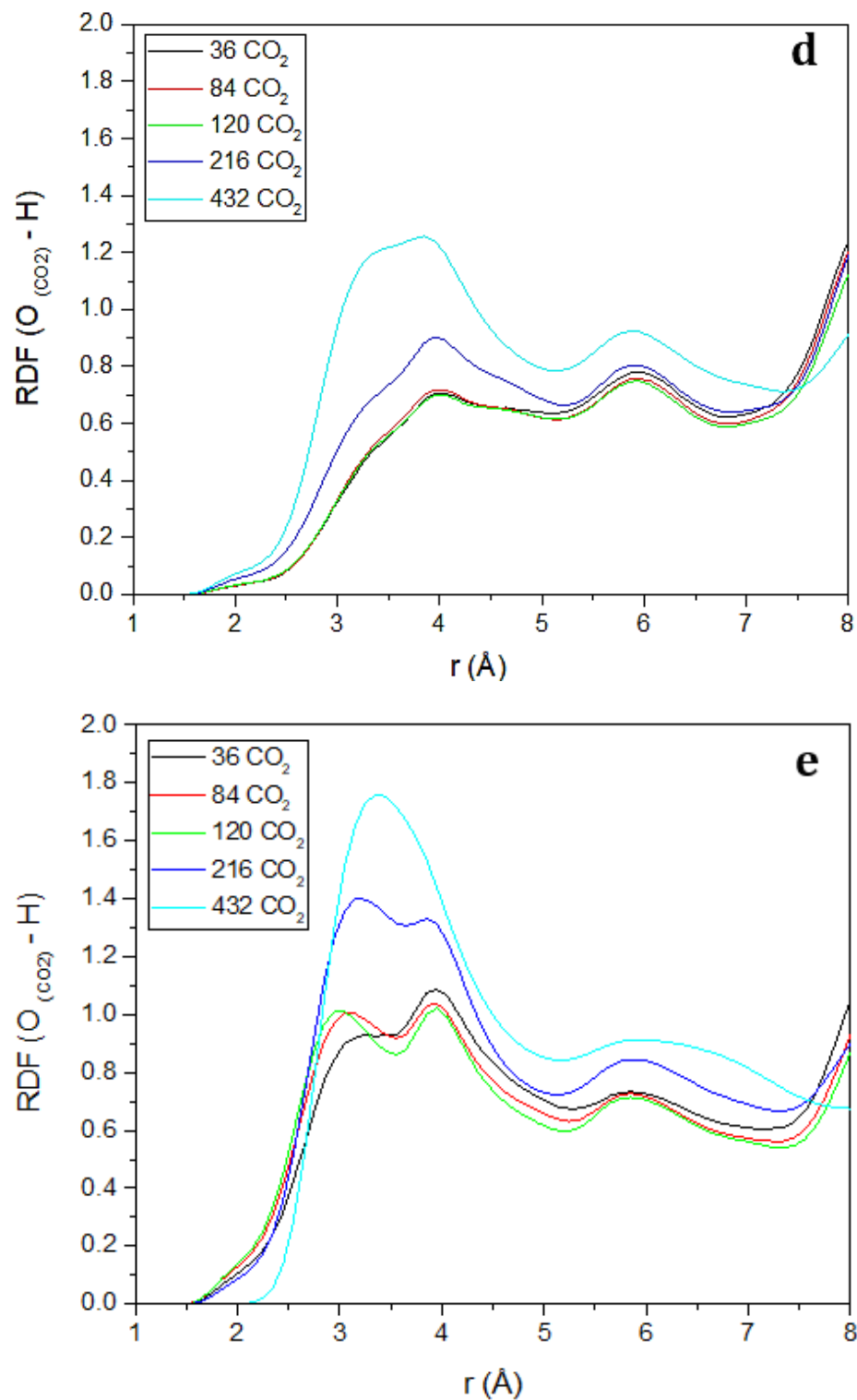


Figure 7-6 O (CO<sub>2</sub>) - H (H<sub>2</sub>O) radial distribution function at different water concentrations: (a) 36 H<sub>2</sub>O, (b) 72 H<sub>2</sub>O, (c) 144 H<sub>2</sub>O, (d) 432 H<sub>2</sub>O, and (e) 864 H<sub>2</sub>O.

The swelling behavior is also manifested in the self-diffusion coefficient of CO<sub>2</sub> molecules in the interlayer spacing as shown in Figure 7-7. In particular, the high diffusivity of CO<sub>2</sub> in swollen systems E4, D5 and E5 leads to a minimum in the series 4 (i.e., 1 H<sub>2</sub>O/hydrootalcite unit cell) and series 5 (i.e., 2 H<sub>2</sub>O/hydrootalcite unit cell) data. Nonetheless, the data suggest that the CO<sub>2</sub> diffusivity and the CO<sub>2</sub> storage capacity of the model Cl<sup>-</sup> ions bearing hydrootalcite are not related which differs from the observation of Choi et al.<sup>167</sup> that the existence of H<sub>2</sub>O molecules positively affects the CO<sub>2</sub> adsorption capacities of hydrootalcite-like compounds.

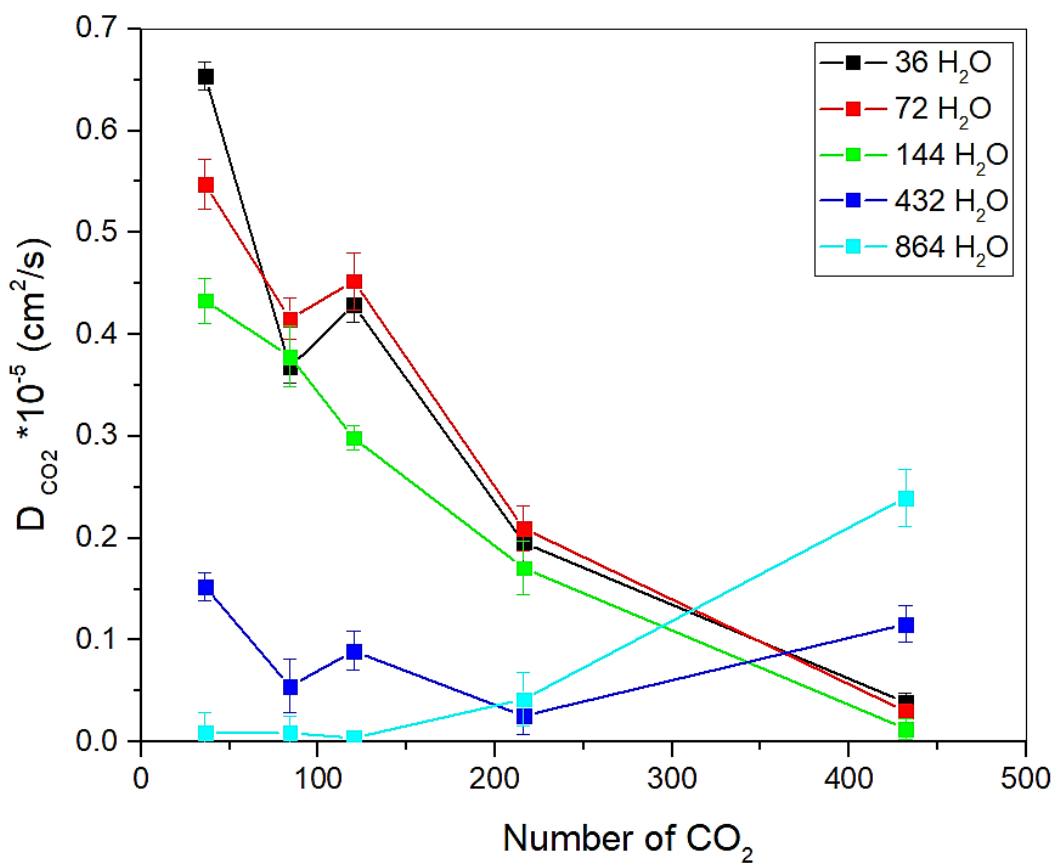


Figure 7-7 CO<sub>2</sub> diffusion coefficient as a function of CO<sub>2</sub> concentration in Cl<sup>-</sup> ions bearing hydrootalcite with different H<sub>2</sub>O concentrations.

Table 7-2 The number of H<sub>2</sub>O and CO<sub>2</sub> close contacts due to dipole-quadrupole interaction for the systems listed in Table 7-1.

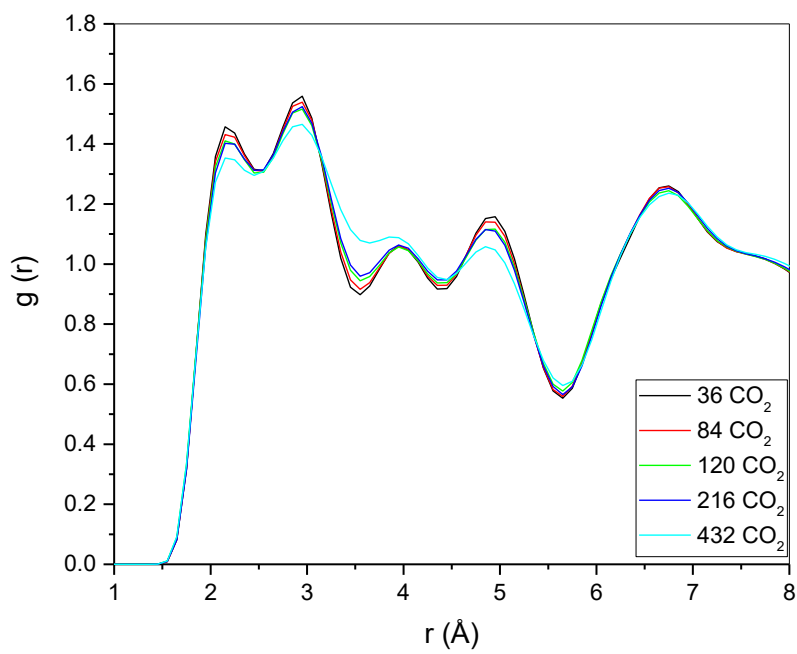
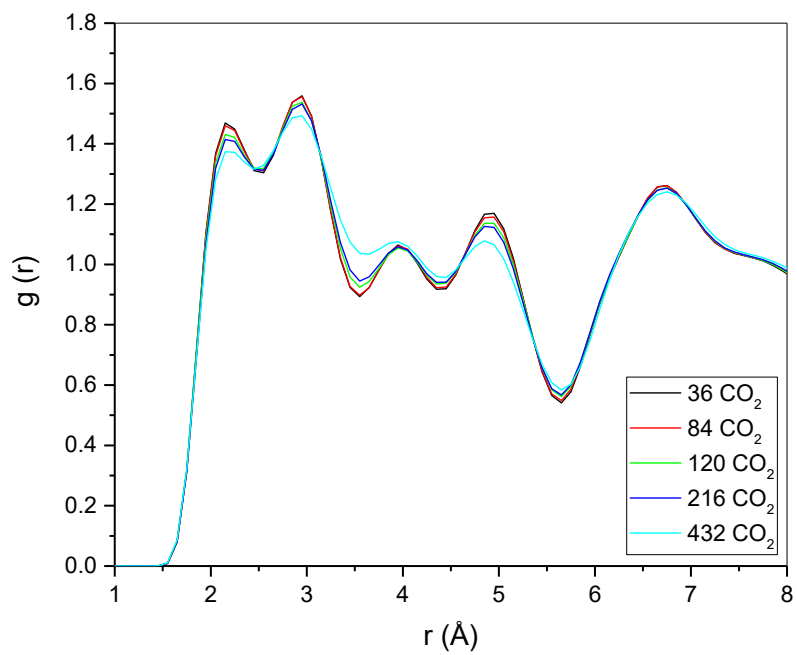
H <sub>2</sub> O content	Concentration of CO <sub>2</sub>				
	36 CO <sub>2</sub> (0.08/unit cell) (0.32 mmolg <sup>-1</sup> )	84 CO <sub>2</sub> (0.2/unit cell) (0.75 mmolg <sup>-1</sup> )	120 CO <sub>2</sub> (0.27/unit cell) (1.12 mmolg <sup>-1</sup> )	216 CO <sub>2</sub> (0.5/unit cell) (1.92 mmolg <sup>-1</sup> )	432 CO <sub>2</sub> (1/unit cell) (3.85 mmolg <sup>-1</sup> )
<b>36 H<sub>2</sub>O</b> <b>0.084/unit cell</b>	0.1 ± 0.01	0.1 ± 0.02	0.1 ± 0.02	0.1 ± 0.02	0.2 ± 0.01
<b>72 H<sub>2</sub>O</b> <b>0.167/unit cell</b>	0.2 ± 0.01	0.2 ± 0.02	0.5 ± 0.03	0.5 ± 0.03	0.5 ± 0.03
<b>144 H<sub>2</sub>O</b> <b>0.334/unit cell</b>	0.3 ± 0.01	0.4 ± 0.01	0.5 ± 0.01	0.5 ± 0.01	1 ± 0.20
<b>432 H<sub>2</sub>O</b> <b>1.00/unit cell</b>	1.7 ± 0.15	2.1 ± 0.20	2.3 ± 0.10	2.6 ± 0.10	3.1 ± 0.10
<b>864 H<sub>2</sub>O</b> <b>2.00/unit cell</b>	2.1 ± 0.30	2.2 ± 0.30	2.6 ± 0.25	3.8 ± 0.40	5.8 ± 0.45

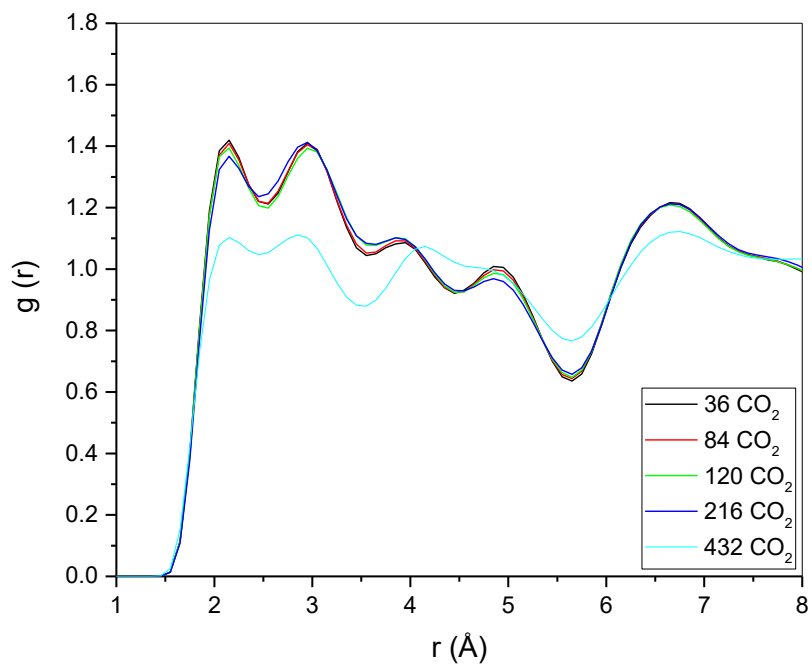
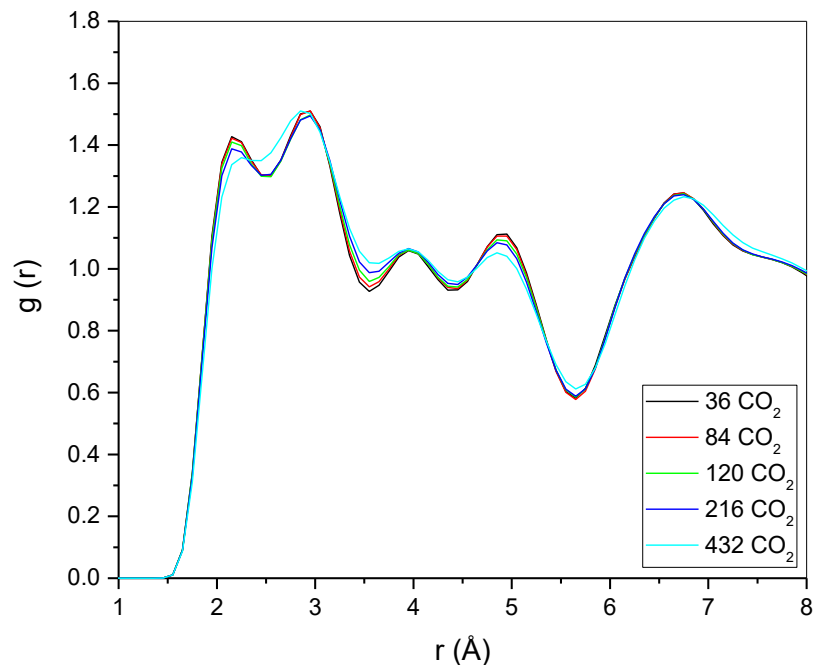
Numbers of hydrogen bonds donated by water to water and chloride ions of the systems at various H<sub>2</sub>O and CO<sub>2</sub> concentrations are shown in Table 3. As indicated, increase in the water content within the interlayer regions led to the formation of larger hydrogen bond network. This result seems to suggest that extensive hydrogen bond network and orientation of CO<sub>2</sub> molecules led to the interlayer spacing expansion<sup>56,168</sup>. The RDF graphs representing the hydrogen bond analysis can be found in Appendix B.

Table 7-3 Number of hydrogen bonds of the systems at different H<sub>2</sub>O and CO<sub>2</sub> concentrations listed in Table 7-1.

H <sub>2</sub> O content	Concentration of CO <sub>2</sub>				
	36 CO <sub>2</sub> (0.08/unit cell) (0.32 mmolg <sup>-1</sup> )	84 CO <sub>2</sub> (0.2/unit cell) (0.75 mmolg <sup>-1</sup> )	120 CO <sub>2</sub> (0.27/unit cell) (1.12 mmolg <sup>-1</sup> )	216 CO <sub>2</sub> (0.5/unit cell) (1.92 mmolg <sup>-1</sup> )	432 CO <sub>2</sub> (1/unit cell) (3.85 mmolg <sup>-1</sup> )
<b>36 H<sub>2</sub>O</b> <b>0.084/unit cell</b>	1.1 ± 0.1	1.1 ± 0.1	1.1 ± 0.1	1.1 ± 0.1	1.2 ± 0.2
<b>72 H<sub>2</sub>O</b> <b>0.167/unit cell</b>	1.3 ± 0.1	1.3 ± 0.1	1.3 ± 0.2	1.3 ± 0.2	1.5 ± 0.2
<b>144 H<sub>2</sub>O</b> <b>0.334/unit cell</b>	1.5 ± 0.1	1.5 ± 0.1	1.5 ± 0.1	1.5 ± 0.1	1.6 ± 0.2
<b>432 H<sub>2</sub>O</b> <b>1.00/unit cell</b>	2.2 ± 0.1	2.2 ± 0.1	2.2 ± 0.2	2.3 ± 0.2	2.3 ± 0.2
<b>864 H<sub>2</sub>O</b> <b>2.00/unit cell</b>	2.9 ± 0.1	2.9 ± 0.1	3.0 ± 0.1	3.0 ± 0.2	3.1 ± 0.1

The RDF graphs of interlayer CO<sub>2</sub> molecules and hydrotalcite -OH groups showed that low to moderate concentrations of water do not affect the interaction of CO<sub>2</sub> and the OH groups (Fig. 7- 8a-c); however, by increasing the water content to 432 H<sub>2</sub>O, in the presence of 432 CO<sub>2</sub> molecules, the number of CO<sub>2</sub> molecules surrounding -OH groups decreased (Fig. 7-8d). Likewise, the number of CO<sub>2</sub> molecules around -OH groups in the presence of 864 water in the interlayer region was decreased. A shift of first peak to the right (Fig. 7-8e) indicated an increase in the distance between the CO<sub>2</sub> and -OH groups. A more significant shift from 2 Å to 3.5 Å in the RDF first peak took place particularly for the E5 system (in the presence of high number of water and CO<sub>2</sub> molecule). This behavior could be explained in terms of the simulation cell expansion at this concentration as well as formation of a large hydrogen bond network of water.





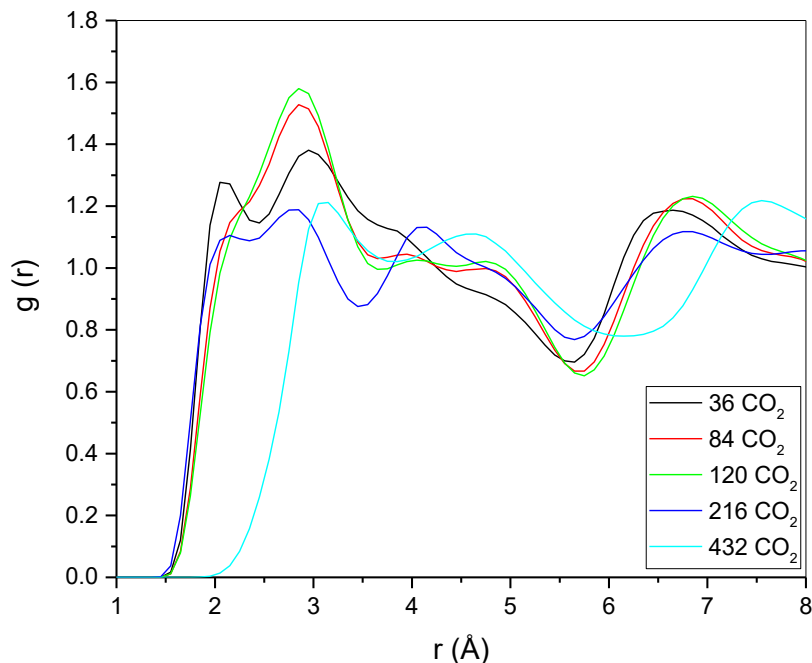


Figure 7-8.  $O_{(CO_2)} - H_{(OH)}$  radial distribution function at different water concentrations: (a) 36 H<sub>2</sub>O, (b) 72 H<sub>2</sub>O, (c) 144 H<sub>2</sub>O, (d) 432 H<sub>2</sub>O, and (e) 864 H<sub>2</sub>O.

#### 7.4. Conclusions

Hydrotalcite mineral is experimentally shown to be a potential CO<sub>2</sub> capture and storage material at ambient conditions. In this work, we used molecular dynamics simulation to study the role of interlayer water in CO<sub>2</sub> capture of Mg-Al-Cl-hydrotalcite mineral. CO<sub>2</sub> concentrations used in this work encompassed a range of storage capacities of the mineral (0.32 – 3.85 mmolg<sup>-1</sup>) while water concentration varied from 0.084 to 2.00 water molecules/hydrotalcite unit cell. Simulation results showed that the difference between the mineral with low and high water concentrations was the orientation of the CO<sub>2</sub> molecules and the extent of hydrogen bonds network formed by water. At low water concentration, majority of CO<sub>2</sub> molecules in the interlayer spacing aligned parallel to the mineral surface while at high water concentrations, they tended to adopt a wider range of orientations with

a significant fraction of them orientating perpendicular to the mineral surface as high water concentrations encouraged more dipole interaction between water and CO<sub>2</sub> molecules. Also, water molecules in such cases formed extensive hydrogen bonds.

## Chapter 8

### 8. Conclusion and Future Work

#### 8.1. Summary and conclusion

Minerals are considered as decent candidates for solving environmental problems such as oil sands tailings and CO<sub>2</sub> emission. Clay minerals are the main component of MFT (mature fine tailing) and kaolinite is abundantly found in this tailing and many other waste disposals. Therefore, treatment of this mineral can be considered as an applicable solution to solidify oil sands tailings. Furthermore, due to the layered structure of the clay minerals, they can be used as a container or storage for small molecules or ions.

Geopolymerization is newly developed method in which the aluminosilicate source materials turn into inorganic cement or geopolymer. In this process aluminosilicate source material should dissolve into the alkali solution and then go through condensation and solidification. However, this process is very fast and complicated and not easy to understand by experimental process. Also clay minerals have complicated structure and chemistry of their dissolution needs to be studied precisely to be able to control the condensation and solidification process. Molecular simulation is a very powerful tool to study the dissolution of clay minerals and in this work kaolinite basal surfaces dissolution in alkali solutions was studied by molecular dynamics simulation.

In chapter 4, the dissolution of the basal surfaces of kaolinite in the alkali solutions containing Na<sup>+</sup>, K<sup>+</sup> and 50/50 Na<sup>+</sup>/K<sup>+</sup> cations were described at low (1 M) and medium (5 M)

concentrations at 298 K and 1 atm, using molecular dynamics (MD) simulation along with the CLAYFF force field. The adsorption of the cations on the partially deprotonated octahedral surface resulted in the dissolution of the surface hydroxyl groups near the adsorption sites and the aluminum atoms (in the form of aluminates) associated with them. The MD simulation results are in agreement with the experimental observations performed by Huertas *et al.* (1999) in which the authors suggested that dissolution of kaolinite in alkali solution started with the de-protonation of the octahedral surface followed by the interaction of solution with the octahedral surface. The MD results showed that the Na<sup>+</sup> solution triggered more surface hydroxyl groups to dissociate from the octahedral surface than the K<sup>+</sup> solution. In contrast, the K<sup>+</sup> solution resulted in more dissociation of the aluminate groups than the Na<sup>+</sup> solution. The different dissolution mechanism of the two cations was attributed to the difference in the charge density of the two cations. However, when the octahedral surface was exposed to a 50/50 Na<sup>+</sup>/K<sup>+</sup> solution, more distortion to the surface occurred, suggesting that there was a synergistic effect of both Na<sup>+</sup> and K<sup>+</sup> cations. Dissolution of the tetrahedral surface was not observed.

Vacancies are common point defects which exist in most of the crystalline materials. In order to study the effect of structural vacancies on the clay dissolution process, the dissolution of the two basal surfaces of kaolinite (i.e., tetrahedral and partially deprotonated octahedral surfaces) with different amounts of Al and Si vacancies exposed to two alkali solutions, one with Na<sup>+</sup> cations only while the other K<sup>+</sup> cations only, at concentrations of 3 M and 5 M and ambient conditions was studied using molecular dynamics (MD) simulation along with the CLAYFF force field. The existence of Al vacancies on the partially deprotonated octahedral surface resulted in more dissociation of Al groups compared with

the octahedral surface with no Al vacancies. However, the dissolution amount exhibited a maximum at a relatively low vacancy concentration (2 vacancies per 576 Al atoms), above which the dissolution amount decreased with increasing concentration of Al vacancy. However, increasing the number of Al vacancies led to more distortion to the octahedral surface, thereby decreasing its crystallinity as confirmed by the corresponding radial distribution functions. And such observations took place in both Na<sup>+</sup> and K<sup>+</sup> solutions. Si vacancies in the tetrahedral surface of kaolinite increased the interaction of cations with the surface; however, no Si groups dissociated from the surface even at the existence of high numbers of vacancies, thereby retaining its crystallinity.

The surface dissolution of kaolinite's basal surfaces in neat Na<sup>+</sup> or K<sup>+</sup> alkali solutions with inorganic salt contaminants at room temperature and pressure was studied. MgCl<sub>2</sub> and CaCl<sub>2</sub>, the two typical contaminants present in industrial water, were used in this work. In general, in the case of K<sup>+</sup> cations, more aluminate groups dissociated from the kaolinite octahedral surface in comparison with the Na<sup>+</sup> solution due to the lower charge density of K<sup>+</sup> than that of Na<sup>+</sup>. It was observed that aqueous contaminants such as MgCl<sub>2</sub> and CaCl<sub>2</sub> influenced the amount of the aluminate groups dissociated from the octahedral surface. Low concentration of contaminants in both neat Na<sup>+</sup> and K<sup>+</sup> solutions triggered more dissolution of aluminate group from the octahedral surface due to the higher charge density values of Ca<sup>2+</sup> and Mg<sup>2+</sup> cations relative to those of Na<sup>+</sup> and K<sup>+</sup> cations. However, at highest concentration of contaminants used (i.e., 0.5 M), a considerable amount of Cl<sup>-</sup> anions clustered around the cations nearby the octahedral surface and screened the interaction between such cations and the octahedral surface, decreasing the number of aluminate groups dissociated from the surface. In all systems, the crystallinity of the octahedral surface decreased as a result of the

surface aluminate groups changing their 6-fold position to 4-fold. Nonetheless, there was no dissolution taking place on the tetrahedral surface, at least within the simulation time used.

Hydrotalcite mineral is experimentally shown to be a potential CO<sub>2</sub> capture and storage material at ambient conditions. In this work, we used molecular dynamics simulation to study the role of interlayer water in CO<sub>2</sub> capture of Mg-Al-Cl-hydrotalcite mineral. CO<sub>2</sub> concentrations used in this work encompassed a range of storage capacities of the mineral (0.32 – 3.85 mmolg<sup>-1</sup>) while water concentration varied from 0.084 to 2.00 water molecules/hydrotalcite unit cell. Simulation results showed that the difference between the mineral with low and high water concentrations was the orientation of the CO<sub>2</sub> molecules and the extent of hydrogen bonds network formed by water. At low water concentration, majority of CO<sub>2</sub> molecules in the interlayer spacing aligned parallel to the mineral surface while at high water concentrations, they tended to adopt a wider range of orientations with a significant fraction of them orientating perpendicular to the mineral surface as high water concentrations encouraged more dipole interaction between water and CO<sub>2</sub> molecules. Also, water molecules in such cases formed extensive hydrogen bonds.

## 8.2. Recommendation for the future work

Dissolution of clay minerals is very complex topic and understanding the chemistry of this process needs more work and knowledge. The dissolution of kaolinite basal surfaces was studied in this work. However, the dissolution of other surfaces of kaolinite specially edge surfaces can reveal important information about the dissolution process.

Structural defects affect the rate of the dissociation of clay minerals. The effect of structural vacancy on the kaolinite octahedral surfaces dissolution was described in chapter

5. Other kind of defects, such as structural impurities and stacking faults, are abundantly found in clay minerals structure. The influence of these types of defects in the structure of kaolinite can affect the dissolution process.

There are other kinds of clay minerals in the oil sands tailings and some other waste disposals. Studying the effect of alkali solution on different clay minerals can provide insightfully information about the chemistry of the dissolution process of the tailings.

## References

- (1) Boden, T. A.; Marland, G.; Andres, R. J. *Global, Regional, and National Fossil-Fuel CO<sub>2</sub> Emissions*; 2010.
- (2) Galkin, O.; Vekilov, P. G. Mechanisms of Homogeneous Nucleation of Polymers of Sickle Cell Anemia Hemoglobin in Deoxy State. *J. Mol. Biol.* **2004**, *336* (1), 43–59.
- (3) Cygan, R. T. Molecular Modeling in Mineralogy and Geochemistry. *Rev. Mineral. Geochemistry* **2001**, *42* (1), 1 LP-35.
- (4) Engels, J. [Http://www.tailings.info/basics/tailings.htm](http://www.tailings.info/basics/tailings.htm).
- (5) Madden, P. B.; Morawski, J. D. The Future of the Canadian Oil Sands: Engineering and Project Management Advances. *Energy Environ.* **2011**, *22* (5), 579–596.
- (6) Beier, N.; Wilson, W.; Dunmola, A.; Segó, D. Impact of Flocculation-Based Dewatering on the Shear Strength of Oil Sands Fine Tailings. *Can. Geotech. J.* **2013**, *50* (9), 1001–1007.
- (7) Siddique, T.; Fedorak, P. M.; Foght, J. M. Biodegradation of Short-Chain N-Alkanes in Oil Sands Tailings under Methanogenic Conditions. *Environ. Sci. Technol.* **2006**, *40* (17), 5459–5464.
- (8) Zhang, P.; Bogan, M. Recovery of Phosphate from Florida Beneficiation Slimes I. Re-Identifying the Problem. *Miner. Eng.* **1995**, *8* (4), 523–534.
- (9) BGC Engineering Inc. Oil Sands Tailings Technology Review. *Oil Sands Res. Inf. Netw.* **2010**, *OSRIN Repo* (July), OSRIN Report No. TR-1. 136 .
- (10) Adiansyah, J. S.; Rosano, M.; Vink, S.; Keir, G. A Framework for a Sustainable Approach to Mine

- Tailings Management: Disposal Strategies. *J. Clean. Prod.* **2015**, *108*, 1050–1062.
- (11) Siddique, T.; Penner, T.; Klassen, J.; Nesbø, C.; Foght, J. M. Microbial Communities Involved in Methane Production from Hydrocarbons in Oil Sands Tailings. *Environ. Sci. Technol.* **2012**, *46* (17), 9802–9810.
- (12) Mohammadijoo, M. Development of a Welding Process to Improve Welded Microalloyed Steel Characteristics, University of Alberta, 2017.
- (13) Liu, J.; Xu, Z.; Masliyah, J. Interaction between Bitumen and Fines in Oil Sands Extraction System: Implication to Bitumen Recovery. *Can. J. Chem. Eng.* **2004**, *82* (4), 655–666.
- (14) Jiang, T.; Hirasaki, G. J.; Miller, C. A.; Ng, S. Wettability Alteration of Clay in Solid-Stabilized Emulsions. *Energy & Fuels* **2011**, *25* (6), 2551–2558.
- (15) Nusri, S.; Tan, X.; Choi, P.; Liu, Q. Using Surface Geopolymerization Reactions to Strengthen Athabasca Oil Sands Mature Fine Tailings. *Can. J. Chem. Eng.* **2016**, *94* (9), 1640–1647.
- (16) Davidovits, J. Geopolymers - Inorganic Polymeric New Materials. *J. Therm. Anal.* **1991**, *37* (8), 1633–1656.
- (17) Provis, J. L.; Van Deventer, J. S. J. *Geopolymers: Structures, Processing, Properties and Industrial Applications*, 1st ed.; Provis, J. L., Van Deventer, J. S. J., Eds.; Woodhead Publishing: Cambridge, UK, 2009.
- (18) Davidovits, J. *Geopolymer Chemistry and Applications*; Davidovits, J., Ed.; Institut Géopolymère: Saint-Quentin, 2015.
- (19) Davidovits, J. Geopolymers. *J. Therm. Anal.* **1991**, *37* (8), 1633–1656.

- (20) Provis, J. L.; Duxson, P.; Van Deventer, J. S. J.; Lukey, G. C. The Role of Mathematical Modelling and Gel Chemistry in Advancing Geopolymer Technology. *Chem. Eng. Res. Des.* **2005**, *83* (7), 853–860.
- (21) Roy, D. M. Alkali-Activated Cements Opportunities and Challenges. *Cem. Concr. Res.* **1999**, *29* (2), 249–254.
- (22) Palomo, A.; Grutzeck, M. W.; Blanco, M. T. Alkali-Activated Fly Ashes: A Cement for the Future. *Cem. Concr. Res.* **1999**, *29* (8), 1323–1329.
- (23) Cheng, T. W.; Chiu, J. P. Fire-Resistant Geopolymer Produced by Granulated Blast Furnace Slag. *Miner. Eng.* **2003**, *16* (3), 205–210.
- (24) Van Jaarsveld, J. G. S.; Van Deventer, J. S. J.; Lorenzen, L. The Potential Use of Geopolymeric Materials to Immobilise Toxic Metals: Part I. Theory and Applications. *Miner. Eng.* **1997**, *10* (7), 659–669.
- (25) Allahverdi, A.; ??kv??ra, F. Nitric Acid Attack on Hardened Paste of Geopolymeric Cements. *Ceram. - Silikaty* **2001**, *45* (4), 143–149.
- (26) Davidovits, J. Mineral Polymers and Methods of Making Them. Google Patents 1982.
- (27) Palomo, A.; Glasser, F. P. Chemically-Bonded Cementitious Material Based on Metakaolin. *Br. Ceram. Trans.* **1992**, *91*, 107–112.
- (28) Rahier, H.; Van Mele, B.; Biesemans, M.; Wastiels, J.; Wu, X. Low-Temperature Synthesized Aluminosilicate Glasses. *J. Mater. Sci.* **1996**, *31* (1), 71–79.
- (29) Xu, H.; Van Deventer, J. S. J. The Geopolymerisation of Alumino-Silicate Minerals. *Int. J. Miner. Process.* **2000**, *59* (3), 247–266.

- (30) Xu, H.; van Deventer, J. S. J.; Lukey, G. C. Effect of Alkali Metals on the Preferential Geopolymerization of Stilbite/Kaolinite Mixtures. *Ind. Eng. Chem. Res.* **2001**, *40* (17), 3749–3756.
- (31) Khale, D.; Chaudhary, R. Mechanism of Geopolymerization and Factors Influencing Its Development: A Review. *J. Mater. Sci.* **2007**, *42* (3), 729–746.
- (32) Van Jaarsveld, J. G. S.; Van Deventer, J. S. J.; Lorenzen, L.; Jaarsveld, J. G. S. Van; Deventer, J. S. J. Van. The Potential Use of Geopolymeric Materials to Immobilise Toxic Metals : Part 1. Theory and Applications. *Miner. Eng.* **1997**, *10* (7), 1–10.
- (33) Duxson, P.; Fernández-Jiménez, A.; Provis, J. L.; Lukey, G. C.; Palomo, A.; van Deventer, J. S. J. Geopolymer Technology: The Current State of the Art. *J. Mater. Sci.* **2007**, *42* (9), 2917–2933.
- (34) Bergaya, F.; Lagaly, G. Chapter 1 General Introduction: Clays, Clay Minerals, and Clay Science. *Dev. Clay Sci.* **2006**, *1*, 1–18.
- (35) Chan, M. C. W. A Novel Flocculant for Enhanced Dewatering of Oil Sands Tailings, University of Alberta, 2011.
- (36) Wilson, J.; Wilson, L.; Patey, I. *The Influence of Individual Clay Minerals on Formation Damage of Reservoir Sandstones: A Critical Review with Some New Insights*; 2014; Vol. 49.
- (37) Aharoni, C.; Sparks, D. L. Kinetics of Soil Chemical Reactions—A Theoretical Treatment. In *Rates of Soil Chemical Processes*; SSSA Special Publication SV - 27; Soil Science Society of America: Madison, WI, 1991; pp 1–18.
- (38) Hochella, M. F.; Banfield, J. F. Chemical Weathering of Silicates in Nature; a Microscopic Perspective with Theoretical Considerations. *Rev. Mineral. Geochemistry* **1995**, *31* (1), 353 LP-

406.

- (39) Blum AlexAntonio, L. Role of Surface Speciation in the Low-Temperature Dissolution of Minerals. *Nature* **1988**, *331* (6155), 431–433.
- (40) Vekilov, P. G. Dense Liquid Precursor for the Nucleation of Ordered Solid Phases from Solution. *Cryst. Growth Des.* **2004**, *4* (4), 671–685.
- (41) Arrhenius, S.; Holden, E. S. ON THE INFLUENCE OF CARBONIC ACID IN THE AIR UPON THE TEMPERATURE OF THE EARTH. *Publ. Astron. Soc. Pacific* **1897**, *9* (54), 14–24.
- (42) Ghoniem, A. F. Needs, Resources and Climate Change: Clean and Efficient Conversion Technologies. *Prog. Energy Combust. Sci.* **2011**, *37* (1), 15–51.
- (43) Lemay, L. Concrete and Climate Change. **2008**.
- (44) Song, C. Global Challenges and Strategies for Control, Conversion and Utilization of CO<sub>2</sub> for Sustainable Development Involving Energy, Catalysis, Adsorption and Chemical Processing. *Catal. Today* **2006**, *115* (1), 2–32.
- (45) Folger, P. *The Carbon Cycle: Implications for Climate Change and Congress*; Washington D.C., 2008.
- (46) Watson, R. T.; Core Writing Team. *Third Assessment Report of the Intergovernmental Panel on Climate Change*; 2001.
- (47) Wong, S.; Bioletti, R. *Carbon Dioxide Separation Technologies*; 2002.
- (48) Aaron, D.; Tsouris, C. Separation of CO<sub>2</sub> from Flue Gas: A Review. *Sep. Sci. Technol.* **2005**, *40* (1–3), 321–348.

- (49) Feron, P. H. M.; Hendriks, C. A. CO<sub>2</sub> Capture Process Principles and Costs. *Oil Gas Sci. Technol. – Rev. IFP* **2005**, *60* (3), 451–459.
- (50) Anderson, S.; Newell, R. PROSPECTS FOR CARBON CAPTURE AND STORAGE TECHNOLOGIES. *Annu. Rev. Environ. Resour.* **2004**, *29* (1), 109–142.
- (51) Alsamaq, S. CARBON CYCLE : CAPTURE AND ACTIVATION OF CARBON DIOXIDE USING HYDROTALCITES BY School of Chemical Engineering The University of Birmingham, The University of Birmingham, 2012.
- (52) House, K. Z.; Harvey, C. F.; Aziz, M. J.; Schrag, D. P. The Energy Penalty of Post-Combustion CO<sub>2</sub> Capture & Storage and Its Implications for Retrofitting the U.S. Installed Base. *Energy Environ. Sci.* **2009**, *2* (2), 193–205.
- (53) Cen, P.; Yang, R. T. Bulk Gas Separation by Pressure Swing Adsorption. *Ind. Eng. Chem. Fundam.* **1986**, *25* (4), 758–767.
- (54) Chou, C.-T.; Chen, C.-Y. Carbon Dioxide Recovery by Vacuum Swing Adsorption. *Sep. Purif. Technol.* **2004**, *39* (1), 51–65.
- (55) Yong, Z.; Mata, V.; Rodrigues, A. E. Adsorption of Carbon Dioxide at High Temperature—a Review. *Sep. Purif. Technol.* **2002**, *26* (2), 195–205.
- (56) Ding, Y.; Alpay, E. Equilibria and Kinetics of CO<sub>2</sub> Adsorption on Hydrotalcite Adsorbent. *Chem. Eng. Sci.* **2000**, *55* (17), 3461–3474.
- (57) Yong, Z.; Rodrigues, A. E. Hydrotalcite-like Compounds as Adsorbents for Carbon Dioxide. *Energy Convers. Manag.* **2002**, *43* (14), 1865–1876.
- (58) Forano, C.; Hibino, T.; Leroux, F.; Taviot-Guého, C. Chapter 13.1 Layered Double Hydroxides.

- Dev. Clay Sci.* **2006**, *1*, 1021–1095.
- (59) Kang, M. R.; Lim, H. M.; Lee, S. C.; Lee, S.-H.; Kim, K. J. Layered Double Hydroxide and Its Anion Exchange Capacity. *Azo J. Mater. Online* **2005**.
- (60) Frenkel, D.; Smit, B. *Understanding Molecular Simulation*; 2002.
- (61) Verlet, L. Computer “Experiments” on Classical Fluids. I. Thermodynamical Properties of Lennard-Jones Molecules. *Phys. Rev.* **1967**, *159* (1), 98–103.
- (62) Nosé, S. A Molecular Dynamics Method for Simulations in the Canonical Ensemble. *Mol. Phys.* **1984**, *52* (2), 255–268.
- (63) Hoover, W. G. Canonical Dynamics: Equilibrium Phase-Space Distributions. *Phys. Rev. A* **1985**, *31* (3), 1695–1697.
- (64) Andersen, H. C. Molecular Dynamics Simulations at Constant Pressure And/or Temperature. *J. Chem. Phys.* **1980**, *72* (4), 2384–2393.
- (65) Parrinello, M.; Rahman, A. Polymorphic Transitions in Single Crystals: A New Molecular Dynamics Method. *J. Appl. Phys.* **1981**, *52* (12), 7182–7190.
- (66) Melchionna, S.; Ciccotti, G.; Lee Holian, B. Hoover NPT Dynamics for Systems Varying in Shape and Size. *Mol. Phys.* **1993**, *78* (3), 533–544.
- (67) Ewald, P. P. Die Berechnung Optischer Und Elektrostatischer Gitterpotentiale. *Ann. Phys.* **1921**, *369* (3), 253–287.
- (68) Deserno, M.; Holm, C. How to Mesh up Ewald Sums. II. An Accurate Error Estimate for the Particle–particle–particle-Mesh Algorithm. *J. Chem. Phys.* **1998**, *109* (18), 7694–7701.

- (69) Hockney, R. .; Eastwood, J. . *Computer Simulation Using Particles*; New York: McGraw-Hill, 1981.
- (70) Gartner, E. Industrially Interesting Approaches to “low-CO<sub>2</sub>” Cements. *Cem. Concr. Res.* **2004**, *34* (9), 1489–1498.
- (71) Habert, G.; d’Espinose de Lacaillerie, J. B.; Roussel, N. An Environmental Evaluation of Geopolymer Based Concrete Production: Reviewing Current Research Trends. *J. Clean. Prod.* **2011**, *19* (11), 1229–1238.
- (72) Davidovits, J. GEOPOLYMERS: Inorganic Polymeric New Materials. *J. Mater. Educ.* **1994**, *16* (2,3), 91–138.
- (73) Rovnaník, P. Effect of Curing Temperature on the Development of Hard Structure of Metakaolin-Based Geopolymer. *Constr. Build. Mater.* **2010**, *24* (7), 1176–1183.
- (74) Huertas, F. J.; Chou, L.; Wollast, R. Mechanism of Kaolinite Dissolution at Room Temperature and Pressure Part II: Kinetic Study. *Geochim. Cosmochim. Acta* **1999**, *63* (19–20), 3261–3275.
- (75) Grutzeck, M. W.; Siemer, D. D. Zeolites Synthesized from Class F Fly Ash and Sodium Aluminate Slurry. *J. Am. Ceram. Soc.* **1997**, *80* (9), 2449–2453.
- (76) Xu, H.; van Deventer, J. S. J. The Effect of Alkali Metals on the Formation of Geopolymeric Gels from Alkali-Feldspars. *Colloids Surfaces A Physicochem. Eng. Asp.* **2003**, *216* (1–3), 27–44.
- (77) Van Jaarsveld, J. G. S.; Van Deventer, J. S. J.; Lorenzen, L. Factors Affecting the Immobilization of Metals in Geopolymerized Flyash. *Metall. Mater. Trans. B* **1998**, *29* (1), 283–291.
- (78) Catauro, M.; Bollino, F.; Papale, F.; Lamanna, G. Investigation of the Sample Preparation and Curing Treatment Effects on Mechanical Properties and Bioactivity of Silica Rich Metakaolin

- Geopolymer. *Mater. Sci. Eng. C* **2014**, *36*, 20–24.
- (79) Vasconcelos, I. F.; Bunker, B. A.; Cygan, R. T. Molecular Dynamics Modeling of Ion Adsorption to the Basal Surfaces of Kaolinite. *J. Phys. Chem. C* **2007**, *111* (18), 6753–6762.
- (80) Iler, R. K. *The Chemistry of Silica: Solubility, Polymerization, Colloid and Surface Properties and Biochemistry of Silica*; 1979.
- (81) Šolc, R.; Gerzabek, M. H.; Lischka, H.; Tunega, D. Wettability of Kaolinite (001) Surfaces — Molecular Dynamic Study. *Geoderma* **2011**, *169*, 47–54.
- (82) Blum, W.; Niss, M. Applied Mathematical Problem Solving, Modelling, Applications, and Links to Other Subjects — State, Trends and Issues in Mathematics Instruction. *Educ. Stud. Math.* **1991**, *22* (1), 37–68.
- (83) Bauer, A.; Berger, G. Kaolinite and Smectite Dissolution Rate in High Molar KOH Solutions at 35° and 80°C. *Appl. Geochemistry* **1998**, *13* (7), 905–916.
- (84) Carroll, S.; Walther, J. V. Kaolinite Dissolution at 25, 60 and 80 °C. *Am. J. Sci.* **1990**, *290*, 797–810.
- (85) Brady, P. V; Walther, J. V. Controls on Silicate Dissolution Rates in Neutral and Basic pH Solutions at 25°C. *Geochim. Cosmochim. Acta* **1989**, *53* (11), 2823–2830.
- (86) Walther, J. Relation between Rates of Aluminosilicate Mineral Dissolution, pH, Temperature, and Surface Charge. *Am. J. Sci.* **1996**, *296*(7), 693–728.
- (87) Panagiotopoulou, C.; Kontori, E.; Perraki, T.; Kakali, G. Dissolution of Aluminosilicate Minerals and by-Products in Alkaline Media. *J. Mater. Sci.* **2007**, *42* (9), 2967–2973.

- (88) Hajimohammadi, A.; Provis, J. L.; van Deventer, J. S. J. Effect of Alumina Release Rate on the Mechanism of Geopolymer Gel Formation. *Chem. Mater.* **2010**, *22* (18), 5199–5208.
- (89) Aldabsheh, I.; Khoury, H.; Wastiels, J.; Rahier, H. Dissolution Behavior of Jordanian Clay-Rich Materials in Alkaline Solutions for Alkali Activation Purpose. Part I. *Appl. Clay Sci.* **2015**, *115*, 238–247.
- (90) Cygan, R. T.; Liang, J.-J.; Kalinichev, A. G. Molecular Models of Hydroxide, Oxyhydroxide, and Clay Phases and the Development of a General Force Field. *J. Phys. Chem. B* **2004**, *108* (4), 1255–1266.
- (91) Wang, J.; Kalinichev, A. G.; Kirkpatrick, R. J.; Cygan, R. T. Structure, Energetics, and Dynamics of Water Adsorbed on the Muscovite (001) Surface: A Molecular Dynamics Simulation. *J. Phys. Chem. B* **2005**, *109* (33), 15893–15905.
- (92) Greathouse, J. A.; Cygan, R. T. Molecular Dynamics Simulation of Uranyl(vi) Adsorption Equilibria onto an External Montmorillonite Surface. *Phys. Chem. Chem. Phys.* **2005**, *7* (20), 3580–3586.
- (93) Payne, M. C.; Teter, M. P.; Allan, D. C.; Arias, T. A.; Joannopoulos, J. D. Iterative Minimization Techniques for Ab Initio Total-Energy Calculations: Molecular Dynamics and Conjugate Gradients. *Rev. Mod. Phys.* **1992**, *64* (4), 1045–1097.
- (94) Berendsen, H. J. C.; Postma, J. P. M.; Gunsteren, W. F. van; Hermans, J. Interaction Models for Water in Relation to Protein Hydration. In *Intermolecular Forces*; 1981; pp 331–342.
- (95) Teleman, O.; Jönsson, B.; Engström, S. A Molecular Dynamics Simulation of a Water Model with Intramolecular Degrees of Freedom. *Mol. Phys.* **1987**, *60* (1), 193–203.

- (96) Wallqvist, A.; Teleman, O. Properties of Flexible Water Models. *Mol. Phys.* **1991**, *74* (3), 515–533.
- (97) Smith, D. E.; Haymet, A. D. J. Simulations of Aqueous Solutions: The Role of Flexibility and the Treatment of Long-Range Forces. *Fluid Phase Equilib.* **1993**, *88*, 79–87.
- (98) Bish, D. L. Rietveld Refinement of the Kaolinite Structure at 1.5 K. *Clays Clay Miner.* **1993**, *41* (6), 738 LP-744.
- (99) Hocine, S.; Hartkamp, R.; Siboulet, B.; Duvail, M.; Coasne, B.; Turq, P.; Dufrêche, J.-F. How Ion Condensation Occurs at a Charged Surface: A Molecular Dynamics Investigation of the Stern Layer for Water–Silica Interfaces. *J. Phys. Chem. C* **2016**, *120* (2), 963–973.
- (100) Martyna, G. J.; Tobias, D. J.; Klein, M. L. Constant Pressure Molecular Dynamics Algorithms. *J. Chem. Phys.* **1994**, *101* (5), 4177–4189.
- (101) Nosé, S. A Molecular Dynamics Method for Simulations in the Canonical Ensemble. *Mol. Phys.* **1984**, *52* (2), 255–268.
- (102) Hoover, W. G. Constant-Pressure Equations of Motion. *Phys. Rev. A* **1986**, *34* (3), 2499–2500.
- (103) Verlet, L. Computer “Experiments” on Classical Fluids. II. Equilibrium Correlation Functions. *Phys. Rev.* **1968**, *165* (1), 201–214.
- (104) Plimpton, S.; Pollock, R.; Stevens, M. Particle-Mesh Ewald and rRESPA for Parallel Molecular Dynamics Simulations. In *Eighth SIAM Conference on Parallel Processing for Scientific Computing*; 1997.
- (105) Plimpton, S. Fast Parallel Algorithms for Short-Range Molecular Dynamics. *J. Comput. Phys.* **1995**, *117* (1), 1–19, (<http://lammps.sandia.gov>).

- (106) Lanaro, G.; Patey, G. N. Molecular Dynamics Simulation of NaCl Dissolution. *J. Phys. Chem. B* **2015**, *119* (11), 4275–4283.
- (107) Sperinck, S.; Raiteri, P.; Marks, N.; Wright, K. Dehydroxylation of Kaolinite to Metakaolin-a Molecular Dynamics Study. *J. Mater. Chem.* **2011**, *21* (7), 2118–2125.
- (108) Duxson, P.; Fernández-Jiménez, A.; Provis, J. L.; Lukey, G. C.; Palomo, A.; Van Deventer, J. S. J. Geopolymer Technology: The Current State of the Art. *J. Mater. Sci.* **2007**, *42* (9), 2917–2933.
- (109) Hooshiar, A.; Uhlik, P.; Ivey, D. G.; Liu, Q.; Etsell, T. H. Clay Minerals in Nonaqueous Extraction of Bitumen from Alberta Oil Sands: Part 2. Characterization of Clay Minerals. *Fuel Process. Technol.* **2012**, *96*, 183–194.
- (110) Xu, H.; van Deventer, J. S. J. Effect of Source Materials on Geopolymerization. *Ind. Eng. Chem. Res.* **2003**, *42* (40), 1698–1706.
- (111) Panagiotopoulou, C.; Kontori, E.; Perraki, T.; Kakali, G. Dissolution of Aluminosilicate Minerals and by-Products in Alkaline Media. *J. Mater. Sci.* **2007**, *42* (9), 2967–2973.
- (112) Morris, J. W. Chapter 4 : Defects in Crystals. *Mater. Sci.* **2007**, 76–107.
- (113) He, M.-C.; Fang, Z.-J.; Zhang, P. Theoretical Studies on Defects of Kaolinite in Clays. *Chinese Phys. Lett.* **2009**, *26* (5), 59101.
- (114) Nisar, J.; Arhammar, C.; Jämstorp, E.; Ahuja, R. Optical Gap and Native Point Defects in Kaolinite Studied by the GGA-PBE, HSE Functional, and GW Approaches. *Phys. Rev. B* **2011**, *84* (7), 75120.
- (115) Yang, G.; Zhou, L. Zwitterionic versus Canonical Amino Acids over the Various Defects in Zeolites: A Two-Layer ONIOM Calculation. *Sci. Rep.* **2014**, *4*, 6594.

- (116) Kogure, T.; Inoue, A. Stacking Defects and Long-Period Polytypes in Kaolin Minerals from a Hydrothermal Deposit. *Eur. J. Mineral.* **2005**, *17* (3), 465–473.
- (117) Corkhill, C. L.; Bailey, D. J.; Tocino, F. Y.; Stennett, M. C.; Miller, J. A.; Provis, J. L.; Travis, K. P.; Hyatt, N. C. Role of Microstructure and Surface Defects on the Dissolution Kinetics of CeO<sub>2</sub>, a UO<sub>2</sub> Fuel Analogue. *ACS Appl. Mater. Interfaces* **2016**, *8* (16), 10562–10571.
- (118) Kogure, T.; Inoue, A. Determination of Defect Structures in Kaolin Minerals by High-Resolution Transmission Electron Microscopy (HRTEM). *Am. Mineral.* **2005**, *90* (1), 85–89.
- (119) Zhu, X.; Zhu, Z.; Lei, X.; Yan, C. Defects in Structure as the Sources of the Surface Charges of Kaolinite. *Appl. Clay Sci.* **2016**, *124–125*, 127–136.
- (120) Li, X.; Li, H.; Yang, G. Promoting the Adsorption of Metal Ions on Kaolinite by Defect Sites: A Molecular Dynamics Study. *Sci Rep* **2015**, *5*, 14377.
- (121) Grangeon, S.; Claret, F.; Tournassat, C.; Linard, Y.; Grangeon, S.; Claret, F.; Tournassat, C.; Linard, Y.; Lanson, B. Structural Defects in Layered Structures : Their Determination and Their Impact on Reactivity To Cite This Version : Structural Defects in Layered Structures : Their Determination and Their Impact on Reactivity. **2015**.
- (122) Bookin, a. S. Stacking Faults in Kaolin-Group Minerals in the Light of Real Structural Features. *Clays Clay Miner.* **1989**, *37* (4), 297–307.
- (123) Xia, L.; Zhong, H.; Liu, G.; Li, X. Electron Bandstructure of Kaolinite and Its Mechanism of Flotation Using Dodecylamine as Collector. *J. Cent. South Univ. Technol.* **2009**, *16* (1), 73–79.
- (124) Solc, R.; Gerzabek, M. H.; Lischka, H.; Tunega, D. Wettability of Kaolinite (001) Surfaces - Molecular Dynamic Study. *Geoderma* **2011**, *169* (December), 47–54.

- (125) Huertas, F. J.; Chou, L.; Wollast, R. Mechanism of Kaolinite Dissolution at Room Temperature and Pressure: Part 1. Surface Speciation. *Geochim. Cosmochim. Acta* **1998**, *62* (3), 417–431.
- (126) Bish, D. L. Rietveld Refinement of the Kaolinite Structure at 1.5 K. *Clays Clay Miner.* **1993**, *41* (6), 738–744.
- (127) Wypych, F. *Clay Surfaces: Fundamentals and Applications*, 1st Editio.; Academic Press, 2004.
- (128) Papoulis, D.; Tsolis-Katagas, P. Formation of Alteration Zones and Kaolin Genesis, Limnos Island, Northeast Aegean Sea, Greece. *Clay Miner.* **2008**, *43* (4), 631–646.
- (129) Valášková, M.; Rieder, M.; Matějka, V.; Čapková, P.; Slíva, A. Exfoliation/delamination of Kaolinite by Low-Temperature Washing of Kaolinite–urea Intercalates. *Appl. Clay Sci.* **2007**, *35* (1–2), 108–118.
- (130) Croteau, T.; Bertram, A. K.; Patey, G. N. Water Adsorption on Kaolinite Surfaces Containing Trenches. *J. Phys. Chem. A* **2010**, *114* (5), 2171–2178.
- (131) Haq, A.; Iqbal, Y.; Khan, M. R. Phase and Microstructural Characterization of Kaolin Clays from North Western Pakistan. *J. Pakistan Mater. Soc.* **2009**, *3* (2), 77–90.
- (132) Aparicio, P.; Galán, E.; Valdrè, G.; Moro, D. Effect of Pressure on Kaolinite Nanomorphology under Wet and Dry Conditions: Correlation with Other Kaolinite Properties. *Appl. Clay Sci.* **2009**, *46* (2), 202–208.
- (133) Cygan, R. T.; Liang, J.-J.; Kalinichev, A. G. Molecular Models of Hydroxide, Oxyhydroxide, and Clay Phases and the Development of a General Force Field. *J. Phys. Chem. B* **2004**, *108* (4), 1255–1266.
- (134) Ngouana W., B. F.; Kalinichev, A. G. Structural Arrangements of Isomorphous Substitutions in

- Smectites: Molecular Simulation of the Swelling Properties, Interlayer Structure, and Dynamics of Hydrated Cs-Montmorillonite Revisited with New Clay Models. *J. Phys. Chem. C* **2014**, *118* (24), 12758–12773.
- (135) Berendsen, H. J. C.; Postma, J. P. M.; van Gunsteren, W. F.; Hermans, J. Interaction Models for Water in Relation to Protein Hydration BT - Intermolecular Interaction Models of Water in Relation to Protein Hydration. In: *Intermolecular Forces: Proceedings of the Fourteenth Jerusalem Symposium on Quantum Chemistry and Biochemis*; Pullman, B., Ed.; Springer Netherlands: Dordrecht, 1981; pp 331–342.
- (136) Humphrey, W.; Dalke, A.; Schulten, K. VMD: Visual Molecular Dynamics. *J. Mol. Graph.* **1996**, *14* (1), 33–38.
- (137) Martyna, G. J.; Tobias, D. J.; Klein, M. L. + E. **1994**, *101* (September), 4177–4189.
- (138) Plimpton, S.; Pollock, R.; Stevens, M. J. Particle Mesh Ewald and rRESPA for Parallel Molecular Dynamics Simulations. *Proc. Eighth Siam Conf. Parallel Process. Sci. Comput.* **1997**, 1–13.
- (139) Levine, B. G.; Stone, J. E.; Kohlmeyer, A. Fast Analysis of Molecular Dynamics Trajectories with Graphics Processing units—Radial Distribution Function Histogramming. *J. Comput. Phys.* **2011**, *230* (9), 3556–3569.
- (140) Duxson, P.; Provis, J. L.; Lukey, G. C.; van Deventer, J. S. J. The Role of Inorganic Polymer Technology in the Development of “green Concrete.” *Cem. Concr. Res.* **2007**, *37* (12), 1590–1597.
- (141) Hajimohammadi, A.; Provis, J. L.; Van Deventer, J. S. J. Effect of Alumina Release Rate on the Mechanism of Geopolymer Gel Formation. *Chem. Mater.* **2010**, *22* (18), 5199–5208.

- (142) Velde, B. Experimental Determination of Muscovite Polymorph Stabilities. *Am. Mineral.* **1965**, *50*, 436–449.
- (143) Eberl, D. D.; Hower, J. Kinetics of Illite Formation. *Geol. Soc. Am. Bull.* **1976**, *87* (9), 1326 LP-1330.
- (144) Eberl, D. D.; Khoury, H. N. Bubble-Wall Shards Altered to Montmorillonite. *Clays Clay Miner.* **1979**, *27* (4), 291–292.
- (145) Chermak, J. A. Low Temperature Experimental Investigation of the Effect of High pH NaOH Solution on the Opalinus Shale, Switzerland. *Clays Clay Miner.* **1992**, *40*, 650–658.
- (146) Chermak, J. A. Low Temperature Experimental Investigation of the Effect of High pH KOH Solutions on the Opalinus Shale. *Clays Clay Miner.* **1993**, *41* (3), 365–372.
- (147) Eberl, D. D.; Velde, B.; McCormick, T. Synthesis of Illite-Smectite from Smectite at Earth Surface Temperature and High pH. *Clay Miner.* **1993**, *28*, 49–60.
- (148) Fernández-Jiménez, A.; Palomo, A.; Sobrados, I.; Sanz, J. The Role Played by the Reactive Alumina Content in the Alkaline Activation of Fly Ashes. *Microporous Mesoporous Mater.* **2006**, *91* (1), 111–119.
- (149) Silva, P. De; Sagoe-Crenstil, K.; Sirivivatnanon, V. Kinetics of Geopolymerization: Role of Al<sub>2</sub>O<sub>3</sub> and SiO<sub>2</sub>. *Cem. Concr. Res.* **2007**, *37* (4), 512–518.
- (150) Crundwell, F. K. The Mechanism of Dissolution of Minerals in Acidic and Alkaline Solutions: Part VI a Molecular Viewpoint. *Hydrometallurgy* **2016**, *161*, 34–44.
- (151) Brantley, S. L.; Kubicki, J. D.; White, A. F. *Kinetics of Water-Rock Interaction*; Springer.

- (152) Naderi Khorshidi, Z.; Tan, X.; Liu, Q.; Choi, P. Molecular Dynamics Study of the Dissolution Mechanism of Kaolinite Basal Surfaces in Alkali Media. *Appl. Clay Sci.* **2017**.
- (153) Naderi Khorshidi, Z.; Tan, X.; Liu, Q.; Choi, P. Influence of Structural Al and Si Vacancies on the Interaction of Kaolinite Basal Surfaces with Alkali Cations: A Molecular Dynamics Study. *Comput. Mater. Sci.* **2017**, *140*, 267–274.
- (154) Mullaney, J. R.; Lorenz, D. L.; Arntson, A. D. *Chloride in Groundwater and Surface Water in Areas Underlain by the Glacial Aquifer System, Northern United States Scientific Investigations Report 2009 – 5086*; Virginia, 2009.
- (155) Lee, W. K. W.; Van Deventer, J. S. J. The Effects of Inorganic Salt Contamination on the Strength and Durability of Geopolymers. *Colloids Surfaces A Physicochem. Eng. Asp.* **2002**, *211* (2–3), 115–126.
- (156) Kucche, K. J.; Jamkar, S. S.; Sadgir, P. A. Quality of Water for Making Concrete : A Review of Literature. *Int. J. Sci. Res. Publ.* **2015**, *5* (1), 1–10.
- (157) Wang, J.; Kalinichev, A. G.; Kirkpatrick, R. J. Effects of Substrate Structure and Composition on the Structure, Dynamics, and Energetics of Water at Mineral Surfaces: A Molecular Dynamics Modeling Study. *Geochim. Cosmochim. Acta* **2006**, *70* (3), 562–582.
- (158) Bourg, I. C.; Sposito, G. Molecular Dynamics Simulations of the Electrical Double Layer on Smectite Surfaces Contacting Concentrated Mixed Electrolyte (NaCl–CaCl<sub>2</sub>) Solutions. *J. Colloid Interface Sci.* **2011**, *360* (2), 701–715.
- (159) Liu, X.-D.; Lu, X.-C. A Thermodynamic Understanding of Clay-Swelling Inhibition by Potassium Ions. *Angew. Chemie Int. Ed.* **2006**, *45* (38), 6300–6303.

- (160) Greathouse, J. A.; Cygan, R. T. Water Structure and Aqueous Uranyl(VI) Adsorption Equilibria onto External Surfaces of Beidellite, Montmorillonite, and Pyrophyllite: Results from Molecular Simulations. *Environ. Sci. Technol.* **2006**, *40* (12), 3865–3871.
- (161) Stukowski, A. Visualization and Analysis of Atomistic Simulation Data with OVITO—the Open Visualization Tool. *Model. Simul. Mater. Sci. Eng.* **2010**, *18* (1), 15012.
- (162) Metz, B.; Davidson, O.; Coninck, H. de; Loos, M.; Meyer, L. *IPCC*; Cambridge University Press, UK. Available from Cambridge University Press, The Edinburgh Building Shaftesbury Road, Cambridge CB2 2RU ENGLAND, 2005.
- (163) Zhang, W.; Sun, C.; Snape, C. E.; Irons, R.; Stebbing, S.; Alderson, T.; Fitzgerald, D.; Liu, H. Process Simulations of Post-Combustion CO<sub>2</sub> Capture for Coal and Natural Gas-Fired Power Plants Using a Polyethyleneimine/silica Adsorbent. *Int. J. Greenh. Gas Control* **2017**, *58*, 276–289.
- (164) States, D. C. U. FETC Programs for Reducing Greenhouse Gas Emissions USDOE Federal Energy Technology Center , Pittsburgh , PA ( United States ). Funding Organisation : USDOE Assistant Secretary for Fossil. **1998**, *1*, 42.
- (165) Yong, Z.; Mata, V.; Rodrigues, E. Adsorption of Carbon Dioxide onto Hydrotalcite-like Compounds ( HTlcs ) at High Temperatures. *Ind. Eng. Chem. Res.* **2001**, *40*, 204–209.
- (166) Leung, D. Y. C.; Caramanna, G.; Maroto-Valer, M. M. An Overview of Current Status of Carbon Dioxide Capture and Storage Technologies. *Renew. Sustain. Energy Rev.* **2014**, *39*, 426–443.
- (167) Choi, S.; Drese, J. H.; Jones, C. W. Adsorbent Materials for Carbon Dioxide Capture from Large Anthropogenic Point Sources. *ChemSusChem* **2009**, *2*, 796–854.
- (168) Myshakin, E. M.; Saidi, W. A.; Romanov, V. N.; Cygan, R. T.; Jordan, K. D. Molecular Dynamics

- Simulations of Carbon Dioxide Intercalation in Hydrated Na-Montmorillonite. *J. Phys. Chem. C* **2013**, *117*, 11028–11039.
- (169) Allen, P. A.; Allen, J. R. *Basin Analysis: Principles and Applications*; Wiley-Blackwell: Malden, MA, 2005.
- (170) Yong, Z.; Rodrigues, E. Hydrotalcite-like Compounds as Adsorbents for Carbon Dioxide. *Energy Convers. Manag.* **2002**, *43*, 1865–1876.
- (171) Wang, J.; Kalinichev, A. G.; Amonette, J. E.; Kirkpatrick, R. J. Interlayer Structure and Dynamics of Cl-Bearing Hydrotalcite : Far Infrared Spectroscopy and Molecular Dynamics Modeling. *Am. Mineral.* **2003**, *88*, 398–409.
- (172) Cygan, R. T.; Greathouse, J. A.; Heinz, H.; Kalinichev, A. G. Molecular Models and Simulations of Layered Materials. *J. Mater. Chem.* **2009**, *19* (17), 2470–2481.
- (173) Forano, C.; Hibino, T.; Leroux, F.; Taviot-Guého, C. Layered Double Hydroxides. *Handb. Clay Sci. Dev. Clay Sci. Chapter 13.1* **2006**, *1*, 1021–1095.
- (174) Li, S. P.; Hou, W. G.; Han, S. H.; Li, L. F.; Zhao, W. A. Studies on Intrinsic Ionization Constants of Fe–Al–Mg Hydrotalcite-like Compounds. *J. Colloid Interface Sci.* **2003**, *257* (2), 244–249.
- (175) Cavani, F.; Trifirò, F.; Vaccari, A. Hydrotalcite-Type Anionic Clays: Preparation, Properties and Applications. *Catal. Today* **1991**, *11* (2), 173–301.
- (176) Fu, M. H.; Zhang, Z. Z.; Low, P. F. Changes in the Properties of a Montmorillonite-Water System during the Adsorption and Desorption of Water; Hysteresis. *Clays Clay Miner.* **1990**, *38* (5), 485 LP-492.
- (177) Wang, J.; Kalinichev, A. G.; Kirkpatrick, R. J.; Hou, X. Molecular Modeling of the Structure and

- Energetics of Hydrotalcite Hydration. *Chem. Mater.* **2001**, *13* (1), 145–150.
- (178) Ram Reddy, M. K.; Xu, Z. P.; Diniz da Costa, J. C. Influence of Water on High-Temperature CO<sub>2</sub> Capture Using Layered Double Hydroxide Derivatives. *Ind. Eng. Chem. Res.* **2008**, *47* (8), 2630–2635.
- (179) Oliveira, E. L. G.; Grande, C. A.; Rodrigues, E. CO<sub>2</sub> Sorption on Hydrotalcite and Alkali-Modified (K and Cs) Hydrotalcites at High Temperatures. *Sep. Purif. Technol.* **2008**, *62*, 137–147.
- (180) Lee, K. B.; Verdooren, A.; Caram, H. S.; Sircar, S. Chemisorption of Carbon Dioxide on Potassium-Carbonate-Promoted Hydrotalcite. *J. Colloid Interface Sci.* **2007**, *308*, 30–39.
- (181) Hufton, J. R.; Mayorga, S.; Sircar, S. Sorption-Enhanced Reaction Process for Hydrogen Production. *AIChE J.* **1999**, *45* (2), 248–256.
- (182) Kwak, J. H.; Hu, J. Z.; Turcu, R. V. F.; Rosso, K. M.; Ilton, E. S.; Wang, C.; Sears, J. A.; Engelhard, M. H.; Felmy, A. R.; Hoyt, D. W. The Role of H<sub>2</sub>O in the Carbonation of Forsterite in Supercritical CO<sub>2</sub>. *Int. J. Greenh. Gas Control* **2011**, *5* (4), 1081–1092.
- (183) Cygan, R. T.; Romanov, V. N.; Myshakin, E. M. Molecular Simulation of Carbon Dioxide Capture by Montmorillonite Using an Accurate and Flexible Force Field. *J. Phys. Chem. C* **2012**, *116* (24), 13079–13091.
- (184) Allen, M. P.; Tildesley, D. J. *Computer Simulation of Liquids*; Clarendon Press: Oxford, U.K., 1987.
- (185) Allmann, R.; Jepsen, H. P. Die Struktur Des Hydrotalkits. *Neues Jahrb. Miner. Monatsh* **1969**, *12*, 544–551.

# Appendix A

## Radial Distribution Function Graphs

The RDF graphs of 5 M Na<sup>+</sup> and 3 M K<sup>+</sup> systems containing different concentrations of CaCl<sub>2</sub> and MgCl<sub>2</sub> impurities are shown in Fig. A-1.

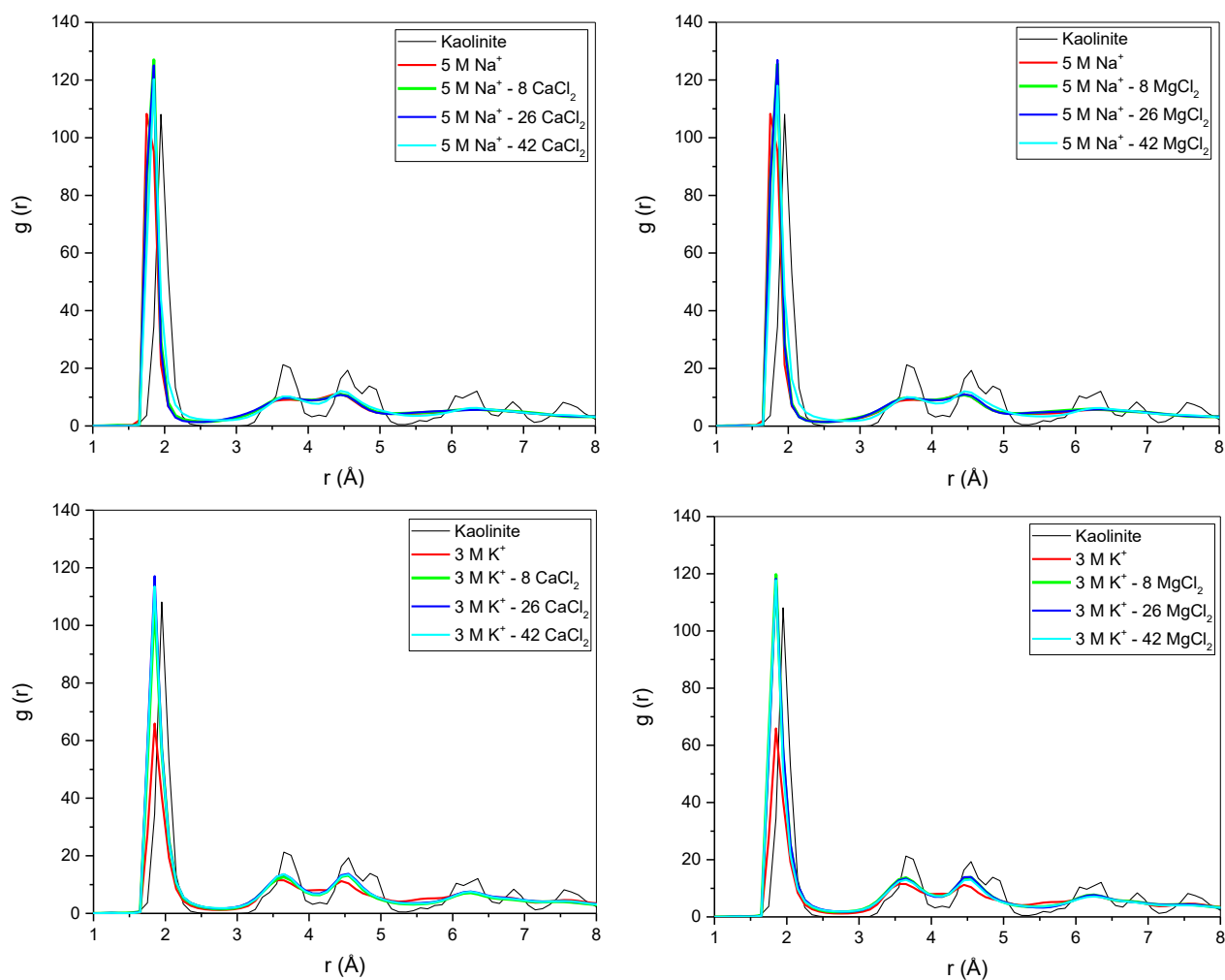


Figure A- 1 Radial distribution functions of Al – O of the octahedral surface for the systems of (a) 5 M Na<sup>+</sup> CaCl<sub>2</sub>, (b) 5 M Na<sup>+</sup> MgCl<sub>2</sub>, (c) 3 M K<sup>+</sup> CaCl<sub>2</sub> and (d) 3 M K<sup>+</sup> MgCl<sub>2</sub>.

# Atomic Density Profile

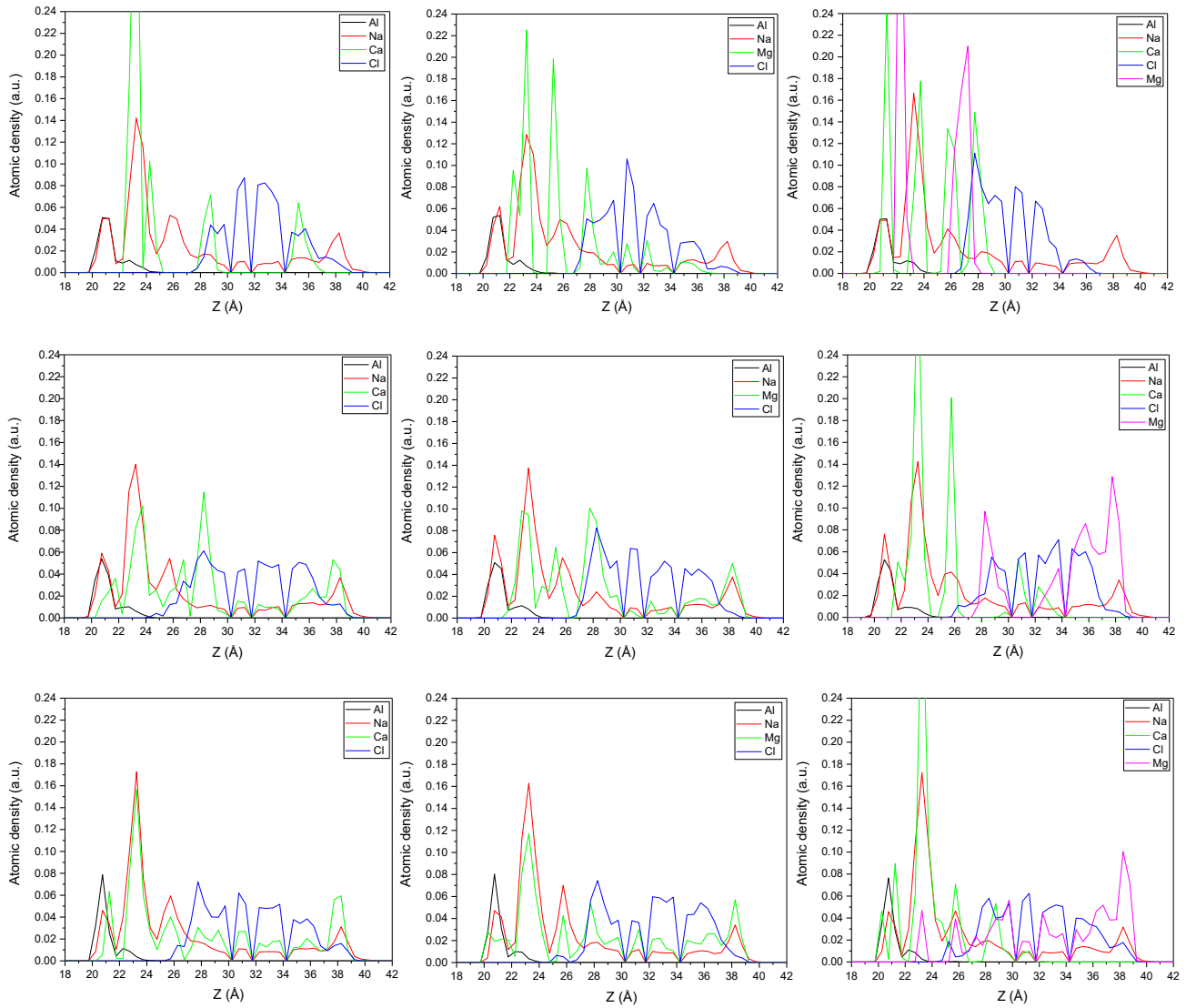


Figure A- 2 Atomic density profile of the 5 M Na<sup>+</sup> systems containing (a-c) CaCl<sub>2</sub> molecules, (d-f) MgCl<sub>2</sub> molecules and (g-i) CaCl<sub>2</sub>+MgCl<sub>2</sub> molecules.

# Appendix B

## Atomic Density Profile

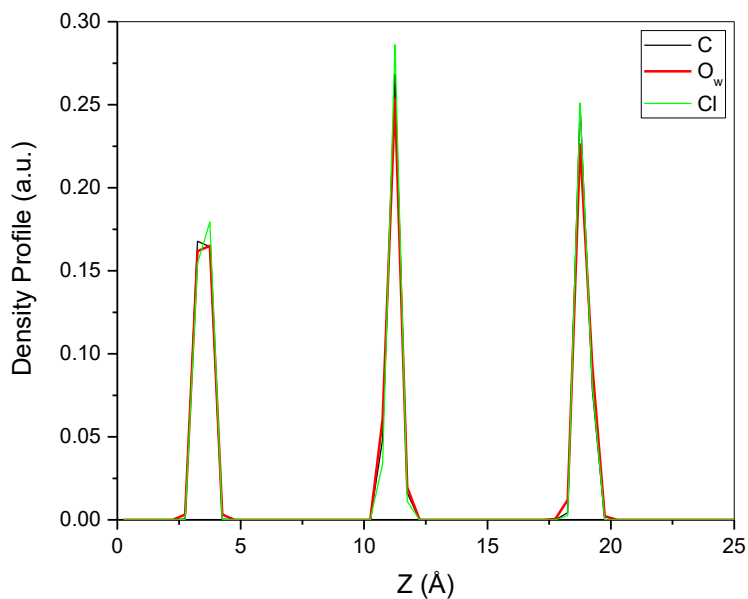


Figure B- 1 Atomic density profiles of interlayer H<sub>2</sub>O and CO<sub>2</sub> in the simulation cell along the z dimension (perpendicular to the mineral surface) for the system containing 36 CO<sub>2</sub> and 36 H<sub>2</sub>O.

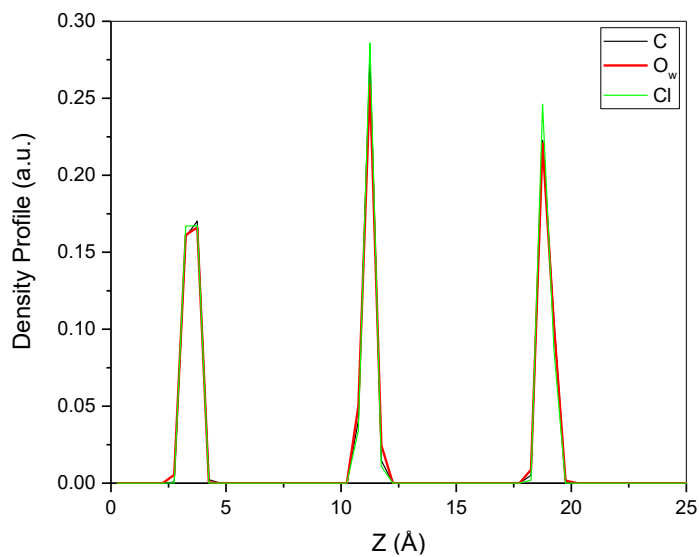


Figure B- 2 Atomic density profiles of interlayer H<sub>2</sub>O and CO<sub>2</sub> in the simulation cell along the z dimension (perpendicular to the mineral surface) for the system containing 84 CO<sub>2</sub> and 36 H<sub>2</sub>O.

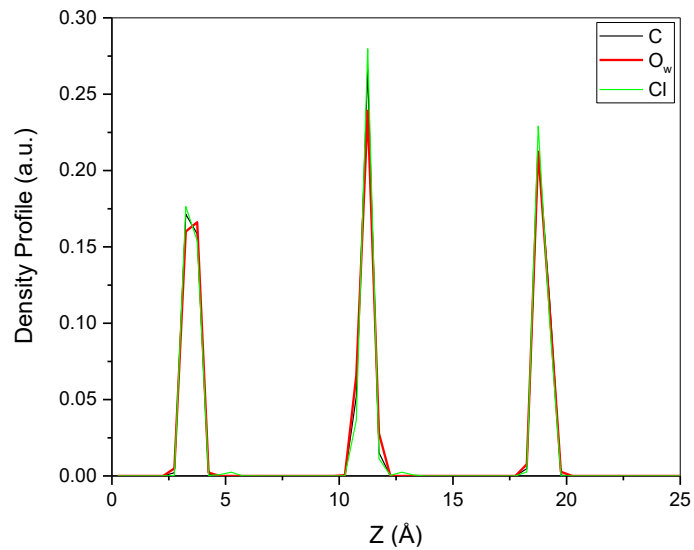


Figure B- 3 Atomic density profiles of interlayer H<sub>2</sub>O and CO<sub>2</sub> in the simulation cell along the z dimension (perpendicular to the mineral surface) for the system containing 120 CO<sub>2</sub> and 36 H<sub>2</sub>O.

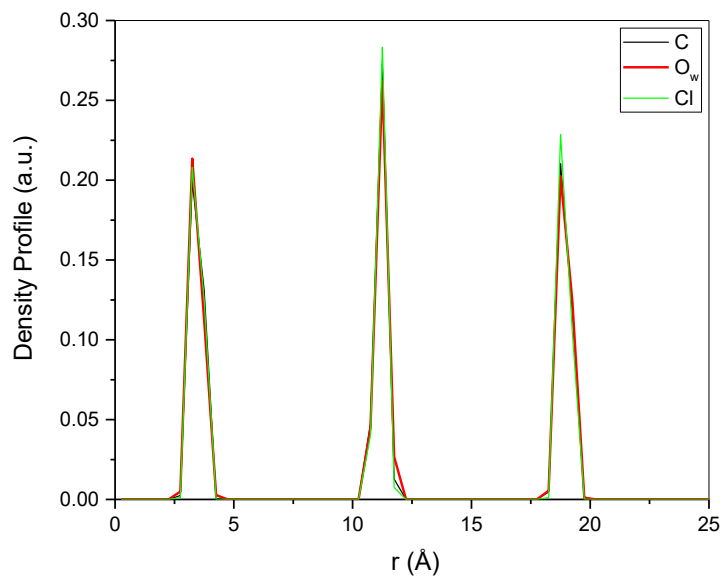


Figure B- 4 Atomic density profiles of interlayer H<sub>2</sub>O and CO<sub>2</sub> in the simulation cell along the z dimension (perpendicular to the mineral surface) for the system containing 216 CO<sub>2</sub> and 36 H<sub>2</sub>O.

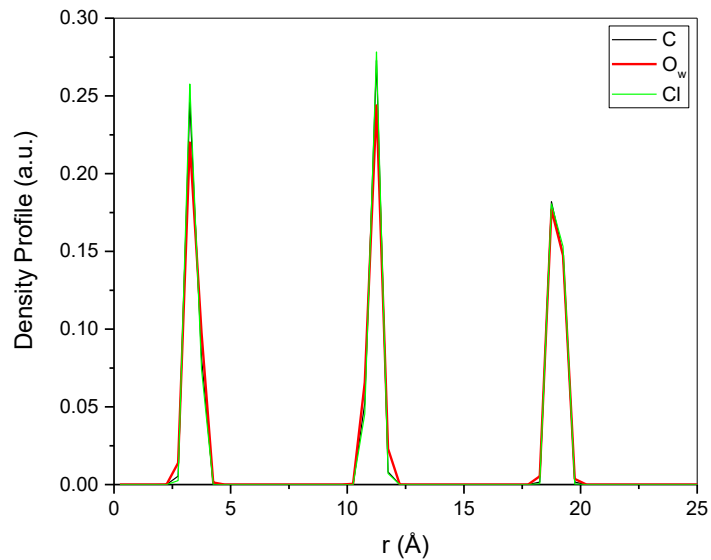


Figure B- 5 Atomic density profiles of interlayer H<sub>2</sub>O and CO<sub>2</sub> in the simulation cell along the z dimension (perpendicular to the mineral surface) for the system containing 432 CO<sub>2</sub> and 36 H<sub>2</sub>O.

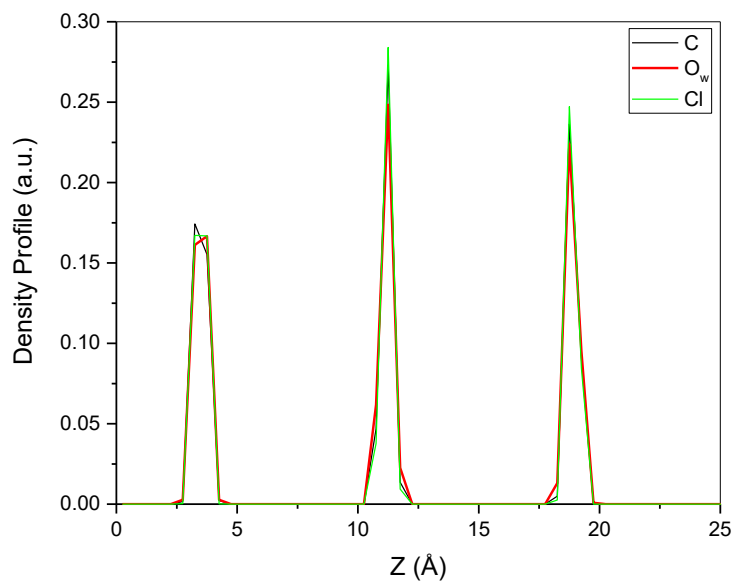


Figure B- 6 Atomic density profiles of interlayer H<sub>2</sub>O and CO<sub>2</sub> in the simulation cell along the z dimension (perpendicular to the mineral surface) for the system containing 36 CO<sub>2</sub> and 72 H<sub>2</sub>O.

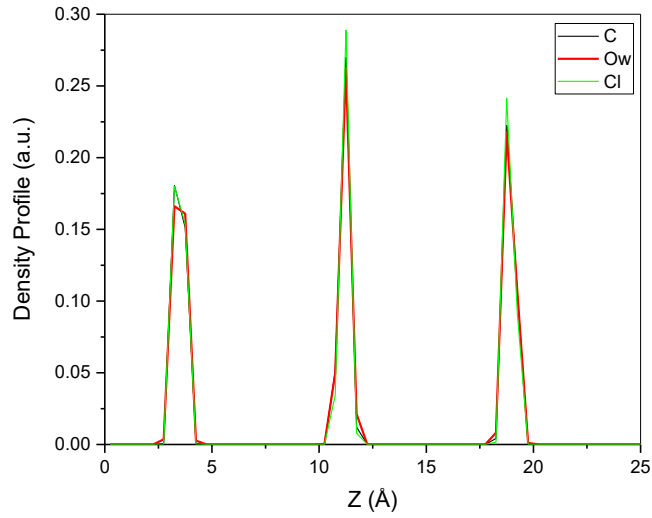


Figure B- 7 Atomic density profiles of interlayer H<sub>2</sub>O and CO<sub>2</sub> in the simulation cell along the z dimension (perpendicular to the mineral surface) for the system containing 84 CO<sub>2</sub> and 72 H<sub>2</sub>O.

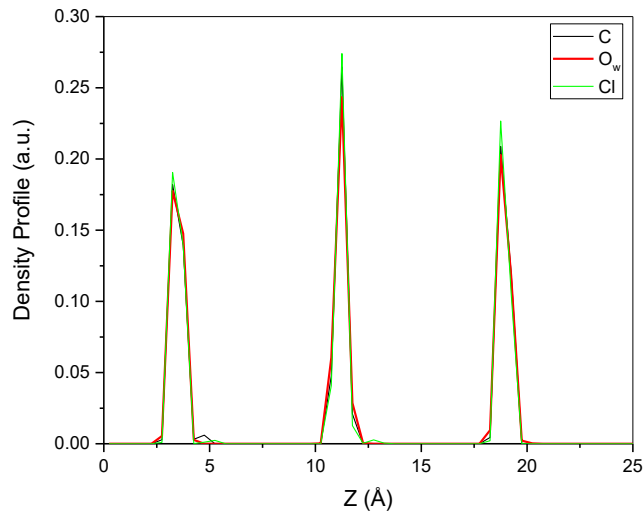


Figure B- 8 Atomic density profiles of interlayer H<sub>2</sub>O and CO<sub>2</sub> in the simulation cell along the z dimension (perpendicular to the mineral surface) for the system containing 120 CO<sub>2</sub> and 72 H<sub>2</sub>O.

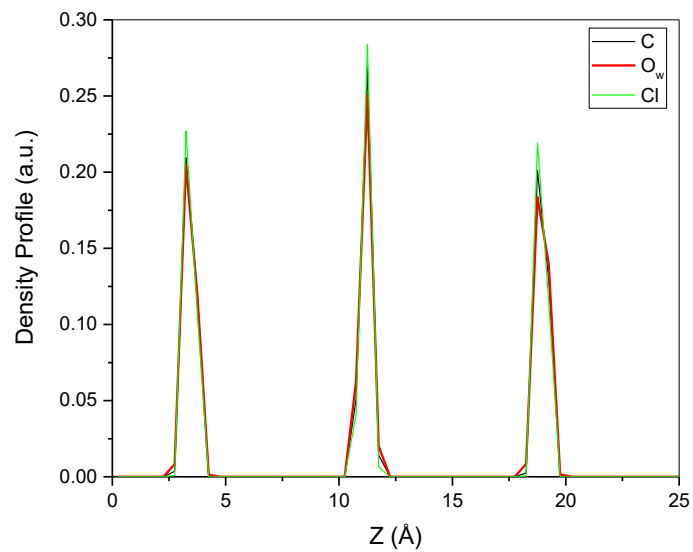


Figure B- 9 Atomic density profiles of interlayer H<sub>2</sub>O and CO<sub>2</sub> in the simulation cell along the z dimension (perpendicular to the mineral surface) for the system containing 216 CO<sub>2</sub> and 72 H<sub>2</sub>O.

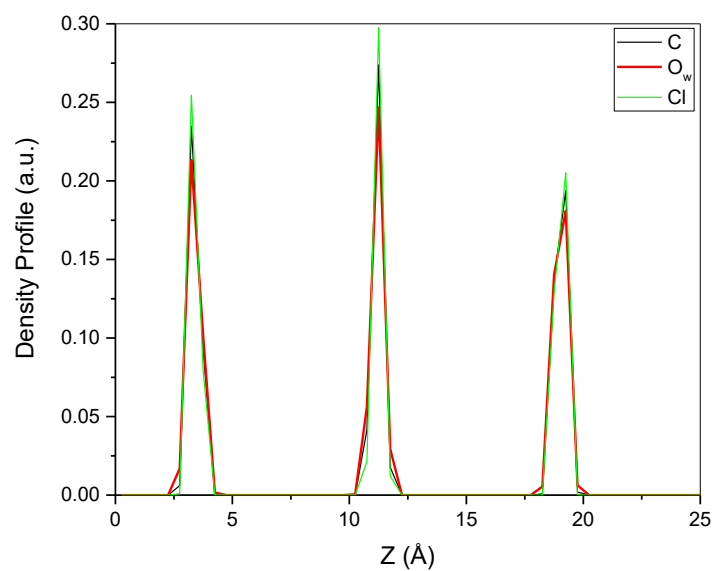


Figure B- 10 Atomic density profiles of interlayer H<sub>2</sub>O and CO<sub>2</sub> in the simulation cell along the z dimension (perpendicular to the mineral surface) for the system containing 432 CO<sub>2</sub> and 72 H<sub>2</sub>O.

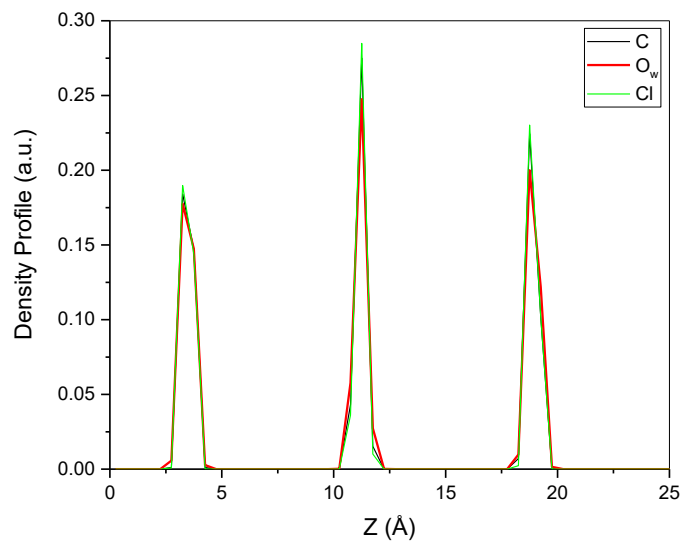


Figure B- 11 Atomic density profiles of interlayer H<sub>2</sub>O and CO<sub>2</sub> in the simulation cell along the z dimension (perpendicular to the mineral surface) for the system containing 36 CO<sub>2</sub> and 144 H<sub>2</sub>O.

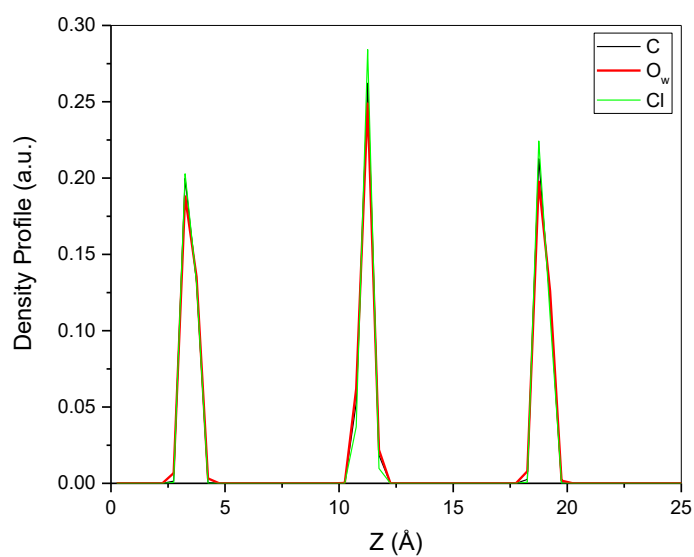


Figure B- 12 Atomic density profiles of interlayer H<sub>2</sub>O and CO<sub>2</sub> in the simulation cell along the z dimension (perpendicular to the mineral surface) for the system containing 84 CO<sub>2</sub> and 144 H<sub>2</sub>O.

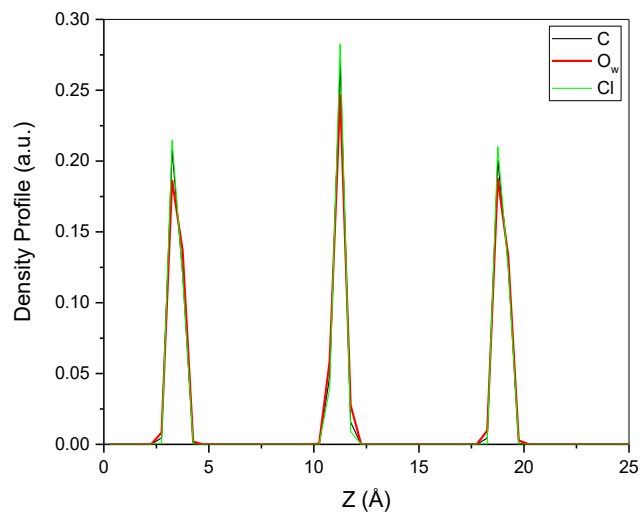


Figure B- 13 Atomic density profiles of interlayer H<sub>2</sub>O and CO<sub>2</sub> in the simulation cell along the z dimension (perpendicular to the mineral surface) for the system containing 120 CO<sub>2</sub> and 144 H<sub>2</sub>O.

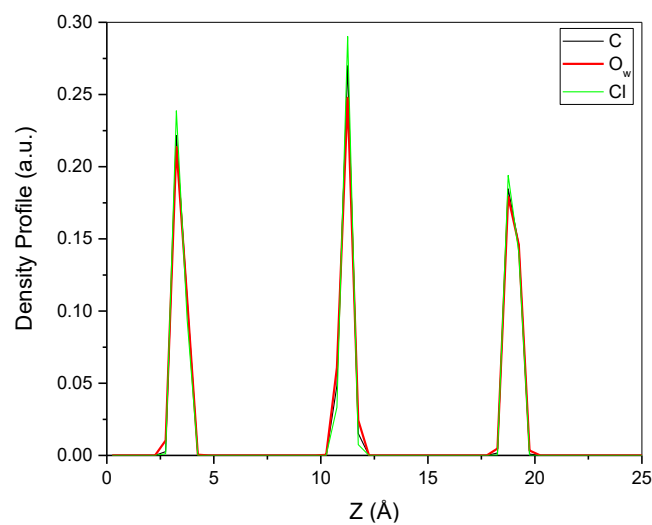


Figure B- 14 Atomic density profiles of interlayer H<sub>2</sub>O and CO<sub>2</sub> in the simulation cell along the z dimension (perpendicular to the mineral surface) for the system containing 216 CO<sub>2</sub> and 144 H<sub>2</sub>O.

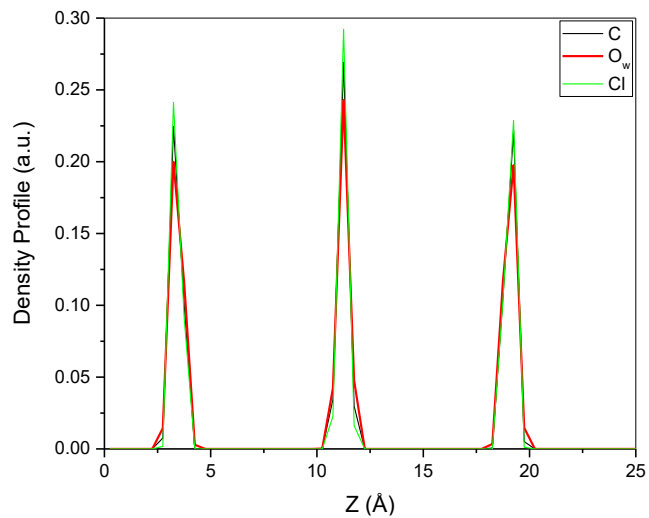


Figure B- 15 Atomic density profiles of interlayer H<sub>2</sub>O and CO<sub>2</sub> in the simulation cell along the z dimension (perpendicular to the mineral surface) for the system containing 432 CO<sub>2</sub> and 144 H<sub>2</sub>O.

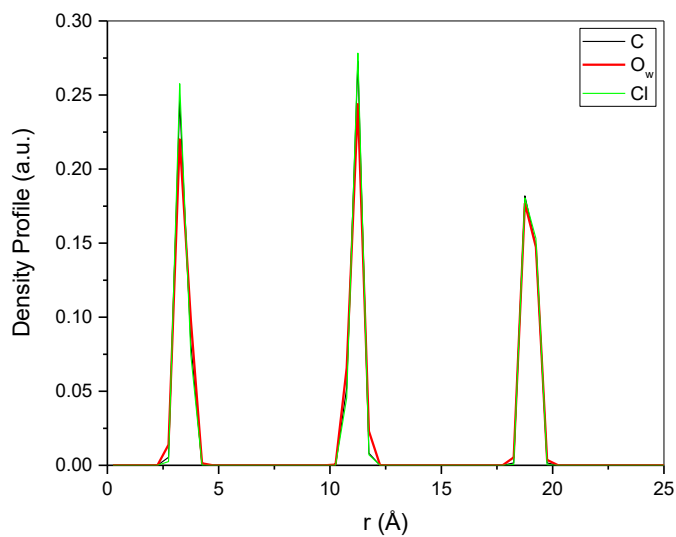


Figure B- 16 Atomic density profiles of interlayer H<sub>2</sub>O and CO<sub>2</sub> in the simulation cell along the z dimension (perpendicular to the mineral surface) for the system containing 36 CO<sub>2</sub> and 432 H<sub>2</sub>O.

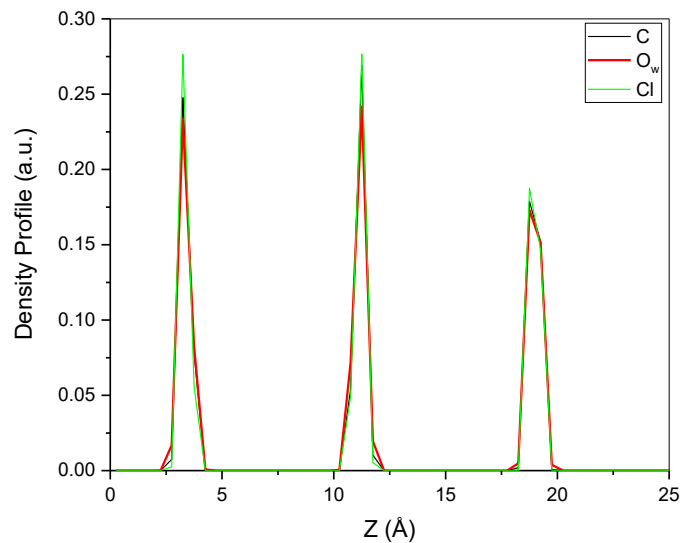


Figure B- 17 Atomic density profiles of interlayer H<sub>2</sub>O and CO<sub>2</sub> in the simulation cell along the z dimension (perpendicular to the mineral surface) for the system containing 84 CO<sub>2</sub> and 432 H<sub>2</sub>O.

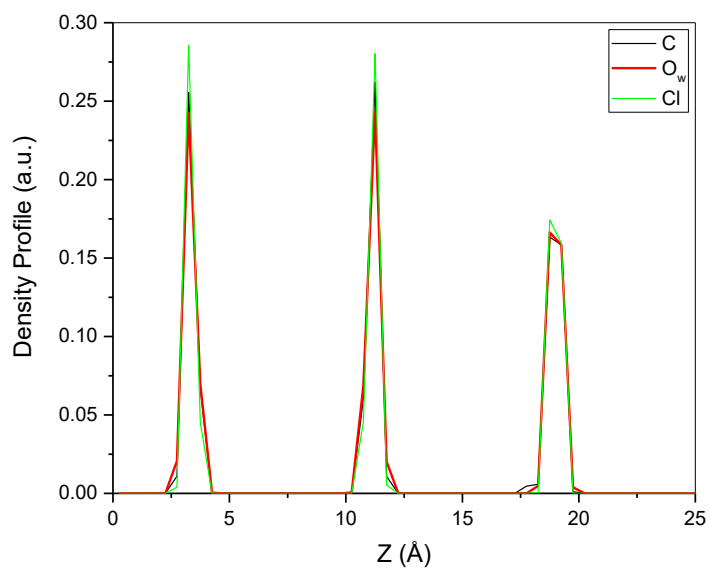


Figure B- 18 Atomic density profiles of interlayer H<sub>2</sub>O and CO<sub>2</sub> in the simulation cell along the z dimension (perpendicular to the mineral surface) for the system containing 120 CO<sub>2</sub> and 432 H<sub>2</sub>O.

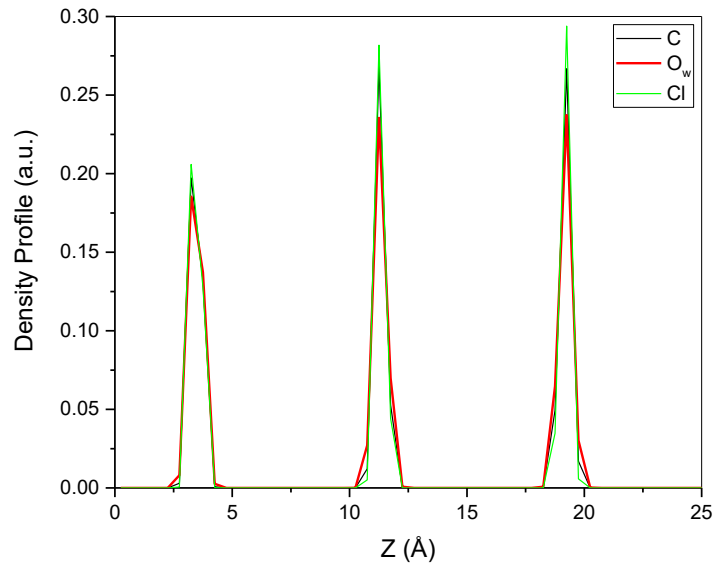


Figure B- 19 Atomic density profiles of interlayer H<sub>2</sub>O and CO<sub>2</sub> in the simulation cell along the z dimension (perpendicular to the mineral surface) for the system containing 216 CO<sub>2</sub> and 432 H<sub>2</sub>O.

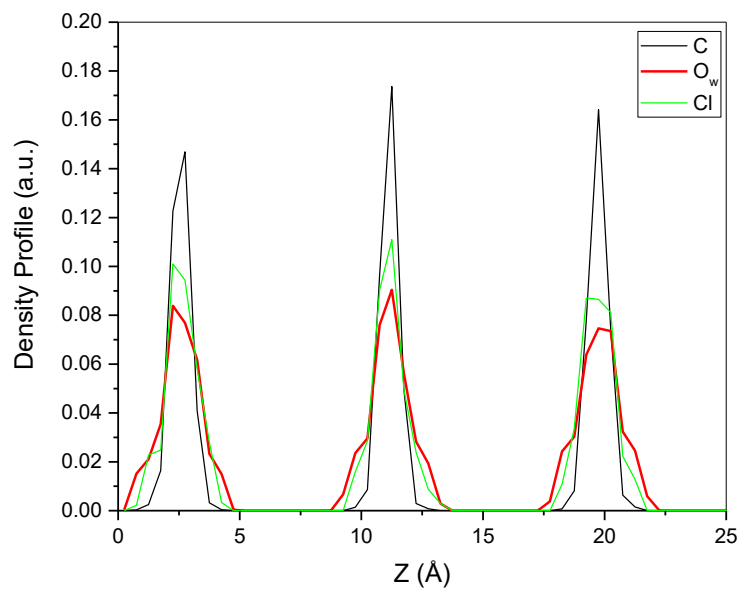


Figure B- 20 Atomic density profiles of interlayer H<sub>2</sub>O and CO<sub>2</sub> in the simulation cell along the z dimension (perpendicular to the mineral surface) for the system containing 432 CO<sub>2</sub> and 432 H<sub>2</sub>O.

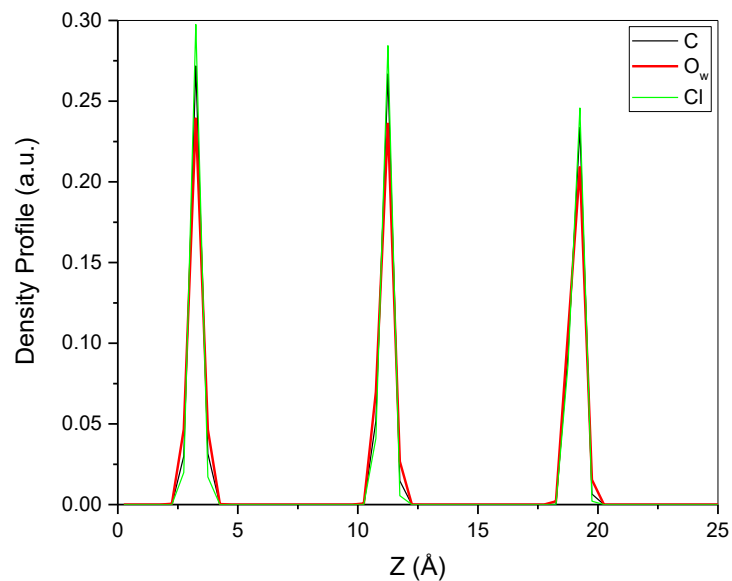


Figure B- 21 Atomic density profiles of interlayer H<sub>2</sub>O and CO<sub>2</sub> in the simulation cell along the z dimension (perpendicular to the mineral surface) for the system containing 36 CO<sub>2</sub> and 864 H<sub>2</sub>O.

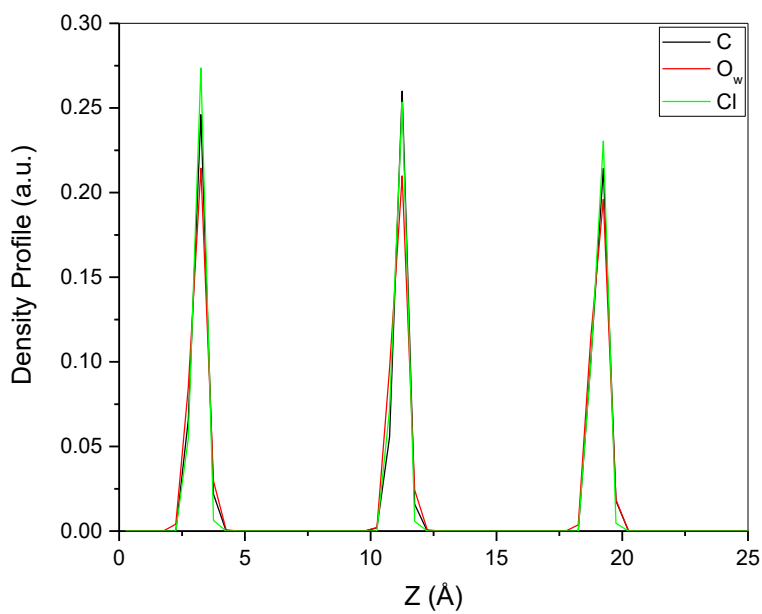


Figure B- 22 Atomic density profiles of interlayer H<sub>2</sub>O and CO<sub>2</sub> in the simulation cell along the z dimension (perpendicular to the mineral surface) for the system containing 84 CO<sub>2</sub> and 864 H<sub>2</sub>O.

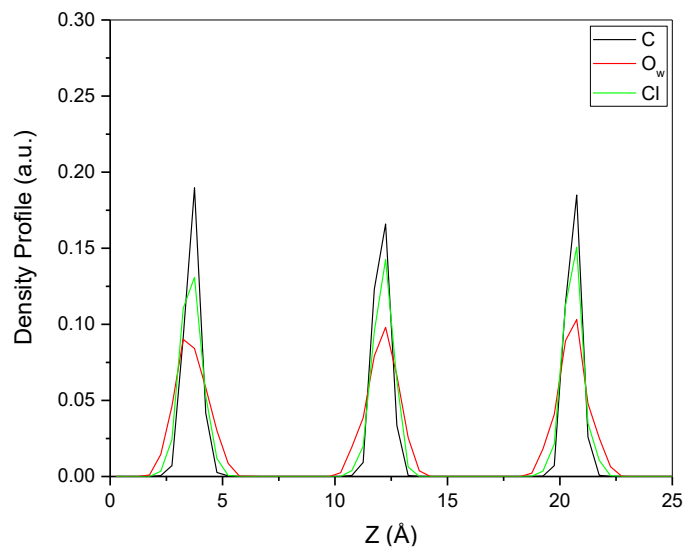


Figure B- 23 Atomic density profiles of interlayer H<sub>2</sub>O and CO<sub>2</sub> in the simulation cell along the z dimension (perpendicular to the mineral surface) for the system containing 216 CO<sub>2</sub> and 864 H<sub>2</sub>O.

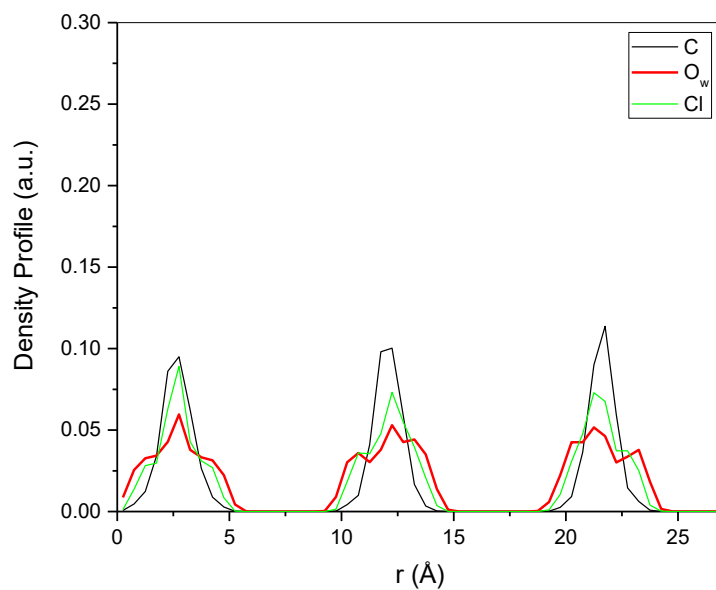


Figure B- 24 Atomic density profiles of interlayer H<sub>2</sub>O and CO<sub>2</sub> in the simulation cell along the z dimension (perpendicular to the mineral surface) for the system containing 432 CO<sub>2</sub> and 864 H<sub>2</sub>O.

# Radial Distribution Function Graphs

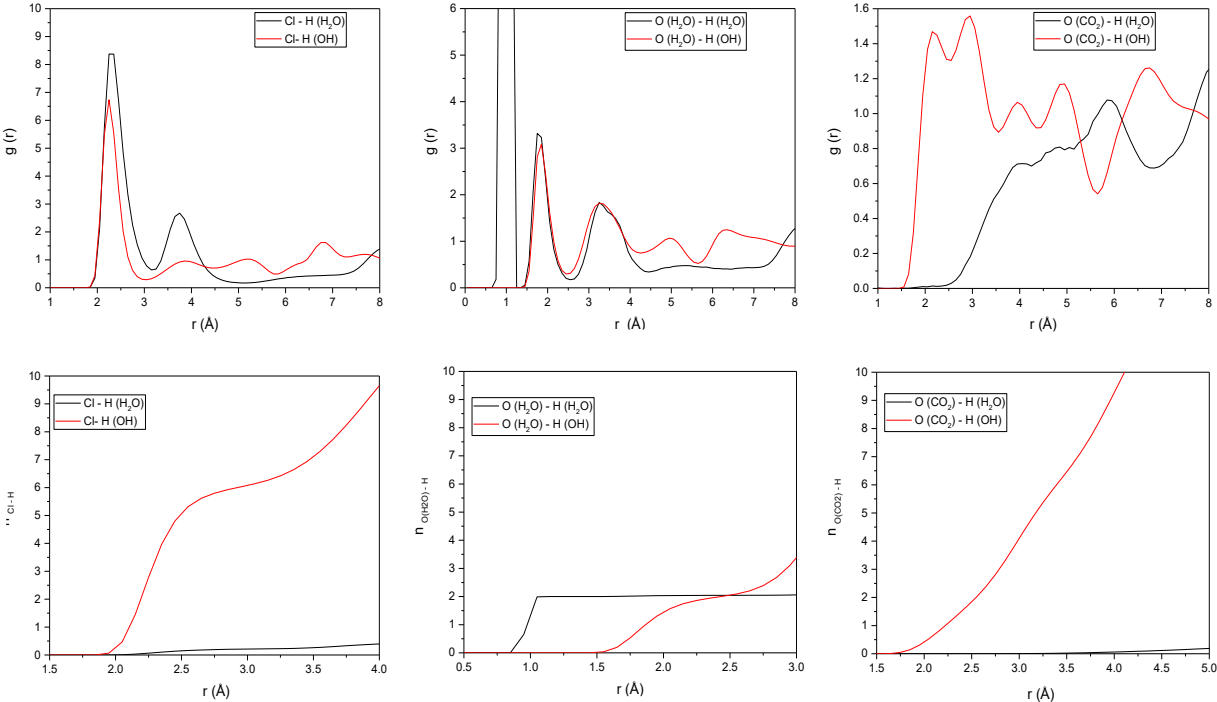


Figure B- 25 Pair Radial distribution functions and integrated nearest-neighbor coordination numbers for Cl<sup>-</sup> - H pairs and O (H<sub>2</sub>O) - H pairs and O (CO<sub>2</sub>) - H pairs in the interlayer of Mg/Al Cl<sup>-</sup> - hydrocalcite computed from MD simulations. There are 36 CO<sub>2</sub> and 36 H<sub>2</sub>O in the interlayer region.

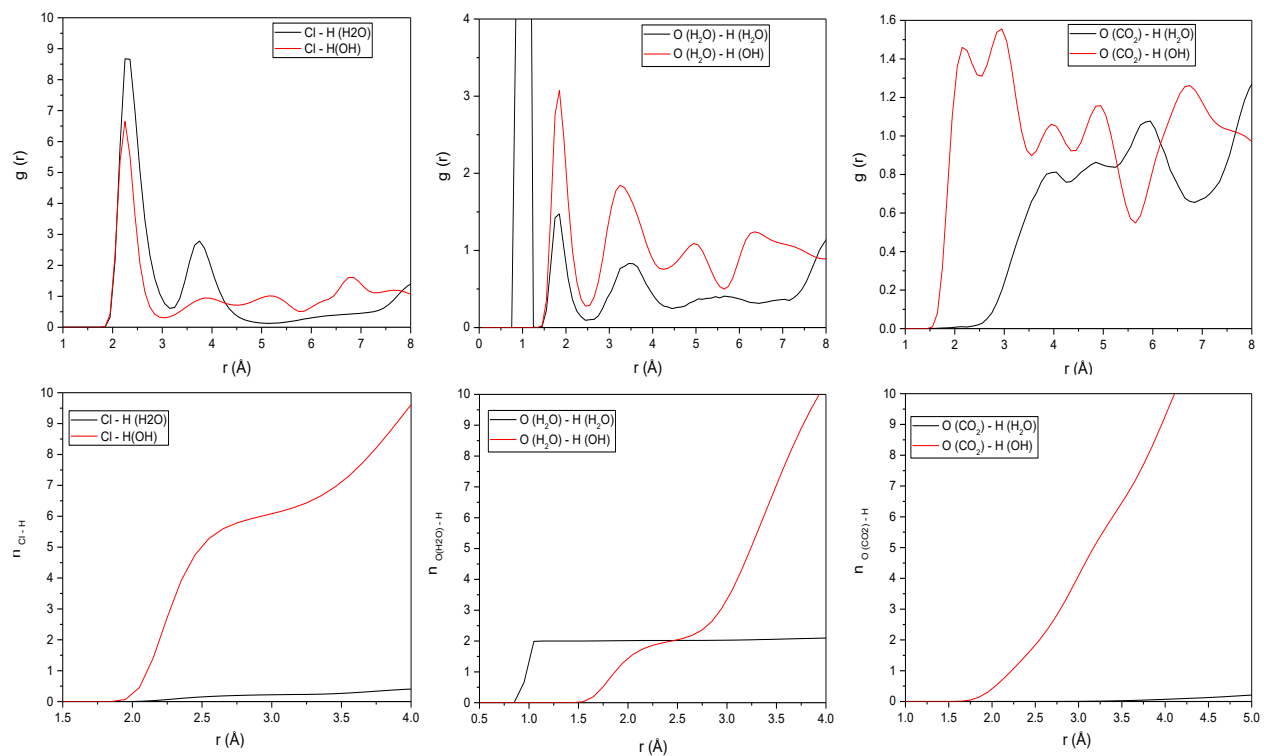


Figure B- 26 Pair Radial distribution functions and integrated nearest-neighbor coordination numbers for Cl<sup>-</sup> - H pairs and O (H<sub>2</sub>O) - H pairs and O (CO<sub>2</sub>) - H pairs in the interlayer of Mg/Al Cl<sup>-</sup> hydroxalcite computed from MD simulations. There are 84 CO<sub>2</sub> and 36 H<sub>2</sub>O in the interlayer region.

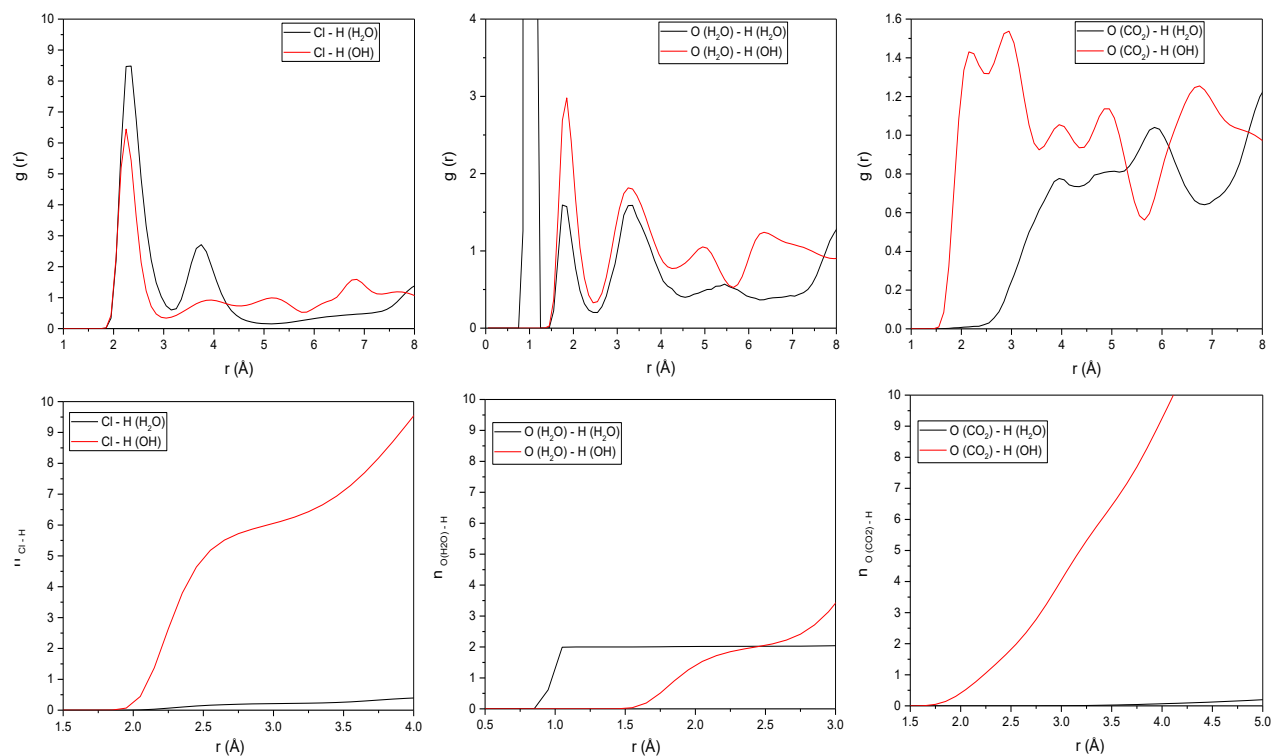


Figure B- 27 Pair Radial distribution functions and integrated nearest-neighbor coordination numbers for Cl<sup>-</sup> - H pairs and O (H<sub>2</sub>O) - H pairs and O (CO<sub>2</sub>) - H pairs in the interlayer of Mg/Al Cl<sup>-</sup> hydroxalcite computed from MD simulations. There are 120 CO<sub>2</sub> and 36 H<sub>2</sub>O in the interlayer region.

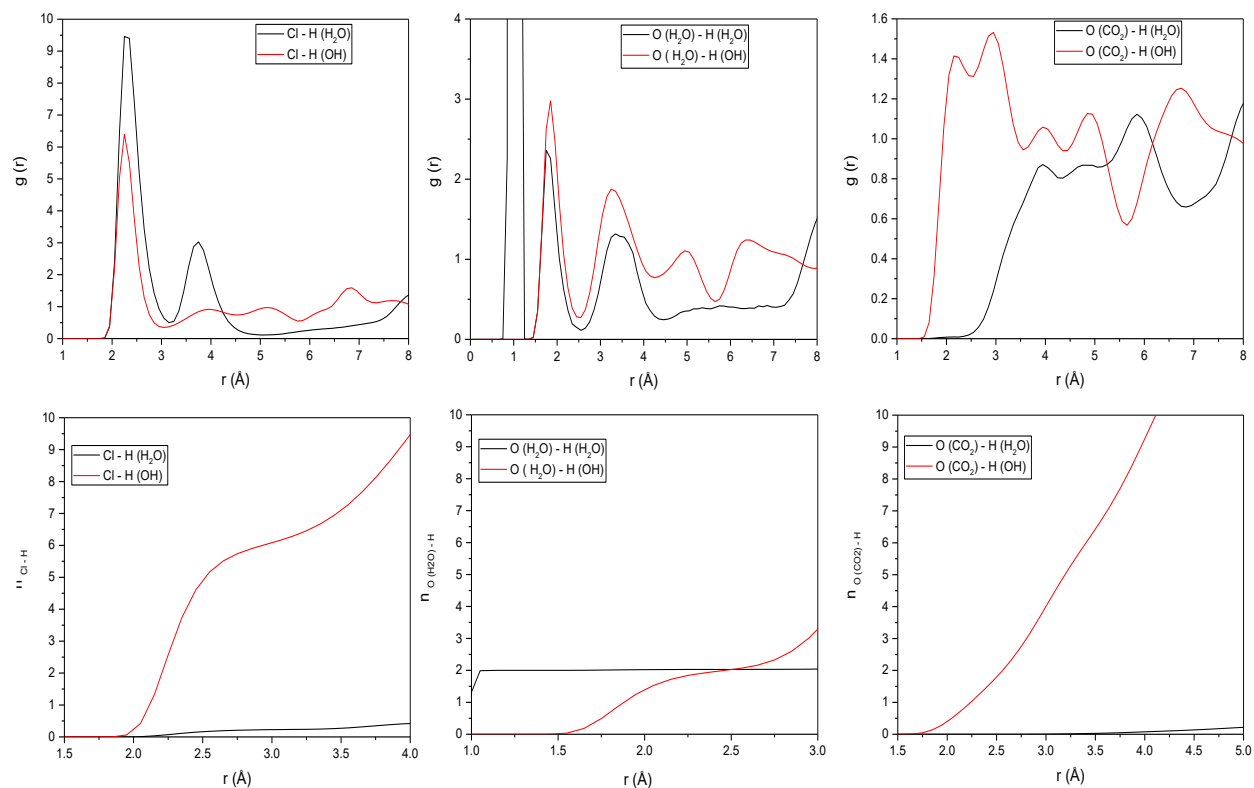


Figure B- 28 Pair Radial distribution functions and integrated nearest-neighbor coordination numbers for Cl<sup>-</sup> - H pairs and O (H<sub>2</sub>O) - H pairs and O (CO<sub>2</sub>) - H pairs in the interlayer of Mg/Al Cl<sup>-</sup> hydroxalcite computed from MD simulations. There are 216 CO<sub>2</sub> and 36 H<sub>2</sub>O in the interlayer region.

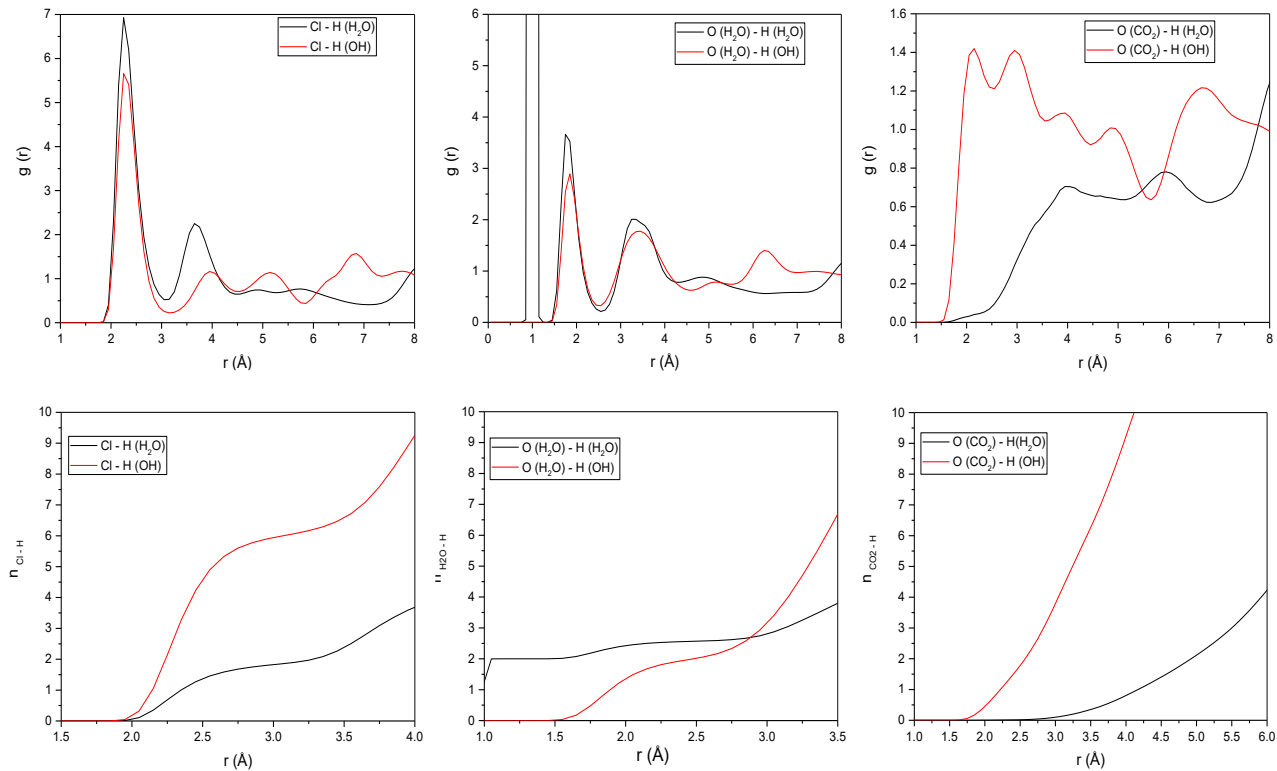


Figure B- 29 Pair Radial distribution functions and integrated nearest-neighbor coordination numbers for Cl<sup>-</sup> - H pairs and O (H<sub>2</sub>O) - H pairs and O (CO<sub>2</sub>) - H pairs in the interlayer of Mg/Al Cl<sup>-</sup> hydrotalcite computed from MD simulations. There are 432 CO<sub>2</sub> and 36 H<sub>2</sub>O in the interlayer region.

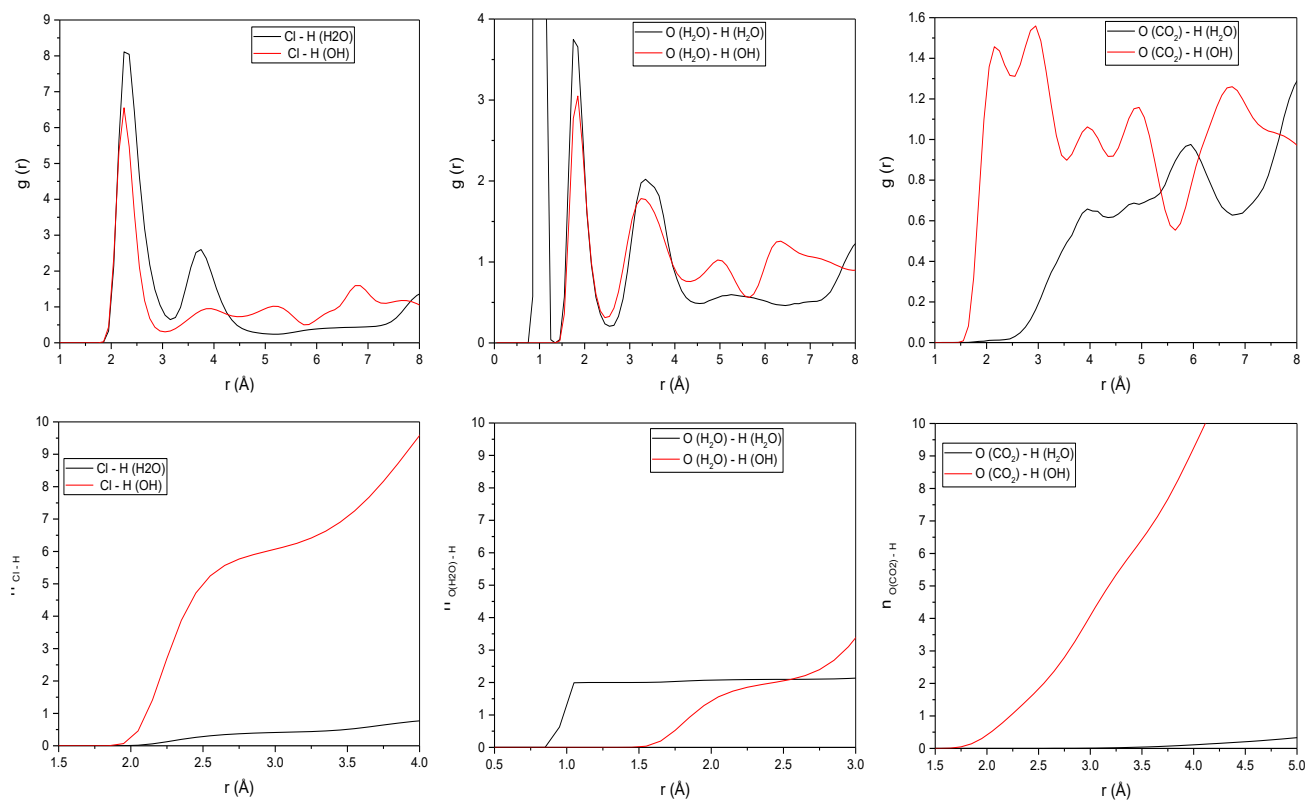


Figure B- 30 Pair Radial distribution functions and integrated nearest-neighbor coordination numbers for Cl<sup>-</sup> - H pairs and O (H<sub>2</sub>O) - H pairs and O (CO<sub>2</sub>) - H pairs in the interlayer of Mg/Al Cl<sup>-</sup> - hydrocalcite computed from MD simulations. There are 36 CO<sub>2</sub> and 72 H<sub>2</sub>O in the interlayer region.

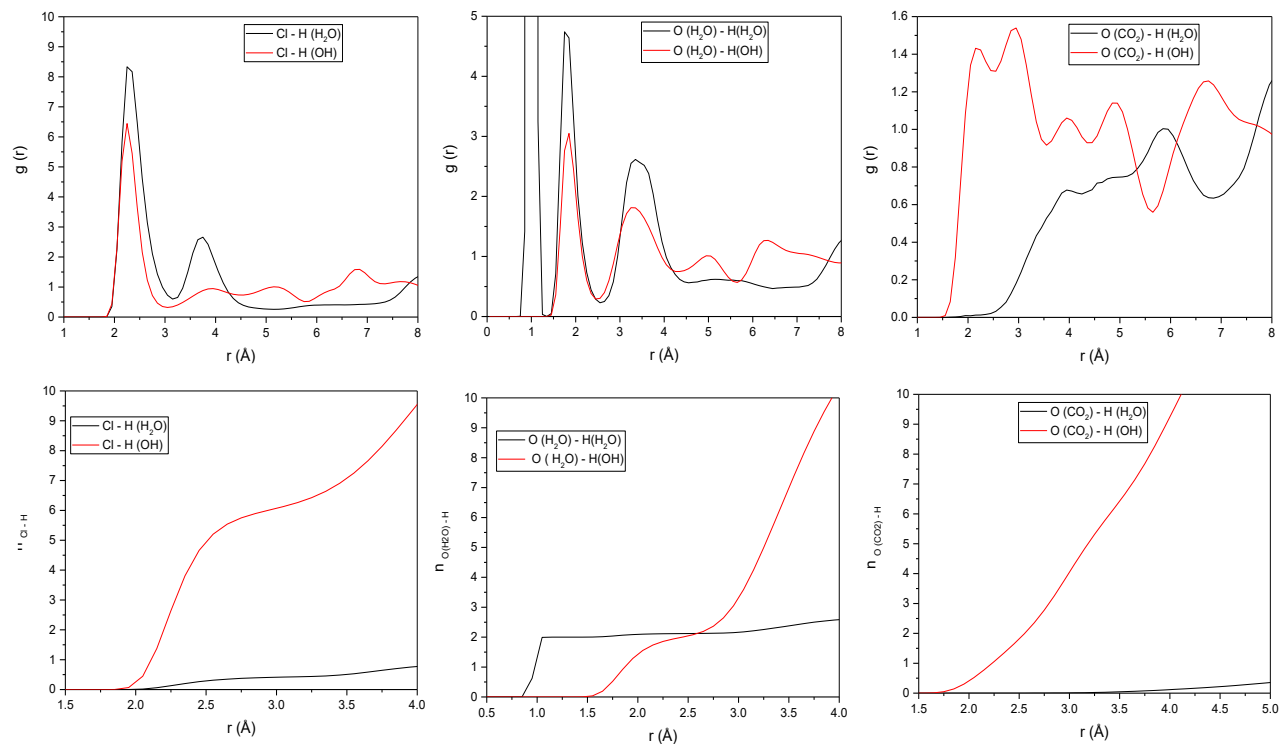


Figure B- 31 Pair Radial distribution functions and integrated nearest-neighbor coordination numbers for Cl<sup>-</sup> - H pairs and O (H<sub>2</sub>O) - H pairs and O (CO<sub>2</sub>) - H pairs in the interlayer of Mg/Al Cl<sup>-</sup> hydrotalcite computed from MD simulations. There are 84 CO<sub>2</sub> and 72 H<sub>2</sub>O in the interlayer region.

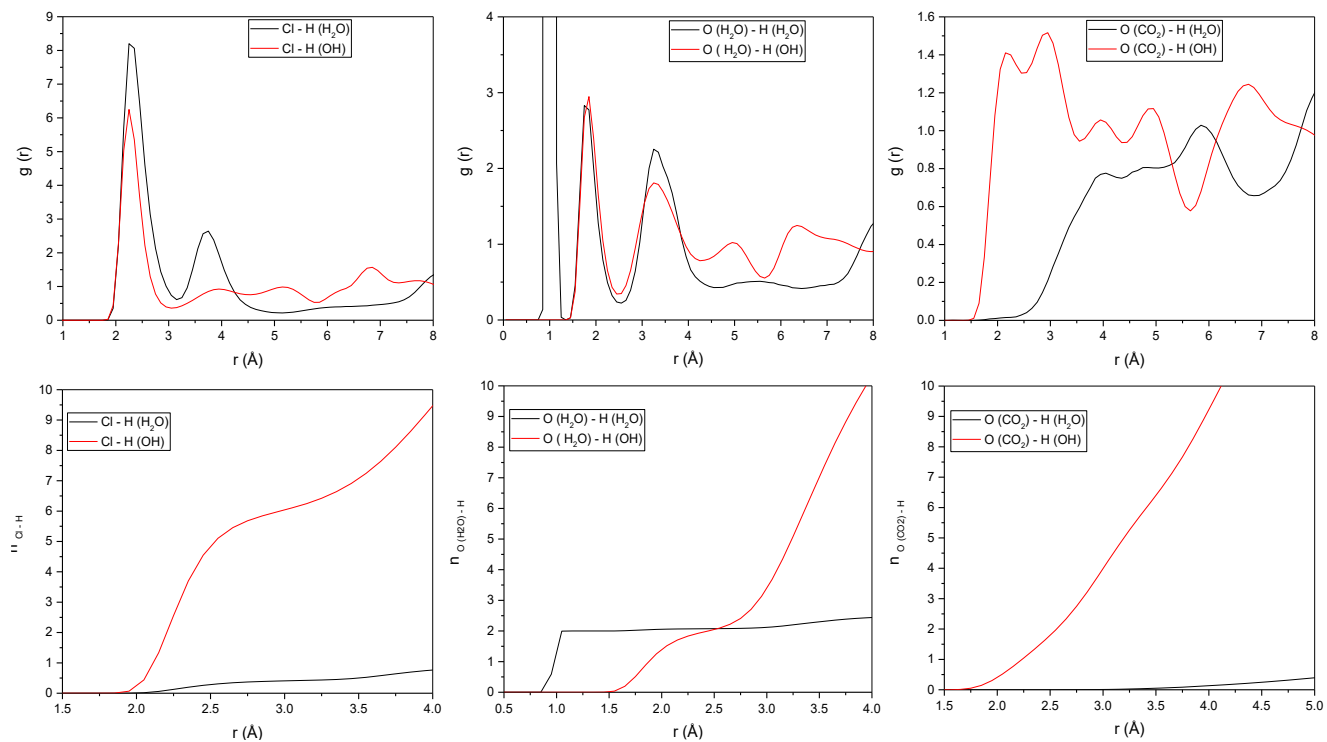


Figure B- 32 Pair Radial distribution functions and integrated nearest-neighbor coordination numbers for  $\text{Cl}^-$  - H pairs and O ( $\text{H}_2\text{O}$ ) - H pairs and O ( $\text{CO}_2$ ) - H pairs in the interlayer of Mg/Al  $\text{Cl}^-$  - hydrotalcite computed from MD simulations. There are 120  $\text{CO}_2$  and 72  $\text{H}_2\text{O}$  in the interlayer region.

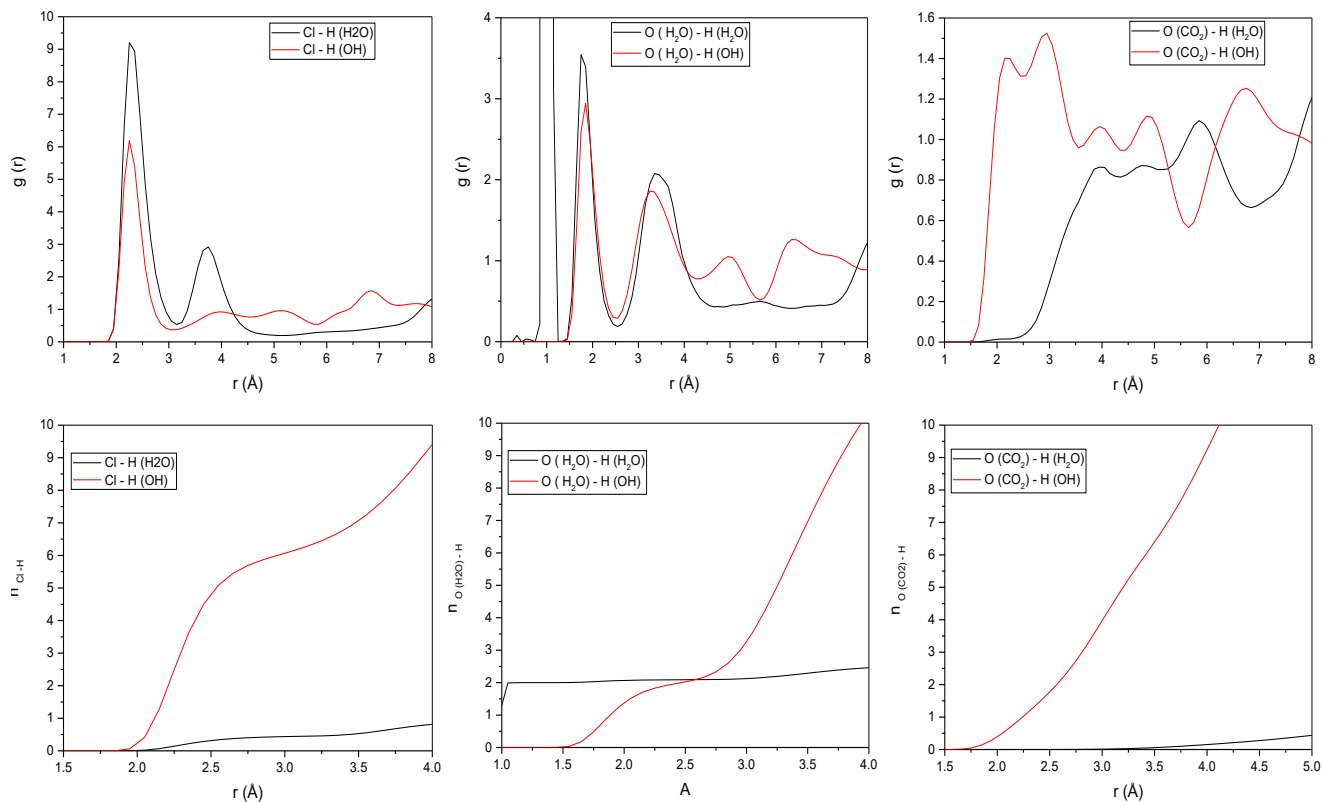


Figure B- 33 Pair Radial distribution functions and integrated nearest-neighbor coordination numbers for Cl<sup>-</sup> - H pairs and O (H<sub>2</sub>O) - H pairs and O (CO<sub>2</sub>) - H pairs in the interlayer of Mg/Al Cl<sup>-</sup> hydrotalcite computed from MD simulations. There are 216 CO<sub>2</sub> and 72 H<sub>2</sub>O in the interlayer region.

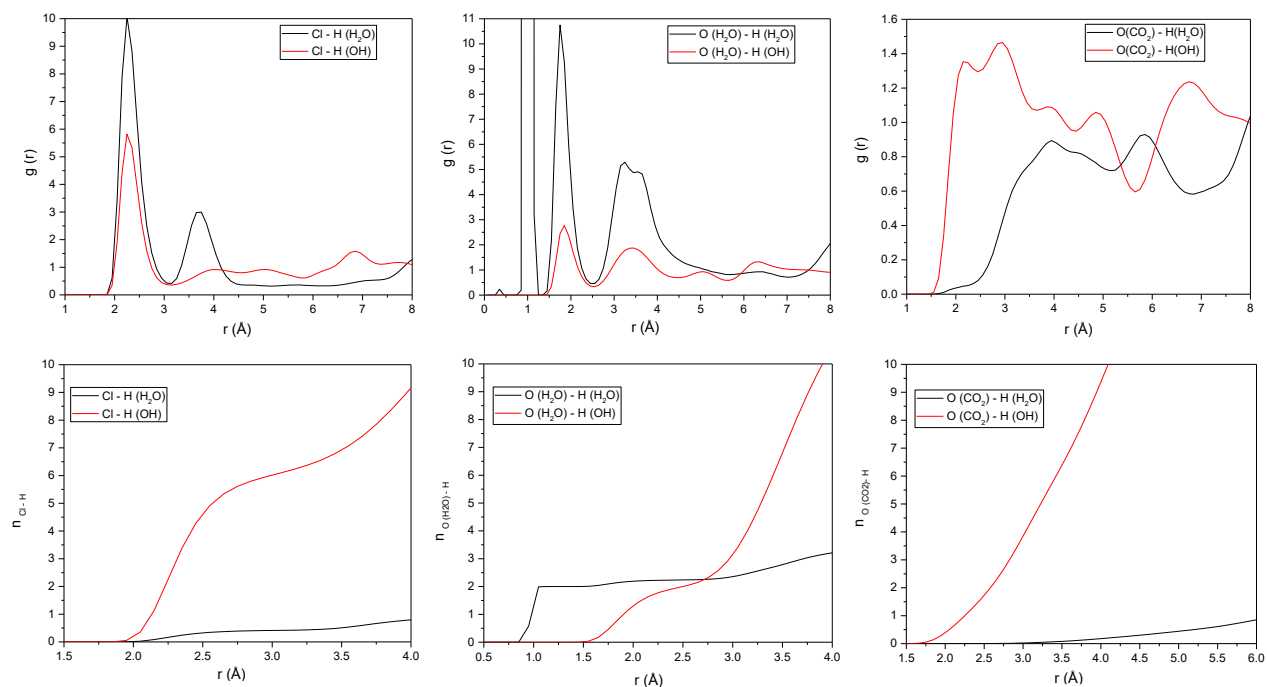


Figure B- 34 Pair Radial distribution functions and integrated nearest-neighbor coordination numbers for Cl<sup>-</sup> - H pairs and O (H<sub>2</sub>O) - H pairs and O (CO<sub>2</sub>) - H pairs in the interlayer of Mg/Al Cl<sup>-</sup> hydrotalcite computed from MD simulations. There are 432 CO<sub>2</sub> and 72 H<sub>2</sub>O in the interlayer region.

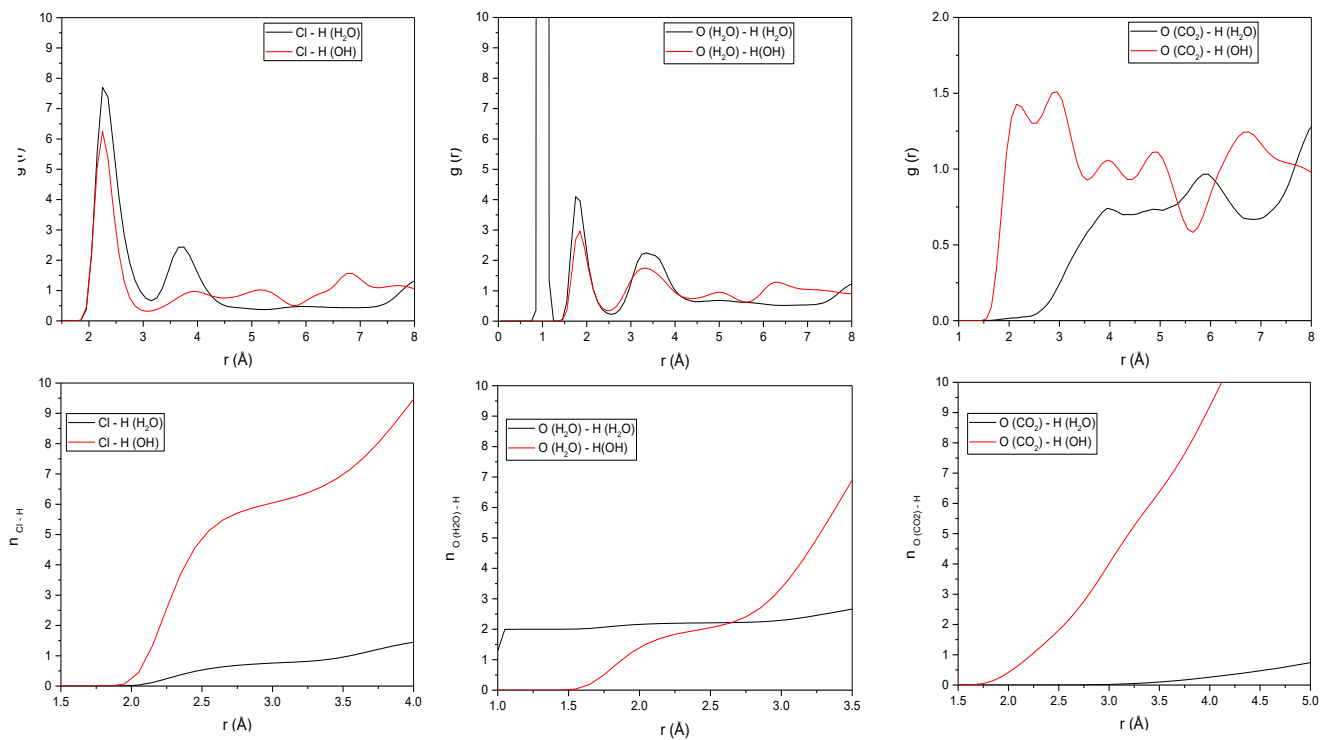


Figure B- 35 Pair Radial distribution functions and integrated nearest-neighbor coordination numbers for Cl<sup>-</sup> - H pairs and O (H<sub>2</sub>O) - H pairs and O (CO<sub>2</sub>) - H pairs in the interlayer of Mg/Al Cl<sup>-</sup> hydrotalcite computed from MD simulations. There are 36 CO<sub>2</sub> and 144 H<sub>2</sub>O in the interlayer region.

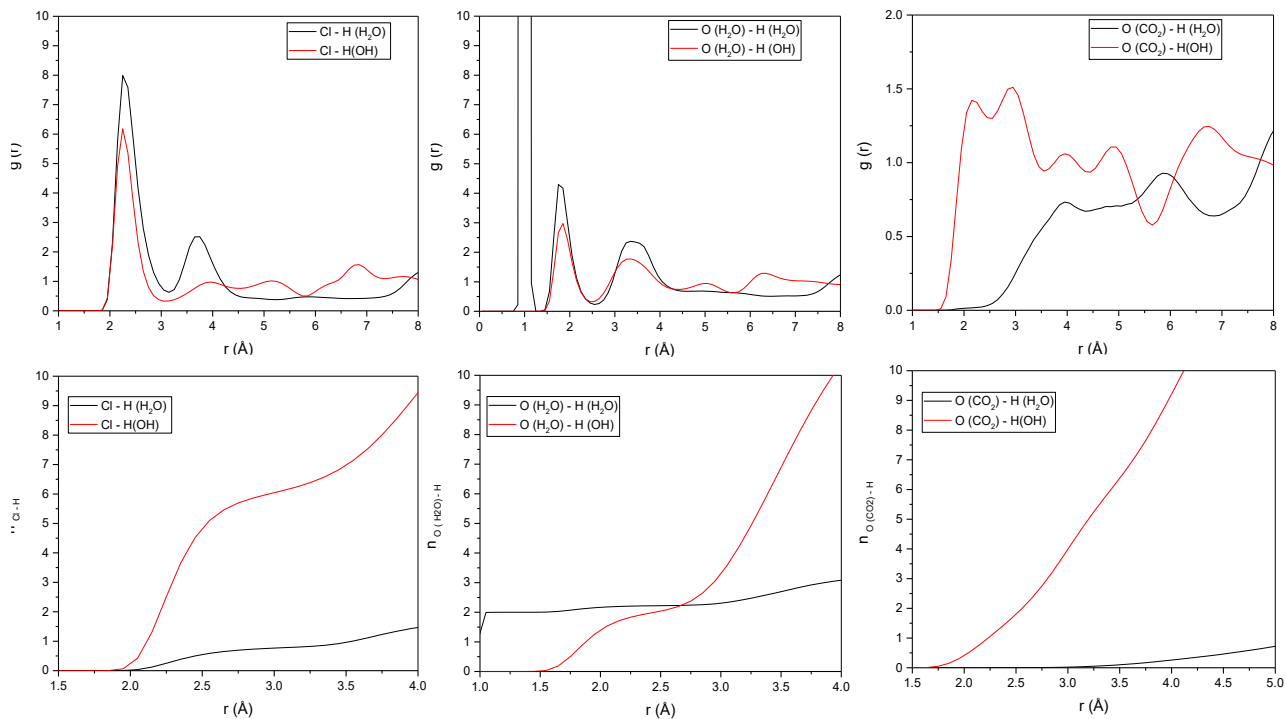


Figure B- 36 Pair Radial distribution functions and integrated nearest-neighbor coordination numbers for  $\text{Cl}^-$  - H pairs and O ( $\text{H}_2\text{O}$ ) - H pairs and O ( $\text{CO}_2$ ) - H pairs in the interlayer of Mg/Al  $\text{Cl}^-$  hydroxalcite computed from MD simulations. There are 84  $\text{CO}_2$  and 144  $\text{H}_2\text{O}$  in the interlayer region.

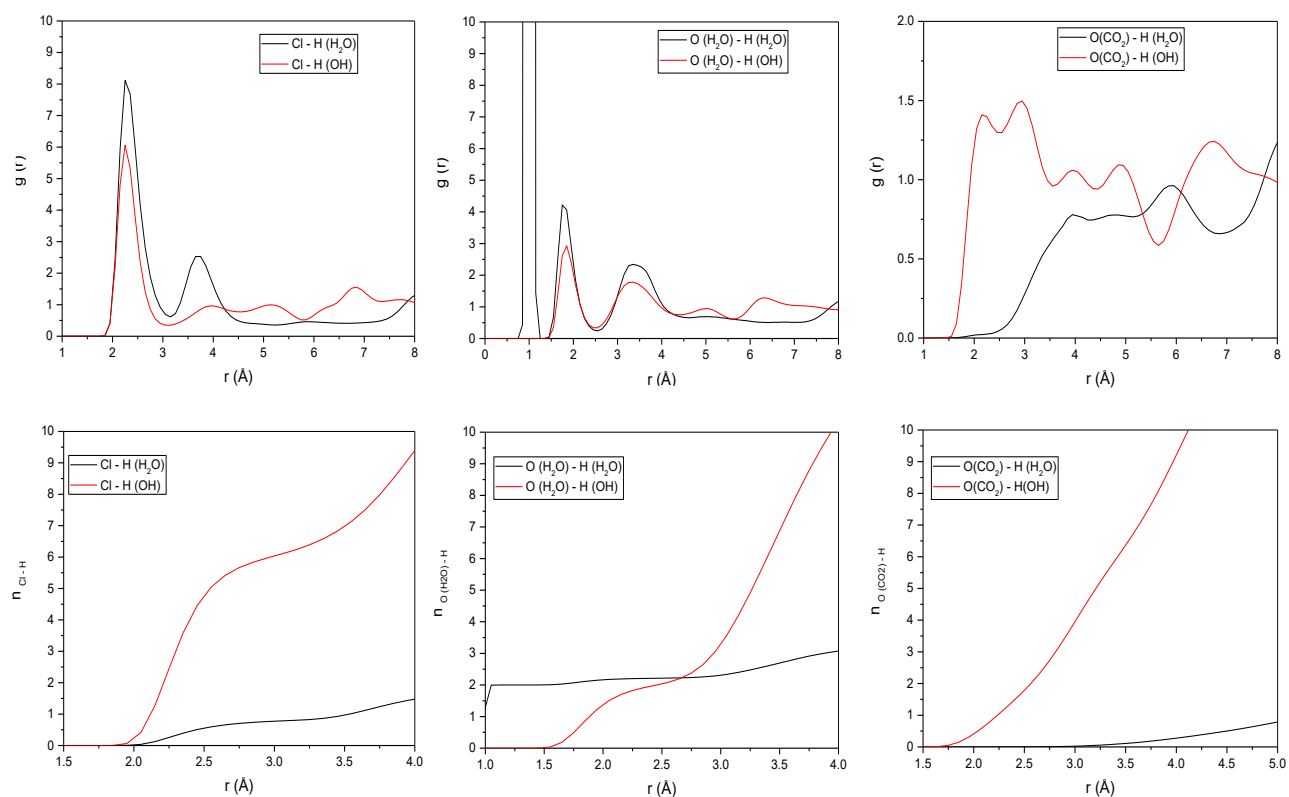


Figure B- 37 Pair Radial distribution functions and integrated nearest-neighbor coordination numbers for Cl<sup>-</sup> - H pairs and O (H<sub>2</sub>O) - H pairs and O (CO<sub>2</sub>) - H pairs in the interlayer of Mg/Al Cl<sup>-</sup> hydrotalcite computed from MD simulations. There are 120 CO<sub>2</sub> and 144 H<sub>2</sub>O in the interlayer region.

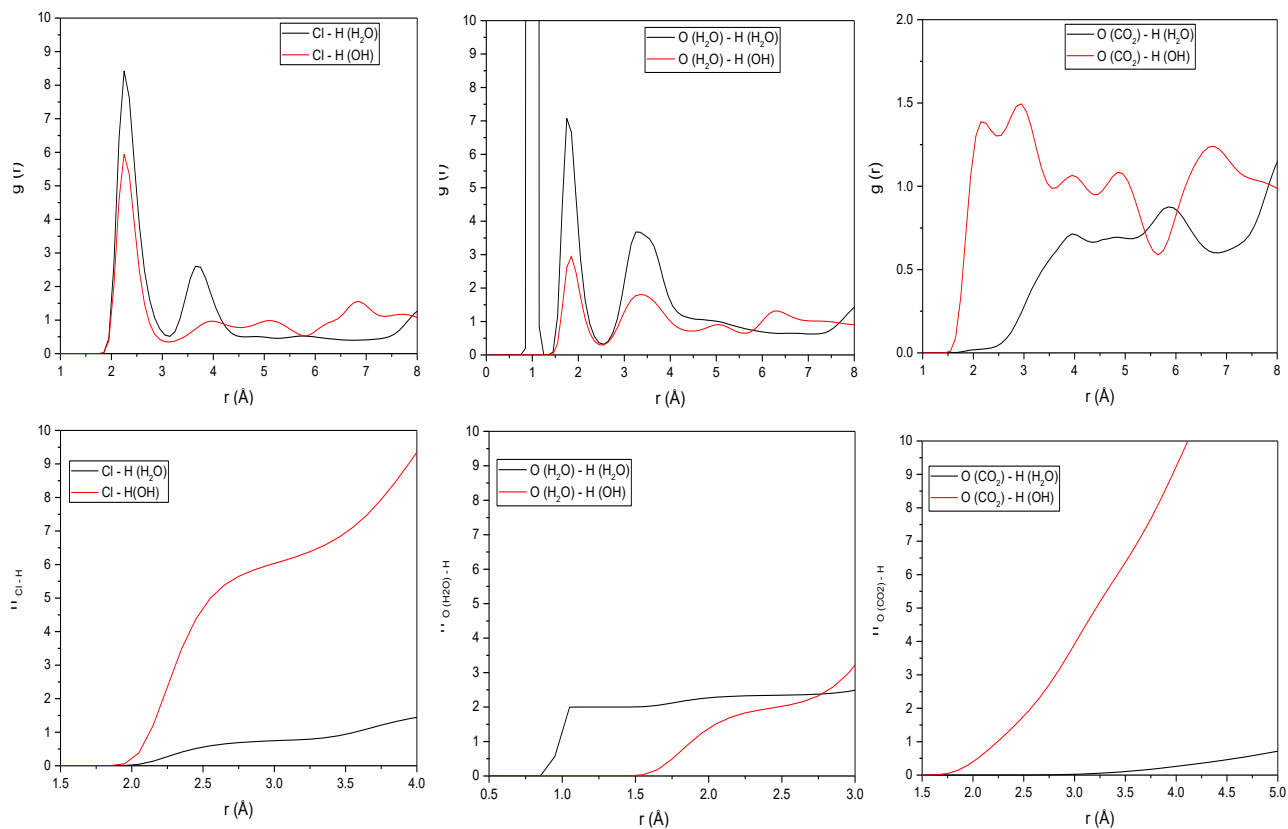


Figure B- 38 Pair Radial distribution functions and integrated nearest-neighbor coordination numbers for Cl<sup>-</sup> - H pairs and O (H<sub>2</sub>O) - H pairs and O (CO<sub>2</sub>) - H pairs in the interlayer of Mg/Al Cl<sup>-</sup> - hydrotalcite computed from MD simulations. There are 216 CO<sub>2</sub> and 144 H<sub>2</sub>O in the interlayer region.

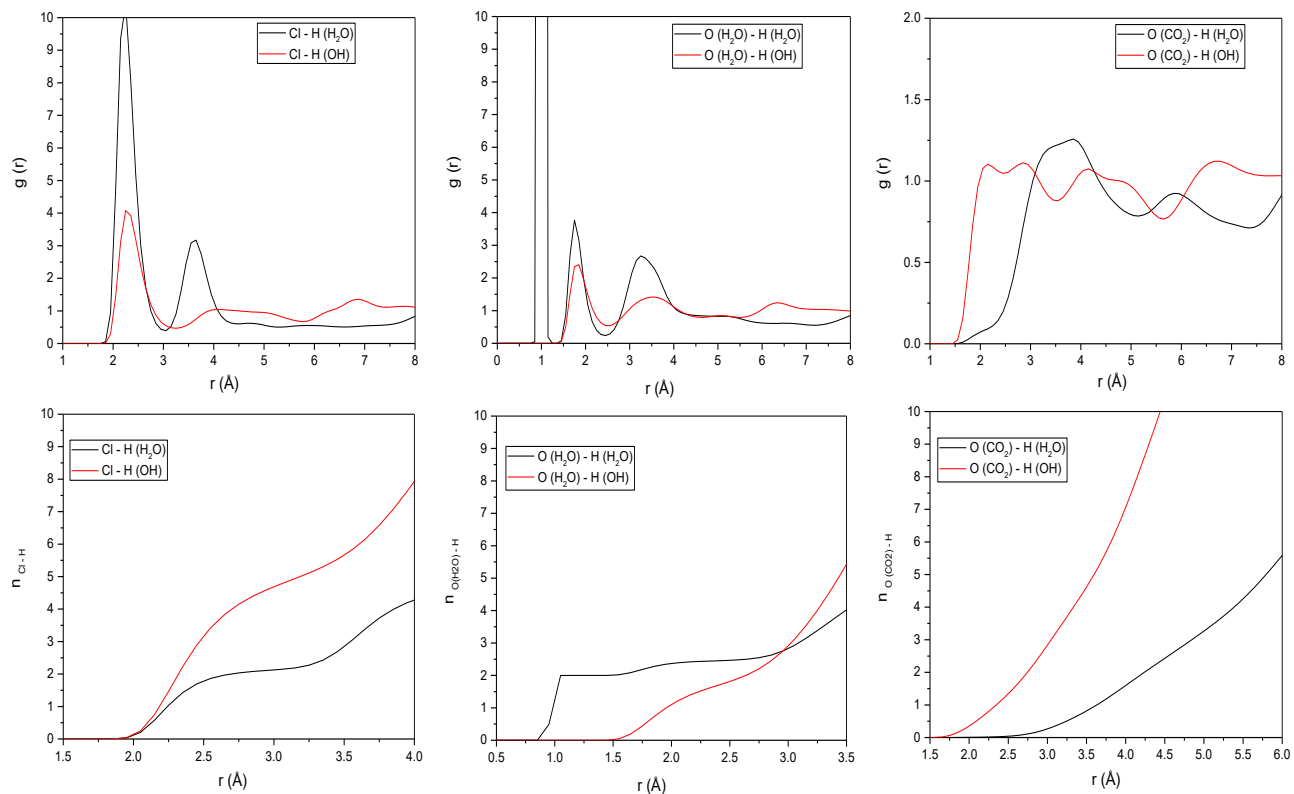


Figure B- 39 Pair Radial distribution functions and integrated nearest-neighbor coordination numbers for  $Cl^-$  - H pairs and O ( $H_2O$ ) - H pairs and O ( $CO_2$ ) - H pairs in the interlayer of Mg/Al  $Cl^-$  hydrotalcite computed from MD simulations. There are 432  $CO_2$  and 144  $H_2O$  in the interlayer region.

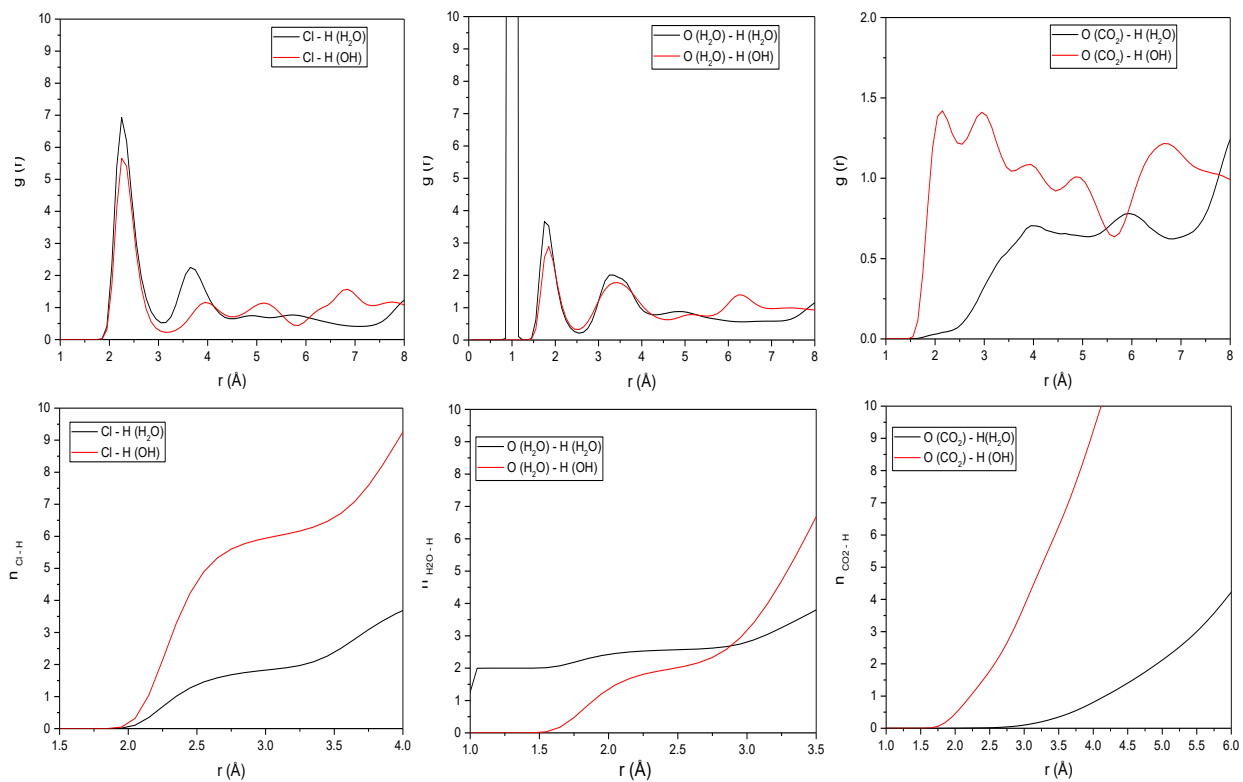


Figure B- 40 Pair Radial distribution functions and integrated nearest-neighbor coordination numbers for Cl<sup>-</sup> - H pairs and O (H<sub>2</sub>O) - H pairs and O (CO<sub>2</sub>) - H pairs in the interlayer of Mg/Al Cl<sup>-</sup> hydrocalcite computed from MD simulations. There are 36 CO<sub>2</sub> and 432 H<sub>2</sub>O in the interlayer region.

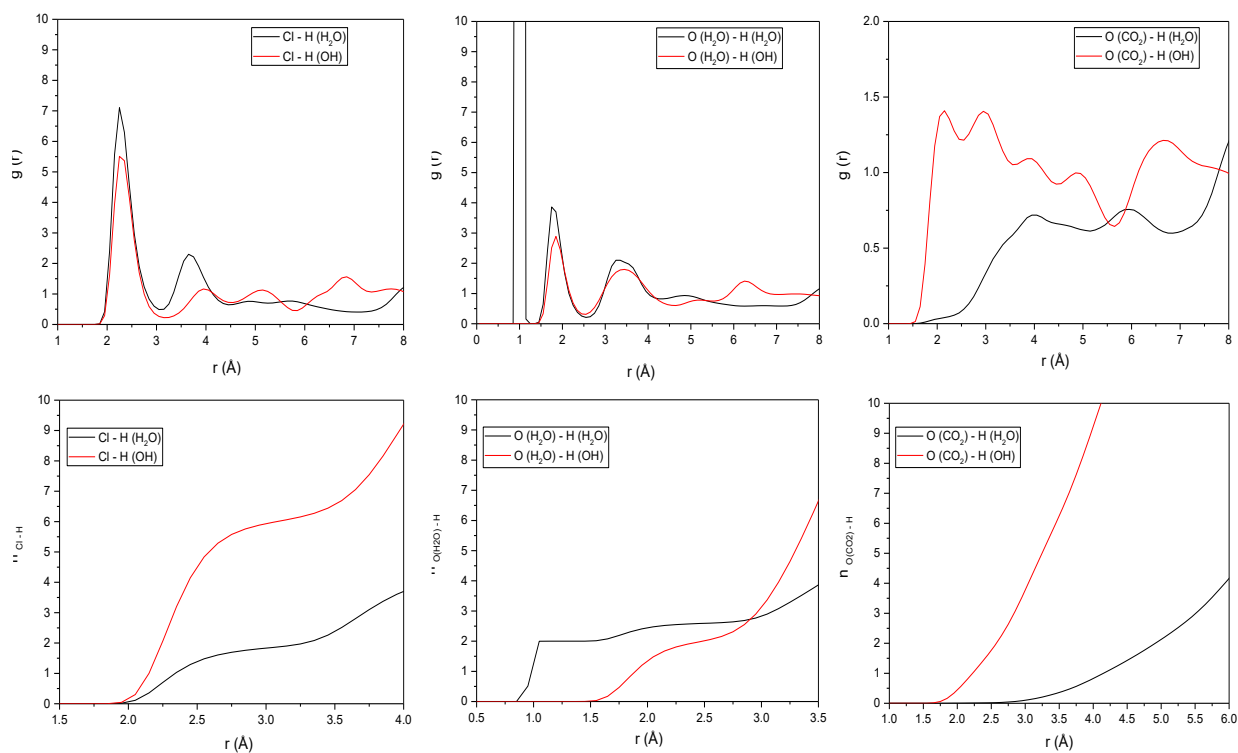


Figure B- 41 Pair Radial distribution functions and integrated nearest-neighbor coordination numbers for Cl<sup>-</sup> - H pairs and O (H<sub>2</sub>O) - H pairs and O (CO<sub>2</sub>) - H pairs in the interlayer of Mg/Al Cl<sup>-</sup> hydrocalcite computed from MD simulations. There are 84 CO<sub>2</sub> and 432 H<sub>2</sub>O in the interlayer region.

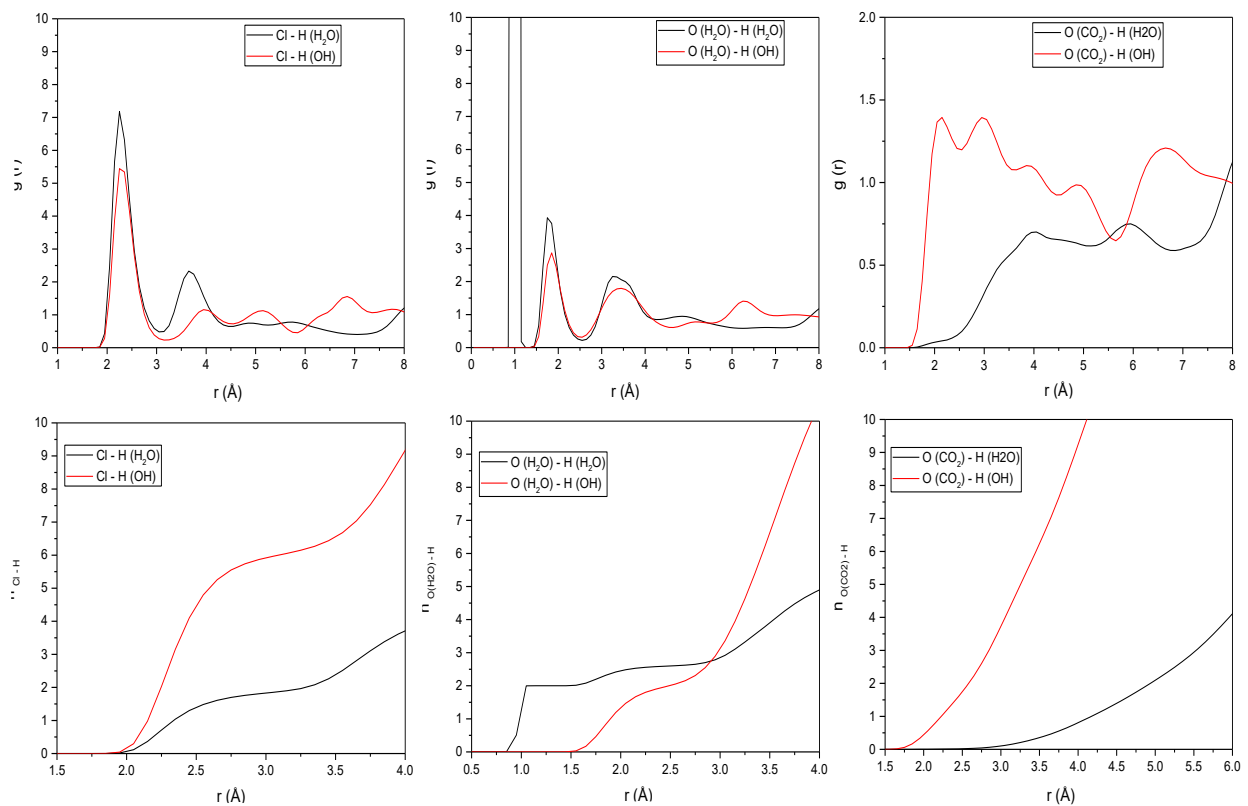


Figure B- 42 Pair Radial distribution functions and integrated nearest-neighbor coordination numbers for Cl<sup>-</sup> - H pairs and O (H<sub>2</sub>O) - H pairs and O (CO<sub>2</sub>) - H pairs in the interlayer of Mg/Al Cl<sup>-</sup> hydrotalcite computed from MD simulations. There are 120 CO<sub>2</sub> and 432 H<sub>2</sub>O in the interlayer region.

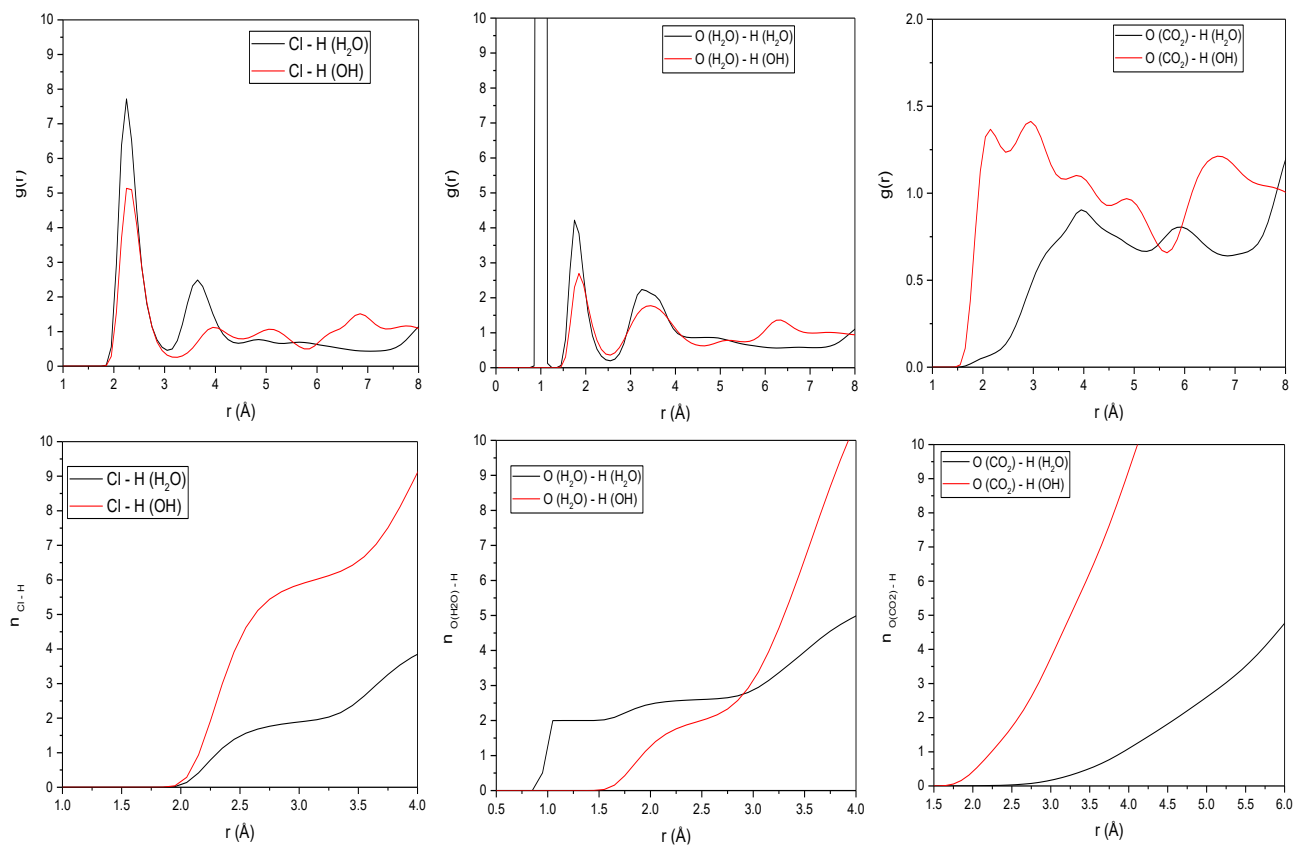


Figure B- 43 Pair Radial distribution functions and integrated nearest-neighbor coordination numbers for Cl<sup>-</sup> - H pairs and O (H<sub>2</sub>O) - H pairs and O (CO<sub>2</sub>) - H pairs in the interlayer of Mg/Al Cl<sup>-</sup> hydrotalcite computed from MD simulations. There are 216 CO<sub>2</sub> and 432 H<sub>2</sub>O in the interlayer region.

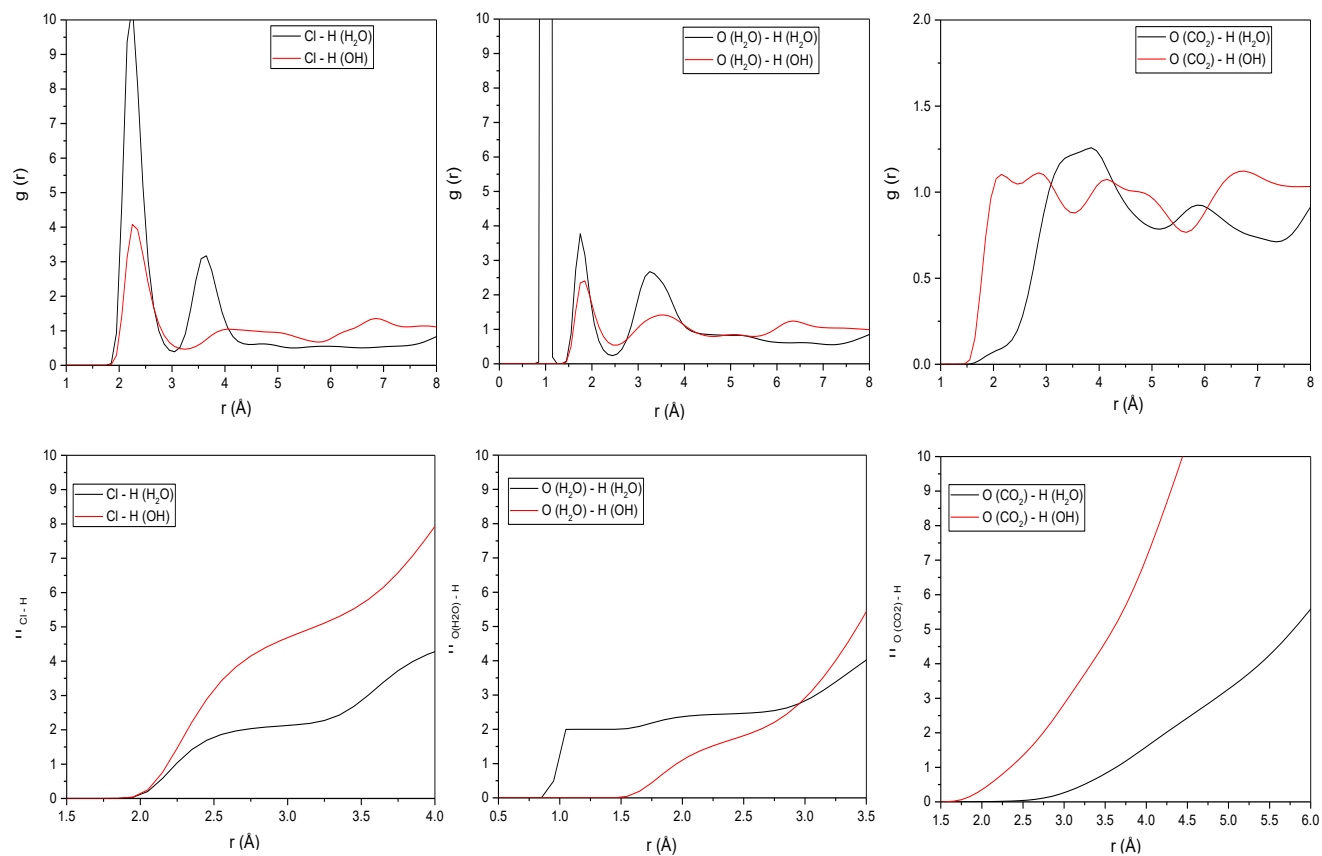


Figure B- 44 Pair Radial distribution functions and integrated nearest-neighbor coordination numbers for Cl<sup>-</sup> - H pairs and O (H<sub>2</sub>O) - H pairs and O (CO<sub>2</sub>) - H pairs in the interlayer of Mg/Al Cl<sup>-</sup> hydrotalcite computed from MD simulations. There are 432 CO<sub>2</sub> and 432 H<sub>2</sub>O in the interlayer region.

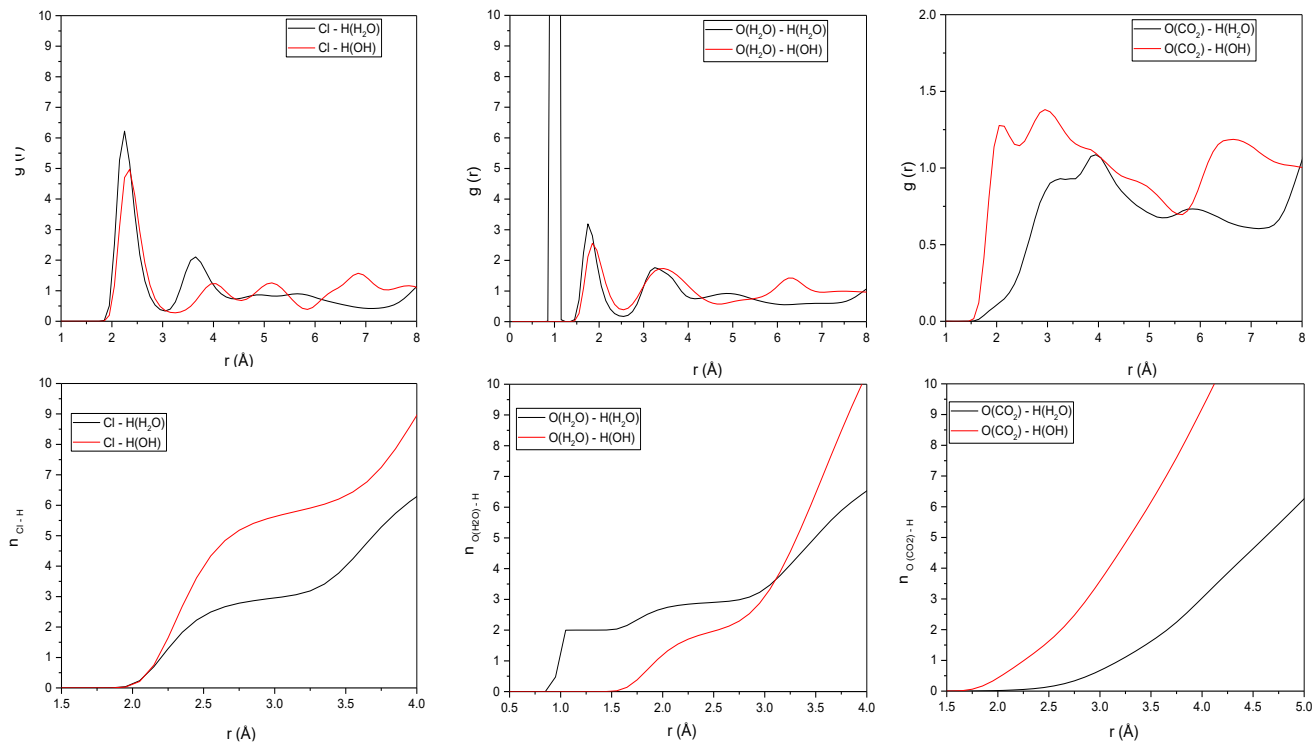


Figure B- 45 Pair Radial distribution functions and integrated nearest-neighbor coordination numbers for Cl<sup>-</sup> - H pairs and O (H<sub>2</sub>O) - H pairs and O (CO<sub>2</sub>) - H pairs in the interlayer of Mg/Al Cl<sup>-</sup> hydrotalcite computed from MD simulations. There are 36 CO<sub>2</sub> and 864 H<sub>2</sub>O in the interlayer region.

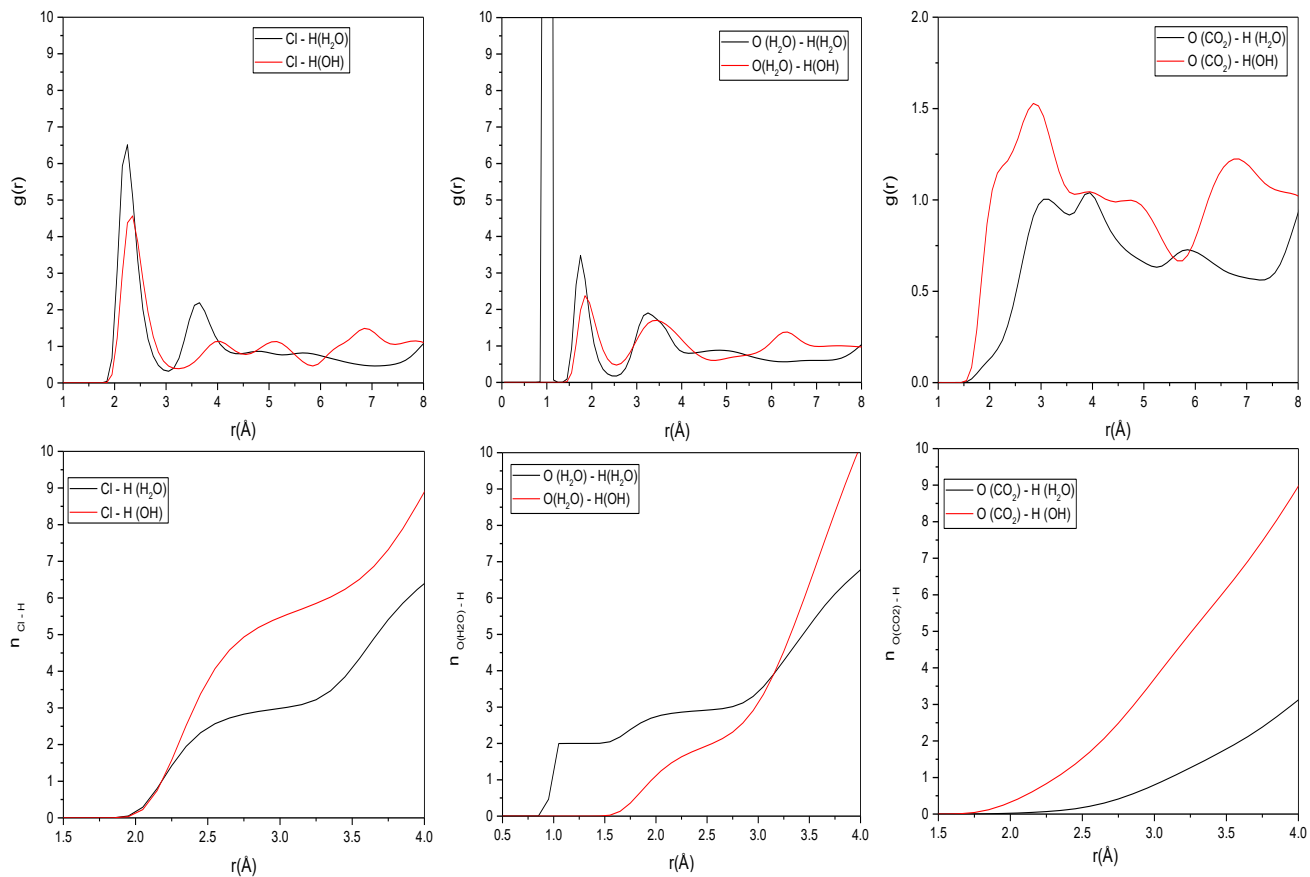


Figure B- 46 Pair Radial distribution functions and integrated nearest-neighbor coordination numbers for Cl<sup>-</sup> - H pairs and O (H<sub>2</sub>O) - H pairs and O (CO<sub>2</sub>) - H pairs in the interlayer of Mg/Al Cl<sup>-</sup> hydrotalcite computed from MD simulations. There are 84 CO<sub>2</sub> and 864 H<sub>2</sub>O in the interlayer region.

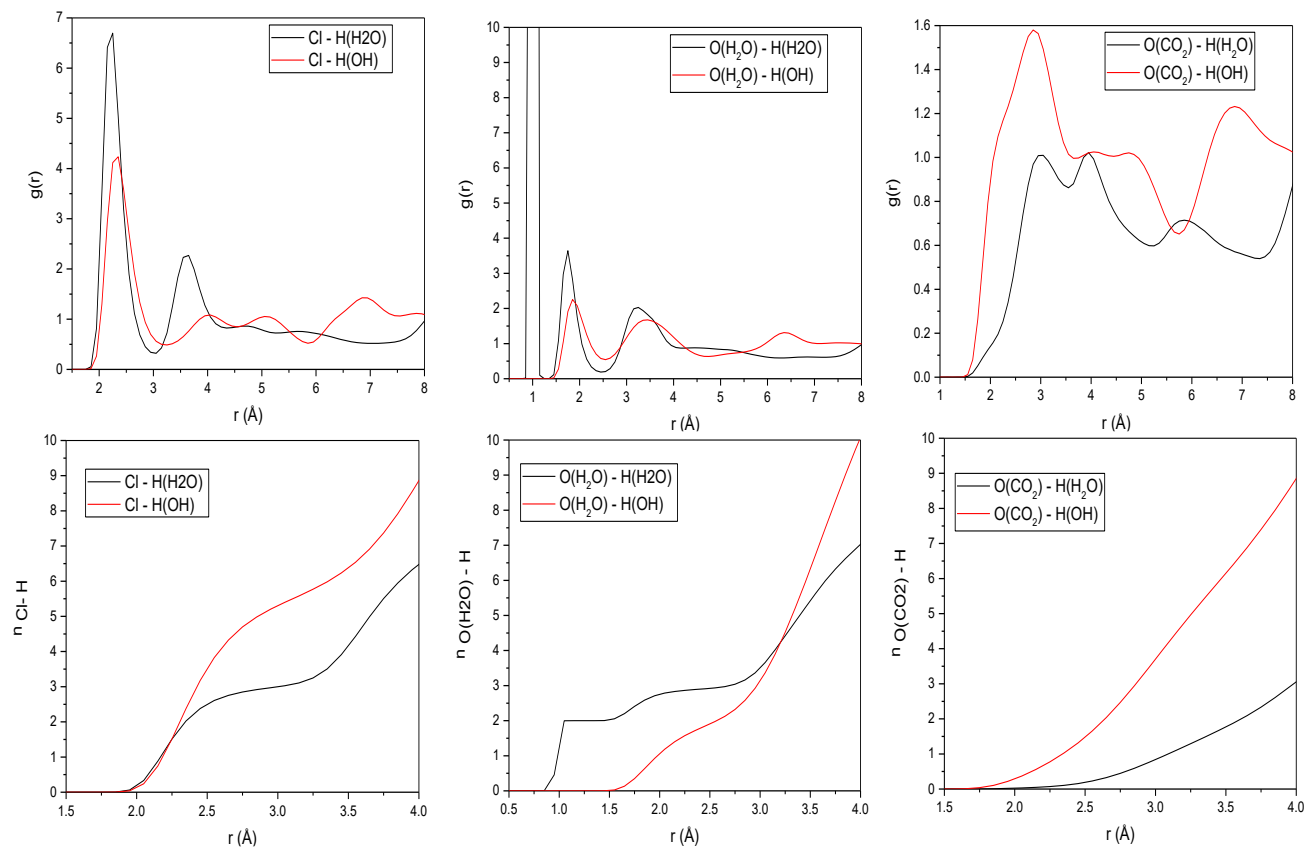


Figure B- 47 Pair Radial distribution functions and integrated nearest-neighbor coordination numbers for Cl<sup>-</sup> - H pairs and O (H<sub>2</sub>O) - H pairs and O (CO<sub>2</sub>) - H pairs in the interlayer of Mg/Al Cl<sup>-</sup> - hydrotalcite computed from MD simulations. There are 120 CO<sub>2</sub> and 864 H<sub>2</sub>O in the interlayer region.

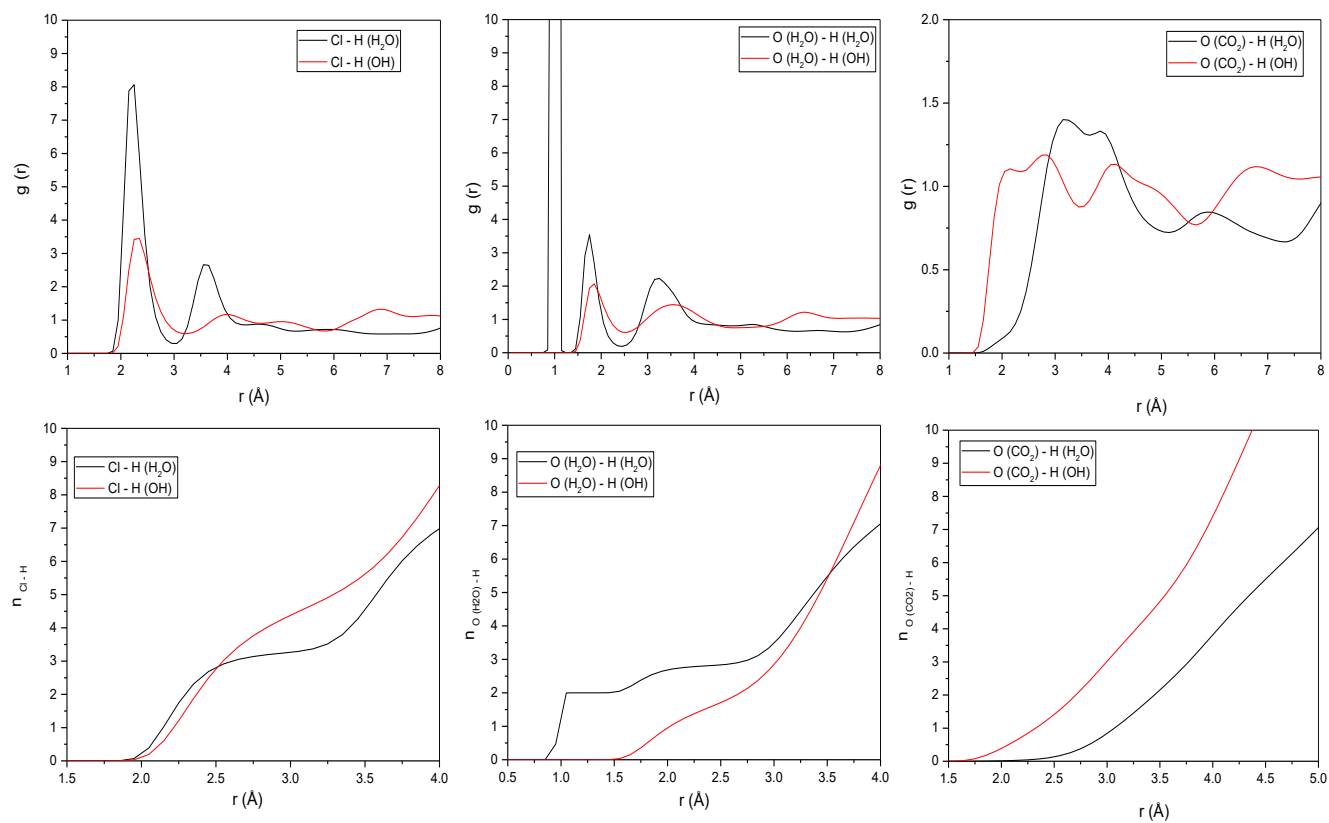


Figure B- 48 Pair Radial distribution functions and integrated nearest-neighbor coordination numbers for Cl<sup>-</sup> - H pairs and O (H<sub>2</sub>O) - H pairs and O (CO<sub>2</sub>) - H pairs in the interlayer of Mg/Al Cl<sup>-</sup> hydrotalcite computed from MD simulations. There are 216 CO<sub>2</sub> and 864 H<sub>2</sub>O in the interlayer region.

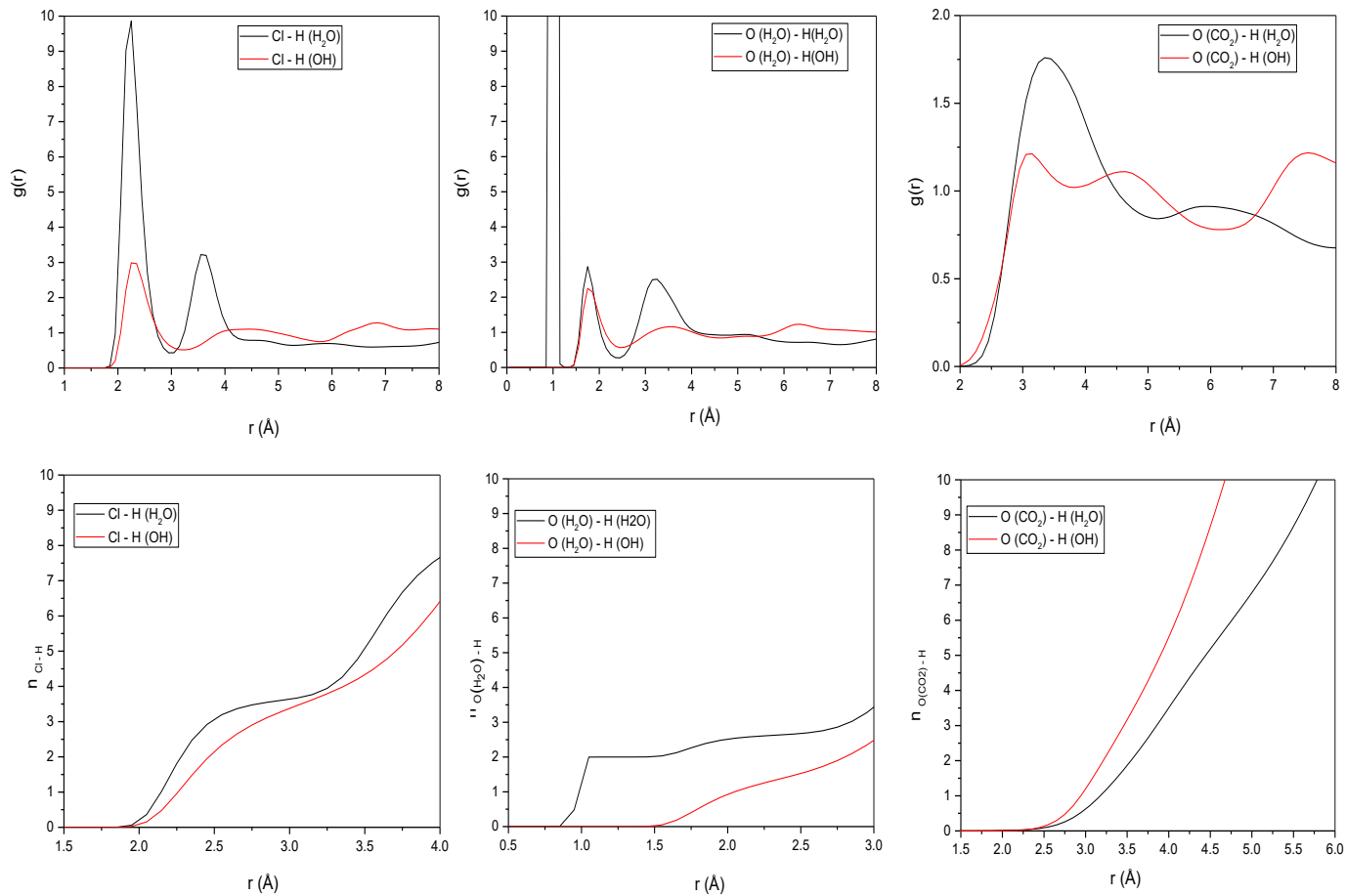


Figure B- 49 Pair Radial distribution functions and integrated nearest-neighbor coordination numbers for Cl<sup>-</sup> - H pairs and O (H<sub>2</sub>O) - H pairs and O (CO<sub>2</sub>) - H pairs in the interlayer of Mg/Al Cl<sup>-</sup> hydrocalcite computed from MD simulations. There are 432 CO<sub>2</sub> and 864 H<sub>2</sub>O in the interlayer region.